



UNIVERSITAT DE BARCELONA

Pharmaceutical development of nanosystems for the delivery of drugs in epidermis and hair follicles, skin biodistribution studies

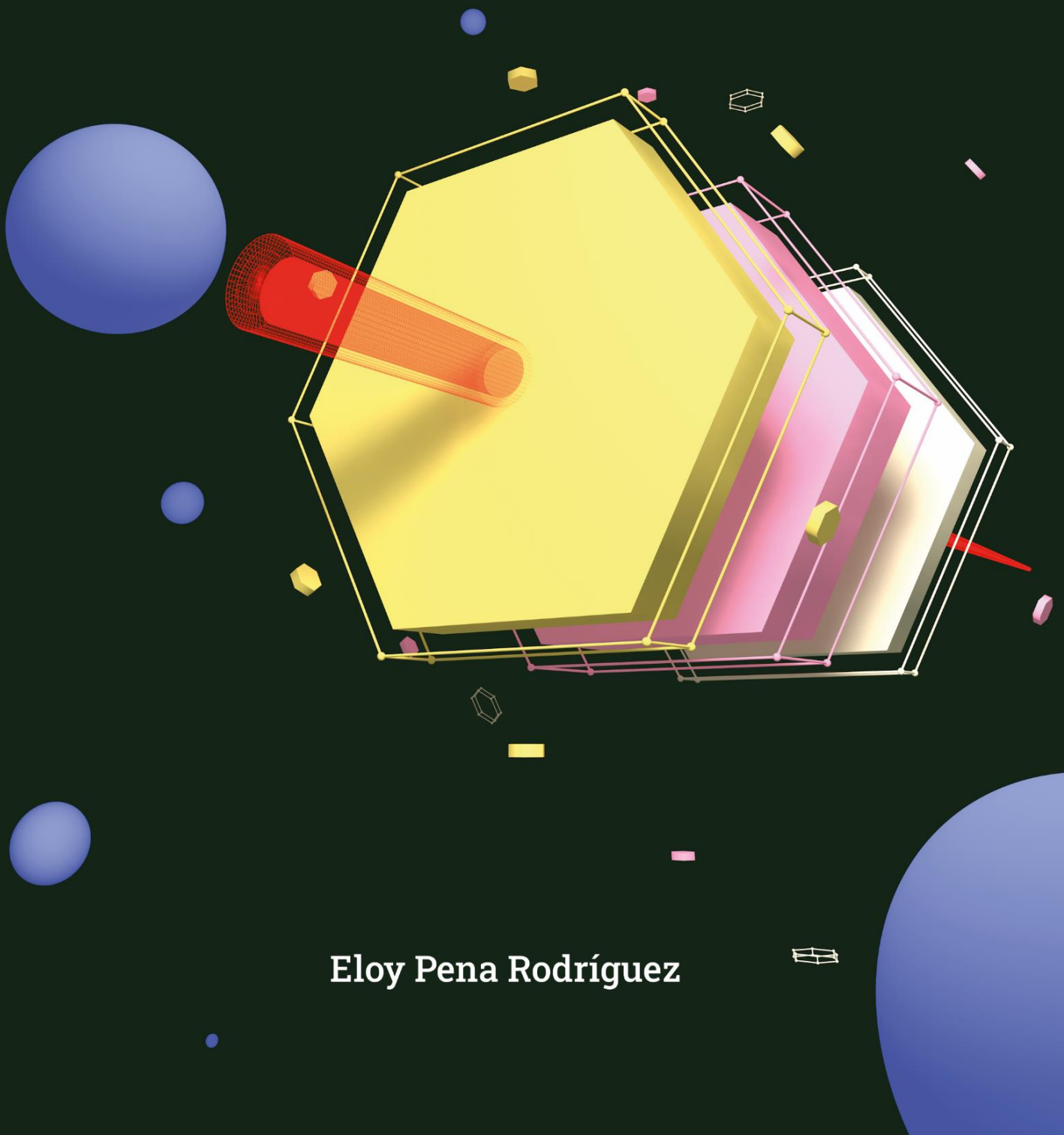
Eloy Pena Rodríguez

ADVERTIMENT. La consulta d'aquesta tesi queda condicionada a l'acceptació de les següents condicions d'ús: La difusió d'aquesta tesi per mitjà del servei TDX (www.tdx.cat) i a través del Dipòsit Digital de la UB (diposit.ub.edu) ha estat autoritzada pels titulars dels drets de propietat intel·lectual únicament per a usos privats emmarcats en activitats d'investigació i docència. No s'autoritza la seva reproducció amb finalitats de lucre ni la seva difusió i posada a disposició des d'un lloc aliè al servei TDX ni al Dipòsit Digital de la UB. No s'autoritza la presentació del seu contingut en una finestra o marc aliè a TDX o al Dipòsit Digital de la UB (framing). Aquesta reserva de drets afecta tant al resum de presentació de la tesi com als seus continguts. En la utilització o cita de parts de la tesi és obligat indicar el nom de la persona autora.

ADVERTENCIA. La consulta de esta tesis queda condicionada a la aceptación de las siguientes condiciones de uso: La difusión de esta tesis por medio del servicio TDR (www.tdx.cat) y a través del Repositorio Digital de la UB (diposit.ub.edu) ha sido autorizada por los titulares de los derechos de propiedad intelectual únicamente para usos privados enmarcados en actividades de investigación y docencia. No se autoriza su reproducción con finalidades de lucro ni su difusión y puesta a disposición desde un sitio ajeno al servicio TDR o al Repositorio Digital de la UB. No se autoriza la presentación de su contenido en una ventana o marco ajeno a TDR o al Repositorio Digital de la UB (framing). Esta reserva de derechos afecta tanto al resumen de presentación de la tesis como a sus contenidos. En la utilización o cita de partes de la tesis es obligado indicar el nombre de la persona autora.

WARNING. On having consulted this thesis you're accepting the following use conditions: Spreading this thesis by the TDX (www.tdx.cat) service and by the UB Digital Repository (diposit.ub.edu) has been authorized by the titular of the intellectual property rights only for private uses placed in investigation and teaching activities. Reproduction with lucrative aims is not authorized nor its spreading and availability from a site foreign to the TDX service or to the UB Digital Repository. Introducing its content in a window or frame foreign to the TDX service or to the UB Digital Repository is not authorized (framing). Those rights affect to the presentation summary of the thesis as well as to its contents. In the using or citation of parts of the thesis it's obliged to indicate the name of the author.

Pharmaceutical development of nanosystems for the delivery of drugs in epidermis and hair follicles, skin biodistribution studies.



Eloy Pena Rodríguez



UNIVERSITAT DE
BARCELONA

REIG  JOFRE



R&D Department - Reig Jofre Laboratories S. L.

Faculty of Biology - University of Barcelona

Industrial doctorate

HDK06 Biotechnology doctoral program

Pharmaceutical development of nanosystems for the delivery of drugs in epidermis and hair follicles, skin biodistribution studies

Memoria presentada por el doctorando Eloy Pena Rodríguez para optar al grado de doctor por la Universitat de Barcelona

PhD student: Eloy Pena-Rodríguez

Industrial doctoral director:

Dr. Francisco Fernández-Campos

Academic director:

Dra. Sandra Pérez Torras

Thesis tutor: Dr. Marçal Pastor Anglada

Acknowledgements

A la hora de agradecer, me gustaría separar entre el ámbito profesional y el personal:

En cuanto a lo profesional:

- A Mari, María y a Jodar, vosotros fuisteis en gran parte las manos de esta tesis, trabajar con personas tan proactivas y metódicas como vosotros es lo que hizo posible que hayamos llegado hasta aquí.
- A Fran, muchas gracias, por haber confiado en mí, por todo lo que me enseñaste a nivel técnico durante estos años.
- A Francesc, a Toni y a Mónica, muchas gracias por vuestros consejos farmacéuticos y por hacer más fácil el día a día.
- A Sandra, Aida, y Marçal gracias por vuestros bio-consejos y sobre todo por vuestra paciencia pese a todas las células que asesiné.

En cuanto a lo personal, tengo a demasiadas personas a las que agradecerle su apoyo, pero se lo agradeceré tan solo a las más importantes en mi vida, pues eso hace el agradecimiento más especial:

- Ao Dr. Manuel Pena, manda carallo que vaya a presentar todo este trabajo y aun así siga siendo el hermano tonto. Ya te lo dije varias veces pero que sepas que mi objetivo siempre será parecerme a ti.
- Á miña mamaiña e ao meu papaiño, por la infancia que me regalasteis, por el amor que me disteis siempre, por todo lo que representáis para mí, me es imposible expresarlo. Haceros sentir orgullosos a vosotros es la mayor de mis motivaciones.
- Al resto de mi familia, Bea, Candidiño, abuelas, abuelos, Vizoso, Beiña, Xianziño, Sariña, Pepoliño muchísimas gracias a todos.
- A Brión, imposible no agradecértelo, parecías un perro, pero nunca lo fuiste.
- Y bueno ya acabé. Es broma, a ti Sara, a concha na area, por hacerme la persona más feliz, te quiero para siempre.

“A personalidade de cada un vén sendo, por tanto, como un pequerrecho vagalume, como un lucecú que dá, na noite, un puntinho de brillo discreto. A escuridade é o termo que fai posible a existencia do bichiño” – Álvaro Cunqueiro



LIST OF ABBREVIATIONS

- %EE: Encapsulation efficiency percentage
- %LC: Loading capacity percentage
- %ME: Matrix effect percentage
- 5AR: 5 alpha-reductase
- AA: Areata alopecia
- AGA: Androgenic alopecia
- AHCI: arts and humanities citation index
- AIC: Akaike information criterion
- ANOVA: Analysis of variance
- API: Active pharmaceutical ingredient
- B: Bulge
- BAK: Benzalkonium chloride
- C: Capillary loop
- C6: Coumarin 6
- C_d : Concentration of the drug in the donor compartment
- CHCA: A-Cyano-4-hydroxycinnamic acid
- D1: First decile
- DEX: Dexamethasone
- DI: Deformability index
- DLS: Dynamic light scattering
- DMEM: Dulbecco's modified Eagke's medium
- DNA: Deoxyribonucleic acid
- DoE: Design of experiments
- DP: Dermal papilla
- DPCs: Dermal papilla cells
- DSC: Differential scanning calorimetry
- EA: Ethyl acetate
- EC: Ethyl cellulose
- EDTA: Ethylenediaminetetracetic acid
- EGF: Epidermal growth factor
- ESCI: Emerging source citation index
- ET: Ethanol absolute
- FBS: Fetal bovine serum
- FD: Freeze-drying
- FDM: Freeze drying microscopy
- FFD: Fractional factorial design
- F_{max} : Maximum fraction of active released
- FS: Follicle sheath
- G^* : Complex modulus
- G' : storage modulus
- G'' : loss modulus
- GirT: Girard's T reagent
- Gln: L-glutamine

- GMPs: Good manufacturing practices
- HEK: Human epidermal keratinocytes
- HPLC: High performance liquid chromatography
- HR: Relative humidity
- HS: Hair shaft
- ICH: International conference on harmonization
- IgG: Immunoglobulin G
- IHF: Immunohistofluorescence
- IL: Interleukin
- IRS: Inner root sheath
- IVPT: *In vitro* permeation test
- IVRT: *In vitro* release test
- JCR: Journal citation report
- JIF: Journal impact factor
- J_{sup} : transdermal flux at steady state
- K₁: First order coefficient
- K_H: Higuchi coefficient
- K_{KP}: Korsmeyer-Peppas coefficient
- K_p: Permeability coefficient
- KSF: Keratinocyte serum free
- LAT: Latanoprost
- LOD: Limit of detection
- LOQ: Limit of quantification
- LPNCs: Lipid core polymeric nanocapsules
- LPS: Lipopolysaccharide
- LRB: Lissamine Rhodamine B
- M: Arrector pili muscle
- MALDI-TOF-MSI: Matrix assisted laser desorption ionization time of flying mass spectrometry imaging
- MCT: Medium chain triglycerides
- MD: Medula
- MTT: 3-[4,5-dimethylthiazol-2-yl]-2,5 diphenyl tetrazolium bromide
- NaFl: Sodium fluorescein
- NLCs: Nanostructured lipid carriers
- NT-cream: Non-transfersome cream
- o/w: Oil in water
- OCT: Optimal cutting temperature compound
- ORS: Outer root sheath
- P₁: Diffusion-related parameter
- P₂: Partitioning-related parameter
- PBS: Phosphate buffer saline
- PCR: Polymerase chain reaction
- PDA: Photodiode array
- PDI: Polydispersity index
- PEG: Polyethylene glycol
- PF: Paraformaldehyde

List of abbreviations

- PLGA: Poly-lactic-co-glycolic acid
- PVDF: Polyvinylidene difluoride
- Q1: First quartile
- qs: Quantum satis
- Q_t : Permeated amount at time t
- r_m : Membrane pore radius
- RM: Receptor médium
- RNA: Ribonucleic acid
- ROI: Region of interest
- r_p : Extruded radius
- RP: Retinyl palmitate
- RT-PCR: Real time polymerase chain reaction
- S: diffusional area
- SC: Stratum corneum
- SCIE: Science citation index expanded
- SG: Sebaceous gland
- SLNPs: Solid lipid nanoparticles
- SSCI: Social sciences citation index
- t: time
- $\tan \delta$: Tangent of the phase angle
- T-cream: Transfersome cream
- TEM: Transmission electron microscopy
- TEWL: Transepidermal water loss
- TFA: Trifluoroacetic acid
- TIC: Total ion count
- T_{lag} : latency time
- TNF: Tumor necrosis factor
- TPBS: Tween 20 phosphate buffer saline
- UAB: Universidad Autónoma de Barcelona
- UB: Universidad de Barcelona
- USC: Universidad de Santiago de Compostela
- UV: Ultraviolet
- w/o: Water in oil
- w/w: weight per weight
- WNE: Non encapsulated amount
- WoS: Web of science
- WT: Total amount

Abstract

Different transdermal drug delivery platforms have been developed for epidermal and follicular targeting. Nanoformulations have been developed, optimised and physicochemically characterised with complementary techniques. In addition, studies have been carried out to characterise qualitatively and quantitatively their biodistribution in the skin using different techniques.

Retinyl palmitate (RP) transfersomes formulated in cream were developed and their skin biodistribution was evaluated. The transfersomes demonstrated a significant increase in the administration of RP to the epidermis. These results suggested that transfersomes may be an efficient vehicle for the delivery of retinoids to the inner layers of the skin such as the epidermis.

Ethyl cellulose lipomers were developed and optimised. Dexamethasone (DEX) was encapsulated into liposomes, which were biopharmaceutically evaluated. Skin was permeated with fluorescent-loaded lipomers, which showed follicular targeting, as revealed by confocal microscopy. Immunohistofluorescence studies of DEX-loaded lipomers (DEX-lipomers) also showed follicular targeting for DEX. The anti-inflammatory effects of DEX-lipomers were demonstrated *in vitro* in human keratinocyte cell cultures. The *in vitro* cytotoxicity of the nanoformulation was investigated.

DEX-lipomers were lyophilised. Then, they were loaded into a hydrogel to study the rheological, release and skin permeation profiles. The freeze-drying process modified the particle size, and the drug release and permeation properties were also altered. In addition, analyses of the cytotoxicity and anti-inflammatory effects of freeze dried (FD) and non-FD particles on human keratinocytes indicated no differences.

Nanostructured lipid carriers (NLCs) were successfully developed and optimised. Predictive models for their size and the polydispersity index (PDI) were obtained. A scale-up was performed with satisfactory results. The NLCs were stable, with a shelf-life of 36 months. The drug absorption-promoting effect of the NLCs was demonstrated by the increased permeation parameters when compared to the control of a hydroalcoholic drug solution after *in vitro* permeation tests (IVPT). Fluorescently labeled NLCs were developed and administered to the skin (human scalp and pig skin were used) to observe their qualitative biodistribution by fluorescence confocal microscopy. Accumulation in hair follicles was observed. Comparing the results in pig skin and human scalp, similar biodistributions were observed, with an accumulation of NLCs in sebaceous glands in the case of human skin. These results were confirmed by immunohistofluorescence after DEX encapsulation.

In vitro proliferation methods were developed in human epidermal keratinocytes (HEK001) and human hair follicle dermal papilla cells (DPCs) to screen the effects of different active ingredients. Cytotoxicity, proliferation, and anti-inflammatory efficacy of different free and nanoencapsulated active ingredients has been determined using the *in vitro* established screening platforms.

Nanotransfersomes were also successfully developed. Latanoprost, a prostaglandin analogue, was encapsulated in these flexible nanovesicles. In addition, fluorescently labelled nanotransfersomes were obtained with a hydrophobic fluorochrome intercalated in their membrane, and a hydrophilic fluorochrome encapsulated in their aqueous core. Ex vivo skin

biodistribution was studied in human scalp and pig skin. By means of confocal laser microscopy, it was observed that both fluorochromes increased their penetration, with similar patterns in both species, compared to fluorochrome solutions that did not contain nanotransfersomes. The nanotransfersomes were shown to be stable for 6 months under accelerated conditions (40°C/75% RH) and for 12 months under long-term conditions (25°C/60% RH), showing no differences in vesicle size or polydispersity when latanoprost was encapsulated. A scale-up study was performed with the sonication method to evaluate significant variables. It was possible to obtain predictive models that allowed determining the amount of energy required per L of batch to obtain the desired size and Pdl.

Human scalp permeations were performed with DEX-lipomers and Free-DEX. DEX and benzalkonium chloride (BAK) calibrators and skin cryo-sections were analysed to study quantitatively the biodistribution of encapsulated DEX and BAK as a tracer of lipomers by confocal Raman and matrix-assisted laser desorption ionisation - time-of-flight mass spectrometry imaging (MALDI-TOF MSI). In Confocal Raman it was not possible to quantify BAK, but the amount of DEX quantified was significantly higher than in MALDI-TOF-MSI. Both techniques were compared as tools to study the quantitative skin biodistribution of different compounds. MALDI-MSI was very useful when analysing larger regions within a tissue, while Confocal Raman allowed to obtain biodistributions of smaller regions but with higher spatial resolutions.

INDEX

LIST OF ABBREVIATIONS.....	3
Abstract	6
INDEX.....	8
Chapter 1 – Introduction.....	12
1.1. Skin structure	12
1.1.1. Epidermis.....	13
1.1.2. Dermis	13
1.1.3. Hipodermis	13
1.2. Skin appendages.....	14
1.2.1 Hair follicles	14
1.2.2. Skin glands.....	15
1.2.2.1. Sebaceous glands	15
1.2.2.2. Sweat glands	15
1.3. Skin penetration pathways	15
1.4. Nanotechnology in dermatology.....	17
1.4.1. Liposomes.....	17
1.4.2. Nanostructured Lipid Carriers (NLC)	18
1.4.3. Polymer nanoparticles	19
1.4.4. Nanoemulsions.....	20
1.5. Epidermal and follicular targeting.....	20
1.5.1. Epidermal targeting.....	20
1.5.2. Follicular targeting	20
1.6. <i>In vitro</i> release and permeation tests.....	22
1.7. Biodistribution studies	22
1.7.1. Qualitative biodistribution techniques	22
1.7.1.1. Fluorescence Microscopy and Confocal Fluorescence Microscopy.....	23
1.7.1.2. Immunohistofluorescence	24
1.7.2. Quantitative biodistribution techniques.....	25
1.7.2.1. Confocal Raman Microscopy.....	25
1.7.2.2. Maldi Imaging.....	26
1.8. Bibliography	27
Chapter 2 -Aims.....	32
Thesis director's report on the impact factor of published articles and the participation of the doctoral candidate in each published article	33

Chapter 3. Epidermal delivery of retinyl palmitate loaded transfersomes: penetration and biodistribution studies	39
Chapter 4. Dexamethasone-loaded lipomers: development, characterization, and skin biodistribution studies	54
Chapter 5. The physicochemical, biopharmaceutical, and <i>in vitro</i> efficacy properties of freeze-dried dexamethasone-loaded lipomers	74
Chapter 6. Nanostructured lipid carriers	96
6.1. Introduction	97
6.2. Materials	98
6.3. Methods	99
6.3.1. Production of ██████-loaded NLCs.....	99
6.3.2. Physicochemical characterisation	100
6.3.3. High Performance Liquid Chromatography	101
6.3.4. Design of experiments and response surface regression at the laboratory scale ..	101
6.3.5. Design of experiments during the scale-up of Finasteride-loaded NLCs	102
6.3.6. Stability studies	103
6.3.7. <i>In vitro</i> permeation tests in dermatomised pig skin	103
6.3.8. <i>In vitro</i> penetration tests with full-thickness pig skin and human scalp.....	104
6.3.9. Confocal fluorescence microscopy to study NLC biodistribution	105
6.3.10. Immunohistofluorescence to study NLC biodistribution	105
6.4. NLCs Results and discussion	107
6.4.1. Design of experiments and response surface regression at the laboratory scale ..	107
6.4.2. Pilot plant scale-up production of ██████-loaded NLCs.....	114
6.4.3. Stability studies	116
6.4.4. <i>In vitro</i> permeation tests on dermatomised pig skin	118
6.4.5. Confocal Fluorescence Microscopy NLCs Biodistribution	120
6.4.6. Immunohistofluorescence to study NLC biodistribution	125
6.5. Conclusions	127
6.6. Bibliography	128
Chapter 7 - <i>In vitro</i> cell culture research.....	130
7.1. Introduction	130
7.2. Materials	130
7.3. Methods	131
7.3.1. DPCs and HEK cell maintenance.....	131
7.3.2. HEK001 cells and DPCs proliferation set up.....	131
7.3.3. <i>In vitro</i> HEK001 cell viability assays with finasteride, minoxidil and ebastine.....	132
7.3.4. <i>In vitro</i> DPCs viability assays with finasteride, minoxidil and testosterone.....	132

7.4. Results	133
7.4.1. HEK001 and DPCs proliferation set up	133
7.4.2. <i>In vitro</i> HEK001 cell viability assays with finasteride, minoxidil and ebastine.....	134
7.4.3. <i>In vitro</i> DPCs viability assays with finasteride, minoxidil and testosterone.....	135
7.5. Conclusions	136
7.6. Bibliography	137
Chapter 8 - Latanoprost-loaded nanotransfersomes for scalp administration: Scale-up and biopharmaceutical studies	138
Chapter 9 - <i>Ex vivo</i> MALDI-TOF mass spectrometry imaging and confocal Raman spectroscopy for the quantitative analysis of the skin biodistribution of dexamethasone-loaded nanoparticles.....	169
9.1. Introduction	170
9.2. Materials	171
9.3. Methods	172
9.3.1. Manufacturing of DEX- loaded lipomers.....	172
9.3.2. Physicochemical characterisation	172
9.3.3. Full thick human scalp <i>In vitro</i> penetration tests.....	172
9.3.4. Cryosectioning.....	172
9.3.5. H&E Staining.....	173
9.3.6. MALDI-TOF set up	173
9.3.7. On tissue and out of tissue DEX and BAK Calibrators for MALDI and Confocal Raman quantification	173
9.3.8. Confocal Raman spectroscopy	175
9.3.9. DEX derivatisation for MALDI-TOF detection.....	177
9.3.10. MALDI-TOF spectrometry.....	177
9.4. Results and discussion.....	178
9.4.1. Confocal Raman microscopy	178
9.4.2. MALDI-TOF set up	181
9.4.3. MALDI-MSI and quantification.....	183
9.4.4. Confocal Raman and MALDI-MSI comparison	189
9.5. Conclusions	190
9.6. Bibliography	191
Chapter 10 - Overall discussion of the results obtained	193
10.1. Physico-chemical comparison of nanoparticles	193
10.2. Scalability of nanoparticles	196
10.3. <i>In vitro</i> cell culture studies	197
10.4. Biodistribution comparison of nanoparticles.....	197

10.5. *Ex vivo* skin quantitative techniques setting up and comparison 199

10.6. Bibliography 202

Chapter 11 - Conclusions..... 203

Chapter 12 – RESUMEN GLOBAL..... 204

Annex 1 - Transungual delivery, anti-inflammatory activity, and *in vivo* assessment of a cyclodextrin polypseudorotaxanes nail lacquer..... 207

Chapter 1 – Introduction

The skin, the largest organ in human beings, forms a highly efficient physical and immunological barrier. The skin is also a complex organ, with different delivery routes and regions that can be targeted. One of the biggest challenges in this regard is getting large enough quantities of drugs to reach target sites within the skin. The administration of drugs through the topical route avoids the obstacles common in the oral route such as the hepatic first-pass effect, variations in gastric pH and fluctuations in plasma levels, among others. The use of pharmaceutical and cosmetic formulations based on nanotechnology is one of the most important technological approximations to achieve this goal. Furthermore, nanoformulations can help produce different benefits such as a reduction in adverse effects, an increase in bioavailability and a reduction in the administration frequency due to sustained and localised release or an increase in the stability of the drug in the skin microenvironment or in the pharmaceutical form.

The precise and robust study of skin penetration and biodistribution is necessary for the correct development of new formulations and the evaluation of their effectiveness in delivering drugs to target sites in the skin. For ethical reasons, data collection for skin biodistribution studies is usually performed *in vitro* or *ex vivo*.

1.1. Skin structure

The skin is a complex barrier structure composed of different cell types (for example, keratinocytes) and interkeratinocyte substances in several differentiated layers and cutaneous annexes and subdermal structures. The skin can be divided into three layers: the epidermis, dermis and hypodermis (Figure 1).

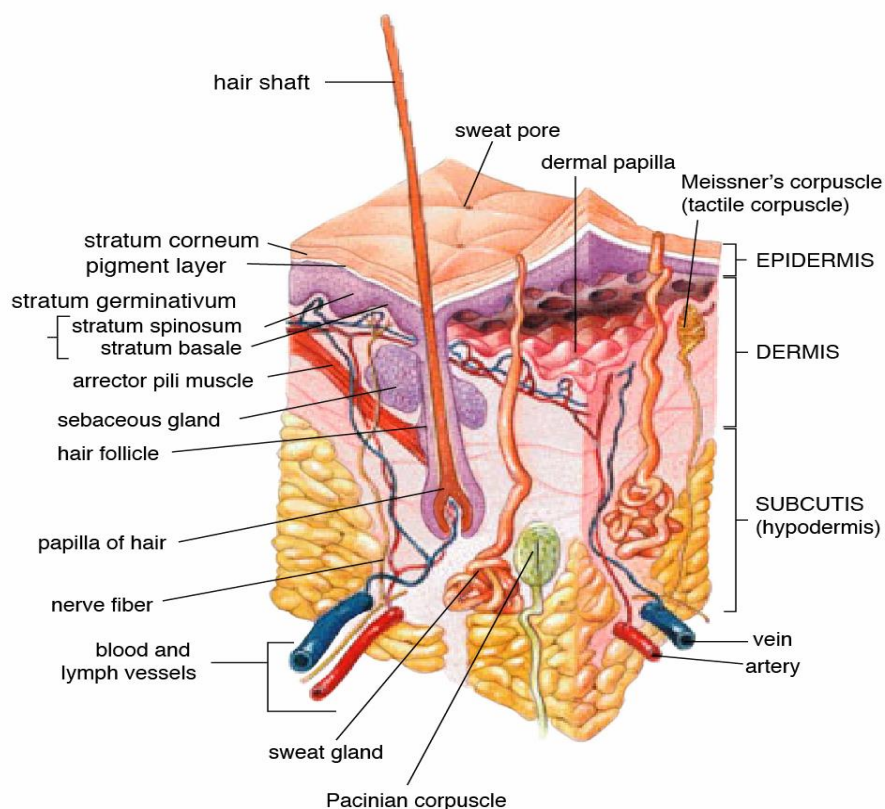


Figure 1 Anatomy of human skin. [Training.seer.cancer.gov](https://www.training.seer.cancer.gov/), via Wikimedia Commons, public domain licence

The most superficial layer, the epidermis, is made up mainly of keratinocytes. Collagen is a fibrillar type protein and is the main component of the middle layer, the dermis. The deepest layer, the hypodermis, is composed of fat cells or lipocytes among other substances. The thickness of these layers varies depending on the area of the body. For example, the epidermis measures about 0.1 mm in the eyelid area and approximately 1.5 mm in other areas such as the palm of the hand or the sole of the foot [Paul A. J. et al 2011, S. W. Lanigan et al 2010].

1.1.1. Epidermis

The epidermis is constantly regenerating from epidermal stem cells. This regeneration is responsible for maintaining homeostasis thanks to natural exfoliation. It contains different types of cells, with approximately 95% being keratinocytes and the remaining being melanocytes, Langerhans cells and Merkel cells. The epidermis does not contain blood vessels. Thus, nutrients reach this layer through the diffusion of the blood vessels present in the dermis. The keratin produced by keratinocytes belongs to a family of 30 proteins, which are found in different areas of the epidermis depending on the state of differentiation. The cells become elongated and thinner as they differentiate towards the most superficial part of the skin [S. W. Lanigan et al 2010]. The epidermis is made up of different sublayers:

- Stratum corneum: the outermost layer of the skin that is responsible for the barrier function and the low penetration of many drugs. It is formed by a matrix, between 10 and 20 μm thick, of dead and dehydrated corneocytes that is embedded in a highly ordered lipid bilayer. The main lipid components are ceramides (45-50%), free fatty acids (25%) and cholesterol (5%) [Ritu Goyal et al. 2015, Clive R. Harding et al. 2004].
- Viable epidermis: this is located below the stratum corneum and is made up of 4-5 layers of fibroblasts and keratinocytes. It is usually about 60-150 μm thick, but it can be thicker in some other parts of the body such as the palms of the hands or soles of the feet because the epidermis there contains an extra layer, the stratum lucidum [Ritu Goyal Et al. 2004].

1.1.2. Dermis

Located below the epidermis, the dermis is a fibrous layer of the skin, made up of collagen fibres, elastic fibres, blood vessels, ground substances, fibroblasts, histiocytes, dermal dendrocytes, mast cells, nerves and lymphatic vessels.

Collagen fibres provide toughness and mechanical support to the skin. Elastic fibres are arranged in all directions, which provide flexibility to the skin. The damage produced in these fibres by ultraviolet light during ageing is responsible for the appearances of wrinkles. The blood vessels present in the dermis allow the arrival of nutrients from the blood and help to maintain the body temperature. The ground substance is the matrix that supports the collagen and elastic fibres. It holds water and allows the passage of nutrients through the dermis. The nerves present in the dermis are responsible for cutaneous sensations. The soft musculature of the skin (the arrector pili muscle) allows the erection of hair, which serves to trap warm air in the skin and protect it from the cold [S. W. Lanigan et al 2010].

1.1.3. Hipodermis

The hypodermis is the deepest layer of the skin. It consists of lipocytes or fat cells, separated by connective tissue containing large blood vessels and collagen. This layer stores energy and provides buoyancy to the skin [Paul A. J. Et al 2011].

1.2. Skin appendages

1.2.1 Hair follicles

The hair follicle itself is a small but complex organ. More than 20 different mesenchymal and epithelial cells coexist in each hair follicle. The dimensions and proportions of each hair follicle vary depending on the mammalian species and the anatomical region in which they are located. The hair follicle can be divided into the superficial permanent zone and the transient cyclic component of the bulb zone. The anatomical line dividing these two regions is the bulge (B), located below the arrector pili muscle (M). The pilosebaceous unit consists of the hair shaft (HS), together with the M and the sebaceous gland (SG). The region from the skin surface to the opening of the sebaceous gland is called the infundibulum. The isthmus is the region dividing the aperture of the SG and the B.

Figure 2 shows the different anatomical parts of a hair follicle. The permanent hair follicle zone is the region that runs from the surface of the skin to the bulge and does not undergo significant cyclical changes. The cycling part, which goes from the lower part of the bulge to the deepest part of the hair follicle, is formed of the bulb and suprabulb regions. There are inner (IRS) and outer (ORS) root sheaths within the cycling part. The ORS extends from the bulb to the opening of the SG. The IRS is formed of three keratinised layers (Henle's layer, Huxley's layer and the cuticle) and controls the shape and structure of the hair.

There are also nerve endings that allow pilo-neural interactions of the hair follicle [**Montagna W, et al 1958**]. Hair growth depends on the proliferation of the keratinocyte matrix, which pushes the hair shaft to the surface. These keratinocytes are located in the bulb region and lie on the dermal papilla cells (DPCs). DPCs play a very important role as signalling centres in hair follicles as they are involved in hair growth and the formation of new follicles. The capillary loop (C), located at the base of the bulb, is responsible for the supply of nutrients to the hair follicle.

Hair follicles can be vellus or terminal. In vellus follicles, unlike in terminal follicles, the HS is composed of a medulla (MD). In addition, vellus follicles are not irrigated by capillary loops, but terminal follicles are.

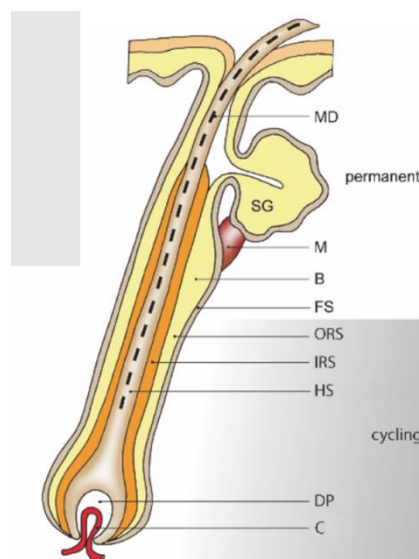


Figure 2 Schematic representation and terminology of the hair follicle. The hair follicle, together with the sebaceous gland (SG) and the arrector pili muscle (M), make up the so-called pilosebaceous unit. As for the follicle sheath (FS), it is composed of concentric layers of inner and outer sheaths (IRS and ORS) surrounding the hair shaft (HS). The bulge (B) is the anatomical line on which lies the M. The deepest part contains the bulb where the dermal papilla (DP) and

the capillary loop (C), responsible for the supply of nutrients to the hair follicle, are located. The MD is the medulla, present in the vellus HS. Image taken from [Annika Vogt et al. 2008 Hair Growth and disorders Chapter 1].

1.2.2. Skin glands

The skin contains sweat and sebaceous glands. The main function of the sweat glands is human thermoregulation. It is also believed that sweat glands may have an excretory role, similar to that of the renal apparatus, although there is no scientific evidence about the excretory efficiency of these glands. The main function of the sebaceous glands is to secrete sebum through the hair follicles.

1.2.2.1. Sebaceous glands

The sebaceous glands are attached to hair follicles in different parts of the body, such as the face, upper chest and back. They are formed from sebaceous stem cells that lie between the bulge of the hair follicle and the orifice that joins the gland to the follicle. These stem cells differentiate into sebocytes, which are responsible for secreting sebum through the orifice into the hair follicle. In diseases such as acne, the sebaceous glands, influenced by androgens, oversecrete sebum.

1.2.2.2. Sweat glands

There are two types of sweat glands, the eccrine glands and the paracrine glands:

- Eccrine sweat glands have a function in thermoregulation through the cooling effect of sweat production and through the secretion of electrolytes. These thermoregulatory phenomena can occur either as a response to an illness (through fever) or, for example, during sweating when exercising.
- Unlike eccrine glands, paracrine glands secrete sweat autonomously (i.e., release of part of the cytoplasm). This occurs in areas such as the axillae, groin, soles, palms and inframammary areas. This sweating mechanism is controlled autonomously, for example, in a stressful situation.

1.3. Skin penetration pathways

Percutaneous/dermal absorption consists of the passage of compounds through the skin. It can be described in three steps: penetration or entry of a substance into any layer of the skin; permeation, which consists of transport from one membrane to another; and resorption, which consists of uptake into the vascular system. The mechanisms of molecular penetration through the skin can be divided into transport through the stratum corneum and through cutaneous appendages (Figure 3).

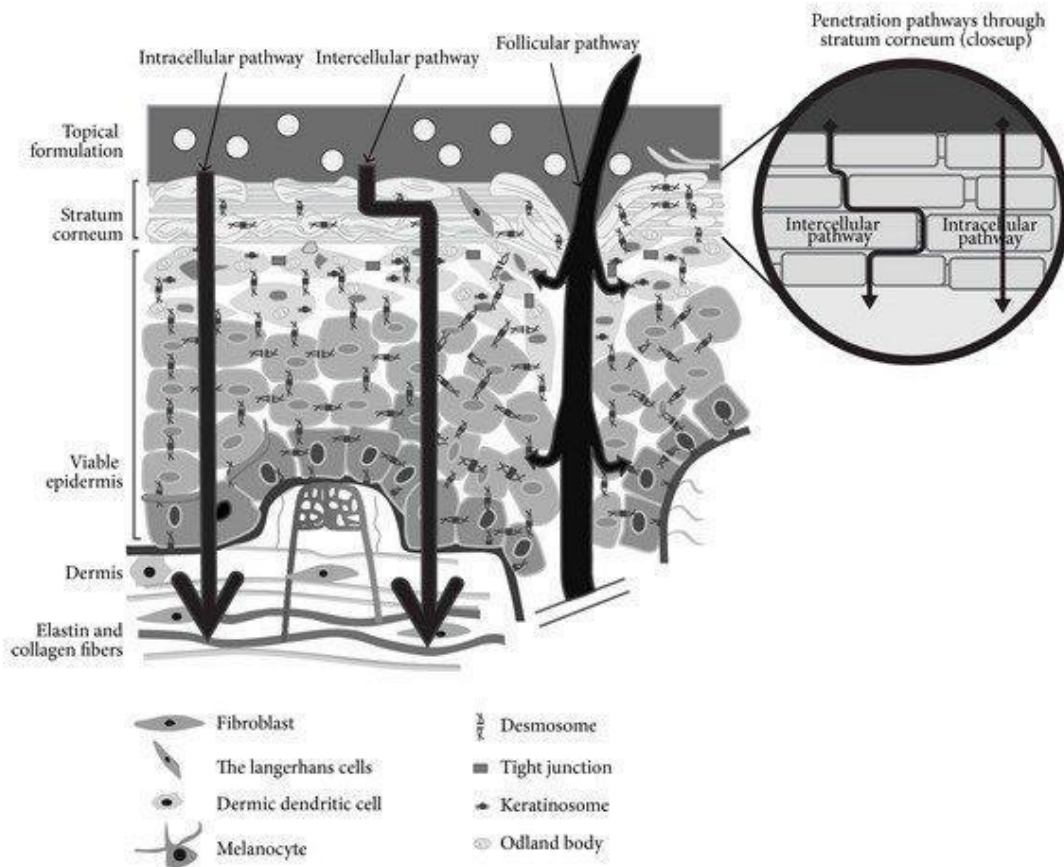


Figure 3 Skin penetration pathways (intracellular, intercellular, and follicular) [Marie-Alexandrine Bolzinger et al. 2012].

Transport through the transappendageal or follicular route is gaining interest. Invaginations provide an increase in surface area and are surrounded by blood capillaries, increasing systemic absorption [Blume-Peytavi et al. 2011]. In addition, hair follicles can act as a drug reservoir for up to 10 days [Jacobi et al 2007]. Specifically, in the case of nanostructured systems, this pathway is highly involved due to the geometry of the nanoparticles. The chemical nature, size and surface charge significantly affect the accumulation of these systems in the different anatomical regions of a hair follicle [Lademann, J et al 2006].

The stratum corneum limits the absorption of drugs through the skin. Due to the presence of lipids in the stratum corneum, this layer is practically impermeable to water. Transport through the stratum corneum can occur via the intercellular or intracellular route.

As for the intracellular route, the drug penetrates into the deeper layers by partitioning into and out of the cell membrane. Due to the low permeability of these cell membranes, this route is not considered to be the preferred route of absorption [Marie-Alexandrine Bolzinger et al 2012].

The intercellular route is the most common route of penetration through the stratum corneum, especially when a steady state is reached. In this case, the drug permeates the stratum corneum through the channels surrounding the corneocytes. These protein-rich corneocytes covalently bound to intercellular lipids form a barrier against water and hydrophilic compounds. Hence, this route is mainly limited to very hydrophobic drugs. Drug permeation through the stratum

corneum is a diffusion-based process. The high diffusion coefficient of lipophilic drugs in the stratum corneum lipid matrix makes the intercellular route the main path of permeation through the stratum corneum for most molecules. In addition, the permeation rate can be modulated by incorporating certain excipients into the formulation [Victor Carrer Vives et al. 2018]. There are excipients (ethanol or propylene glycol) that alter protein conformation and/or dissolve intercellular lipids. This causes an increased penetration of substances into the epidermis and dermis [Zoe Diana Draelos 2013]. Another possibility is the use of nanocarriers, which encapsulate active substances and help them penetrate through the stratum corneum.

1.4. Nanotechnology in dermatology

In recent decades, the field of nanomedicine has grown rapidly due to the wide variety of applications and the benefits on offer. Nanomaterials are substances with at least one dimension below 100 nm. The high surface-to-volume ratio makes the properties of a material at the nanoscale different from those at the macroscale. However, nanoformulation is still a complex field that requires fine-tuning in terms of scale-up, stability and compatibility with other types of formulations.

The size, morphology, surface characteristics and flexibility of nanoparticles determine the permeation rate of these systems through different biological membranes. The topical delivery of nanoparticles not only increases the penetration of different drugs, but it also serves as a strategy for stabilisation, release modulation, and/or anatomical specific targeting. All these possibilities have led both the cosmetic and pharmaceutical industries to increase their interest in nanoparticles as drug delivery systems [Nancy A. Montero-Riviere et al. 2013]. The most commonly used nanocarriers to deliver drugs through the skin are liposomes, nanostructured lipid carriers, polymeric nanoparticles and nanoemulsions.

1.4.1. Liposomes

Liposomes are spherical vesicles with a uni- or multilamellar membrane and an aqueous core. This allows them to encapsulate both hydrophobic drugs (intercalated in the lipid membrane) and hydrophilic drugs (encapsulated in the aqueous core). A. D. Bangham discovered them in 1965 by dispersing phospholipids in water. There are different types of liposomes. Transfersomes, first introduced by Cevc 1996, are liposomes in which a surfactant or “edge activator” is added to the lipid membrane, increasing their flexibility and, consequently, their ability to penetrate through biological membranes such as the stratum corneum (Figure 4). Ethosomes are liposomes with a high ethanol content (between 20 and 45% approximately). The absorption-promoting effect of alcohol added to the use of lipid vesicles makes it one of the systems showing the highest transdermal penetration of hydrophobic substances [Marco Bragagni et al 2012].

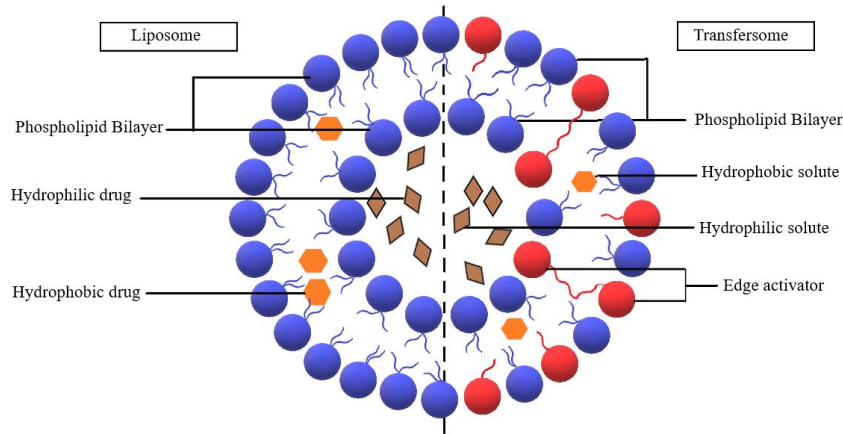


Figure 4 Representation of conventional liposomes and transfersomes. [Sivarajakumar Raahulan et al 2019].

1.4.2. Nanostructured Lipid Carriers (NLC)

Nanostructured lipid carriers (NLCs) are the second generation of solid lipid nanoparticles discovered by Professor R. H. Müller (Germany) and Professor M. Gasco (Italy) in 1990. NLCs consist of a mixture of solid and liquid lipids stabilised in water by emulsifiers. They are of interest as they do not require the use of organic solvents, they can encapsulate a high amount of drug in their interior, and they are usually stable against *in vivo* aggregation (Figure 5). NLCs are currently classified into three different models: the imperfect crystal model, the multiple type model and the amorphous model.

- The imperfect crystal model consists of a highly disordered lipid matrix with spaces where drugs can be encapsulated. These imperfections are produced by mixing fatty acids of different chain lengths and mixtures of mono-, di- and triacylglycerols. This model allows for an increased loading capacity but tends to have lower encapsulation yields.
- The multiple type model of NLCs are oil/lipid/water mixtures. In these nanoparticles, the liquid lipid content is higher, which allows better solubilisation of lipophilic drugs. This model minimises drug leakage, increases encapsulation yields and modulates drug release kinetics.
- The amorphous model is obtained by mixing specific lipids, such as isopropyl myristate or hydroxyl stearate, which form non-crystalline particles. This minimises the drug leakage caused by the crystallisation process [Iti Chauhan et al 2020].

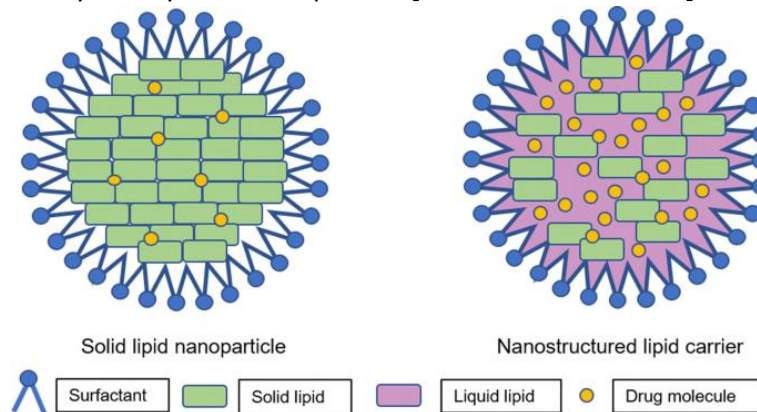


Figure 5 Schematic representation of solid lipid nanoparticles and nanostructured lipid carriers. Image taken from Iti Chauhan et al 2020].

1.4.3. Polymer nanoparticles

Polymeric nanoparticles are characterised by the self-assembling of one or more polymers trapping the active ingredient inside. They are very versatile nanoparticles and easy to adjust chemically and physically. There are different types, such as natural polymeric nanoparticles, nanospheres and lipid-polymer hybrid nanoparticles or lipomers.

- Natural polymeric nanoparticles are formed from naturally occurring polymers such as chitosan, alginate, or albumin. They generally form hydrogels through the interaction of the polymer chains with multivalent cations or cross linkers such as calcium or tripolyphosphate. Due to the surface charge of these polysaccharides, it is possible to obtain good encapsulation performances for hydrophilic ionised drugs [**Zheng Zhang et al 2013**].
- Polymeric nanospheres and nanocapsules are formed from different synthetic polymers that are generally biodegradable. A commonly used polymer is poly-lactic-co-glycolic acid (PLGA). This polymer is particularly interesting as it can modulate the release of encapsulated drugs. By varying the ratio of lactic and glycolic acid monomers, the number of glycosidic bonds between the monomers, which are hydrolysable bonds, can be changed. Depending on the molecular weight of the encapsulated drug and the porosity of the polymeric lattice, the predominant release mechanism is the diffusion of the external solvent through the pores or the erosion of the polymeric chains and release. Sustained releases over months can be achieved for high molecular weight biomolecules, thus considerably reducing the frequency of administration. The disadvantage is that these polymers tend to be expensive at the industrial scale. Therefore, other types of polymers, such as those based on cellulose derivatives (e.g., ethyl cellulose), are attracting interest in the pharmaceutical industry. In addition, this type of polymeric nanoparticles can protect drugs from hydrolysis and increase their stability.
- Lipomers, or lipid-core polymeric nanocapsules, are lipid vesicles surrounded by a polymeric wall [**Venturini et al 2010**]. In polymeric nanospheres, the active ingredient is trapped both on the surface of the particle and in its core. They usually have a burst release effect, due to the desorption of the active ingredient from the surface, followed by a plateau based on diffusion/erosion mechanisms. Urzula Bazylińska et al. compared the release of a lipophilic active ingredient encapsulated in nanospheres and lipid-polymer hybrid nanocapsules, verifying that the presence of the lipid nucleus increased the encapsulation efficiency and decreased the burst release effect, producing a more sustained release [**Bazylińska et al 2014**]. Figure 6 shows a schematic representation of ethyl cellulose lipomers.

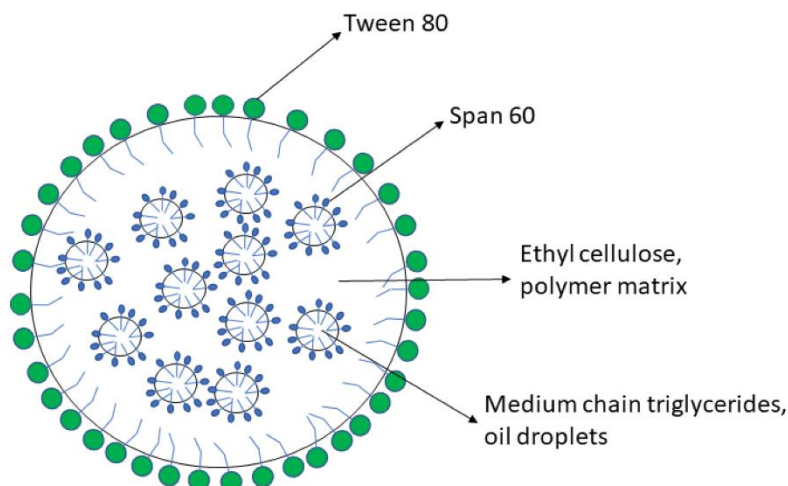


Figure 6 Schematic representation of lipomers [Eloy Pena-Rodriguez et al 2021b].

1.4.4. Nanoemulsions

Nanoemulsions are emulsions with a droplet size between 20 and 200 nm. Microemulsions are thermodynamically stable systems. Nanoemulsions are kinetically, but not thermodynamically stable systems. The term nanoemulsion is preferred because it gives an idea of the droplet size range and avoids confusion with the term microemulsion, which is a thermodynamically stable system [David Julian McClements 2012]. Because of their size, nanoemulsions appear transparent or translucent. They are stable against aggregation and sedimentation.

There are mainly two types of nanoemulsions: oil in water (o/w) nanoemulsions, where the external phase is aqueous, and water in oil (w/o) nanoemulsions, where the external phase is organic. Both types of nanoemulsions are attracting interest in the pharmaceutical and cosmetic industry as topical delivery systems [C. Solans 2005 et al.].

1.5. Epidermal and follicular targeting

1.5.1. Epidermal targeting

Many cutaneous diseases like atopic dermatitis, early melanomas and psoriasis occur in the epidermis. Due to the barrier effect of the stratum corneum, it is difficult for many drugs to reach the site of action when administered topically. Factors that promote absorption, such as ethanol and propylene glycol, may lead to too high permeation. If the drug permeates into the deeper layers of the skin and systemic absorption occurs, there may be a risk depending on the potency and toxicity of the drug. The possibility of designing nanoformulations that deliver the drug into the epidermis in a targeted manner avoids regulatory problems at the safety level and increases the bioavailability and efficacy of treatments.

1.5.2. Follicular targeting

Hair follicles can act as cutaneous reservoirs and as pathways to viable skin layers. Different studies have compared the cutaneous permeation of skin with and without hair follicles in different animal models. The importance of the transfollicular route and the increased permeation in the presence of hair follicles and invaginations have been demonstrated by different methods. Oestradiol permeation was compared between normal skin and the skin of newborn rats that was free of invaginations. The results showed that the reservoir function of the stratum corneum of appendage-free skin was more pronounced than that of normal skin,

whereas the concentration appearing in the epidermis and dermis was greater in normal skin [Hueber F et al 1992]. Barry et al. developed the sandwich method for Franz cells, in which two skin membranes overlapped, assuming that the follicles did not coincide exactly in the same position [Barry et al 2002]. Studies were also performed by selectively blocking hair follicles in pig and human skin. Permeation of caffeine shampoo formulations in these models demonstrated the importance of the transfollicular pathway for hydrophilic drugs [Otberg et al 2008]. Inorganic nanoparticles, nanostructured lipid carriers, liposomes, and polymeric micro/nanoparticles up to 10 μm have been observed to remain in hair follicles when topically administered [Annika Vogt et al 2005]. These findings have led to the focus on targeting hair follicles through nanoformulations.

The use of nanotechnology allows the administration of active ingredients not only to the hair follicle, but also to specific anatomical regions such as the sebaceous glands, the bulb or specific cell populations. The type of nanoparticle as well as its physicochemical and morphological properties are significant factors for its biodistribution within hair follicles. Annika Vogt et al. observed the influence of the hydrodynamic diameter of nanoparticles on the hair follicle biodistribution. Using fluorescence and confocal laser microscopy (Figure 7), they observed that nanoparticles of a smaller size (40 nm) were able to accumulate throughout the hair follicle, as opposed to particles of 750 and 1500 nm that accumulated on the skin surface [Annika Vogt et al 2006]. Alvarez-Roman et al. observed that 20- and 200-nm polymeric nanoparticles accumulated in hair follicles in a size-dependent manner. Smaller nanoparticles accumulated more in hair follicles than the larger nanoparticles [R. Alvarez-Roman et al 2004].

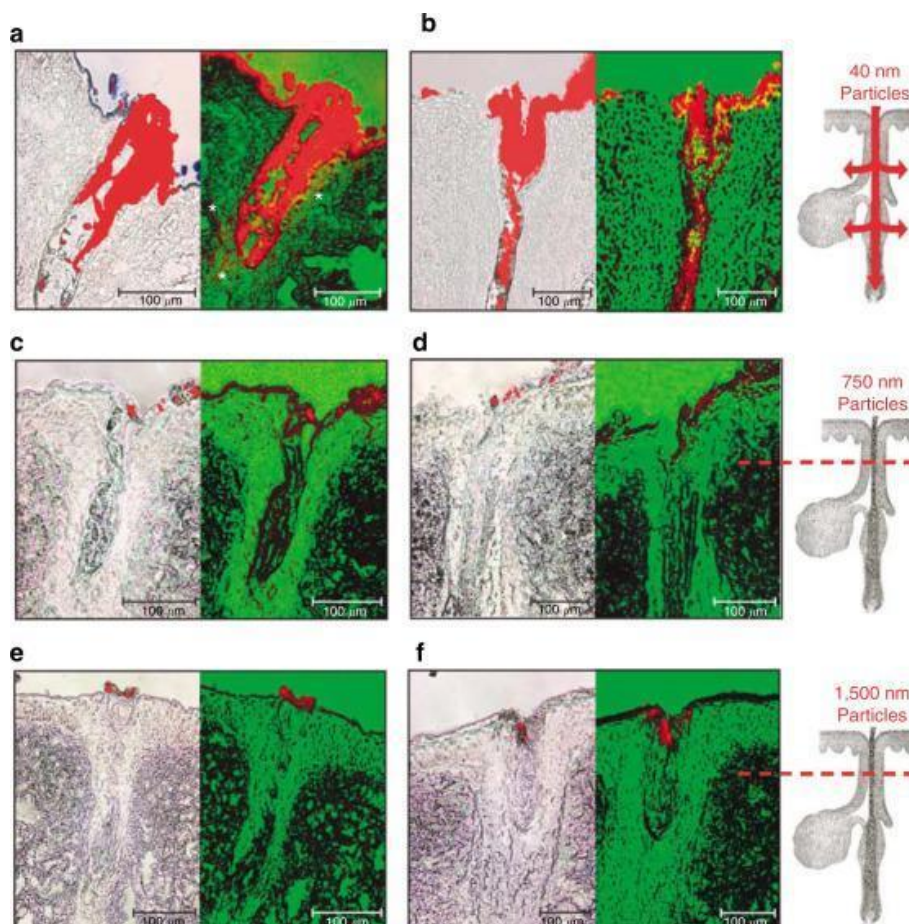


Figure 7 40-nm nanoparticles but not 750- or 1,500-nm nanoparticles penetrate via the vellus hair follicle into the surrounding tissue. Image taken from Annika Vogt et al., 2006 [Annika Vogt et al 2006].

The accumulation of nanoparticles in hair follicles has been observed for a wide range of nanoparticles of different sizes. The vast majority of techniques to characterise particle accumulation in different regions of the hair follicle are qualitative. In addition, it is still unknown whether in different nanosystems, the active ingredient accumulates in the same areas as the nanoparticles or whether it is released once in contact with the lipids of the stratum corneum. The development of quantitative techniques to test the accumulation of nanoparticles and encapsulated drugs simultaneously in hair follicles is a challenge for the pharmaceutical industry [Fiorenza Rancan et al 2013].

1.6. *In vitro* release and permeation tests.

The main technique used to study diffusion through synthetic membranes and *in vitro* permeation in the skin are Franz diffusion cells. It is a simple technology, consisting of a donor compartment, where the formulation to be studied is placed, and a receptor compartment that is generally under magnetic agitation. The synthetic or skin membrane is placed between the two compartments. The system has an arm to obtain a sample and, thus, determine the amount that passes through the membrane at different times. It also has a thermal jacket connected to a water or air circuit to control the temperature of the experiment (Figure 8).

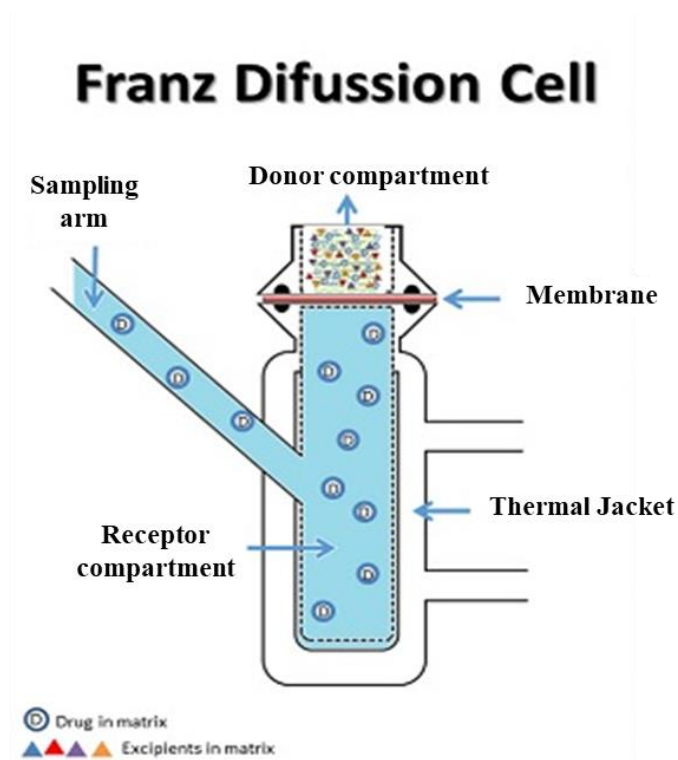


Figure 8 Diagram of Franz cells. Image taken from Constantin H. Salamanca et al. [Constantin H. Salamanca et al 2018].

1.7. Biodistribution studies

1.7.1. Qualitative biodistribution techniques

One of the most important challenges of transdermal absorption is to know the biodistribution of excipients and active ingredients in the different anatomical regions of the skin. Greater knowledge about where, when, and how much of these compounds accumulate would help

researchers design topical formulations with improved bioavailability and efficacy. Different techniques are available to qualitatively visualise biodistributions in the skin.

1.7.1.1. Fluorescence Microscopy and Confocal Fluorescence Microscopy

Fluorescence microscopy is a commonly used technique in skin imaging. In fluorescence, the emission wavelength is longer than the excitation wavelength. In the skin, fluorescence can come from cutaneous autofluorophores such as lipofuscin or NAD(P)H, from fluorescent markers present in the skin after *in vitro* permeation, or from specific staining protocols. An interesting aspect of fluorescence microscopy is the possibility of combining fluorescent markers, emitting at different wavelengths, and recognising different skin structures, to be visualised in parallel channels. It is possible to nanoencapsulate fluorescent molecules and/or label the nanoparticles with fluorescent markers and then permeate them into different tissues for *in vitro* analysis with fluorescence microscopy. This technique can be used to observe the biodistribution of fluorescent molecules and trace the nanoparticles to check where they accumulate in the skin.

Confocal laser fluorescence microscopy is a more modern technique that produces high-resolution images of different Z-planes of the same biological tissue or sample. The concept of confocal microscopy was patented by Marvin Minsky et al. [**Marvin Minsky et al 1957**]. In the mid-1980s, the equipment for confocal microscopy became commercially available. In the last few decades, the resolution and speed of the latest instruments have improved exponentially due to more effective computers and optics.

Confocal fluorescence microscopy shows increased lateral and axial resolution compared to conventional fluorescence microscopy. Confocal technology consists of focusing the excitation light at a point to scan the sample in the x, y and z directions. The illumination, the sample and the detector have the same focus, hence the name "confocal". A confocal microscope contains pinholes, which are spatial filters placed before and behind the light source and in front of the detector to eliminate any noise coming from the out-of-focus light.

Due to the higher spatial resolution, higher contrast and the omission of out-of-focus fluorescence, a more precise localisation of fluorescent markers can be obtained by confocal microscopy [**Fatima A. Merchant et al**]. In addition, by reconstructing virtual planes, it is possible to obtain three-dimensional images of intact tissue accurately and with high resolution. Figure 9 shows a confocal fluorescence image of a human skin cross-section.

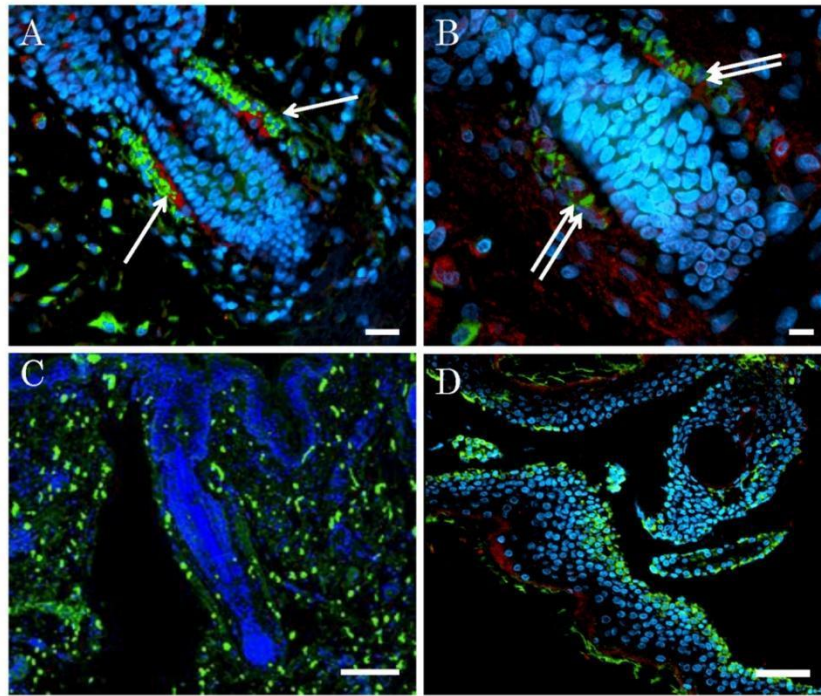


Figure 9 Confocal fluorescence image of a human skin cross-section. Image taken from Hiroshi Kanno et al. [Hiroshi Kanno et al 2013].

1.7.1.2. Immunohistofluorescence

Immunohistofluorescence (example in Figure 10) is based on analysing tissue sections and staining them with specific antibodies. In dermatology, antibodies that recognise specific cellular structures, proteins, active ingredients, or excipients that have been previously permeated are used to study their biodistribution. These primary antibodies can emit fluorescence and biodistribution can be directly observed by fluorescence microscopy. It is also possible to use fluorescent secondary antibodies to amplify the fluorescence signal intensity.

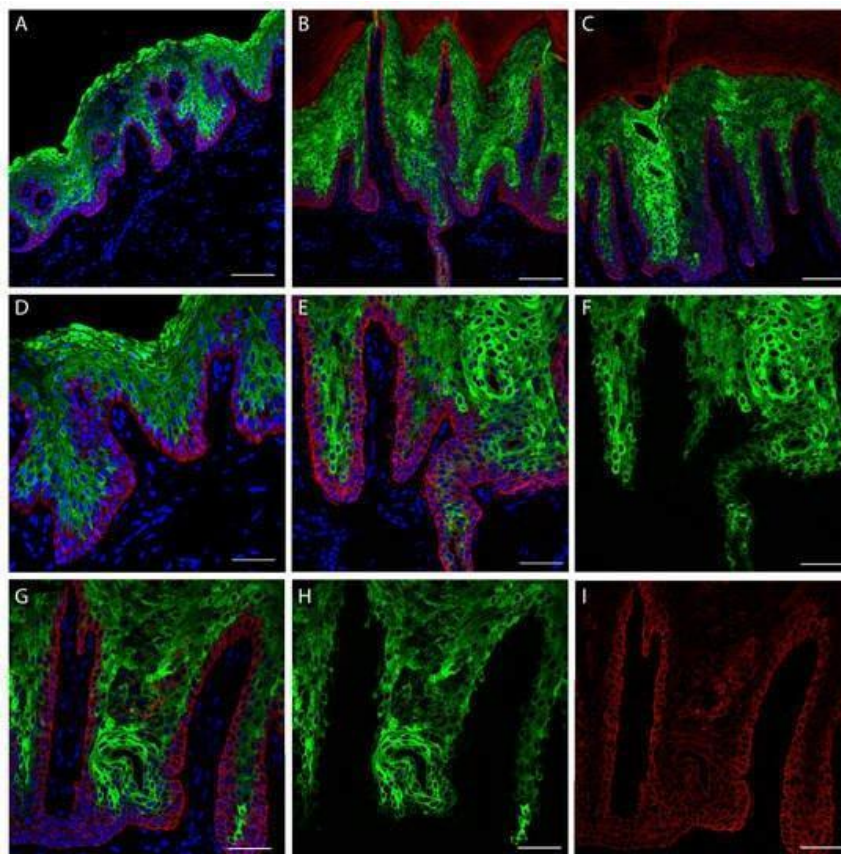


Figure 10 Immunohistofluorescence image of a human skin cross-section. Image taken from Sabrina Caporali et al. [Sabrina Caporali et al 2021].

1.7.2. Quantitative biodistribution techniques

There are other techniques for the visualisation of skin tissues such as cryo-transmission electron microscopy, scanning electron microscopy and optical coherence tomography. However, almost all of them have the limitation of being qualitative.

In recent years, researchers have begun to study techniques that allow the quantitative or quantitative analysis of compounds after permeation into the skin. Quantitative techniques include the following:

1.7.2.1. Confocal Raman Microscopy

When a photon beam interacts with matter, some of the light is deflected from the initial direction. This phenomenon is known as scattering. Most of the scattered light scatters elastically, maintaining the same frequency as that of the incident light. A lower intensity of light is scattered inelastically. This is known as Stokes Raman scattering, when the frequency is increased, and anti-Stokes Raman scattering, when the frequency is decreased (Figure 11).

In quantum physics, a change in frequency leads to a change in vibrational energy. In Raman spectroscopy, a change in vibrational energy results in an equal shift of the energy of the scattered photon. Decreasing the vibrational energy of a molecule adds energy to the scattered photon, shortening the wavelength. On the other hand, increasing the vibrational energy of the molecule subtracts energy from the scattered photon and, consequently, increases the wavelength.

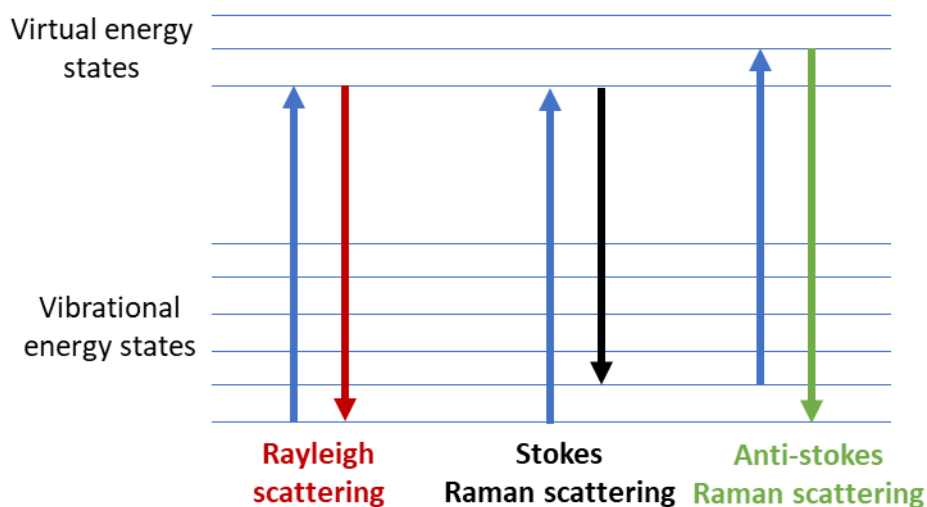


Figure 11 Energy level diagram showing the states involved in the Raman signal.

Each molecule has a unique combination of quantum vibrational levels, which translate into a specific Raman spectrum. In addition, the number of photons scattered is directly proportional to the number of molecules irradiated. This means that the intensity of the Raman spectrum can be used to quantify the number of molecules in a particular tissue or sample.

The confocal technology described for confocal fluorescence microscopy is also transferable to Raman spectroscopy. In this way, it is possible to determine the skin biodistribution of active ingredients and excipients both *in vivo* and *in vitro* since it is a non-destructive technique [Mao G. et al 2012].

1.7.2.2. Maldi Imaging

In the past, different techniques based on mass spectroscopy have been used in pharmaceutical research on tissues such as the skin. This technique qualitatively analyses the biodistribution of endogenous molecules in the skin, as well as that of active ingredients or permeated excipients *in vitro*.

Since its introduction in the mid-1980s, matrix-assisted laser desorption ionisation (MALDI) coupled to mass spectrometry imaging (MSI) has been shown to be a promising technology in terms of the possibility of quantifying the biodistribution of these molecules in different tissues such as the skin (Figure 12). Quantitative analysis by MALDI imaging in biological tissues is yet to be researched and fine-tuned, and there is still no consensus on how to construct calibration lines and analyse tissue concentrations [Anne Mette Handler et al 2021].

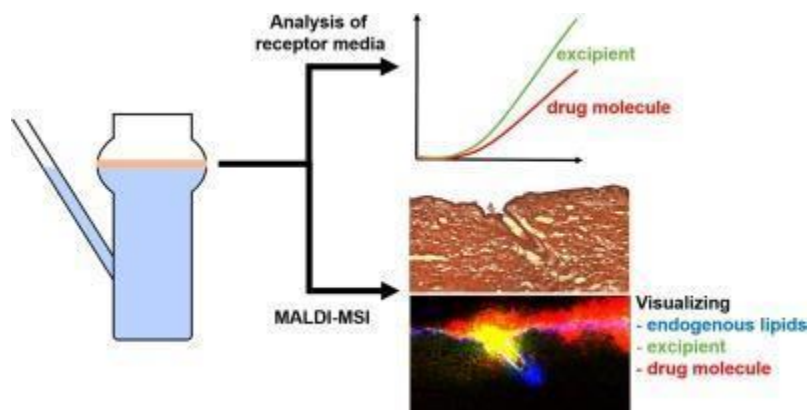


Figure 12 Scheme for MALDI-MSI analysis of human skin cross-sections by vertical diffusion Franz cells. Image taken from Anne Mette Handler et al. [Anne Mette Handler et al 2020].

Compared to other classical techniques such as immunohistofluorescence, confocal fluorescence microscopy and Raman spectroscopy, MALDI-MSI has the great advantage of rapidly detecting the biodistribution of many species of molecules without the need for prior knowledge of the tissue composition and without the requirement of antibodies [Bernd Enthaler et al 2012].

One of the best-known applications of MALDI-MSI is the identification of disease biomarkers by proteomics analysis.

1.8. Bibliography

A.D. Bangham, M.M. Standish, J.C. Watkins, Diffusion of univalent ions across the lamellae of swollen phospholipids, *Journal of Molecular Biology*, Volume 13, Issue 1, 1965, Pages 238-277, DOI: 10.1016/S0022-2836(65)80093-6.

Alvarez-Román R, Naik A, Kalia YN, Guy RH, Fessi H. Skin penetration and distribution of polymeric nanoparticles. *J Control Release*. 2004 Sep 14;99(1):53-62. DOI: 10.1016/j.jconrel.2004.06.015.

Anne Mette Handler, Gitte Pommergaard Pedersen, Kim Troensegaard Nielsen, Christian Janfelt, Anders Just Pedersen, Malcolm R. Clench, Quantitative MALDI mass spectrometry imaging for exploring cutaneous drug delivery of tofacitinib in human skin, *European Journal of Pharmaceutics and Biopharmaceutics*, Volume 159, 2021, Pages 1-10, DOI: 10.1016/j.ejpb.2020.12.008.

Anne Mette Handler, Mariam Fallah, Anders Just Pedersen, Gitte Pommergaard Pedersen, Kim Troensegaard Nielsen, Christian Janfelt, MALDI mass spectrometry imaging as a complementary analytical method for improved skin distribution analysis of drug molecule and excipients, *International Journal of Pharmaceutics*, Volume 590, 2020, 119949, DOI: 10.1016/j.ijpharm.2020.119949.

B.W Barry, Drug delivery routes in skin: a novel approach, *Advanced Drug Delivery Reviews*, Volume 54, Supplement, 2002, Pages S31-S40, DOI: 10.1016/S0169-409X(02)00113-8.

Bazylińska U., Lewińska A., Lamch Ł., Wilk K.A. Polymeric nanocapsules and nanospheres for encapsulation and long sustained release of hydrophobic cyanine-type photosensitizer. *Colloids Surf. A Physicochem. Eng. Asp.* 2014;442:42–49. doi: 10.1016/j.colsurfa.2013.02.023.

Blume-Peytavi U, Vogt A. Human hair follicle: reservoir function and selective targeting. *Br J Dermatol.* 2011 Oct;165 Suppl 2:13-7. DOI: 10.1111/j.1365-2133.2011.10572.x.

Bragagni M, Mennini N, Maestrelli F, Cirri M, Mura P. Comparative study of liposomes, transfersomes and ethosomes as carriers for improving topical delivery of celecoxib. *Drug Deliv.* 2012 Sep-Oct;19(7):354-61. DOI: 10.3109/10717544.2012.724472.

Caporali, Sabrina & Didona, Biagio & Paradisi, Mauro & Mauriello, Alessandro & Campione, Elena & Falconi, Mattia & Iacovelli, Federico & Minieri, Marilena & Pieri, Massimo & Bernardini, Sergio & Terrinoni, Alessandro. (2021). Post Zygotic, Somatic, Deletion in KERATIN 1 V1 Domain Generates Structural Alteration of the K1/K10 Dimer, Producing a Monolateral Palmar Epidermolytic Nevus. *International Journal of Molecular Sciences.* 22. 6901. DOI: 10.3390/ijms22136901.

Carrer Vives, Victor. Skin permeability methodologies for topical absorption prediction. Pharmacy, Pharmaceutical Technology and Physico chemical department, University of Barcelona, 2018. <http://hdl.handle.net/2445/128151>.

Cevc G. Transfersomes, liposomes and other lipid suspensions on the skin: permeation enhancement, vesicle penetration, and transdermal drug delivery. *Crit Rev Ther Drug Carrier Syst.* 1996;13(3-4):257-388. DOI: 10.1615/critrevtherdrugcarriersyst.v13.i3-4.30.

Chauhan I, Yasir M, Verma M, Singh AP. Nanostructured Lipid Carriers: A Groundbreaking Approach for Transdermal Drug Delivery. *Adv Pharm Bull.* 2020;10(2):150-165. doi:10.34172/apb.2020.021.

Clive R. Harding. The stratum corneum: structure and function in health and disease. *Dematologic Therapy*, Volume 17, 2004, Pages 6-15. DOI: 10.1111/j.1396-0296.2004.04s1001.x.

Cristina G. Venturini, Eliézer Jäger, Catiúscia P. Oliveira, Andressa Bernardi, Ana M.O. Battastini, Silvia S. Guterres, Adriana R. Pohlmann, Formulation of lipid core nanocapsules, *Colloids and Surfaces A: Physicochemical and Engineering Aspects*, Volume 375, Issues 1–3, 2011, Pages 200-208, DOI: 10.1016/j.colsurfa.2010.12.011.

Daniela Karadzovska, James D. Brooks, Nancy A. Monteiro-Riviere, Jim E. Riviere, Predicting skin permeability from complex vehicles, *Advanced Drug Delivery Reviews*, Volume 65, Issue 2, 2013, Pages 265-277. DOI: 10.1016/j.addr.2012.01.019.

David Julian McClements. Nanoemulsions versus microemulsions: terminology, differences, and similarities, *Soft Matter*, Issue 6, 2012, 8, 1719-1729. DOI: 10.1039/C2SM06903B.

Draelos, Z.D. (2013). Enhancement of Topical Delivery with Nanocarriers. In: Nasir, A., Friedman, A., Wang, S. (eds) *Nanotechnology in Dermatology*. Springer, New York, NY. DOI: 10.1007/978-1-4614-5034-4_8.

Enthaler, Bernd & Riedner, Maria & Fischer, Markus & Rapp, Claudius & Pruns, Julia & Vietzke, Jens-Peter. (2012). MALDI imaging in human skin tissue sections: Focus on various matrices and enzymes. *Analytical and bioanalytical chemistry*. 405. DOI: 10.1007/s00216-012-6508-3.

Fatima A. Merchant, Keith A. Bartels, Alan C. Bovik, Kenneth R. Diller, 10.9 - Confocal Microscopy, Editor(s): AL BOVIK, In *Communications, Networking and Multimedia, Handbook of Image and Video Processing (Second Edition)*, Academic Press, 2005, Pages 1291-XLI, DOI: 10.1016/B978-012119792-6/50135-2.

Hueber F, Wepierre J, Schaefer H. Role of transepidermal and transfollicular routes in percutaneous absorption of hydrocortisone and testosterone: *in vivo* study in the hairless rat. *Skin Pharmacol*. 1992;5(2):99-107. doi: 10.1159/000211026. PMID: 1637565.

Jacobi U, Kaiser M, Toll R, Mangelsdorf S, Audring H, Otberg N, Sterry W, Lademann J. Porcine ear skin: an *in vitro* model for human skin. *Skin Res Technol*. 2007 Feb;13(1):19-24. DOI: 10.1111/j.1600-0846.2006.00179.x. PMID: 17250528.

Kanno, H.; Kubo, A.; Yoshizumi, T.; Mikami, T.; Maegawa, J. Isolation of Multipotent Nestin-Expressing Stem Cells Derived from the Epidermis of Elderly Humans and TAT-VHL Peptide-Mediated Neuronal Differentiation of These Cells. *Int. J. Mol. Sci*. 2013, 14, 9604-9617. DOI: 10.3390/ijms14059604.

Lademann J, Knorr F, Richter H, Blume-Peytavi U, Vogt A, Antoniou C, Sterry W, Patzelt A: Hair Follicles – An Efficient Storage and Penetration Pathway for Topically Applied Substances. *Skin Pharmacol Physiol* 2008;21:150-155. DOI: 10.1159/000131079.

Mao, G., Flach, C.R., Mendelsohn, R. et al. Imaging the Distribution of Sodium Dodecyl Sulfate in Skin by Confocal Raman and Infrared Microspectroscopy. *Pharm Res* 29, 2189–2201 (2012). DOI: 10.1007/s11095-012-0748-y.

Marie-Alexandrine Bolzinger, Stéphanie Briçon, Jocelyne Pelletier, Yves Chevalier, Penetration of drugs through skin, a complex rate-controlling membrane, *Current Opinion in Colloid & Interface Science*, Volume 17, Issue 3, 2012, Pages 156-165, DOI: 10.1016/j.cocis.2012.02.001.

Marie-Alexandrine Bolzinger, Stéphanie Briçon, Jocelyne Pelletier, Yves Chevalier, Penetration of drugs through skin, a complex rate-controlling membrane, *Current Opinion*

in *Colloid & Interface Science*, Volume 17, Issue 3, 2012, Pages 156-165 DOI: 10.1016/j.cocis.2012.02.001.

Minsky, M. (1957). Confocal patent focal scanning microscope. US3013467A (Accessed on 16th of May, 2022) US patent, serial, 3.

Müller RH, Mäder K, Gohla S. Solid lipid nanoparticles (SLN) for controlled drug delivery - a review of the state of the art. *Eur J Pharm Biopharm.* 2000 Jul;50(1):161-77. DOI: 10.1016/s0939-6411(00)00087-4.

Otberg N, Patzelt A, Rasulev U, Hagemeister T, Linscheid M, Sinkgraven R, Sterry W, Lademann J. The role of hair follicles in the percutaneous absorption of caffeine. *Br J Clin Pharmacol.* 2008 Apr;65(4):488-92. DOI: 10.1111/j.1365-2125.2007.03065.x.

Paul A. J. Kolarisk, BS, Maria Ann Kolarisk, MSN, ARHP-C, Carolyn Goodwin, APRN-BC, FNP. Anatomy and Physiology of the Skin. *Journal of the Dermatology Nurses' Association*, 3(4), 203-213 - July 2011. DOI: 10.1097/jdn.0b013e3182274a98.

Raahulan, Sivarajakumar & Sanapalli, Bharat & Pindiprolu, Sai Kiran & Karri, Veera Venkata Satyanarayana Reddy. (2019). Transfersome vs liposomes as drug delivery vehicle for the treatment of skin cancers. *International Journal of Research in Pharmaceutical Sciences.* 10. 1795-1807. DOI: 10.26452/ijrps.v10i3.1375.

Rancan, F., Afraz, Z., Combadiere, B., Blume-Peytavi, U., Vogt, A. (2013). Hair Follicle Targeting with Nanoparticles. In: Nasir, A., Friedman, A., Wang, S. (eds) *Nanotechnology in Dermatology*. Springer, New York, NY. DOI: 10.1007/978-1-4614-5034-4_9.

Ritu Goyal, Lauren K. Macri, Hilton M. Kaplan, Joachim Kohn. Nanoparticles and nanofibers for topical drug delivery. *Journal of Controlled Release*, Volume 240, 2016, Pages 77-92. DOI: 10.1016/j.jconrel.2015.10.049.

Salamanca CH, Barrera-Ocampo A, Lasso JC, Camacho N, Yarce CJ. Franz Diffusion Cell Approach for Pre-Formulation Characterisation of Ketoprofen Semi-Solid Dosage Forms. *Pharmaceutics.* 2018 Sep 5;10(3):148. DOI: 10.3390/pharmaceutics10030148.

Solans, C. & Izquierdo, Paqui & Nolla, J. & Azemar, N. & García-Celma, Maria. (2005). Nano-emulsion. *Current Opinion in Colloid & Interface Science.* 10. 102-110. DOI: 10.1016/j.cocis.2005.06.004.

Vogt A, Combadiere B, Hadam S, Stieler KM, Lademann J, Schaefer H, Autran B, Sterry W, Blume-Peytavi U. 40 nm, but not 750 or 1,500 nm, nanoparticles enter epidermal CD1a+ cells after transcutaneous application on human skin. *J Invest Dermatol.* 2006 Jun;126(6):1316-22. DOI: 10.1038/sj.jid.5700226.

Vogt A, Mandt N, Lademann J, Schaefer H, Blume-Peytavi U. Follicular targeting--a promising tool in selective dermatotherapy. *J Investig Dermatol Symp Proc.* 2005 Dec;10(3):252-5. DOI: 10.1111/j.1087-0024.2005.10124.x.

Vogt, Annika & Blume-Peytavi, Ulrike. (2015). *Biology of the hair follicle. Hair Growth and Disorders.* 1-22. 10.1201/b19440-2.

William Montagna, Eugene J. Van Scott. CHAPTER 3 - The Anatomy of the Hair Follicle, Editors: William Montagna, Richard A. Ellis, *The Biology of Hair Growth*, Academic Press, 1958, Pages 39-64. DOI: 10.1016/B978-1-4832-3287-4.50009-X.

Z. Zaidi, S. W. Lanigan, *Dermatology in Clinical Practice*, 1. © Springer-Verlag London Limited 2010 DOI: 10.1007/978-1-84882-862-9_1.

Zhang Z, Tsai PC, Ramezanli T, Michniak-Kohn BB. Polymeric nanoparticles-based topical delivery systems for the treatment of dermatological diseases. *Wiley Interdiscip Rev Nanomed Nanobiotechnol.* 2013;5(3):205-218. doi:10.1002/wnan.1211.

Chapter 2 -Aims

In recent decades, nanotechnology has provided one of the largest sources of innovation in dermatology and cosmetics. The properties of certain materials at the nanoscale can be used to improve the bioavailability, stability or efficacy of different active ingredients. Basic research in this field has led to the development of very sophisticated nanosystems, which allow the release of active ingredients at very specific targets and can even control the release by both internal and external pulses.

Although the opportunities offered by nanodermatology are very promising and despite the increase in research in this field in recent decades, significant challenges still remain. Most of these sophisticated nanosystems present problems of scale-up, a lack of reproducibility, high production costs and a low correlation between *in vitro* and *in vivo* efficacy.

Another of the great unknowns in nanodermatology is about what happens to both the nanoparticles and the encapsulated active ingredients once they penetrate the different layers of the skin. The physicochemical properties of nanoparticles can be determined in a very precise way thanks to the great variety of characterisation techniques available. However, to date, there is still a great deal of uncertainty about where the nanoparticles and the encapsulated active ingredients end up, what their cutaneous biodistribution is, and whether the active ingredient and the nanoparticle travel together once in contact with the different intercellular and intracellular environments.

For these nanoformulations to reach patients, they must be designed from the very beginning to be safe, effective and industrialisable. It is also necessary to carry out studies using different techniques to test the cutaneous biodistribution of the nanoformulations.

The main objective of this thesis was to develop different drug delivery platforms for epidermal and follicular targeting. In addition, the specific objectives to achieve the main objective were the following:

- To perform *in vitro* screenings on different cell lines, present in the skin to select active ingredients for encapsulation.
- To develop and characterise different nanoencapsulation platforms (liposomes, NLCs and polymeric nanoparticles) from an industrial point of view, to demonstrate their stability and scalability.
- To include the nanosystems in galenic formulations and to study their stability as final products.
- To perform different qualitative and quantitative *ex vivo* techniques for the biodistribution analysis of nanoparticles and active ingredients in the skin.

Thesis director's report on the impact factor of published articles and the participation of the doctoral candidate in each published article

La tesis doctoral presentada por el candidato al grado de Doctor, Eloy Pena-Rodriguez, contiene 3 artículos publicados, uno preparado para someterlo y otro en elaboración para su sometimiento en un breve periodo de tiempo. En estos artículos el doctorando aparece como primer autor, por tanto, como autor principal. De forma adicional, fruto de una colaboración, el doctorando aparece como coautor de otro artículo.

A continuación, se pasa a detallar los artículos en los que ha participado.

Título: Epidermal Delivery of Retinyl Palmitate Loaded Transfersomes: Penetration and Biodistribution Studies

Autores/as (por orden de firma): Pena-Rodríguez, E.; Moreno, M.C.; Blanco-Fernandez, B.; González, J.; Fernández-Campos, F

Año: 2020

Clave (A: artículo, R: review): A

Revista (título, volumen, página inicial-final): *Pharmaceutics*, 12(2), 112

ISSN: 1999-4923

DOI (o URL en su defecto): <https://doi.org/10.3390/pharmaceutics12020112>

<p>Indexado en WoS Core Collection (SCIE, SSCI, AHCI o ESCI)</p> <p>(SI/NO): si</p>	<p>Indexado en Scopus</p> <p>(SI/NO): si</p>
<p>Número de citas del artículo (Wos Core Collection):</p> <p>14</p>	<p>Número de citas del artículo: 15</p>

JIF del JCR SCIE/SSCI: 6.321 (2020)	Índice SJR: 1.054 (2020)
Journal Impact Factor (JIF) Pharmacy and pharmacology: 29/276 Primer cuartil Q1	Cuartil y categoría SJR: Q2. Pharmaceutical sciences
Journal Citation Report (JCI) Pharmacy and pharmacology: 32/357 Primer decil D1	

Eloy Pena, autor principal del artículo ha desarrollado todos los experimentos relativos al desarrollo y caracterización de las nanopartículas, tanto desde el punto de vista fisicoquímico, como del punto de vista biofarmacéutico (estudios de liberación y permeación). Además, Eloy analizó los datos, creó los gráficos y redactó el documento.

Adicionalmente hay que comentar que este artículo ha recibido un alto número de citas de otros autores en un relativo corto espacio de tiempo, por lo que parece tener una alta repercusión en la comunidad científica.

Título: Dexamethasone-Loaded Lipomers: Development, Characterization, and Skin Biodistribution Studies.

Autores/as (por orden de firma): Pena-Rodríguez, E.; Lajarin-Reinares, M.; Mata-Ventosa, A.; Pérez-Torras, S.; Fernández-Campos, F.

Año: 2021

Clave (A: artículo, R: review): A

Revista (título, volumen, página inicial-final): *Pharmaceutics* 13: 533

ISSN: 1999-4923

DOI (o URL en su defecto): <https://doi.org/10.3390/pharmaceutics13040533>

<p>Indexado en WoS Core Collection (SCIE, SSCI, AHCI o ESCI)</p> <p>(SI/NO): si</p>	<p>Indexado en Scopus</p> <p>(SI/NO): si</p>
<p>Número de citas del artículo (Wos Core Collection):</p> <p>2</p>	<p>Número de citas del artículo:</p> <p>2</p>
<p>JIF del JCR SCIE/SSCI: 6.321 (2020)</p>	<p>Índice SJR: 1.054 (2020)</p>
<p>Journal Impact Factor (JIF) Pharmacy and pharmacology: 29/276 Primer cuartil Q1</p> <p>Journal Citation Report (JCI) Pharmacy and pharmacology: 32/357 Primer decil D1</p>	<p>Cuartil y categoría SJR: Q2. Pharmaceutical sciences</p>

Eloy Pena, autor principal del artículo ha desarrollado todos los experimentos relativos al desarrollo y caracterización de las nanopartículas, tanto desde el punto de vista fisicoquímico, como del punto de vista biofarmacéutico (estudios de liberación y permeación). Eloy Pena participó en la conceptualización, metodología, visualización, validación, uso de software, curado de datos, adquisición de fondos para el proyecto, administración del proyecto, análisis formal, redacción, revisión y edición del documento,

Título: The Physicochemical, Biopharmaceutical, and *In Vitro* Efficacy Properties of Freeze-Dried Dexamethasone-Loaded Lipomers

Autores/as (por orden de firma): Pena-Rodríguez, E.; Mata-Ventosa, A.; Garcia-Vega, L.; Pérez-Torras, S.; Fernández-Campos, F

Año: 2021

Clave (A: artículo, R: review): A

Revista (título, volumen, página inicial-final): *Pharmaceutics*, 13: 1322

ISSN: 1999-4923

DOI (o URL en su defecto): [obligatorio en publicación electrónica]: <https://doi.org/10.3390/pharmaceutics13081322>

<p>Indexado en WoS Core Collection (SCIE, SSCI, AHCI o ESCI) (SI/NO): si</p>	<p>Indexado en Scopus (SI/NO): si</p>
<p>Número de citas del artículo (Wos Core Collection): 1</p>	<p>Número de citas del artículo: 2</p>
<p>JIF del JCR SCIE/SSCI: 6.321 (2020)</p>	<p>Índice SJR: 1.054 (2020)</p>
<p>Cuartil y categoría JCR SCIE/SSCI: Q1. Pharmacy and pharmacology</p>	<p>Cuartil y categoría SJR: : Q2. Pharmaceutical sciences</p>

Eloy Pena, autor principal del artículo ha desarrollado todos los experimentos relativos al desarrollo, liofilización y caracterización de las nanopartículas, tanto desde el punto de vista fisicoquímico, como del punto de vista biofarmacéutico (estudios de liberación y permeación). Eloy Pena participó en la conceptualización, metodología, visualización, validación, uso de

software, curado de datos, adquisición de fondos para el proyecto, administración del proyecto, análisis formal, redacción, revisión y edición del documento,

Título: Transungual Delivery, Anti-Inflammatory Activity, and *In Vivo* Assessment of a Cyclodextrin Polypseudorotaxanes Nail Lacquer

Autores/as (por orden de firma): Francisco Fernandez-Campos; Francesc Navarro; Adrian Corrales; Jordi Picas; Eloy Pena; Jordi Gonzalez; Francisco J. Otero-Espinar.

Año: 2020

Clave (A: artículo, R: review): A

Revista (título, volumen, página inicial-final): *Pharmaceutics* 2020, 12, 730.

ISSN: 1999-4923

DOI (o URL en su defecto): [obligatorio en publicación electrónica]: <https://doi.org/10.3390/pharmaceutics12080730>

<p>Indexado en WoS Core Collection (SCIE, SSCI, AHCI o ESCI) (SI/NO): si</p>	<p>Indexado en Scopus (SI/NO): si</p>
<p>Número de citas del artículo (Wos Core Collection): 0</p>	<p>Número de citas del artículo: 0</p>
<p>JIF del JCR SCIE/SSCI: 6.321 (2020)</p>	<p>Índice SJR: 1.054 (2020)</p>
<p>Cuartil y categoría JCR SCIE/SSCI: Q1. Pharmacy and pharmacology</p>	<p>Cuartil y categoría SJR: Q2. Pharmaceutical sciences</p>

Eloy Pena ha colaborado en los estudios de liberación de la formulación desarrollada.

La revista en la que se ha publicado (Pharmaceutics) es una revista open Access con un elevado factor de impacto (6.321) en el año de la publicación (2020), situada en el Q1 de la categoría de Pharmacy and Pharmacology del JCR. De hecho, el factor de impacto de la revista está en el primer decil del ranking en el JCR (32/357)

Finalmente, se han escrito dos artículos (capítulos 8 y 9) que serán sometidos en un corto periodo de tiempo.

El artículo que será enviado primero (capítulo 8) es el siguiente: Latanoprost-loaded nanotransfersomes for scalp administration. Scale up and biopharmaceutical studies.

Eloy Pena, autor principal del artículo ha trabajado en el desarrollo, escalado y caracterización de los nanotransfersomas, tanto desde el punto de vista fisicoquímico, como del punto de vista biofarmacéutico (estudios de liberación y permeación). Eloy Pena participó en la conceptualización, metodología, visualización, validación, uso de software, curado de datos, adquisición de fondos para el proyecto, administración del proyecto, análisis formal, redacción, revisión y edición del documento.

El Segundo artículo (capítulo 9) que está en preparación se basará en la comparación de dos técnicas ampliamente usadas para evaluar la penetración de activos dentro de la piel tras su administración tópica: MALDI-Imaging y Confocal Raman Spectroscopy.

Eloy Pena, autor principal del artículo ha desarrollado todos los experimentos en colaboración con la Universidad de Santiago de Compostela (USC) y la Universidad Autónoma de Barcelona (UAB). Eloy Pena participó en la conceptualización, metodología, visualización, puesta a punto de las técnicas, uso de software, curado de datos, adquisición de fondos para el proyecto, administración del proyecto, análisis formal, redacción, revisión y edición del documento,

Ambos artículos serán enviados a la revista Asian Journal of Pharmaceutical Sciences, que está en el primer Decil del área de Pharmacology & Pharmacy en los rankings del JIF (24/276) y JCR (35/357).

Chapter 3. Epidermal delivery of retinyl palmitate loaded transfersomes: penetration and biodistribution studies

Resumen

La alteración de los niveles de retinoides en la piel puede provocar diferentes trastornos en la maduración de las células cutáneas epiteliales. La administración tópica de estas moléculas lipofílicas es un reto que puede abordarse mediante la encapsulación en sistemas de administración de fármacos. En este estudio se desarrollaron transfersomas de palmitato de retinilo formulados en crema y se evaluaron los incrementos en la penetración de los principios activos así como la biodistribución *in vitro* y *ex vivo*. Se observó un aumento significativo en la acumulación de palmitato de retinilo en la epidermis mediante separación de las diferentes capas de la piel y análisis mediante cromatografía líquida. Además, mediante microscopía de fluorescencia de biopsias de piel de oreja de cerdo no dermatomizada se confirmó la acumulación de los transfersomas encapsulando retinil palmitato marcados fluorescentemente. Estos resultados sugieren que los transfersomas pueden ser un vehículo eficaz para la administración de retinoides a las capas internas de la piel, como la epidermis.



Article

Epidermal Delivery of Retinyl Palmitate Loaded Transfersomes: Penetration and Biodistribution Studies

Eloy Pena-Rodríguez , Mari Carmen Moreno, Bárbara Blanco-Fernandez , Jordi González and Francisco Fernández-Campos *

Topical & Oral development R+D Reig Jofre Laboratories, Gran Capitan Street 10, San Joan Despi, 08970 Barcelona, Spain; eloy.pena@reigjofre.com (E.P.-R.); maricarmen.moreno@reigjofre.com (M.C.M.); barbara.blanco.fernandez@gmail.com (B.B.-F.); jordi.gonzalez@reigjofre.com (J.G.)

* Correspondence: Francisco.fernandez@reigjofre.com; Tel.: +34-935-507-718

Received: 16 December 2019; Accepted: 27 January 2020; Published: 30 January 2020



Abstract: The alteration of retinoids levels in the skin can cause different disorders in the maturation of epithelial skin cells. Topical administration of these lipophilic molecules is a challenge that can be addressed by encapsulation into drug delivery systems. In this study, retinyl palmitate transfersomes formulated in cream were developed and the increases in the penetration of the active ingredients as well as the biodistribution were evaluated *in vitro* and *in vivo*. Transfersomes demonstrated a significant increase in the administration of retinyl palmitate to the epidermis by quantification of the active ingredients in the different layers of the skin, as well as by fluorescence microscopy of biopsies of non-dermatomized pig-ear skin. These results suggest that transfersomes may be an efficient vehicle for the delivery of retinoids to inner layers of the skin, such as the epidermis.

Keywords: transfersomes; retinyl palmitate; biodistribution; skin; penetration; drug release

1. Introduction

Vitamin A derivatives are a group of lipid-soluble compounds including retinol, retinal, retinyl acetate, retinyl linoleate and retinyl palmitate (RP). Retinoids have important effects on skin cells. Retinoid levels in the skin are involved in the correct cellular maturation of keratinocytes, and when the skin is damaged, they induce keratinocyte proliferation and modulate epidermal differentiation [1]. Moreover, retinoids stimulate the production of extracellular matrix proteins such as collagen I by dermal fibroblasts. Alterations in these levels produce a de-structuring of corneocytes' layers and, consequently, an increase in transepidermal water loss. Retinoids can also lighten hyperpigmented skin by decreasing melanocyte tyrosinase activity, inhibit the sebocyte proliferation and lipid synthesis, and alter their keratin expression. Alterations in retinoids skin levels can cause skin dehydration, lack of elasticity, sebum overproduction and hyperpigmentation, among other effects [2,3].

As retinoids cannot be synthesized by the body, they must be supplied through other sources [4]. Since these molecules are easily degraded by oxidation or photodegradation, and they are very hydrophobic, their topical bioavailability when applied on the skin surface remains quite low. In addition, retinoids have adverse effects such as hepatotoxicity, changes in lipid metabolism and bone density, teratogenicity, and they can cause significant skin irritation. Most of these effects occur after oral administration. Regarding topical administration, the main adverse effects are phototoxicity and skin irritation. One plausible mechanism of phototoxicity may be related to the formation of free radicals after the exposure of retinoids to UV light that damages the DNA. Relevant clinical studies or studies in animal models are therefore needed to establish whether the pro-oxidant activity of photoexcited vitamin A is observed *in vivo*, and to assess the related risks [5].

Skin irritation is linked to retinoids due to its pharmacological effects through retinoic acid receptor signaling [6]. Cytokines such as IL-1, TNF- α , IL-6, and IL-8 are thought to be more important in retinoid-induced dermatitis [7]. Retinyl Palmitate was irritating to rabbits' skin, and a slight irritant to rabbit eyes. [4]. Thus, although retinoids have been classically incorporated into emulsions to overcome some of these limitations, skin irritation and photodegradability issues are still a problem [8]. The inclusion of retinol derivatives such as retinyl palmitate into nanocarriers for topical delivery is an interesting strategy that can lead to higher stability and enhance skin penetration [9]. Liposomes are a suitable choice for retinoids' encapsulation, as the active ingredients can be incorporated into the membrane of the particles, ending in skin penetration and enhanced stability.

Liposomes are spherical vesicles formed of a lipid bilayer and an aqueous cavity. They consist of phospholipids or synthetic amphiphilic molecules, usually combined with sterols to reduce their membrane permeability. Phospholipids tend to self-assemble in the presence of water due to their amphiphilic nature. The hydrophilic head is oriented towards the water, while the apolar tails are located in the inner part of the bilayer. The nature of the lipids will determine the liposomes' properties. Saturated phospholipids can obtain liposomes with a lower permeability and greater stability than unsaturated phospholipids [10].

Classic liposomes usually accumulate in the stratum corneum and skin annexes. Therefore, they are not a good means to reach deeper layers of the skin or for transdermal absorption [11]. Therefore, different liposomal approaches have appeared. One example of these are ethosomes, which have ethanol in the vesicle cavity that behaves as a penetration promoter [12]. Another example are transfersomes, which are ultra-deformable liposomes [13]. This type of liposome has an "edge activator" (i.e., sodium cholate, sodium deoxycholate, span 80, Tween 80 or dipotassium glycyrrhizinate, among others) in its lipid membrane that allows it to increase its elasticity. There are several theories that explain the high penetration ability of these vesicles. The most accepted theory is that the high deformability of the transfersomes allows them to cross the intercellular channels of the stratum corneum [14,15]. Several researchers have demonstrated the improvement in topical penetration, for example, with retinol in dermatomized human skin and the keratinocytes 3D model [9], and with lidocaine-loaded transfersomes, in order to avoid a painful local anesthetic injection [16].

The bilayer lipid matrix of cell membranes is composed of a mixture of different lipids. Among them, there is a growing interest in sphingolipids due their effects on skin cellular processes. Ceramides are a structurally heterogeneous and complex group of sphingolipids. It is well known that ceramides play an essential role in structuring and maintaining the water permeability barrier function of the skin. Ceramides maintain the dense crystalline structure of the lamellar lipids that are arranged between the corneocytes. They represent the 50% of lipids in the stratum corneum [17]. The rest of the lipids of the stratum corneum are cholesterol and free fatty acids. Together, they keep the lamellar structure of the stratum corneum and the barrier function of healthy skin in good condition. However, most skin disorders that have a diminished barrier function present a decrease in total ceramide content, with some differences in the ceramide pattern. Alterations in ceramide III levels are related to different skin diseases. In psoriatic skin, ceramides III and VII show a significant decrease versus normal stratum corneum [18]. In patients with atopic dermatitis, a decrease in the amount of ceramide III has been demonstrated to be correlated with an increase in transepidermal water loss [19]. Formulations containing lipids identical to those in skin and, in particular, ceramide supplementation, could improve disturbed skin conditions. Several authors have introduced ceramides in lipid-based vesicles to deliver them into the skin to restore lipid composition and to improve altered skin permeability [20,21]. Exogenously supplied, short-chain ceramides, such as ceramide III, induced keratinocyte differentiation *in vitro* and reinforced the pro-differentiation effects of other drugs [17].

Based on the effects of ceramide III and retinyl palmitate, as previously described, the formulations in this study were designed to improve and maintain the skin's barrier properties. The aims of this work were the development and characterization of a ceramide III-based transfersome cream formulation encapsulating retinyl palmitate, and the study of RP biodistribution through the different skin layers.

2. Materials and Methods

2.1. Materials

Ceramide III (Evonik Nutrition & Care, Essen, Germany), α -Tocopherol (Merck Chemicals and life, Barcelona, Spain), phosphatidylcholine (Lipoid, Ludwigshafen, Germany), Tween 80 (Croda Iberica S.A., Barcelona, Spain), Retinyl Palmitate and Ethanol Absolute (Scharlab S.L. Barcelona, Spain) and purified water (Inhouse) were used to formulate the transfersomes. Dissodium EDTA (Sucesores de Jose Escuder, S.L., Barcelona, Spain), PEG-6 stearate (and) Ceteth-20 (and) Steareth-20 (Gattefosse España, Madrid, Spain), Cetyl Stearyl alcohol (BASF, Barcelona, Spain), medium chain triglycerides (Oximed expres S.A., Barcelona, Spain) and Xanthan gum (Azelis España S.A., Barcelona, Spain) were used to formulate the emulsion. Metanol (Scharlab S.L., Barcelona, Spain), Nile Red, Hoeschst, phosphate buffer saline, paraformaldehyde (Sigma Aldrich, Madrid, Spain), uranyl acetate, optimal cutting temperature compound (IESMAT S.A., Barcelona, Spain), were used to perform the different analyses.

2.2. Production of Retinyl Palmitate-Loaded Transfersomes

Transfersomes were manufactured by the sonication method [22,23]. α -Tocopherol (0.02% *w/w*), ceramide III (0.10% *w/w*), phosphatidylcholine (1.78% *w/w*), tween 80 (0.10% *w/w*) and RP (1.10% *w/w*) were dissolved in ethanol (10% *w/w*) (organic phase). Then, milliQ water (qs 100% *w/w*) was added to the organic phase, and the system was vortexed for 1 min. Afterwards, the mixture was sonicated with a probe sonicator (amplitude of 80%, 5 min, Energy 7000 Ws, Frequency 23.88 kHz). The transfersomes' suspension was left to settle at room temperature, protected from the light. Additionally, empty transfersomes (without RP) were fabricated, to study the effect of RP on the physio-chemical characteristics of the nanosystems.

2.3. Transfersome Incorporation in a Cream Formulation

A mixture of surfactants (PEG-6 stearate (and) Ceteth-20 (and) Steareth-20 4% *w/w* and Cetyl Stearyl Alcohol 0.5% *w/w*), oils (Medium Chain Triglycerides or MCT 3% *w/w*) and an aqueous phase (12.6% *w/w*) with Xanthan gum (0.1% *w/w*) and disodium EDTA (0.1% *w/w*) were warmed up separately at 70–80 °C in a thermostatic bath. Once both phases were heated, the oil phase was added to the aqueous phase under mechanical stirring at 15,000 rpm for 2 min (Ultra-Turrax IKA T25, disperser unit S25KD 25F), and the mixture was allowed to cool down at 30 °C. Then, the transfersomes aqueous suspension, with RP at a concentration of 1.1% *w/w*, was added to the cream at a ratio of 1:1, so that the final RP concentration was 0.55% *w/w* (chosen taking the recommended concentrations for Retinol and Retinyl palmitate into account [5]). For the manufacture of the non-transfersomes emulsion, water was added up to 100%.

2.4. Transfersomes Physic-Chemical Characterization

RP-loaded transfersomes were subjected to a stability study in 25 ± 2 °C/60% \pm 5% RH and 40 ± 2 °C/75% \pm 5% RH chambers for 18 and 6 months, respectively, and conditioned in hermetically sealed glass vials.

Hydrodynamic size, polydispersion index (PDI) and zeta potential were studied through dynamic light scattering (DLS) using a Zetasizer Nano ZS (Malvern, UK). Dilutions of 1:10 in water were used for the measurements.

Transfersome morphology was studied through transmission electron microscopy (TEM) using a Jeol JEM 1010 100 kv (Jeol, Tokyo, Japan). TEM grids were coated with formvar of a 1:10 transfersome dilution in milliQ water and incubated for 1 min at room temperature. Grids were then washed with water and stained with a 2% *w/w* uranyl acetate solution for 1 min at room temperature. Afterwards, they were dried overnight and analyzed within two weeks of staining.

The flexibility of the transfersomes was analyzed by extruding the transfersomes solution in an Avanti Mini Extruder with a 100 nm pore size polycarbonate membrane, at 1 mL of volume capacity. Pressure was applied by hand. The ability of the transfersomes to recover their initial size after extrusion was analyzed through DLS. The deformability index (DI) was defined as Equation (1),

$$DI = \left(\frac{r_p}{r_m} \right)^2 \quad (1)$$

where r_p is the radius of a the extruded transfersomes and r_m is the radius of the membrane pores [24].

2.5. Cream Physic-Chemical Characterization

Appearance (visual observation), pH (pHmeter Crison Instruments S.A. Alella, Spain) and viscosity (Brookfield RDV-III Ultra, Spain. Spindler: SC4-21, Speed: 200 rpm, Temperature: 25 °C, Spain) were studied for the transfersome- and non-transfersome-loaded emulsions.

2.6. Diffusion Assay of RP-Loaded Transfersomes

In vitro diffusion of free RP and RP from the transfersomes ($n = 6$) was studied using vertical Franz Cells (VidraFoc, Spain, receptor compartment of 12 mL, diffusional area of 2.54 cm²). MCT was used as a receptor medium (RM) to keep sink conditions along the experiment. The dose of each formulation tested in the donor compartment was 240 mg (1.04 mg/cm²). The temperature of the experiment was maintained at 32 °C, and the stirring speed of the RM was 500 rpm. The membrane used was Polyvinylidene Fluoride (PVDF, Millipore, Spain) of a pore diameter 0.22 µm.

Aliquots of 300 µL were taken at times 1, 2, 3, 4, 6, 24 and 30 h and injected into HPLC to quantify the amount of diffused RP.

2.7. RP HPLC Analysis and Encapsulation Efficiency

The encapsulation efficiency (% EE) of RP in the liposomes was determined indirectly (Equation (2)). Briefly, transfersomes were centrifuged in 30 KDa Amicon ultracentrifugal filter (Merck Millipore) at 4500 rpm for 30 min. The amount of RP in the filtrate and in transfersomes were analyzed using a HPLC (Waters 2695, Spain), with a photodiode array detector (Waters 2996, Spain) with the corresponding calibration curve (Range 3.40 to 280 µg/mL with an $r^2 > 0.999$). The column was a C18 (12.5 × 4.6 mm) with particle size of 5 µm. The mobile phase was an isocratic mixture of Metanol:water (98:2). The flow rate was 1.8 mL/min and the injection volume was 20 µL. the samples' temperature was set at 5 °C and column temperature at 40 °C. % EE was determined using Equation (2),

$$\% EE = \frac{W_{NE} - W_T}{W_T} \times 100 \quad (2)$$

where W_{NE} is the amount of RP quantified in the filtrate (RP not encapsulated) and W_T is the RP quantified in the total amount of RP used for the preparation of transfersomes.

2.8. Pig Skin Penetration Assays

Three to four month old male and female pigs were obtained from the Animal Facility at Bellvitge Campus of Barcelona University (Barcelona, Spain). Immediately after the animals ($n = 3$) were sacrificed, using an overdose of sodium thiopental anesthesia, the ears were surgically removed and frozen. On the day of experiment, ears were defrosted and the skin was excised.

2.8.1. Skin Penetration Assay: Full Thickness Pig Ear Skin

Skin samples were mounted on Franz-cells ($n = 6$) according to the description in Section 2.6. The following formulations were tested: RP-loaded transfersomes, a free RP solution in MCT,

transfersome-loaded emulsion (T emulsion) and a non-encapsulated RP emulsion. An amount of 240 mg of formula was administered in infinite doses in non-occluded conditions.

After 24 h, RP mass-balance was performed: RM was analyzed directly by mean HPLC, then the non-penetrated formulation in the donor compartment (non-penetrated) was recovered and RP was extracted from the emulsion according to the method described in Section 2.7. Skin pieces were taken and washed with distilled water (wash), and stratum corneum, epidermis and dermis were obtained, and RP extracted according to the methodology described in Section 2.8.2 and analyzed by HPLC [25,26].

2.8.2. Skin Layers Recovery

An incubation solution of RP in receptor medium at a concentration of 0.22 mg/mL was prepared, then skin layers were separated and incubated for 24 h with the incubation solution. After incubation, an extraction process was performed. Skin samples were subjected to 20 min of bath sonication in Metanol:water (98:2) and RP from the different skin layers was quantified by means of HPLC (Section 2.7). Stratum corneum was removed by applying 30 tape strips (pressure 225 g/cm² for three seconds [27]). To separate epidermis and dermis, samples (after stripping) were immersed in 60 °C PBS for 2 min and excised with the help of forceps and a scalpel. The recovery percentage was applied to the results obtained in the penetration assays.

$$\% \text{ Recovery} = \frac{\frac{Q_{\text{extracted}}}{\text{Sample mass}}}{\frac{(Q_{0h} - Q_{24h})}{\text{Sample mass}}} \times 100 \quad (3)$$

The percentage of recovery was calculated from Equation (3), where “Q_{extracted}” is the amount of RP extracted from the sample after solvent incubation (Metanol:Water 98:2), “Q_{0h}” is the initial amount of RP in the incubation solution at time 0, “Q_{24h}” is the amount of RP in the incubation formula after 24 h of experiment and “Sample mass” is the mass of each skin layer sample. RP analyses were performed according to Section 2.7.

2.9. Fluorescence Biodistribution Assay

To study the biodistribution of the transfersomes in the skin, fluorescent-marked transfersomes were incubated on top of full-thickness ear pig skin samples using vertical Franz Cells (according to Section 2.8.1). Non-loaded transfersomes (autofluorescence control), Nile red-loaded transfersomes and free Nile red solution were added to the experiment (all at concentrations of 0.312 µg/mL).

After 24 h of incubation, skin samples were taken and cut into 0.25 cm² pieces. They were then fixed with 4% paraformaldehyde (PF) for 30 min. Then, samples were washed with a phosphate buffer solution (PBS), and incubated in increasing concentrations of sucrose (up to 30% w/w) as a cryoprotectant. Samples were mounted in an optimal cutting temperature compound (OCT, from Fischer Scientific) and cut in the cryostat (Leica Biosystems) with a thickness between 30 and 50 µm, and placed on the superfrost slides with poly-lysine coating.

The slides were washed with PBS to remove the remaining OCT and incubated with Hoeschst (2 µg/mL) for 30 min, and then washed with PBS. Samples were visualized by a Leica DMIRB Wide Field Fluorescence and Transmitted Light Microscope [28].

2.10. TEWL after In Vivo Topical Administration

An in vivo test was carried out in humans with T and NT emulsion. The study was conducted according to the Declaration of Helsinki. Volunteers gave their written consent. Transepidermal water loss (TEWL) was measured by the Vapometer (Delfin Technologies, Kuopio, Finland) before and after the application of the different creams to monitor SC removal [29]. A template with three application

zones (NT emulsion, T emulsion and negative control: no emulsion applied) with an area of 2.54 cm² for the forearm was used.

Six male and female individuals ($n = 6$) with ages ranging from 23 to 44 years old participated. An amount of 0.025 g of each emulsion was applied on the skin by the same operator in the same conditions. After 2 h, skin was gently cleaned [30].

3. Results and Discussion

3.1. Transfersomes Physico-Chemical Characterization

The manufacture of empty liposomes (without RP) was unsuccessful. During the cooling process after sonication, the viscosity of the formula increased greatly, forming a gel, and no transfersomes were formed.

The RP-loaded transfersomes obtained had a hydrodynamic diameter of 300.5 nm with PDI = 0.471, and a negative charge (Table 1). The % EE of RP was quantified by HPLC, as 100%. The RP limit of detection (LOD) and limit of quantification (LOQ) of the analytical method were 0.22 and 0.72 µg/mL, calculated by the signal to noise ratio). No RP was observed in the filtrate, demonstrating that all had been encapsulated. This fact, and the increased viscosity in empty transfersomes, seems to indicate that the entire RP is integrated with the transfersome membrane, and its presence is essential for the correct stabilization and formation of the nanosystems.

Table 1. Transfersome physical chemical parameters, measured by dynamic light scattering (DLS) and HPLC. Assay (%) refers to the HPLC retinyl palmitate (RP) quantification assay respect to the nominal value of RP (1.1% *w/w*).

Sample	Hydrodynamic Diameter (nm)	PDI	Z-Potential (mv)	Assay (%)	EE (%)
Transfersomes	300.5 ± 10.9	0.471 ± 0.020	-9.48 ± 1.50	102.63 ± 0.51	100 ± 0

Transfersomes had a spherical shape (Figure 1). Mean particle diameter was also measured by TEM to corroborate the size results obtained in DLS with the TEM images, and to study the morphology of the vesicles. Using Image J software, the diameter obtained was 238.48 ± 29.74 nm. The fact that the diameter obtained in TEM is smaller than in DLS is due to the solvation of the transfersomes when measured in aqueous suspension.

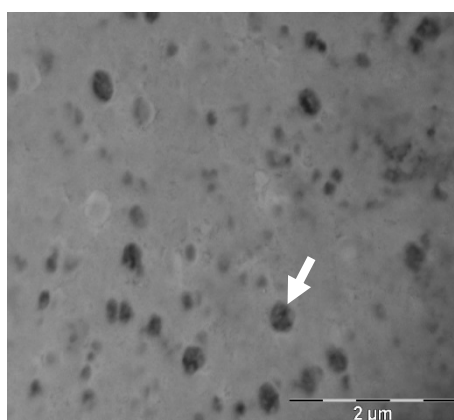


Figure 1. Transmission electron microscopy pictures of negative-stained transfersomes with uranyl acetate.

After manufacturing, transfersomes were stored in climate chambers at 25 °C/60% HR for 18 months and 40 °C/75% HR for six months (as accelerated conditions). Regression analysis of particle size and PDI was performed to check their evolution over time (Figures 2 and 3). As can be seen in

Table 2, the slope’s p-values were above 0.05, so the regression lines are statistically equal to zero, which means the RP-loaded transfersomes kept their hydrodynamic diameter and PDI stable at these conditions. The lack of significant variations at accelerated conditions, according to ICH Q1E [31], means the estimated product shelf-life can be extended to 36 months.

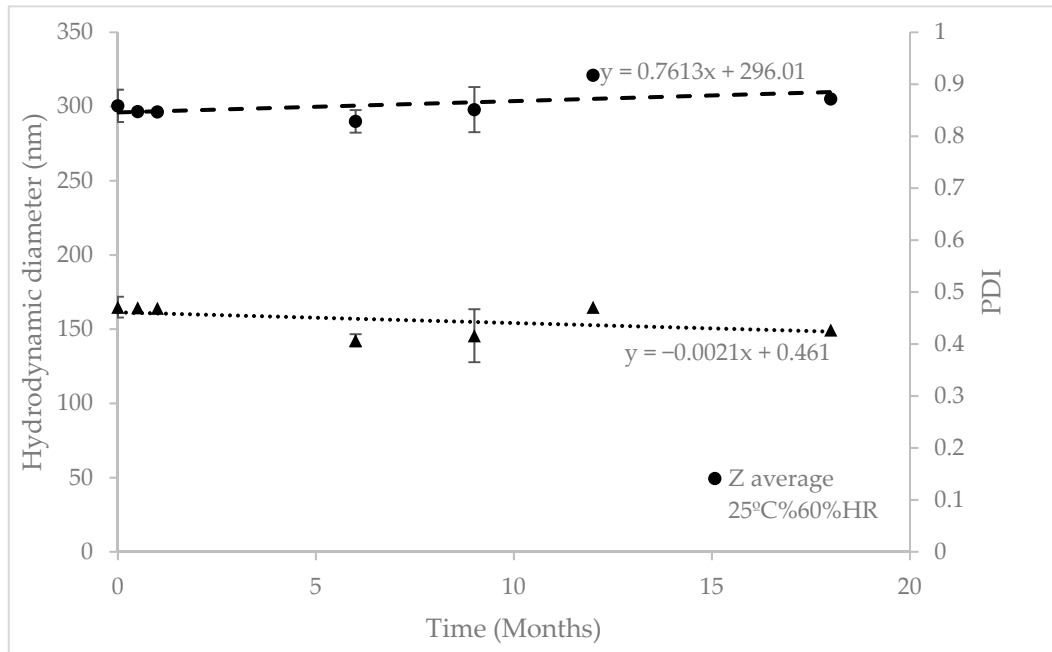


Figure 2. Stability studies at 25 ± 2 °C/60% ± 5% Relative Humidity (HR) over 18 months. RP-loaded transfersomes’ hydrodynamic diameter and polydispersity index, monitored over time.

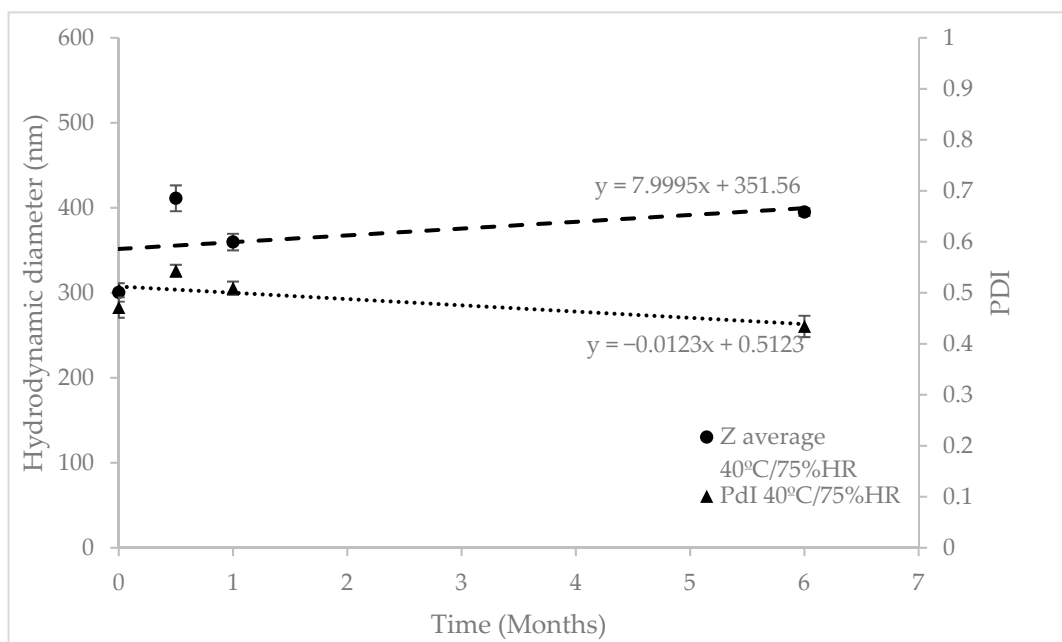


Figure 3. Stability studies at 40 ± 2 °C/75% ± 5% HR for six months. RP-loaded transfersomes’ hydrodynamic diameter and polydispersity index, monitored over time.

Table 2. Transfersome stability regression slopes.

Condition	25 °C/60% HR		40 °C/75% HR	
	Response	Hydrodynamic Diameter	PDI	Hydrodynamic Diameter (nm)
Slope	0.761	−0.002	8.000	−0.012
<i>p</i> -value	0.231	0.277	0.546	0.275

Transfersomes are defined as deformable liposomes, due to the presence of edge activators. To assess their flexibility, the Teixeira et al. method was used. This demonstrated the flexibility of their polymeric nanocapsules, based on the particles' ability to recover their initial size after extrusion [32]. On the other hand, Yu-Kyoung Oh et al. [9] studied the deformability index of transfersomes manufactured with different edge activators. They obtained the highest DI with tween80 and tween20 (DI = 6 and 8.45, respectively).

In this study, RP transfersomes were extruded by a 100 nm pore size membrane, approximately three times smaller than their hydrodynamic diameter. The vesicle size and PDI before and after extrusion is shown in Table 3, as well as the DI. The difference in diameter is very small, showing their ability to recover their size after extrusion. However, a small proportion of the particles, probably the largest, are partially extruded, which explains the PDI decrease. These results are consistent with the results obtained by Teixeira et al. These results are also in agreement with Yu-Kyoung Oh et al., as the DI results are similar when choosing polysorbates as edge activators.

Table 3. Transfersomes' diameter, polydispersion index (PDI) and deformability index.

Sample	Hydrodynamic Diameter (nm)	PDI	Deformability Index
Transfersomes	300.5 ± 10.9	0.471 ± 0.020	8.12
Extruded Transfersomes	285.5 ± 9.7	0.247 ± 0.014	

3.2. Transfersome Cream Physic-Chemical Characterization

Transfersome cream formulation and non-transfersome cream formulation appearance, pH and viscosities are shown in Table 4. The pH was in the same range as the human skin pH (between 4.5 and 5.5). Transfersome cream viscosity was higher, due to the increase in total lipid components. Both cream RP contents were assayed, and the obtained results were between 95% and 105%.

Table 4. Physio-chemical parameters of transfersome and non-transfersome cream formulations.

Sample	Appearance	pH	Viscosity (cP)	Assay (%)
NT Cream	White-yellowish cream	4.86	64.70 ± 0.18	98.07 ± 0.68
T Cream	White-yellowish cream	4.81	100.15 ± 2.35	96.87 ± 0.72

3.3. Synthetic Membrane RP Diffusion Assay

Table 5 shows the % RP released at different timepoints from the transfersomes. Only 7.64% of RP was able to diffuse through the synthetic membrane after 30 h of experiment. Until six hours of experiment, no RP peak appeared in any of the chromatograms. As discussed previously, RP is completely integrated into the liposome membrane, forming a structural part of it. The presence of RP in the receptor medium at longer timepoints could be due to the drug diffusion from the liposomal lamella to the receptor medium (based on sink conditions), which is the classical release theory. However, although the membrane's pore size does not allow transfersome to pass through, it demonstrated their flexibility. Due to the lack of pressure from extrusion, vesicle translocation to RM across membrane pores takes a longer time to occur. Once transfersome crosses the pore, hydrophobic solution make them destructured and causes them to release RP. To ensure that intact transfersomes were able to cross the membrane pore, the experiment was replicated with water as

the receptor medium instead of MCT, because DLS characterization would not be possible in this medium. After 24 h, an aliquot was extracted and measured by DLS. A population with a similar size (approximately 280 nm) appears, even though the count rate (kcps) was low (less than 200), indicating a low concentration of particles in the sample.

Table 5. RP-released percentage through a synthetic membrane from a transfersome formulation.

Time (h)	Mean RP Released (%)	Standard Deviation (%)
4	0	0
6	0.36	0.57
24	6.81	6.19
30	7.64	6.61

3.4. Franz-Cells Full-Thickness Pig Skin Penetration Assays

3.4.1. Transfersomes' RP Penetration

Figure 4 shows the penetration profile of RP from transfersomes and control (free RP solution in MCT) formulations in the different skin layers. Mass balance ranged between 90%–110% recovery in both cases.

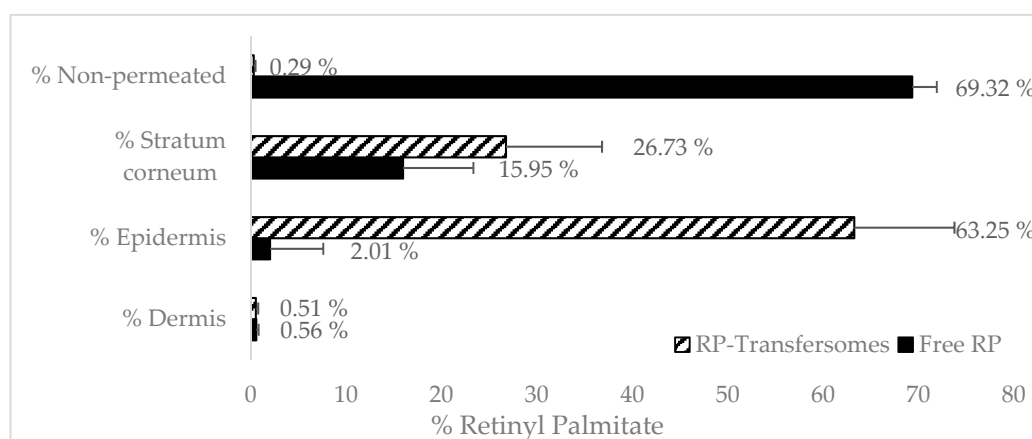


Figure 4. Black bar shows the free retinyl palmitate penetration. The black striped bars show the RP penetration from transfersomes.

RP was not detected in the receptor medium in any of the formulations after 24 h, which seems to indicate that, after topical application, RP would not reach systemic circulation.

Vehiculation in transfersomes has a significant effect on the biodistribution of RP in the different layers of the skin. In the case of non-vehiculated RP, most of the active ingredients did not penetrate the skin (69%) and only 2% reached the epidermis. The RP logP was around 15 [5] which is far from the optimal range (2–3) [33] to obtain maximum transdermal permeability. Its molecular weight is near 500 Da, which is considered the maximum value for transdermal absorption [34]. Therefore, it is expected to have a poor permeability.

The percentage of RP found in the stratum corneum was higher in transfersomes (26%) than in free solution. Stratum corneum can act as a reservoir with a depot effect for epidermis absorption. However, part of this amount will also be eliminated during the natural desquamation cycle of the stratum corneum.

RP found in epidermis was much higher in the case of transfersomes (63%), demonstrating that the increase in the delivery of RP into epidermis results in viable keratinocytes being found, which lead to its pharmacological effect. These results confirm the promoting effect of transfersomes for RP absorption, compared with a free solution of RP. Similar results were found by Yu-Kyoung Oh et

al., who demonstrated an increase in the penetration of deformable liposomes based on the tween20 encapsulating retinol [9] compared with classic liposomes and free retinol solution. An increase in the epidermal delivery of RP loaded in vesicles was also obtained by Clares et al. [35]. In a study with dermatomized skin (0.4 μm) the liposomal systems demonstrates a greater penetration of nanoemulsions and solid lipid nanoparticles. Teixeira et al. [32] performed similar penetration assays on RP loaded in polymeric nanocapsules. Both of them obtained similar results to the ones shown in this research, of an approximately three-fold increase in RP levels in deep skin layers, compared with the amount found in the stratum corneum.

3.4.2. Emulsions RP Penetration

It is very common to introduce liposomes or other topical drug delivery systems into emulsions to improve their attractiveness to final users. The inclusion of these formulations in emulsion could modify their physicochemical and biopharmaceutical characteristics. In order to evaluate the dilution effect and how the emulsification process could affect the transfersomes' properties, a manufacturing simulation was carried out, because of the difficulty of finding transfersomes inside emulsions by electronic microscopy. RP transfersome solution was heated at the emulsion oil phase melting point (70–80 $^{\circ}\text{C}$) for 15 min, then a water phase at the same temperature was added to the transfersome solution and mixed for 2 min with mechanical stirring at 15,000 rpm with the ultraturrax. Resulted solution was allowed to cold down and, after 24 h, vesicle size and PDI were measured by DLS, obtaining transfersomes of 266.4 nm and PDI 0.554. Even though this experiment cannot prove if the transfersomes fuse with the lipid components of the cream or not, it does demonstrate that transfersomes are able to resist the dilution effect and the emulsification process.

Figure 5 shows the penetration of RP T emulsion and NT emulsion. It seems that the inclusion of transfersomes in an emulsion slows down the epidermis absorption, but, conversely, transfersomes increase the delivery of RP into epidermis. It seems that the emulsion could improve the dermis absorption of RT when transfersomes are used. In this case, the RP found in SC did not exhibit large differences between formulations. The presence of additional surfactants and emollients in the emulsion seems to improve RP disposition in SC when they are not loaded in transfersomes, but the epidermal and dermal delivery is still higher in the presence of transfersomes.

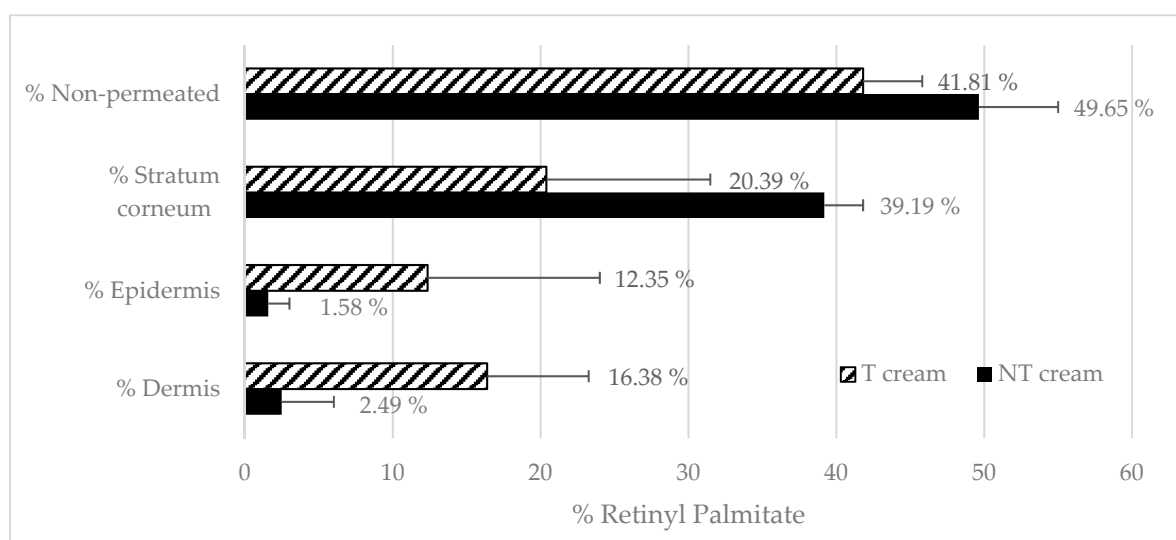


Figure 5. Black bar shows the RP penetration from Non-transfersome (NT) emulsion. The black striped bars show the RP penetration from T emulsion.

3.5. Fluorescence Biodistribution Assay

In order to confirm the increase in the epidermal delivery of RP in transfersomes, a fluorescence microscopy experiment was carried out with Nile red-loaded transfersomes and a free Nile red solution. Figure 6 shows the superposition of two fluorescence emission measurements from the same area of the skin sample (emission in the blue range for the cell nuclei stained by Hoeschst, and red for the Nile red formulation). As can be seen, the control of Nile red free solution (Figure 6a) only shows red fluorescence in the most superficial layer of the skin (stratum corneum), while the fluorescent marker loaded in transfersomes penetrates towards inner layers of the skin and, consequently, red fluorescence is observed (Figure 6b). These results agree with the results of the quantification of RP in the different layers of the skin, in which an accumulation of active ingredients in the epidermis and dermis was observed when it was vehiculized in transfersomes.

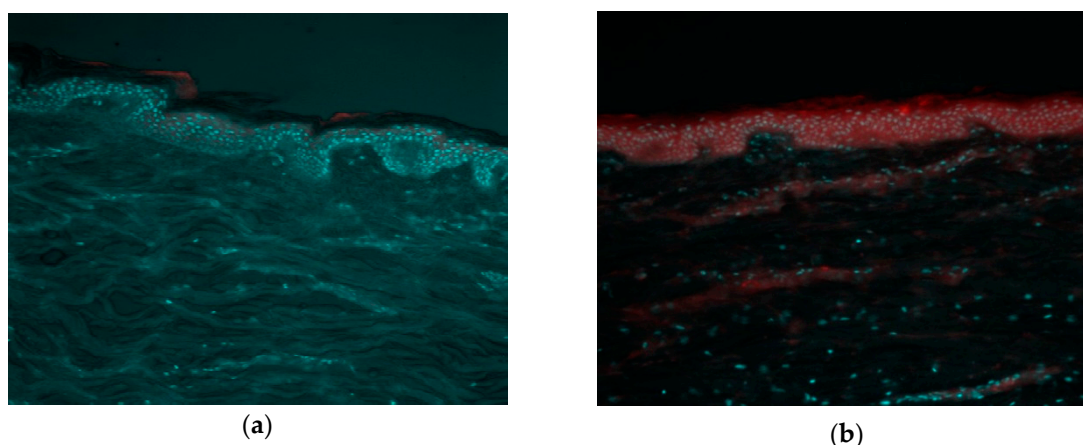


Figure 6. Fluorescence microscopy images of pig-ear skin cross-section. Red color corresponds to Nile red fluorescence and blue to Hoeschst staining of the cell nucleus. (a) Not vehiculized Nile red control (image J, mean epidermis intensity 7846 ± 140 AU); (b) Nile red-marked transfersomes (image J, mean epidermis intensity $12,428 \pm 254$ AU). The images were captured using 10 \times magnifications

3.6. In Vivo Topical RP Penetration

The T and NT emulsions were tested in six volunteers for the screening of skin compatibility (based on TEWL measurement) and for RP quantification in the stratum corneum. Table 6 shows the TEWL ($\text{g}/\text{m}^2 \text{ h}$) measurements for each individual before and after application of the formulations. In order to study the stability of TEWL measurements, a *t*-test between the TEWL ratio and one was performed before and after application. No statistical differences were found, which means that the integrity of the skin is not affected by the formulations.

Table 6. Transepidermal water loss (TEWL) average measures before and after the application of L and NT creams, as well as *p* value of the comparison between the ratio and 1 before and after application.

Time 0 h TEWL ($\text{g}/\text{m}^2 \text{ h}$)	Standard Deviation ($\text{g}/\text{m}^2 \text{ h}$)	Time 2 h after Application TEWL ($\text{g}/\text{m}^2 \text{ h}$)	Standard Deviation ($\text{g}/\text{m}^2 \text{ h}$)	Ratio TEWL 2 h/0 h	<i>p</i> -Value vs. 1
11.17	1.25	10.63	0.99	0.95	0.388

Two hours after application, the skin surface was cleaned, and tape strips were taken from each individual until TEWL values increased to 30–35 $\text{g}/\text{m}^2 \text{ h}$. A two sample *t*-test was performed to analyze the significance of the differences between the ratio and 1 before and after application, and there were no significant differences, as can be seen in Table 4 (*p* value 0.388).

4. Conclusions

Deformable transfersomes were successfully obtained with RP, integrated in the liposome membrane, with an estimated shelf-life of 36 months. RP-loaded transfersomes demonstrated an increase in penetration into the skin layers under the stratum corneum of the skin in vitro compared to a free RP control. Similarly, the inclusion of transfersomes to an emulsion increased RP skin penetration compared to the same emulsion without transfersomes. These results are reinforced thanks to the biodistribution experiment with fluorescence microscopy, where a significant increase in epidermis penetration was observed. The in vivo study demonstrated the compatibility of the tested formulations. Given these results, the developed transfersome formulation is a good candidate to increase the delivery of highly lipophilic drugs such as RP to the epidermis.

Author Contributions: F.F.-C. conceived and designed this study and revised the manuscript; E.P.-R. and M.C.M. performed the studies; B.B.-F. participated in the performance of these studies; E.P.-R. analyzed the data, created the graphics and wrote the paper; J.G. provided funding acquisition and supervised this project. All authors have read and agreed to the published version of the manuscript.

Funding: This research received no external funding.

Acknowledgments: Assistance provided by Manel Bosch and Marta Taulés from the University of Barcelona Scientific-Technical service was greatly appreciated.

Conflicts of Interest: The authors declare no conflict of interest.

References

1. Gerard, J.; James, G.; Mezick, A. Pharmacological effects of retinoids on skin cells. *Ski. Pharm.* **1993**, *6*, 24–34.
2. Mukherjee, S.; Date, A.; Patravale, V.; Korting, H.C.; Roeder, A.; Weindl, G. Retinoids in the treatment of skin aging: An overview of clinical efficacy and safety. *Clin. Interv. Aging.* **2006**, *1*, 327–348. [[CrossRef](#)] [[PubMed](#)]
3. Jean, J.; Soucy, J.; Roxane, P. Effects of Retinoic Acid on Keratinocyte Proliferation and Differentiation in a Psoriatic Skin Model. *Tissue Eng. Part A* **2011**, *17*, 13–14. [[CrossRef](#)] [[PubMed](#)]
4. O’Byrne, S.M.; Blaner, W.S. Retinol and retinyl esters: Biochemistry and physiology. *J. Lipid Res.* **2013**, *54*, 1731–1743. [[CrossRef](#)] [[PubMed](#)]
5. Scientific Committee on Consumer Safety. *Opinion on Vitamin A (Retinol, Retinyl Acetate, Retinyl Palmitate)*; Scientific Committee on Consumer Safety: Brussels, Belgium, 2016.
6. MacGregor, J.L.; Maibach, H.I. The Specificity of Retinoid-Induced Irritation and Its Role in Clinical Efficacy. *Exog. Dermatol.* **2002**, *1*, 68–73. [[CrossRef](#)]
7. Kim, B.H.; Lee, Y.S.; Kang, K.S. The mechanism of retinol-induced irritation and its application to anti-irritant development. *Toxicol. Lett.* **2003**, *146*, 65–73. [[CrossRef](#)]
8. Liu, J.C.; Wang, J.C.T.; Yusuf, M.; Yamamoto, N.; Kazama, S.; Stahl, C.R.; Holland, J.P.; Mather, K.; Aleles, M.A.; Hamada, S.; et al. Topical Oil in Water Emulsions Containing Retinoids. U.S. Patent No. 5976555, 2 November 1999.
9. Oh, Y.; Kim, M.Y.; Shin, J.; Kim, T.W.; Yun, M.; Yang, S.J.; Choi, S.S.; Jung, W.; Kim, J.A.; Choi, H. Skin permeation of retinol in Tween 20-based deformable liposomes: In-vitro evaluation in human skin and keratinocyte models. *J. Pharm. Pharmacol.* **2006**, *58*, 161–166. [[CrossRef](#)]
10. Bozzuto, G.; Molinari, A. Liposomes as nanomedical devices. *Int. J. Nanomed.* **2015**, *10*, 975–999. [[CrossRef](#)]
11. Braun-Falco, O.; Kortung, H.C.; Maibach, H.I. (Eds.) *Griesb Ach Conference: Liposomes Dermatics*; Springer: Berlin/Heidelberg, Germany, 1992.
12. Touitou, E.; Dayan, N.; Bergelson, L.; Godin, B.; Eliaz, M. Ethosomes—novel vesicular carriers for enhanced delivery: Characterization and skin penetration properties. *J. Control. Release* **2000**, *65*, 403–418. [[CrossRef](#)]
13. Jain, S.; Jain, P.; Umamaheshwari, R.B.; Jain, N.K. Transfersomes—A Novel Vesicular Carrier for Enhanced Transdermal Delivery: Development, Characterization, and Performance Evaluation. *Drug Dev. Ind. Pharm.* **2003**, *29*, 1013–1026. [[CrossRef](#)]

14. Paul, A.; Cevc, G.; Bachhawat, B.K. Transdermal immunization with an integral membrane component gap junction protein, by means of ultradeformable drug carriers, transfersomes. *Vaccine* **1998**, *16*, 188–195. [[CrossRef](#)]
15. Cevc, G. Transfersomes, liposomes and other lipid suspension on the skin, permeation enhancement, vesicles penetration and transdermal drug delivery. *Crit. Rev. Ther. Drug Carr. Syst.* **1996**, *13*, 257–388. [[CrossRef](#)] [[PubMed](#)]
16. Omar, M.M.; Hasan, O.A.; El Sisi, A.M. Preparation and optimization of lidocaine transfersosomal gel containing permeation enhancers: A promising approach for enhancement of skin permeation. *Int. J. Nanomed.* **2019**, *14*, 1551–1562. [[CrossRef](#)] [[PubMed](#)]
17. Coderch, L.; López, O.; de la Maza, A.; Parra, J.L. Ceramides and skin function. *Am. J. Clin. Dermatol.* **2003**, *4*, 107–129. [[CrossRef](#)]
18. Motta, S.; Sesana, S.; Monti, M.; Giuliani, A.; Caputo, R. Interlamellar lipid differences between normal and psoriatic stratum corneum. *Acta Derm. Venereologica. Suppl.* **1994**, *186*, 131–132.
19. Matsumoto, N.U.M. Difference in Ceramide Composition between “Dry” and “Normal” Skin in Patients with Atopic Dermatitis. *Acta Derm. Venereol.* **1999**, *79*, 246–247. [[CrossRef](#)]
20. Barbosa-Barros, L.; de la Maza, A.; López-Iglesias, C.; López, O. Ceramide effects in the bicelle structure. *Colloids Surf. A Physicochem. Eng. Asp.* **2008**, *317*, 576–584. [[CrossRef](#)]
21. Shabbits, J.A.; Mayer, L.D. Intracellular delivery of ceramide lipids via liposomes enhances apoptosis in vitro. *Biochim. Biophys. Acta (BBA) Biomembr.* **2003**, *1612*, 98–106. [[CrossRef](#)]
22. Woodbury, D.J.; Richardson, E.S.; Grigg, A.W.; Welling, R.D.; Knudson, B.H. Reducing Liposome Size with Ultrasound: Bimodal Size Distributions. *J. Liposome Res.* **2006**, *16*, 57–80. [[CrossRef](#)]
23. Jesorka, A.; Orwar, O. Liposomes: Technologies and Analytical Applications. *Annu. Rev. Anal. Chem.* **2008**, *1*, 801–832. [[CrossRef](#)]
24. Cevc, G.; Gebauer, D.; Stieber, J.; Schätzlein, A.; Blume, G. Ultraflexible vesicles, Transfersomes, have an extremely low pore penetration resistance and transport therapeutic amounts of insulin across the intact mammalian skin. *Biochim. Et Biophys. Acta (BBA) Biomembr.* **1998**, *1368*, 201–215. [[CrossRef](#)]
25. European Centre for the Validation of Alternative Methods (CVAM). *Test Guideline for Skin Absorption: In Vitro Method*; Official Journal of the European Union Method B.45 of Annex to 4402008/EC; European Commission: Paris, France, 2008.
26. Nangia, A.; Berner, B.; Maibach, H.I. *Transepidermal Water Loss Measurements for Assessing Skin Barrier Functions During in vitro Percutaneous Absorption Studies*; Bronaugh, R.L., Maibach, H.I., Eds.; Percutaneous Absorption Drugs, Cosmetics, Mechanisms Methodology, Drugs and the Pharmaceutical Sciences, Marcel Dekker Inc.: New York, NY, USA, 1999; pp. 587–594.
27. Dabboue, H.; Builles, N.; Frouin, E.; Scott, D.; Ramos, J.; Marti-Mestres, G. Assessing the Impact of Mechanical Damage on Full-Thickness Porcine and Human Skin Using an In Vitro Approach. *BioMed Res. Int.* **2015**, *2015*, 1–10. [[CrossRef](#)]
28. Wilhelm, K.P.; Elsner, P.; Berardesca, E.; Maibach, H.I. *Bioengineering of the Skin: Skin Imaging and Analysis*, 2nd ed.; CRC Press: Boca Raton, FL, USA, 1996.
29. Elmahjoubi, E.; Frum, Y.; Eccleston, G.M.; Wilkinson, S.C.; Meidan, V.M. Transepidermal water loss for probing full-thickness skin barrier function: Correlation with tritiated water flux, sensitivity to punctures and diverse surfactant exposures. *Toxicol. Vitro.* **2009**, *23*, 1429–1435. [[CrossRef](#)] [[PubMed](#)]
30. Klang, V.; Schwarz, J.C.; Lenobel, B.; Nadj, M.; Auböck, J.; Wolzt, M.; Valenta, C. In vitro vs. in vivo tape stripping: Validation of the porcine ear model and penetration assessment of novel sucrose stearate emulsions. *Eur. J. Pharm. Biopharm.* **2012**, *80*, 604–614. [[CrossRef](#)] [[PubMed](#)]
31. Baber, N. International conference on harmonisation of technical requirements for registration of pharmaceutical for human use. *Br. J. Clin. Pharmacol.* **1994**, *37*, 401–404. [[CrossRef](#)] [[PubMed](#)]
32. Teixeira, Z.; Zanchetta, B.; Melo, B.A.; Oliveira, L.L.; Santana, M.H.; Paredes-Gamero, E.J.; Justo, G.Z.; Nader, H.B.; Guterres, S.S.; Durán, N. Retinyl palmitate flexible polymeric nanocapsules: Characterization and permeation studies. *Colloids Surf. B Biointerfaces* **2010**, *81*, 374–380. [[CrossRef](#)] [[PubMed](#)]
33. Benson, H.A.E.; Warkinson, A.C. *Transdermal and Topical Drug Delivery, Principles and Practice*; John Wiley & Sons, Inc.: Hoboken, NJ, USA, 2011; Chapter 1; p. 17.

34. Singh, I.; Morris, A.P. Performance of transdermal therapeutic systems: Effects of biological factors. *Int. J. Pharm. Investig.* **2011**, *1*, 4–9. [[CrossRef](#)]
35. Clares, B.; Calpena, A.C.; Parra, A.; Abrego, G.; Alvarado, H.; Fangueiro, J.F.; Souto, E.B. Nanoemulsions (NEs), liposomes (LPs) and solid lipid nanoparticles (SLNs) for retinyl palmitate: Effect on skin permeation. *Int. J. Pharm.* **2014**, *473*, 591–598. [[CrossRef](#)]



© 2020 by the authors. Licensee MDPI, Basel, Switzerland. This article is an open access article distributed under the terms and conditions of the Creative Commons Attribution (CC BY) license (<http://creativecommons.org/licenses/by/4.0/>).

Chapter 4. Dexamethasone-loaded lipomers: development, characterization, and skin biodistribution studies

Resumen

La administración selectiva de fármacos en folículos pilosos (follicular targeting) ha ganado más atención en las últimas décadas, debido a la posibilidad de obtener un efecto de depósito en la administración tópica y a su potencial como herramienta para tratar enfermedades relacionadas con el folículo piloso. Se desarrollaron y optimizaron lipómeros de etilcelulosa con núcleo lipídico, tras lo cual se llevó a cabo la caracterización de sus propiedades fisicoquímicas. Se encapsuló dexametasona en los lipómeros (con un tamaño promedio de 115 nm; una polidispersión de 0,24 y un potencial zeta de +30 mV) y se investigaron sus perfiles de liberación *in vitro* frente a la dexametasona en solución mediante celdas de Franz de difusión vertical. Se produjeron lipómeros marcados fluorescentemente con dos fluorocromos diferentes. Uno formando parte del núcleo lipídico de los lipómeros (Lissamine Rhodamine B) y otro encapsulado en su interior (Coumarin 6). Se estudió la biodistribución cutánea cualitativa de ambos fluorocromos mediante microscopía confocal. Se observó una acumulación tanto de los lipómeros como de su encapsulado en folículos pilosos de piel de cerdo. Además, se llevaron a cabo estudios de inmunofluorescencia de lipómeros encapsulando dexametasona y también se observó acumulación del activo vehiculizado en folículos pilosos de cerdo confirmando los anteriores resultados. La eficacia antiinflamatoria (vía TNF α) de los lipómeros cargados de dexametasona se demostró *in vitro* en un cultivo celular de queratinocitos humanos (HEK001) y se investigó la citotoxicidad *in vitro* de la nanoformulación.



Article

Dexamethasone-Loaded Lipomers: Development, Characterization, and Skin Biodistribution Studies

Eloy Pena-Rodríguez ¹, Maria Lajarin-Reinares ¹, Aida Mata-Ventosa ^{2,3,4}, Sandra Pérez-Torras ^{2,3,4} and Francisco Fernández-Campos ^{1,*}

- ¹ Topical & Oral Development R+D Reig Jofre Laboratories, 08970 Barcelona, Spain; eloy.pena@reigjofre.com (E.P.-R.); mlajarin@reigjofre.com (M.L.-R.)
- ² Molecular Pharmacology and Experimental Therapeutics, Department of Biochemistry and Molecular Biomedicine, Institute of Biomedicine (IBUB), University of Barcelona, 08028 Barcelona, Spain; aidamatav@ub.edu (A.M.-V.); s.perez-torras@ub.edu (S.P.-T.)
- ³ Biomedical Research Networking Center in Hepatic and Digestive Diseases (CIBEREHD), Carlos III Health Institute, 28029 Madrid, Spain
- ⁴ Sant Joan de Déu Research Institute (IR SJD-CERCA) Esplugues de Llobregat, 08950 Barcelona, Spain
- * Correspondence: Ffernandez@reigjofre.com; Tel.: +34-935-507-718

Abstract: Follicular targeting has gained more attention in recent decades, due to the possibility of obtaining a depot effect in topical administration and its potential as a tool to treat hair follicle-related diseases. Lipid core ethyl cellulose lipomers were developed and optimized, following which characterization of their physicochemical properties was carried out. Dexamethasone was encapsulated in the lipomers (size, 115 nm; polydispersity, 0.24; zeta-potential (Z-potential), +30 mV) and their in vitro release profiles against dexamethasone in solution were investigated by vertical diffusion Franz cells. The skin biodistribution of the fluorescent-loaded lipomers was observed using confocal microscopy, demonstrating the accumulation of both lipomers and fluorochromes in the hair follicles of pig skin. To confirm this fact, immunofluorescence of the dexamethasone-loaded lipomers was carried out in pig hair follicles. The anti-inflammatory (via TNF α) efficacy of the dexamethasone-loaded lipomers was demonstrated in vitro in an HEK001 human keratinocytes cell culture and the in vitro cytotoxicity of the nanoformulation was investigated.

Keywords: follicular targeting; dexamethasone; alopecia areata; lipomers; lipid polymer hybrid nanocapsules; biodistribution; skin; ethyl cellulose



Citation: Pena-Rodríguez, E.; Lajarin-Reinares, M.; Mata-Ventosa, A.; Pérez-Torras, S.; Fernández-Campos, F. Dexamethasone-Loaded Lipomers: Development, Characterization, and Skin Biodistribution Studies.

Pharmaceutics **2021**, *13*, 533. <https://doi.org/10.3390/pharmaceutics13040533>

Academic Editors: Ana Catarina Silva and José Manuel Sousa Lobo

Received: 29 March 2021

Accepted: 8 April 2021

Published: 11 April 2021

Publisher's Note: MDPI stays neutral with regard to jurisdictional claims in published maps and institutional affiliations.



Copyright: © 2021 by the authors. Licensee MDPI, Basel, Switzerland. This article is an open access article distributed under the terms and conditions of the Creative Commons Attribution (CC BY) license (<https://creativecommons.org/licenses/by/4.0/>).

1. Introduction

Nanoparticles are pharmaceutical forms that are used to improve the efficacy and bioavailability of different poorly water-soluble active ingredients. The physicochemical properties of nanoparticles, such as their high surface-to-volume ratio, the ability to increase permeability through different cell tissues, the possibility of increasing the solubility of active ingredients, or the ability to modulate the release kinetics to achieve depot formulations, make nanoparticles a very attractive approach to improve the therapeutic indices of active ingredients through different routes of administration.

In recent decades, there has been a great deal of research related to modulated targeting and localized release in different parts of the body. The stratum corneum, comprised of a group of low water content corneocytes and a lipid matrix made of ceramides and cholesterol as the main components, acts as a barrier for topical products in a very efficient way [1]. In the past few years, different nanoencapsulation platforms have been developed to transport drugs to the inner layers of the skin. Regarding the transdermal route, it is well-known that flexible particles, such as transfersomes, or micellar systems are capable of increasing permeation [2,3]; however, the loading capacity of these systems is usually low. In recent years, the transfollicular route has gained more attention, as it has been suggested to increase dermal absorption, probably due to accumulation in the pilosebaceous unit.

For example, Lademann et al. demonstrated that, by using nanoparticles made of poly (lactic-co-glycolic acid) (PLGA), it was possible to obtain a depot effect for 10 days in porcine hair follicles, whereas nanoparticles on the skin surface were only detectable for 24 h [4]. Furthermore, nanosystems, such as polymeric nanoparticles or nanostructured lipid carriers, have higher loading capacities [5]. However, there is still a lack of information regarding the accumulation of these systems in the anatomy of the hair follicle.

Lipomers, or lipid core polymeric nanocapsules (LPNCs), are oily vesicles surrounded by a polymeric wall [6]. In polymeric nanospheres, the active is trapped both on the surface of the particle and in its core. They usually have a burst release effect, due to the desorption of the active from the surface, followed by a plateau based on diffusion/erosion mechanisms. Urzula Bazylińska et al. compared the release of a lipophilic active encapsulated in nanospheres and lipid polymer hybrid nanocapsules and verified that the presence of the lipid nucleus increased the encapsulation efficiency and decreased the burst release effect, obtaining a more sustained release [7].

Topical corticosteroids are the most frequently used drugs for the treatment of inflammatory diseases. Dexamethasone (DEX) has been used topically to treat ocular inflammation [8], atopic dermatitis [9], and alopecia areata (AA) [10], among other diseases, with a high benefit-to-risk ratio. In the case of AA, topical corticoids are frequently ineffective and oral or intralesional therapy is required; furthermore, the potential adverse effects and patient discomfort caused by scalp injections must be considered [11]. Some authors have used solutions with a high proportion of ethanol (70%), as a permeation enhancer, to deliver DEX [9]. They found drug accumulation exclusively in the lipid interspaces and did not observe efficient penetration into corneocytes. There exist other topical corticoids in the market, such as mometasone or methylprednisolone, which are also formulated in hydroalcoholic vehicles with a high content of ethanol. Ethanol has been associated with skin irritation or contact dermatitis [12], it could alter the stratum corneum structure [13], and modify the skin microbiota [14], which could be related to skin diseases and inflammatory status. Thus, it is preferable to minimize its use in topical formulations. Other authors encapsulated DEX (hemisuccinate) in liposomes by microfluidics and film hydration techniques [15]. Even though liposomes are very attractive drug delivery systems, the loading capacity is usually low and could be an issue for specific indications that require higher doses. Considering the above, the improvement of topical treatment is still required, to increase patient quality of life and to minimize adverse effects. Lipomers are a promising drug delivery system to improve the therapeutical balance of DEX in AA treatment, due to possible accumulation in the pilosebaceous unit, where the disease takes place, and under the hypothesis that the lipid nucleus increases the loading capacity. This fact leads to a higher drug concentration in the LPNCs, compared with similar particles without the lipidic core, for which the DEX loading capacity was about 1–2% [16].

For this study, DEX-LPNCs were developed and characterized, in terms of their physicochemical properties and drug release. A description of the skin biodistribution and its accumulation on hair follicles is given. Additionally, information about the associated *in vitro* cytotoxicity and efficacy is shown. It was found that the proposed DEX-loaded LPNCs have potential as a tool for the topical treatment of AA and other inflammatory skin diseases.

2. Materials and Methods

2.1. Materials

DEX (Fagron Ibérica, Barcelona, Spain), ethyl cellulose (EC) (Ashland Industries Europe GmbH, Rheinweg, Switzerland), Tween 80 and Span 60 (Croda Iberica S.A., Spain), benzalkonium chloride (Sigma Aldrich, Madrid, Spain), medium chain triglycerides (MCT) (Oxi-Med Expres S.A., Barcelona, Spain), ethanol absolute (ET) and ethyl acetate (EA) (Scharlab S.L., Barcelona, Spain), and purified water (Inhouse) were used to formulate the LPNCs. Coumarin 6 (C6) (Sigma Aldrich, St. Louis, MO, USA) and 1,2-dioleoyl-3-[16-N-(lissamine rhodamine B sulfonyl) amino]palmitoyl-sn-glycerol (LRB) (Avanti Polar

Lipids, Alabaster, AL, USA) were used as fluorochromes. Paraformaldehyde (Scharlab S.L., Barcelona, Spain), Sucrose (Acor, Valladolid, Spain), optimal cutting temperature compound (OCT) (Tissue-Tek Sakura Finetek, Torrance, CA, USA), rabbit anti-DEX IgG (Abcam, Cambridge, UK), Alexa Fluor 488 goat anti rabbit (Life Technologies, Carlsbad, CA, USA), Prolong™ Gold Antifade mounting medium (Thermo Fisher Scientific, Barcelona, Spain), and Tween 20 (Sigma-Aldrich, St. Louis, MO, USA) were used to prepare samples for microscopic visualization.

2.2. Synthesis of DEX-Loaded LPNCs, Fluorescent-Loaded LPNCs, and Non-Vesiculated Control Solutions

LPNCs were produced by the Emulsion Solvent Evaporation method invented by Fessi et al. [17]. In this method, an organic phase composed of different ratios of EA and ET, EC (2.33%, *w/w*), MCT (0.2%, *w/w*), DEX (1%, *w/w*), and different concentrations of Span 60, were emulsified in an aqueous phase composed of different concentrations of Tween 80 and benzalkonium chloride (preservative). Emulsification was carried out under probe sonication (amplitude of 40%, 5 min; energy, 7000 W; frequency 23.88 kHz) using a UP400st ultrasonic device (Hielscher Ultrasonics, Germany), to reduce the size of the emulsion droplet. After formation of the emulsion, the system evaporated the organic solvents under vacuum in a rotary evaporator, which led to polymer precipitation and lipomer formation. The whole process was performed at room temperature.

A solution of DEX was prepared in a 1% hydroethanolic solution (90:10 *v/v*, water:ethanol) for use as a non-encapsulated DEX control (FREE-DEX). LRB- and C6-loaded LPNCs (LRB-C6-LPNCs) were manufactured with the same composition as previously described, but without DEX. LRB was added to the lipid nucleus in a mole-to-mole ratio of MCT:LRB of 1:1000, according to Lymberopoulos et al. [18]. In addition, 0.1% *w/w* C6 was incorporated into the organic phase (EA:ET), simulating the encapsulation of a hydrophobic active ingredient. Fluorochrome control aqueous solutions used in confocal microscopy were prepared with 3% Tween 80 of LRB and C6, at the same concentration as in the LRB-C6-LPNCs, for use as a control for non-vehicle fluorophores (FREE-LRB-C6).

2.3. Screening of Experimental Variables on Nanoparticle Properties

The properties of the lipomers are influenced by different experimental variables, such as the amount of ingredients and manufacturing conditions. Some preliminary screening trials were performed.

Different batches were produced to fix the % *w/w* of EC and MCT, in order to maximize the loading capacity of DEX in the LPNCs, while maintaining the hydrodynamic diameter below 150 nm and the polydispersity below 0.3. To select the organic solvent, the viscosity of EC was characterized (Brookfield RDV-III Ultra, Spain. Spindler: SC4-21, speed: 100 rpm; temperature: 25 °C) in EA:ET (1:0, 0:1, 1:1, 1:5, and 5:1 *v/v*) and the mixture with the lowest viscosity was selected.

The samples were subjected to rotary evaporation in a Heidolph VV1 rotary evaporator (Heidolph Instruments, Germany) with a thermostated bath at 40 °C for 5, 7, 10, and 15 min. The residual concentration of EA and ET was analyzed by gas chromatography (Agilent A7890 with Headspace AG1888, Santa Clara, CA, USA) following European Pharmacopoeia 7.0, chapter 2.4.24 (Identification and control of residual solvents) [19]. Briefly, carrier gas (Helium) flowed at 1.5 mL/min in a column (DB-WAX, 60 m, 0.25 mm, 0.25 µm; Agilent Technologies, USA) for 30 min. The split ratio was 20, the injector Temperature (T^a) was 250 °C, and the detector T^a was 270 °C. The T^a ramp was increased by 10 °C/min.

In order to obtain stable nanoformulations against aggregation, the influences of the surfactant Tween 80 and co-surfactant Span 60 (Table 1) on the Z-potential (mV), nanoparticle hydrodynamic diameter or Z-average (nm), polydispersity index (PDI), and encapsulation efficiency (%EE) were studied. Statistical analysis of the variables studied were carried out using Minitab 17 statistical software (Minitab, Inc., 2010, State College, PA, USA), with the significance level set as $\alpha = 0.05$.

Table 1. Levels studied for the surfactants.

Factor	Lower Level	Higher Level
% Tween 80 (<i>w/w</i>)	1.5	2.5
% Span 60 (<i>w/w</i>)	0.16	0.32

2.4. LPNCs Physic-Chemical Characterization

The hydrodynamic size, polydispersity index (PDI), and Z-potential were studied for the LPNCs through Dynamic Light Scattering (DLS) using a Malvern Zetasizer Nano ZS (Malvern Panalytical, Malvern, UK). A dilution of 1:10 in milliQ water was performed to adjust the intensity (attenuator position between 3 and 6).

The LPNCs' morphology, size, and distribution were studied using Transmission Electron Microscopy (TEM). The LPNCs' size was also measured using the particle analysis tool of the Image J software. The TEM grids were coated with formvar of a 1:10 dilution of LPNCs in milliQ water and incubated for 1 min at room temperature. The grids were washed with milliQ water and stained with a 2% *w/w* uranyl acetate solution (Electron Microscopy Sciences, Hatfield, England) during 1 min at room temperature. They were then dried in a petri dish overnight and observed using a TEM microscope (Jeol JEM 1010 100 kv; Jeol, Tokyo, Japan).

2.5. DEX Quantification

DEX was quantified through HPLC, in terms of encapsulation efficiency (%EE), according to an indirect method (Equation (1)):

$$\%EE = \frac{W_T - W_{NE}}{W_T} \times 100, \quad (1)$$

where W_{NE} is the amount of DEX quantified in the filtrate (DEX not encapsulated) and W_T is the DEX quantified in the total formula. The LPNCs were centrifuged in 100 KDa amicon ultra (Merck Millipore, Barcelona, Spain) at 4500 rpm for 30 min. DEX in the filtrate and in LPNCs (total drug content) were analyzed using a High-Performance Liquid Chromatograph (HPLC) Alliance, with a photodiode array detector (PDA). A C18 column (250 × 4.6 mm, 3 μm) was used with an isocratic mixture of acetonitrile:KH₂PO₄ 0.05 M buffer (60:40) as the mobile phase, with a flow rate of 1.8 mL/min and an injection volume of 20 μL. The sample and column temperatures were 25 °C.

The amount of total drug entrapped per weight of nanoparticle or loading capacity (%LC) was calculated using the following equation:

$$\%LC = \%EE \times \frac{M_{DEX}}{M_{LPNCs}}, \quad (2)$$

where M_{DEX} is the amount of active ingredient initially added to the formulation and M_{LPNCs} is the mass of the nanoparticle components.

2.6. In Vitro Release Tests of the DEX-Loaded LPNCs

In vitro release of DEX from the LPNCs was studied using vertical Franz cells (Vidrafoc, Barcelona, Spain) with a 12 mL receptor compartment and an effective diffusion area of 1.54 cm². A mixture of ethanol and purified water (50:50) was used as receptor medium (RM), at 32 °C and stirred at 500 rpm, to keep the sink conditions throughout the experiment. A total of 0.6 g of LPNCs was applied in the donor compartment, corresponding to 60 mg of DEX. The membrane used was a dialysis membrane (Spectrum Chemical, New Brunswick, NJ, USA) with pore diameter of 12–14 kDa.

Aliquots of 300 μL were taken at certain times (1, 2, 3, 4, 5, 21, 22, 23, and 24 h) and injected into the HPLC with the method described in Section 2.5, to quantify the amount of DEX that had diffused through the membrane.

Kinetic modelling of the release data was studied with the DD-solver [20] Excel Add-on, using a non-linear approach. Model selection was based on the lowest Akaike Information Criteria (AIC), reflecting the lowest deviation of the model with respect to the empirical data [21]. Firstly, the mean release values were adjusted to the model described in Table 2, to obtain the mean population behavior. Then, individual data were adjusted, according to the model selected. The mean and standard deviation of the parameters were reported.

Table 2. Different kinetic models and equations tested.

Kinetic Model	Equation
First Order	$F = F_{max} \left(1 - e^{(-K_1 t)}\right)$
Higuchi	$F = K_H \cdot t^{1/2}$
Korsmeyer–Peppas	$F = K_{KP} \cdot t^n$
Weibull	$F = 1 - e^{(-\frac{t}{T_d})^\beta}$

In Table 2, F is the fraction of active released at time t , F_{max} is the maximum fraction of active released (i.e., at infinite time), K_1 is the first-order constant, K_H is the Higuchi constant, K_{KP} is the Korsmeyer–Peppas constant (related to the structural and geometric character of the drug release matrix), n is the diffusional exponent indicating the drug-release mechanism (if n is less than 0.43, then a Fickian diffusion release mechanism is implied; if n is between 0.43 and 0.85, then the release mechanism follows an anomalous transport mechanism), T_d represents the time at which 63.2% of the drug is released, and β is the Weibull shape parameter. For values of β lower than 0.75, the release follows a Fickian diffusion, either in Euclidian ($0.69 < \beta < 0.75$) or fractal ($\beta < 0.69$) space. Values of β in the range of 0.75–1.0 indicate a combined mechanism, which is frequently encountered in release studies [22,23].

2.7. Pig Skin Permeation

Pig skin was obtained from a local abattoir (Barcelona, Spain) at the moment of sacrifice. Full thickness skin pieces were defatted (with a scalpel) and frozen at $-20\text{ }^\circ\text{C}$ until use. On the day of the experiment, skin pieces were mounted on Franz cells with an effective diffusion area of 0.196 cm^2 and around 12 mL of receptor volume capacity (PBS at $32\text{ }^\circ\text{C}$ and stirred at 500 rpm). TEWL measurements were performed, to check the integrity of the skin samples [12] (TEWL Vapometer SWL4549, Delfin Technologies Ltd., Kuopio, Finland). A solution dose of 76 mg of each of the formulations were given in infinite dose in non-occluded conditions.

2.7.1. Confocal Microscopy Biodistribution of Fluorescent Probes

To study the biodistribution of LPNCs in the skin, confocal fluorescence microscopy was used. For this, C6 was encapsulated in the nanoparticles, to simulate the biodistribution of a hydrophobic small molecule, and LRB was used as fluorophore covalently bound to a lipid (palmitic acid) and included in the lipid core of the LPNCs, in order to track the nanoparticles. The labelled LRB-C6-LPNCs were purified using Visking dialysis tubing with a cut-off of 12,000–14,000 Dalton. The non-encapsulated fraction of both fluorophores was quantified by spectrophotometry (VICTOR Multilabel Plate Reader, Perkinelmer, Massachusetts, USA) and the %EE was calculated following Equation (1).

Full thickness pieces of pig skin were warmed and placed in Franz cells, according to Section 2.7. After 18 h of permeation, the diffusion surface was washed with PBS, cut with a scalpel into pieces of about 0.5 cm^2 , and fixed in 4% w/w paraformaldehyde solution for 5 min. Then, the skin samples were incubated in aqueous solutions of increasing sucrose concentration (5%, 15%, and 25% w/w) for 15 min in each solution. They were then placed in plastic molds and dipped in OCT to cut on a cryostat Leica CM 3050 S (Leica Biosystems, Barcelona, Spain) to a $50\text{ }\mu\text{m}$ thickness. The slices were collected on poly-lysine-coated

slides and washed with PBS and 0.05% Tween 20 (TPBS) for 5 min, to remove the OCT and permeabilize the samples. On the day of observation, sections were incubated with 15 μL of Hoescht solution (2 $\mu\text{g}/\text{mL}$) for 10 min and washed with TPBS to stain the cell nuclei. The samples were analyzed under a confocal microscope (Leica Microsystems, Wetzlar, Germany). The emission laser wavelengths were 570, 500, and 525 nm and the excitation wavelengths were 561, 488, and 405 nm for LRB, C6, and Hoescht, respectively. About 20 planes were obtained per image, separated by a 3 μm step. Composites of the different planes were created, in terms of the brightest point for each pixel, through the ImageJ tool Z-stack (ImageJ2 v2.35, National Institutes of Health, Bethesda, MD, USA). A skin blank was processed in the same way as the test samples, to quantify skin autofluorescence. The mean intensity was measured with the ImageJ software and was subtracted from the intensity of the red and green channels of the samples.

2.7.2. Immunohistofluorescence Biodistribution

To study the biodistribution of the DEX carried in the LPNCs, immunohistofluorescence (IHF) experiments were carried out. Permeation and skin slices were carried out in the same way as in Section 2.7.1, but the slices were 10 μm thick. Then, 15 μL of a 1/300 dilution of the rabbit polyclonal primary anti-DEX IgG were added, and the samples were left to incubate in a humid environment overnight at 4 $^{\circ}\text{C}$. Then, the samples were washed with TPBS and incubated with a 1/300 diluted fluorescent secondary goat anti-rabbit IgG Alexa 488 for 2 h under the same incubation conditions. Finally, ProLong Gold Antifade mounting medium was added. The samples were analyzed under a fluorescent field effect microscope. A L5 Leica filter cube was used, and the filters were BP480/40, BS505 for excitation, and BP 527/30 for emission. To study the possible non-specific interactions of the skin, the same process was carried out with non-treated skin samples and processed in the same way as test samples. The resultant intensity was subtracted from the profiles of the samples using the ImageJ software.

2.8. *In Vitro* Cytotoxicity/Anti-TNF α Efficacy

Cell culture: The HEK001 cell line was obtained from ATCC (Promochem Partnership, Manassas, VA, USA). HEK001 was grown in monolayer on a solid support, at 37 $^{\circ}\text{C}$ in a humidified atmosphere with 5% CO_2 and maintained in keratinocyte serum-free media supplemented with 100 $\mu\text{g}/\text{mL}$ epidermal growth factor (EGF) (Life Technologies, Carlsbad, CA, USA), 20 U/mL penicillin, and 20 $\mu\text{g}/\text{mL}$ streptomycin (Life Technologies). Mycoplasma-free maintenance was confirmed every two weeks by PCR amplification.

Cell treatments: For the cell viability assays, HEK001 cells were seeded at a density of 5000 cells/well in 96-well culture plates. At 24 h post-seeding, cells were treated with increasing doses of DEX-charged LPNCs, non-charged LPNCs, or the corresponding amount of benzalkonium chloride for 24 h. After 48 h, cell viability was assessed using an MTT (3-[4,5-dimethylthiazol-2-yl]-2,5 diphenyl tetrazolium bromide) colorimetric assay (Sigma-Aldrich, St. Louis, MO, USA). Cell survival for all experiments was expressed as the percentage of viable cells, relative to that in untreated cells (defined as 100%). For the cytokine modulation assays, HEK001 cells were seeded at a density of 700,000 cells/well in 6-well culture plates. At 24 h post-seeding, cells were pre-treated with 10 $\mu\text{g}/\text{mL}$ of lipopolysaccharide (LPS) for 1 h and then treated with 0.1 mM of DEX or DEX-loaded LPNCs for 24 h.

RNA isolation and RT-PCR: Total RNA was isolated from cultured cells using the SV Total RNA Isolation System (Promega, Madison, WI, USA), following the manufacturer's instructions. A total of 1 μg of RNA was reverse transcribed to cDNA with M-MLV Reverse Transcriptase (Life Technologies) and random hexamers (Life Technologies). Analyses of the TNF α and GAPDH (endogenous control) mRNA levels were performed by RT-PCR, using commercial TaqMan gene expression assays (Applied Biosystems). Relative quantification of gene expression was assessed using the $\Delta\Delta\text{CT}$ method, as described in the TaqMan user manual (User Bulletin no. 2; Applied Biosystems). Gene expression levels

for TNF α were normalized to the GAPDH gene. The amounts of mRNA are expressed as arbitrary units.

Statistical analysis: Results from the cell viability and cytokine modulation were statistically analyzed by using GraphPad Prism (8.0.2, 2019, La Jolla, San Diego, CA, USA), with Student's paired *t* test for cytotoxicity assays and two-way ANOVA for cytokine modulation assays. In all cases, differences were considered significant when the *p*-value < 0.05.

3. Results and Discussion

3.1. Screening of Experimental Variables on Nanoparticle Properties

The pharmaceutical interest of cellulose derivatives has increased in recent years, due to economic factors (usually due to the low-cost of the excipients, compared with synthetic compounds) and as they originate from renewable resources [24]. EC was selected as the LPNC polymer, as it has been approved by the Food and Drug Administration (FDA) for medical and food applications (i.e., vitamin and mineral tablets), and it has shown good biocompatibility in ocular drug delivery systems [25–27]. Furthermore, EC is cheaper than other commonly used polymers, such as PLGA or polycaprolactone. EC is commonly used in the pharmaceutical industry as a coating material for different drug delivery applications, due to its controlled release properties caused by the porous structure, where the drugs can be trapped and diffuse [24].

The choice of organic phase is a parameter to consider, in terms of toxicity. Chloroform and dichloromethane are organic solvents that are commonly used in the Emulsion Solvent Evaporation method; however, due to their toxicity, it is advisable to avoid them when possible. In this case, ethyl acetate and ethanol were selected, as they have been classified as class III (or low toxic potential) solvents by the European Medicines Agency (EMA) [28]. In the Emulsion Solvent Evaporation method, the viscosity of the organic phase influences the diffusion to the aqueous phase. An organic phase that is too viscous will not diffuse adequately, forming large aggregates that cannot be stabilized in the final formulation. This may be attributed to the increase in viscosity of the dispersed phase, resulting in a reduction of the net shear stress and prompting bigger nanodroplets. The ratio between the continuous and dispersed phases is also an important factor: In the solvent evaporation emulsion method, a high proportion of dispersed phase causes an increase in the size of the nanoparticles, due to the increase in droplet size. Furthermore, due to the hydrophobic nature of DEX, the burst effect would increase, and the encapsulation efficiency would decrease. To avoid this problem, dilutions of EC were made in different binary mixtures of ethanol and ethyl acetate and the viscosities of the different organic phases were characterized. The LPNCs were designed with MCT as the oil core, to increase the %EE and reduce the DEX burst release effect. Benzalkonium chloride was incorporated as a preservative.

Table 3 shows the viscosity results for the different binary mixtures of ethyl acetate (EA) and ethanol (ET) with EC at 2% *w/w*. The 1:1 and 5:1 ratios were selected as optimal, as they showed the lowest viscosity values. This means a decrease in the viscous forces resisting droplet breakdown and, thus, smaller oil droplets were formed, resulting in a decreased particle size. When LPNCs were produced at the 1:1 ratio, aggregates were observed; so, finally the 5:1 EA:ET ratio was selected as definitive, as it did not show aggregates and obtained low viscosity. To increase the loading capacity of the LPNCs, the EC concentration was increased to the maximum concentration possible to obtain LPNCs with adequate properties, in term of size and PDI [29]. The final EC concentration was fixed at 2.33% *w/w* in the organic phase (0.35% *w/w* in the final formulation) and the MCT concentration was set at 0.2% *w/w*, since at higher concentrations aggregates began to appear.

The stability of LPNCs is directly related to their size, PDI, and Z-potential. Surfactants have an important role in these characteristics and, so, the effect of surfactant concentration on the physicochemical properties of LPNCs was studied. As in any colloidal suspension, lipomers can undergo destabilization processes, such as Ostwald ripening. This process can be avoided by steric stabilization using Tween 80 [30]. Due to its HLB (14.9), Tween 80 acts

as a stabilizer of the aqueous phase, coating the surfaces of the LPNCs and preventing their aggregation. Due to the more lipophilic nature of Span 60 (HLB 4.7), it becomes dispersed in the LPNC core when MCT is used [31]. In this case, the percentages of Tween 80 and Span 60 were modified between 1.5% and 2.5% *w/w* and 0.16% and 0.32% *w/w*, respectively. As it can be seen from Table 4, four batches were produced and the Z-average, PDI, Z-potential, and %EE were characterized for each of them.

Table 3. Organic phase ethyl cellulose (EC) mixture viscosities.

EA:ET Ratio	Viscosity (cP)
1:1	16
5:1	20.5
1:5	24
1:0	70.5
0:1	25

Table 4. Influence of Span 60 and Tween 80 on the physicochemical parameters.

Batch	% Tween 80	% Span 60	Z-Average (nm)	PDI	Z-Potential (mV)	% EE
LP01	2.5	0.32	117.6 ± 1.2	0.263 ± 0.005	21.7	96.76
LP02	1.5	0.32	130.5 ± 1.1	0.215 ± 0.011	27.2	96.68
LP03	1.5	0.16	114.1 ± 1.1	0.239 ± 0.002	29.1	96.93
LP04	2.5	0.16	125.9 ± 0.5	0.256 ± 0.006	23.5	98.32

A general linear model regression using the Minitab software was performed (with a significance level of $\alpha = 0.05$) to evaluate the effect of the tested experimental variables. The levels of Tween 80 and Span 60 were not significant for the hydrodynamic diameter, the PDI, or for the %EE, but they were significant for the Z-potential ($p = 0.006$ and $p = 0.017$, respectively). In Figure 1, the effects of these surfactants on the surface charge of the LPNCs can be observed. By increasing the amount of surfactant, the positive charge was reduced, as the hydroxyl groups of Tween 80 and Span 60 shielded the positive charge of the nanoparticles.

Thus, formulation LP03 was selected as the final formulation, with lower levels of both surfactants (1.5% *w/w* of Tween 80 and 0.16% *w/w* of Span 60). The %LC of batch LP03 was calculated following Equation (2), which resulted in 30.22%, thus confirming the high loading capacity of this type of nanoencapsulation system [5] compared to other drug delivery systems like liposomes, in which Amin et al. reached an LC of 12.6% [16].

Table 5 shows the residual EA and ET found after the evaporation process. EA has a vapor pressure at 25 °C of 1.23 atm, which is higher than the vapor pressure of ethanol at the same temperature (0.08 atm). Due to the higher volatility of EA than ET, after 5 min of rotary evaporation at 40 °C, the residual quantity was already below the limit of quantification (LOQ). Regarding ethanol, with the mildest evaporation conditions, more residues were found, but they were well below the limit established for residual solvents of class 3 (5000 ppm) in the guideline for residual solvents (ICH Q3C) of the European Medicines Agency. Thus, the evaporation conditions were fixed at 5 min and 40 °C.

Table 5. Residual solvents after evaporation at 40 °C.

Evaporation Time (min)	Residual EA (ppm)	Residual ET (ppm)
5	<LOQ	153.0 ± 10.0
7	<LOQ	34.4 ± 4.5
10	<LOQ	12.5 ± 2.3
15	<LOQ	1.5 ± 0.0

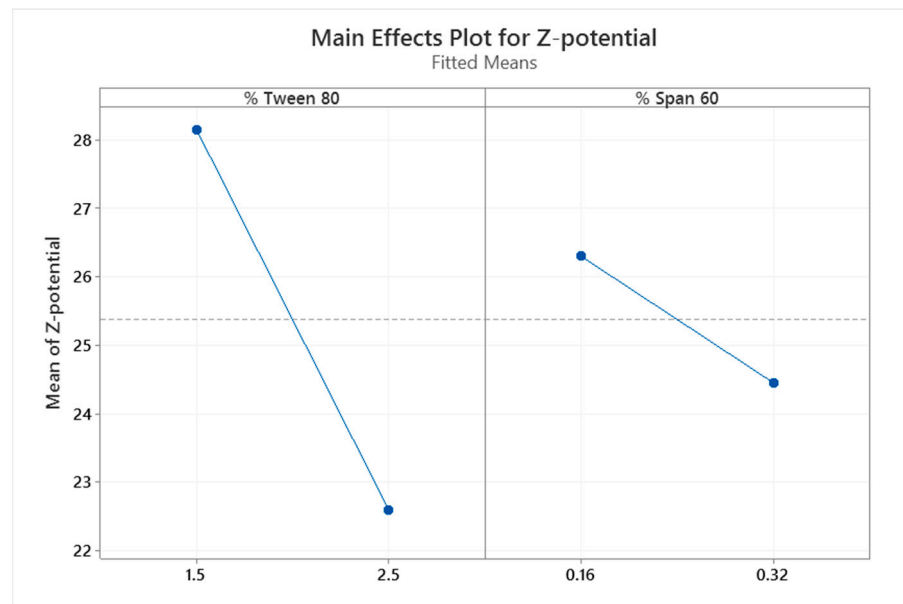


Figure 1. Plots of the main effects of Tween 80 and Span 60 on the Z-potential of the lipid core polymeric nanocapsules (LPNCs).

3.2. Physicochemical Characterization of the LPNCs

Thanks to the high resolution of the TEM images (Figure 2), it is possible to appreciate the lipid nucleus (brighter area) and distinguish it from the polymeric framework (darker area), as can be observed in Figure 2C. Furthermore, the spherical morphology was confirmed. A total of 180 particles were analyzed and a mean size of 126.40 ± 34.93 nm was obtained.

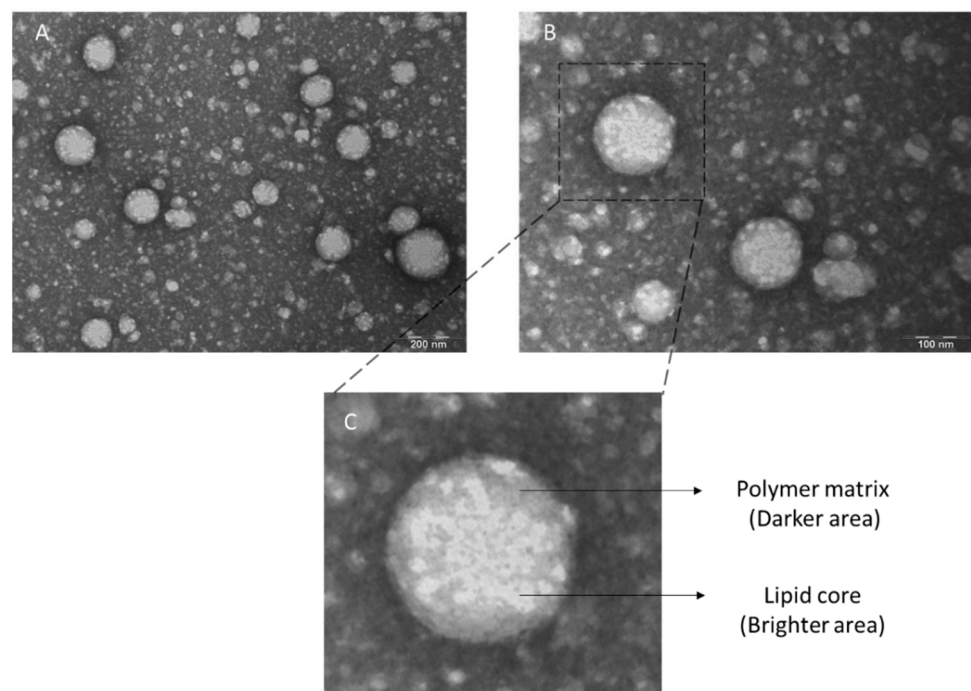


Figure 2. Transmission Electron Microscopy (TEM) images of negative-stained lipid–polymer hybrid LPNCs with 2% uranyl acetate at (A) 250,000× magnification; and (B) 300,000× magnification. (C) Individual nanoparticle representation zoom.

The diameter distribution of the particles, as measured by TEM, is shown in Figure 3 as a histogram. The average obtained was similar using both TEM and DLS techniques and the %BIAS error for the diameter was 10.78%, which is low.

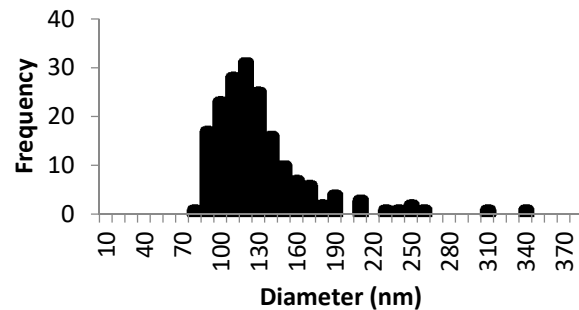


Figure 3. Histogram of lipomers from the measurement of the diameter of the particles ($n = 180$) using ImageJ software.

3.3. In Vitro Release Test of DEX-Loaded LPNCs and Free DEX

The release data of the free DEX and LPNCs can be seen in Figure 4. After 24 h, the DEX formulated in an ethanolic solution (FREE-DEX) was released at 100%, while the release of DEX loaded in LPNCs (LPNCs-DEX) was more sustained, due to diffusion through the polymeric framework and the affinity of the active for the lipid cores of the particles.

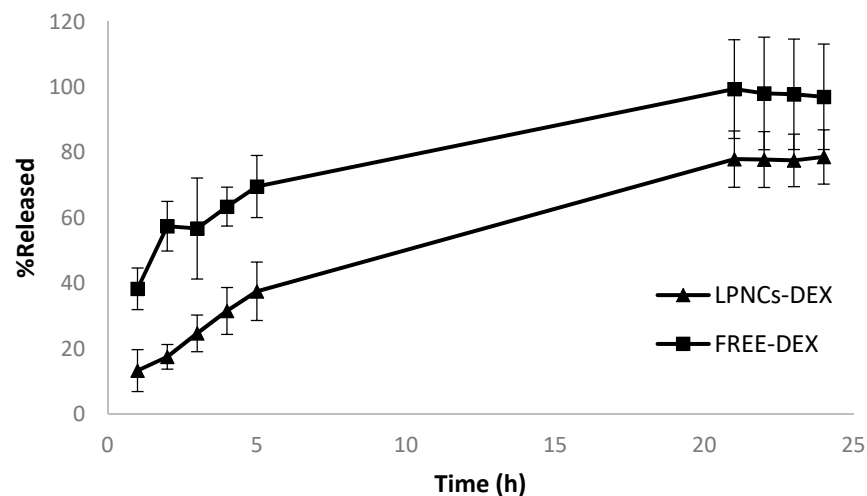


Figure 4. Mean release data obtained from the DEX-loaded LPNCs and from the ethanolic solution of DEX (FREE-DEX) after 24 h of the in vitro release test.

After adjusting the mean release data with the different mathematical models (see Table 6), it was observed that Weibull was the model that best fit (AIC 28.81) the experimental data in the case of LPNCs, and Korsmeyer–Peppas was the model that best fit (AIC 44.86) in the case of DEX formulated in a hydroalcoholic solution.

Once the mean release kinetic behavior was determined, the mean and standard deviation of the individual release data for free DEX and LPNCs-DEX were obtained, as reported in Table 7.

Although the Weibull equation is a non-mechanistic equation, Papadopoulou et al. [22] obtained a relationship between the shape parameter β and the release mechanism, in the same way as the power law equation (Korsmeyer–Peppas equation) does with the exponent n . In the case of LPNCs-DEX, the value of β was between 0.75 and 1, which corresponds to a combined release mechanism; that is, diffusion in a normal Euclidean substrate with the contribution of another release mechanism. This fact was confirmed by the n value (0.573)

found for LPNCs reported in Table 6, corresponding to anomalous transport or a combined mechanism. Due to the hybrid nature of these nanoparticles, the active ingredient could be distributed both in the lipid core and the polymeric framework, resulting in an overlap of both release kinetics, such that anomalous transport would be observed. In the case of FREE-DEX, this study was below the limits set in the Korsmeyer–Peppas model (i.e., 0.43). However, Singhvi and Singh [32] reported that, although the value of n obtained was not in the range suggested in Korsmeyer–Peppas model, it also indicates a diffusion-controlled drug release mechanism. This fact could be confirmed by the Weibull model, which had an AIC value close to that of Korsmeyer–Peppas, where the β value for FREE-DEX was 0.698 (i.e., between 0.69 and 0.75), which would indicate the release as a normal diffusion mechanism dominated by the concentration difference without the contribution of other release mechanisms, unlike the case of LPNCs.

Table 6. Model selection and parameter estimation of the LPNCs-DEX and FREE-DEX. Bold type indicates the selected model, based on the lowest AIC.

Formulation	Model	AIC	Parameters	Value
LPNCs-DEX	First order	31.84	k (h^{-1})	0.128
	Higuchi	39.98	k_H ($\%h^{-1/2}$)	16.263
	Korsmeyer–Peppas	39.13	k_{KP} ($\%h^{-n}$)	7.91
			n	0.573
	Weibull	28.81	T_d (h)	13.49
			β	0.79
FREE-DEX	First-order	68.51	k (h^{-1})	0.192
			F_{max} (%)	104.35
	Higuchi	71.60	k_H ($\%h^{-1/2}$)	22.475
	Korsmeyer–Peppas	44.86	k_{KP} ($\%h^{-n}$)	42.78
			n	0.271
	Weibull	47.43	β	0.698
			T_d (h)	3.21

Table 7. Individual modelling and parameters for the LPNCs and FREE DEX release data.

Formulation	Model	Parameters	Value
LPNCs-DEX	Weibull	β	0.82 ± 0.17
		T_d (h)	14.16 ± 4.11
FREE-DEX	Korsmeyer–Peppas	k_{KP} ($\%h^{-n}$)	42.39 ± 5.96
		n	0.278 ± 0.034

3.4. Confocal Microscopy Biodistribution of Fluorescent Probes

After the permeation experiment, skin was observed under a confocal microscope, to evaluate the skin distribution of both fluorochromes. The literature has described a high number of fluorochromes that are included in nanoparticles for localization in the skin. Usually, the selection of the tracking compound is based on the aim of the experiment. In this case, C6 was selected as the drug model and LRD to track the nanocapsules. According to the structure of LRD, the hydrocarbon tail would be inside the lipid core and the rhodamine head would likely be located in the polymer shell or in the interphase lipid–polymer in the nanoparticle structure, as with Span 60. To improve visualization, cell nuclei were stained with Hoechst (blue color). The results obtained from the confocal biodistribution study are shown in Figure 5. The autofluorescence value in the red channel (corresponding to LRD) was 5.9 AU and that of the green channel (corresponding to C6) was 0.3 AU. These values were subtracted from the mean intensity of the samples. Using ImageJ software, linear segments were drawn to analyze the intensity profile as a function of depth (in μm). Yellow color corresponds to the co-localization of both fluorochromes.

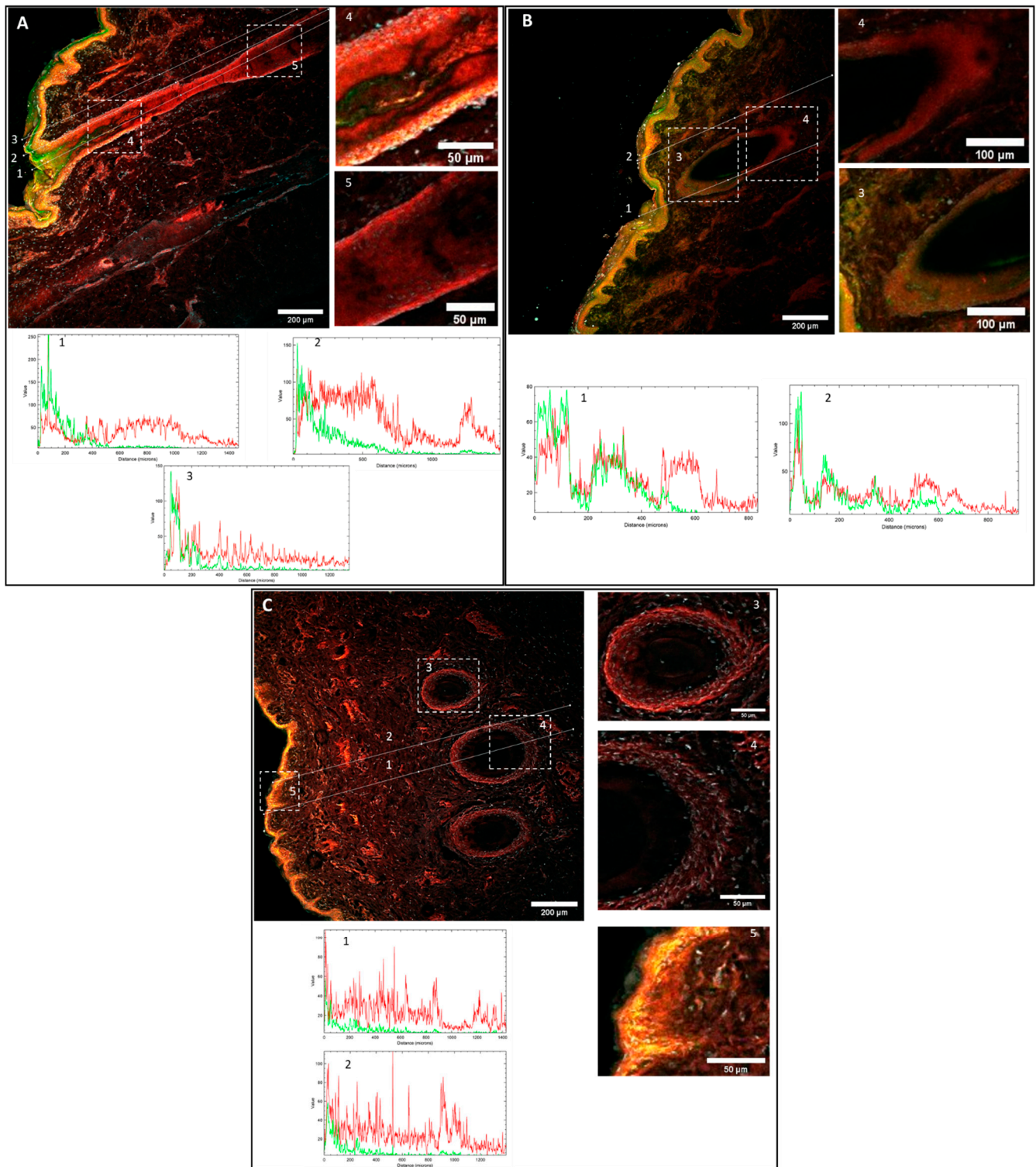


Figure 5. Confocal Microscopy Fluorescence images and plot intensity profiles of pig skin cross-sections. Green color corresponds to C6 and red to LRB fluorescence. Yellow color corresponds to the overlap of C6 and LRB: (A,B) C6-loaded LRB-labelled LPNCs. (C) Free C6 and LRB control solution. Lines numbered 1–3 in Figure 5A; 1–2 in Figure 5B and 1–2 in Figure 5C correspond to Multichannel intensity plot profiles as function of the depth (μm). Dashed squares numbered 4–5 in Figure 5A, 3–4 in Figure 5B and 3–4 in Figure 5C correspond to zoomed in regions. The images were captured using $10\times$ magnification.

Figure 5A,B show the biodistribution patterns of the C6 and LRB fluorophores vehiculated in LPNCs (C6-LRB-LPNCs).

In Figure 5A, three lines are drawn from the stratum corneum to deeper layers of the skin. Line 1 corresponds to the central section of the hair follicle, line 2 corresponds to the follicle edge (outer root sheath area), and line 3 corresponds to a non-follicle section. In the central section (line 1), the intensity of C6 is between 100 and 200 AU in the infundibulum (depth < 100 μm). At depths of 200 μm , the intensity of C6 drops to 50 AU and, as the depth increases, the intensity of the green channel continues to decrease, to about 20 AU at 400 μm (corresponding to the hair follicle isthmus). Beyond 500 μm , in depth (i.e., in the suprabulbar region), the intensity of C6 was low (<10AU), which seems to indicate that C6 does not accumulate in the deeper parts of the follicle. Regarding the intensity in the red color, corresponding to the presence of LRB, a different behavior can be observed. The profile of the center of the follicle (Figure 5A, Line 1) shows an intensity value around 50 AU from the skin surface to 700–800 μm deep. The profile of the border of the follicle (Figure 5A, Line 2) shows a similar profile, with the intensity of the LRB up to 700 μm being around 65 AU. Due to the narrowing of the follicle, the line is outside the follicle, around 1000 μm ; however, near the follicle sheath (1200 μm), it can be seen that the intensity of the LRB was around 50 AU. In the non-follicle area (Figure 5A, Line 3), the C6 intensity profile was high to 200 μm in depth, but then decreased quickly, suggesting the accumulation of C6 in the epidermis. It can also be seen that the intensity of LRB outside the follicle at depths greater than 200 μm was clearly lower than that of the follicle lines. In the epidermis, a yellow color can be observed, corresponding to the co-localization of both fluorochromes in this region. In other words, LRB had accumulated throughout the follicle at depths greater than C6.

In Figure 5B, corresponding to another skin section of the permeation with C6-LRB-LPNCs, a section of the hair follicle can be seen. In this case, the section is not longitudinal but a cross-section. The intensity profiles of the different skin annexes and hair follicles followed the same biodistribution for both fluorophores as previously discussed. Accumulation of C6 and LRB was seen up to about 400–500 μm deep. At deeper follicle depths, only LRB accumulation was observed.

Different magnifications were made on sections of the hair follicle, in order to highlight the fluorochrome distribution in the infundibulum (Figure 5A, zoom 4) and in the isthmus area (Figure 5A, zoom 5). In the zooms of Figure 5B, zoom 3 and zoom 4 highlight the transversal hair follicle section with the different fluorochrome distribution previously described.

In Figure 5C, the zoom after permeation of the FREE-C6-LRB control solution can be observed. In this case, the observed biodistribution was different. As they were not delivered in nanoparticles, the fluorophores did not accumulate in the hair follicles. As can be seen in the profiles of lines 1 and 2 of Figure 5C, the intensity of C6 was around 20 AU in the epidermis and decayed at depths greater than 100 μm . The LRB intensity was around 20 AU throughout the entire zoom where you can see the dermis, as well as the hair follicle cross-section.

In addition, when analyzing zooms 3 and 4 of Figure 5C, it can be observed that the intensity of the yellow color in the follicles is almost non-existent, due to the non-accumulation of C6 in the hair follicle. In zoom 5 of Figure 5C, the accumulation of C6 and LRB in the epidermis of a superficial invagination (<100 μm) can be seen.

These results explain the biodistribution of these two hydrophobic fluorophores carried in the LPNCs. The intensity of the green color, corresponding to the accumulation of C6, was greater in the epidermis and in the upper part of the hair follicle, and decreased with increasing depth in the skin. The images obtained by confocal microscopy seem to indicate that the *in vitro* skin penetration by C6 in the LPNCs accumulated on the epidermis and the hair follicle infundibulum, but did not penetrate into the deepest parts of hair follicles. This fact suggests that C6 is released when it comes into contact with the stratum corneum lipids, due to its hydrophobic nature, leading to greater accumulation in less deep areas.

The intensity in red color, corresponding to LRB, was less than that of C6 in the epidermis but greater than that of C6 when analyzing the profile deeper into the hair follicle. The fact that an accumulation of LRB was observed at these depths suggests that this fluorophore is found in the lipid nucleus of the nanoparticles and travels with them towards the bulb of the follicle. As described in the literature, ethyl cellulose polymer nanoparticles accumulate in skin annexes, due to their geometry and size, and can deliver small molecules to hair follicles through the transfollicular route, limiting distribution to the rest of the skin and to systemic circulation [33].

3.5. Immunohistofluorescence Biodistribution

Confocal laser microscopy is usually employed to study the biodistribution of nanoparticles in different tissues; unfortunately, this is an indirect measurement, as there is no direct tracking of the API. There exist other techniques to study topical biodistribution, such as skin layer separation [34], cyanoacrylate tape-stripping [35], or dermatopharmacokinetics [36]. Techniques such as cyanoacrylate-stripping allow to study hair follicle targeting but usually have a lower spatial resolution than IHF and could have problems, such as analytical interferences, quantification limit issues, lack of complete recovery, or matrix effects. By means of the IHF, it is possible to visualize if there is accumulation in the different anatomical regions of the hair follicle.

Due to this and to confirm the data obtained in the previous section, an IHF experiment was carried out. Rabbit anti-DEX IgG and Alexa Fluor 488 goat anti-rabbit were employed, such that direct visualization of the drug could be performed.

After the IHQ experiment, a different behavior was observed, with respect to the DEX-FREE (Figure 6C,D) and LPNCs-vehiculated DEX (Figure 6A,B). The visualization filter used in ImageJ was Green Fire Blue, where the blue color corresponds to the lowest intensity and the yellow-green color to the highest intensity. Figure 6B shows a longitudinal section of the hair follicle. In panels A, C, and D of Figure 6, cross-sections of the hair follicles are observed. Surface plots were obtained, in order to compare the intensity in a more visual way.

In the same way as in Section 3.6, different lines were drawn to compare the intensity profiles. Line 1 in Figure 6A corresponds to the intensity across the lateral zone of a hair follicle. In this case, an accumulation of DEX was seen (intensity around 140 AU at 500 μ M depth). Line 2 corresponds to permeation outside the follicle, for which it was observed that DEX remained restricted to the epidermis and its invaginations, with an intensity of 60 AU. In Figure 6B, three lines are drawn. Lines 1 and 2 correspond to the central zone and the outer sheath of the follicle, respectively. Although the maximum intensity (approximately 100 AU) was observed at around 250 μ m, DEX accumulation went to 700 μ m, corresponding to the hair follicle bulb (Figure 6B, Zoom 1 and 2). Line 3 corresponds to an area outside the follicle; in this case, the intensity dropped to 25 AU when entering beyond 100 μ m and, again, it was observed that DEX remained restricted to the area of the epidermis and stratum corneum. The intensity along the follicle remained around 40 AU—almost double compared to outside the follicle. Surface plots of both images were also made, to obtain a visual image of the accumulation of DEX. It is clear that accumulation in hair follicles has occurred.

Regarding the permeation of FREE-DEX, the behavior was different. Lines 1 and 2 of Figure 6C,D are very similar and show that DEX did not accumulate in hair follicles when it was formulated in this solution. Beyond 50 μ m in depth (epidermis), the intensity was low (about 20 AU). This behavior is shown in the surface plots in Figure 6C Zoom 3 and Figure 6D Zoom 3, where FREE-DEX did not accumulate in follicles, only in the stratum corneum and part of the epidermis.

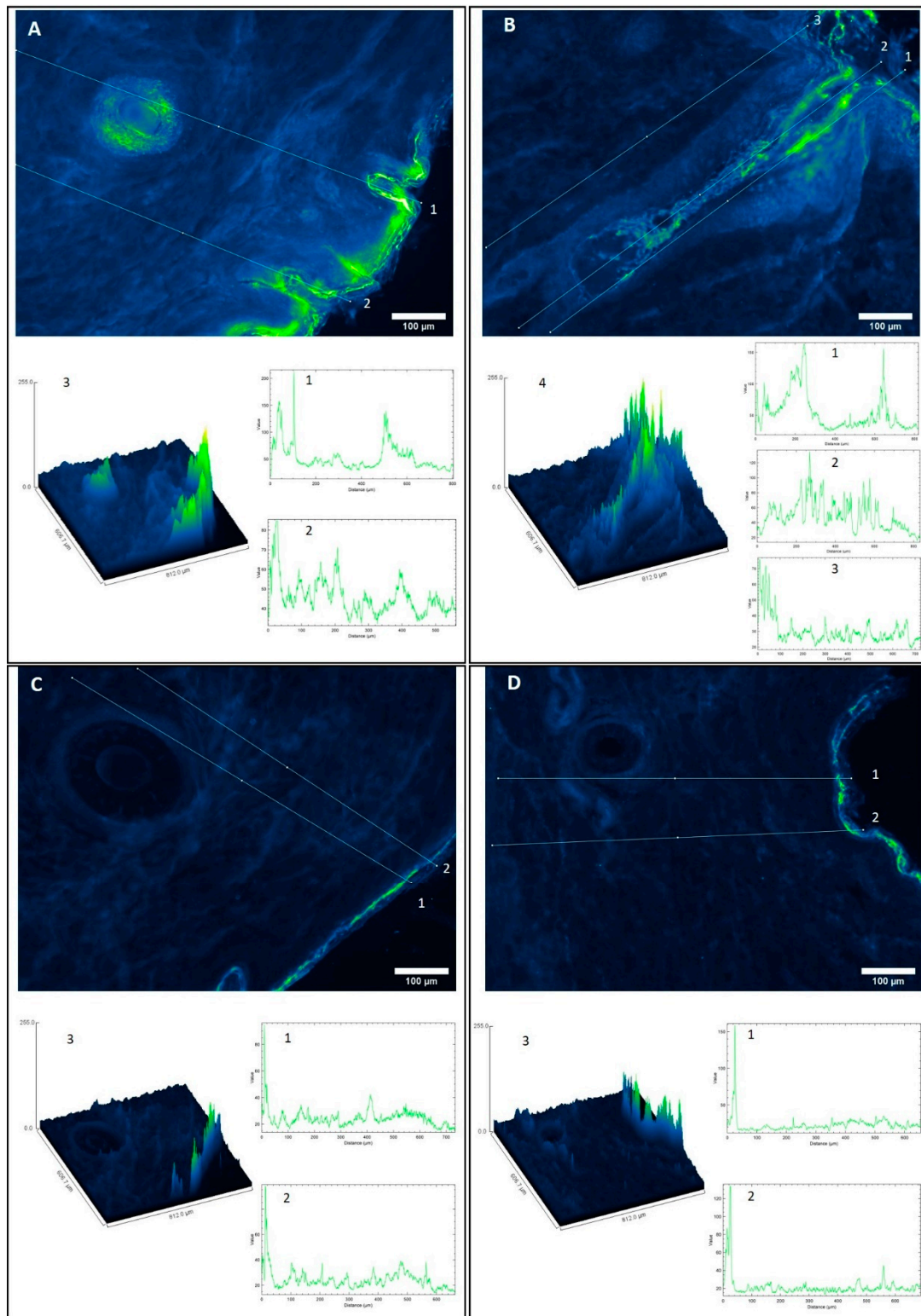


Figure 6. IHF images of a pig skin cross-section. Green color corresponds to high intensity and blue to lower intensity fluorescence of Alexa 488 secondary antibody (Ab)–Primary Ab–DEX complex: (A,B) DEX-loaded LPNCs; (C,D) hydroalcoholic DEX control solution. Figure 6A 1–2, Figure 6B 1–3, Figure 6C 1–2 and Figure 6D 1–2 correspond to green intensity plot profiles as function of the depth (μm). Figure 6A 3, Figure 6B 4, Figure 6C 3 and Figure 6D 3 correspond to surface plots. The images were captured using 10× magnifications and the Lookup Table (LUT) used to show the pictures was Green Fire Blue.

When comparing these results with those obtained by confocal microscopy, it can be observed that the biodistribution of DEX was similar to that of LRB, as it accumulated in the deep areas of the follicles (>400 μm). These results corroborate the high encapsulation efficiency results and suggest that it is possible to achieve a controlled and sustained release in the hair follicle by encapsulation in LPNCs. As a result, a depot effect in the pilosebaceous unit is expected. This effect could, on the one hand, reduce the frequency of administration (from the 12 h usually used in topical corticosteroids to 24 h) and then could reduce the associated adverse effects. On the other hand, a depot effect and the release of the drug in the site of action would improve the treatment efficacy and reduce or avoid the systemic or intralesional administration of the drug, reducing the systemic adverse effects (which are usually worse than the adverse effects of topical administration) and patient discomfort caused by injections (in the intralesional therapy). These facts should be evaluated in future clinical trials.

3.6. Cytotoxicity and Anti-TNF α Efficacy

Human-transformed keratinocytes (HEK001 cells) were chosen to assess the DEX-LPNC cytotoxicity (Figure 7A). Non-loaded LPNCs, benzalkonium chloride, and untreated cells were tested as controls. For loaded LPNCs, the inverse dilution factors (5000, 25,000, 50,000, 100,000, and 250,000) corresponded to the respective concentrations of 5, 1, 0.5, 0.25, and 0.1 μM of DEX. For benzalkonium chloride, proper concentrations were 1, 0.2, 0.1, 0.05, and 0.02 μM . The cell viability profiles of the tested compounds exhibited a similar pattern: there was a viability reduction, compared to untreated cells, at higher concentrations of loaded and non-loaded LPNCs. To ascertain the reason for this toxicity, pure benzalkonium chloride was evaluated with the same dilution scheme as the LPNCs, demonstrating that the reason for the viability reduction was caused by the preservative. Although this fact was observed, there exist different commercial products that use the same preservative for the topical route, as described in the FDA inactive ingredients data base [37], demonstrating the suitability of the selected preservative system.

To evaluate the *in vitro* anti-inflammatory efficacy of the LPNCs, TNF α was selected as a tracker, as it is usually involved in most inflammatory alterations of the skin, particularly in AA [38]. Furthermore, in many cases, it has been identified as a promising target for pharmacological modulation [39]. Figure 7B shows the TNF α expression in HEK001 cells after treatment with DEX-LPNCs and FREE-DEX for 24 h after pre-treatment with 10 $\mu\text{g}/\text{mL}$ of LPS to induce inflammation. LPNCs were tested at a DEX level equivalent to 0.1 μM , as the cell viability was not reduced at this concentration level. FREE-DEX at the same concentration level was used as control. A significant reduction in TNF α can be seen in both cases. The lower efficacy of the lipomers, compared with the solution, could be caused by the differential release pattern observed in Figure 4: at 24 h, the amount of DEX released from the lipomers was around 75%, compared with 100% in the solution. Similarly, the difference between the FREE-DEX and lipomers was about 27%, such that the drug release limited the anti-TNF α efficacy. This difference is not expected to appear in real applications, considering that the LPNCs have accumulated in hair follicles and, so, a depot effect would appear (not evaluated in cell culture), such that the slow degradation of the lipomers in the follicle would release the drug into the surrounding and deeper area. After multiple administrations, an increased exposition of DEX would take place, compared with the free drug.

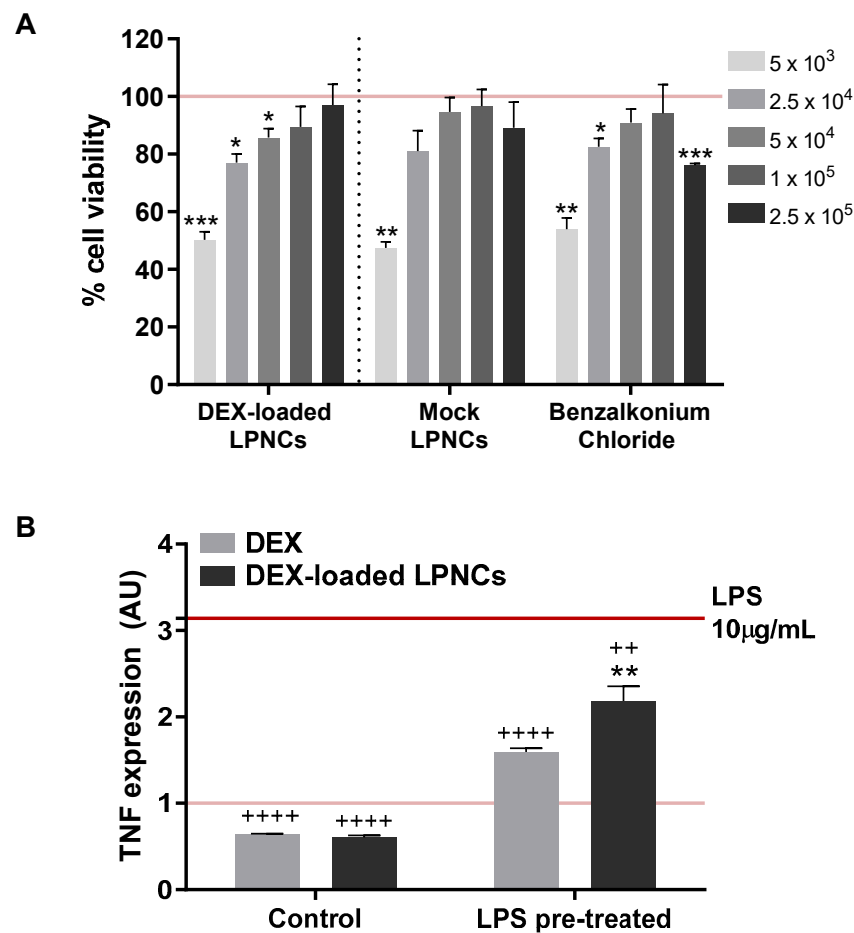


Figure 7. In vitro cell culture studies: (A) HEK001 cell viability with MTT assay. The indicated numbers represent the inverse dilution factors, referring to the composition of synthesized LPNCs. For DEX-loaded LPNCs, the dilution factors correspond to the concentrations of 5, 1, 0.5, 0.25, and 0.1 μM of DEX. For benzalkonium chloride, proper concentrations were 1, 0.2, 0.1, 0.05, and 0.02 μM . Data are represented as the mean \pm SEM ($n = 3$) of the cell viability percentage, referring to untreated controls (horizontal lane). Statistical significance was assessed by Student's paired t-test; * $p < 0.05$; ** $p < 0.01$; *** $p < 0.005$. (B) TNF α mRNA expression was measured after treating cells for 24 h with 0.1 μM of either free dexamethasone (grey) or DEX-loaded LPNCs (dark grey), without (left) or with (right) a 1-h pre-treatment with LPS (10 $\mu\text{g}/\text{mL}$). TNF α expression is represented as the mean \pm SEM ($n = 3$); TNF α expression at control and LPS treatment conditions is indicated with horizontal pink and red lanes, respectively. Statistical significance was evaluated by one-way ANOVA compared to the control (*) or LPS (+); ** $p < 0.01$, ++ $p < 0.01$, ++++ $p < 0.001$.

4. Conclusions

LPNCs with a high carrying capacity were successfully developed for the active dexamethasone. When studying the biodistribution of the nanoparticles using confocal microscopy, accumulation in hair follicles and cutaneous annexes was observed, thus proving their ability to achieve follicular targeting. These results were confirmed for DEX biodistribution by immunofluorescence, where DEX-LPNCs demonstrated an increase in accumulation in hair follicles, compared to FREE-DEX. The cytotoxicity of the particles was studied, where toxicity (caused by the preservative, benzalkonium chloride) was observed only at high doses. The anti-inflammatory efficacy of DEX-LPNCs, with TNF α as a tracker, was demonstrated. Its high %LC and %EE, good physicochemical properties (size of 115 nm, low polydispersity, and Z-potential of +30 mV), sustained in vitro release profile, localized release in hair follicles, and anti-inflammatory efficacy make this nanoformulation a very interesting candidate to improve the efficacy and reduce the adverse effects of

corticosteroids for diseases in which there is inflammation in the hair follicles, such as alopecia areata. Thanks to the follicular targeting obtained, it could be possible to have a depot effect within the pilosebaceous unit, which could allow us to reduce the frequency of administration compared to classical formulations. The safety and efficacy profiles of the DEX-lipomers should be verified in clinical trials to compare side effects.

Author Contributions: Conceptualization, F.F.-C. and E.P.-R.; methodology, F.F.-C., E.P.-R. and S.P.-T.; software, E.P.-R. and A.M.-V.; validation, E.P.-R., F.F.-C.; formal analysis, E.P.-R., A.M.-V. and M.L.-R.; investigation, E.P.-R. and F.F.-C.; resources, F.F.-C. and S.P.-T.; data curation, E.P.-R., F.F.-C.; writing—original draft preparation, E.P.-R.; writing—review and editing, E.P.-R., F.F.-C., A.M.-V., S.P.-T. and M.L.-R.; visualization E.P.-R., F.F.-C., A.M.-V., S.P.-T. and M.L.-R.; supervision, F.F.-C. and S.P.-T.; project administration, E.P.-R. and F.F.-C.; funding acquisition, F.F.-C., E.P.-R. and S.P.-T. All authors have read and agreed to the published version of the manuscript.

Funding: This research received funding from the Generalitat de Catalunya Industrial Doctorate program of the candidate Eloy Pena Rodríguez, expedient number 2019 DI 1989691.

Institutional Review Board Statement: Ethical review and approval were waived for this study, due to the pig skin used was obtained from an abattoir. No animals were sacrificed specifically to carry out this research.

Informed Consent Statement: Not applicable

Data Availability Statement: The data presented in this study are available on request from the corresponding author. The data are not publicly available due to intellectual property.

Acknowledgments: Assistance provided by Manel Bosch from the University of Barcelona Scientific-Technical service, and by Mari Carmen Moreno from Reig Jofre was greatly appreciated. The authors thank Marçal Pastor Anglada and Carlos Nieto Abad for the guidance and advice provided in this project.

Conflicts of Interest: F.F.-C., E.P.-R. and M.L.R. are employees of Reig Jofre. The authors are not involved in any commercial or marketing activities of the developed product. Other authors declare no conflict of interest. The funders had no role in the design of the study; in the collection, analyses, or interpretation of data; in the writing of the manuscript, or in the decision to publish the results.

References

1. Elias, P.M. Stratum Corneum Defensive Functions: An Integrated View. *J. Investig. Dermatol.* **2005**, *125*, 183–200. [\[CrossRef\]](#)
2. Gupta, M.; Agrawal, U.; Vyas, S.P. Nanocarrier-based topical drug delivery for the treatment of skin diseases. *Expert Opin. Drug Deliv.* **2012**, *9*, 783–804. [\[CrossRef\]](#)
3. Pena-Rodríguez, E.; Moreno, M.C.; Blanco-Fernandez, B.; González, J.; Fernández-Campos, F.; Fernandez, B.-. Epidermal Delivery of Retinyl Palmitate Loaded Transfersomes: Penetration and Biodistribution Studies. *Pharmaceutics* **2020**, *12*, 112. [\[CrossRef\]](#)
4. Lademann, J.; Richter, H.; Teichmann, A.; Otberg, N.; Blume-Peytavi, U.; Luengo, J.; Weiss, B.; Schaefer, U.F.; Lehr, C.-M.; Wepf, R. Nanoparticles—An efficient carrier for drug delivery into the hair follicles. *Eur. J. Pharm. Biopharm.* **2007**, *66*, 159–164. [\[CrossRef\]](#) [\[PubMed\]](#)
5. Shen, S.; Wu, Y.; Liu, Y.; Wu, D. High drug-loading nanomedicines: Progress, current status, and prospects. *Int. J. Nanomed.* **2017**, *12*, 4085–4109. [\[CrossRef\]](#) [\[PubMed\]](#)
6. Venturini, C.G.; Jäger, E.; Oliveira, C.P.; Bernardi, A.; Battastini, A.M.; Guterres, S.S.; Pohlmann, A.R. Formulation of lipid core nanocapsules. *Colloids Surf. A Physicochem. Eng. Asp.* **2011**, *375*, 200–208. [\[CrossRef\]](#)
7. Bazylińska, U.; Lewińska, A.; Lamch, Ł.; Wilk, K.A. Polymeric nanocapsules and nanospheres for encapsulation and long sustained release of hydrophobic cyanine-type photosensitizer. *Colloids Surf. A Physicochem. Eng. Asp.* **2014**, *442*, 42–49. [\[CrossRef\]](#)
8. Saraiya, N.V.; A Goldstein, D. Dexamethasone for ocular inflammation. *Expert Opin. Pharmacother.* **2011**, *12*, 1127–1131. [\[CrossRef\]](#)
9. Yamamoto, K.A.; Klossek, R.; Flesch, F.; Rancan, M.; Weigand, I.; Bykova, M.; Bechtel, S.; Ahlberg, A.; Vogt, U.; Blume-Peytavi, P.; et al. Influence of the skin barrier on the penetration of topical-ly-applied dexamethasone probed by soft X-ray spectromicroscopy. *Eur. J. Pharm. Biopharm.* **2017**, *118*, 30–37. [\[CrossRef\]](#)
10. Leyden, J.L.; Kligman, A.M. Treatment of alopecia areata with steroid solution. *Arch Dermatol.* **1972**, *106*, 924. [\[CrossRef\]](#)
11. Shapiro, J. Current Treatment of Alopecia Areata. *J. Investig. Dermatol. Symp. Proc.* **2013**, *16*, S42–S44. [\[CrossRef\]](#)
12. Lachenmeier, D.W. Safety evaluation of topical applications of ethanol on the skin and inside the oral cavity. *J. Occup. Med. Toxicol.* **2008**, *3*, 26. [\[CrossRef\]](#) [\[PubMed\]](#)
13. Kwak, S.; Brief, E.; Langlais, D.; Kitson, N.; Lafleur, M.; Thewalt, J. Ethanol perturbs lipid organization in models of stratum corneum membranes: An investigation combining differential scanning calorimetry, infrared and 2H NMR spectroscopy. *Biochim. Biophys. Acta Biomembr.* **2012**, *1818*, 1410–1419. [\[CrossRef\]](#) [\[PubMed\]](#)

14. McDonnell, G.; Russell, A.D. Antiseptics and disinfectants: Activity, action, and resistance. *Clin. Microbiol. Rev.* **1999**, *12*, 147–179, Erratum in **2001**, *14*, 227. [[CrossRef](#)]
15. Balzus, B.; Sahle, F.F.; Hönzke, S.; Gerecke, C.; Schumacher, F.; Hedtrich, S.; Kleuser, B.; Bodmeier, R. Formulation and ex vivo evaluation of polymeric nanoparticles for controlled delivery of cortico-steroids to the skin and the corneal epithelium. *Eur. J. Pharm. Biopharm.* **2012**, *115*, 122–130. [[CrossRef](#)]
16. Al-Amin, M.D.; Bellato, F.; Mastrotto, F.; Garofalo, M.; Malfanti, A.; Salmaso, S.; Caliceti, P. Dexamethasone Loaded Liposomes by Thin-Film Hydration and Microfluidic Procedures: Formulation Challenges. *Int. J. Mol. Sci.* **2020**, *21*, 1611. [[CrossRef](#)]
17. Fessi, H.; Puisieux, F.; Devissaguet, J.P.; Ammoury, N.; Benita, S. Nanocapsule formation by interfacial polymer deposition following solvent displacement. *Int. J. Pharm.* **1989**, *55*, R1–R4. [[CrossRef](#)]
18. Lymberopoulos, A.; Demopoulou, C.; Kyriazi, M.; Katsarou, M.; Demertzis, N.; Hatziandoniou, S.; Maswadeh, H.; Papaioanou, G.; Demetzos, C.; Maibach, H.; et al. Liposome percutaneous penetration in vivo. *Toxicol. Res. Appl.* **2017**. [[CrossRef](#)]
19. European Directorate for the Quality of Medicines & HealthCare, European Pharmacopoeia 7.0., Chapter 2.4.24. Identification and Control of Residual Solvents, 01/2008:20424. Available online: <https://www.drugfuture.com/Pharmacopoeia/EP7/DATA/20424E.PDF> (accessed on 10 February 2021).
20. Zhang, Y.; Huo, M.; Zhou, J.; Zou, A.; Li, W.; Yao, C.; Xie, S. DDSolver: An Add-In Program for Modeling and Comparison of Drug Dissolution Profiles. *AAPS J.* **2010**, *12*, 263–271. [[CrossRef](#)]
21. Monica, L.-L.; Jordi, G.; Francisco, F.-C. In situ bioadhesive film-forming system for topical delivery of mometasone furoate: Characterization and biopharmaceutical properties. *J. Drug Deliv. Sci. Technol.* **2020**, *59*, 101852. [[CrossRef](#)]
22. Papadopoulou, V.; Kosmidis, K.; Vlachou, M.; Macheras, P. On the use of the Weibull function for the discernment of drug release mechanisms. *Int. J. Pharm.* **2006**, *309*, 44–50. [[CrossRef](#)] [[PubMed](#)]
23. Supramaniam, J.; Adnan, R.; Kaus, N.H.M.; Bushra, R. Magnetic nanocellulose alginate hydrogel beads as potential drug delivery system. *Int. J. Biol. Macromol.* **2018**, *118*, 640–648. [[CrossRef](#)] [[PubMed](#)]
24. Rekhi, G.S.; Jambhekar, S.S. Ethylcellulose—A Polymer Review. *Drug Dev. Ind. Pharm.* **1995**, *21*, 61–77. [[CrossRef](#)]
25. Gurtler, F.; Kaltsatos, V.; Boisramé, B.; Gurny, R. Long-acting soluble bioadhesive ophthalmic drug insert (BODI) containing gentamicin for veterinary use: Optimization and clinical investigation. *J. Control. Release* **1995**, *33*, 231–236. [[CrossRef](#)]
26. Wasilewska, K.; Winnicka, K. Ethylcellulose—A Pharmaceutical Excipient with Multidirectional Application in Drug Dosage Forms Development. *Materials* **2019**, *12*, 3386. [[CrossRef](#)]
27. Kala, S.; Gurudiwan, P.; Juyal, D. Formulation and Evaluation of Besifloxacin Loaded in Situ Gel for Ophthalmic Delivery. *Pharm. Biosci. J.* **2018**, *6*, 36. [[CrossRef](#)]
28. Committee for Human Medicinal Products, ICH guideline Q3C (R6) on impurities: Guideline for residual solvents 9 August 2019, EMA/CHMP/ICH/82260/2006. Available online: <https://www.ema.europa.eu/en/ich-q3c-r6-residual-solvents> (accessed on 18 March 2021).
29. Sharma, N.; Madan, P.; Lin, S. Effect of process and formulation variables on the preparation of parenteral paclitaxel-loaded biodegradable polymeric nanoparticles: A co-surfactant study. *Asian J. Pharm. Sci.* **2016**, *11*, 404–416. [[CrossRef](#)]
30. Tan, T.B.; Chu, W.C.; Yussof, N.S.; Abas, F.; Mirhosseini, H.; Cheah, Y.K.; Nehdi, I.A.; Tan, C.P. Physicochemical, morphological and cellular uptake properties of lutein nanodispersions prepared by using surfactants with different stabilizing mechanisms. *Food Funct.* **2016**, *7*, 2043–2051. [[CrossRef](#)]
31. Jäger, E.; Venturini, C.G.; Poletto, F.S.; Colomé, L.M.; Pohlmann, J.P.U.; Bernardi, A.; Battastini, A.M.O.; Guterres, S.S.; Pohlmann, A.R. Sustained Release from Lipid-Core Nanocapsules by Varying the Core Viscosity and the Particle Surface Area. *J. Biomed. Nanotechnol.* **2009**, *5*, 130–140. [[CrossRef](#)]
32. Singhvi, G.; Singh, M. Review: In vitro drug release characterization models. *Int. J. Pharm. Stud. Res. II* **2011**, 77–84.
33. Morgen, M.; Lu, G.W.; Du, D.; Stehle, R.; Lembke, F.; Cervantes, J.; Ciotti, S.; Haskell, R.; Smithey, D.; Haley, K.; et al. Targeted delivery of a poorly water-soluble compound to hair follicles using polymeric nanoparticle suspensions. *Int. J. Pharm.* **2011**, *416*, 314–322. [[CrossRef](#)] [[PubMed](#)]
34. Döge, N.; Hönzke, S.; Schumacher, F.; Balzus, B.; Colombo, M.; Hadam, S.; Rancan, F.; Blume-Peytavi, U.; Schäfer-Korting, M.; Schindler, A.; et al. Ethyl cellulose nanocarriers and nanocrystals differentially deliver dexamethasone into intact, tape-stripped or sodium lauryl sulfate-exposed ex vivo human skin—Assessment by intradermal microdialysis and extraction from the different skin layers. *J. Control Release.* **2016**, *242*, 25–34. [[CrossRef](#)] [[PubMed](#)]
35. Teichmann, A.; Jacobi, U.; Ossadnik, M.; Richter, H.; Koch, S.; Sterry, W.; Lademann, J. Differential Stripping: Determination of the Amount of Topically Applied Substances Penetrated into the Hair Follicles. *J. Investig. Dermatol.* **2005**, *125*, 264–269. [[CrossRef](#)] [[PubMed](#)]
36. Nicoli, S.; Bunge, A.L.; Delgado-Charro, M.B.; Guy, R.H. Dermatopharmacokinetics: Factors Influencing Drug Clearance from the Stratum Corneum. *Pharm. Res.* **2008**, *26*, 865–871. [[CrossRef](#)]
37. FDA Inactive Ingredient Database. Available online: <http://www.accessdata.fda.gov/scripts/cder/iig/index.cfm> (accessed on 18 March 2021).
38. Kasumagic-Halilovic, E.; Prohic, A.; Cavaljuga, S. Tumor necrosis factor-alpha in patients with alopecia areata. *Indian J. Dermatol.* **2011**, *56*, 494–496. [[CrossRef](#)]
39. Tauber, M.; Buche, S.; Reygagne, P.; Berthelot, J.-M.; Aubin, F.; Ghislain, P.-D.; Cohen, J.-D.; Coquerelle, P.; Goujon, E.; Jullien, D.; et al. Alopecia areata occurring during anti-TNF therapy: A national multicenter prospective study. *J. Am. Acad. Dermatol.* **2014**, *70*, 1146–1149. [[CrossRef](#)]

Chapter 5. The physicochemical, biopharmaceutical, and *in vitro* efficacy properties of freeze-dried dexamethasone-loaded lipomers

Resumen

Se desarrollaron nanopartículas poliméricas híbridas cargadas con dexametasona como una herramienta potencial para tratar la alopecia areata debido a su capacidad de liberación folicular selectiva. La liofilización es una técnica comúnmente utilizada para mejorar la estabilidad de las nanopartículas; sin embargo, hay pocos estudios centrados en su efecto sobre las nanopartículas de etil celulosa con núcleo lipídico. Las nanopartículas se liofilizaron con diferentes crioprotectores. Se seleccionó la sacarosa ya que permitió obtener una buena resuspensión y proporcionó unos parámetros fisicoquímicos aceptables (374,33 nm, +34,7 mV, polidispersión 0,229 y eficiencia de encapsulación del 98,87%). Las nanopartículas obtenidas se incorporaron en un hidrogel de goma xantana de aspecto conforme, y se estudiaron los perfiles reológicos, de liberación y de permeación cutánea de diferentes formulaciones. El proceso de liofilización modificó significativamente el tamaño de las partículas, y también se alteraron las propiedades de liberación y permeación del fármaco. Además, los análisis de la citotoxicidad y la eficacia antiinflamatoria de las partículas liofilizadas y no-liofilizadas en los queratinocitos humanos no indicaron diferencias.



Article

The Physicochemical, Biopharmaceutical, and In Vitro Efficacy Properties of Freeze-Dried Dexamethasone-Loaded Lipomers

Eloy Pena-Rodríguez ¹, Aida Mata-Ventosa ^{2,3,4,†}, Laura Garcia-Vega ^{2,4,†}, Sandra Pérez-Torras ^{2,3,4} and Francisco Fernández-Campos ^{1,*}

¹ Topical & Oral Development R+D Reig Jofre Laboratories, 08970 Sant Joan Despi, Spain; eloy.pena@reigjofre.com

² Molecular Pharmacology and Experimental Therapeutics, Department of Biochemistry and Molecular Biomedicine, Institute of Biomedicine, University of Barcelona (IBUB), 08028 Barcelona, Spain; aidamatav@ub.edu (A.M.-V.); l.garciavega@ub.edu (L.G.-V.); s.perez-torras@ub.edu (S.P.-T.)

³ Biomedical Research Networking Center in Hepatic and Digestive Diseases (CIBEREHD), Carlos III Health Institute, 28029 Madrid, Spain

⁴ Sant Joan de Déu Research Institute (IR SJD-CERCA) Esplugues de Llobregat, 08950 Barcelona, Spain

* Correspondence: Ffernandez@reigjofre.com; Tel.: +34-935-507-718

† These authors contributed equally to this paper.

Abstract: Dexamethasone-loaded polymer hybrid nanoparticles were developed as a potential tool to treat alopecia areata due to their follicular targeting ability. Freeze drying (FD) is a common technique used to improve nanoparticle stability; however, there are few studies focused on its effect on ethyl cellulose lipid-core nanoparticles. Nanoparticles were lyophilized with different cryoprotectants. Sucrose was selected because it allowed for a good resuspension and provided acceptable physicochemical parameters (374.33 nm, +34.7 mV, polydispersion 0.229%, and 98.87% encapsulation efficiency). The nanoparticles obtained were loaded into a pleasant xanthan gum hydrogel, and the rheological, release, and skin permeation profiles of different formulations were studied. The FD formulation significantly modified the particle size, and the drug release and permeation properties were also altered. In addition, analyses of the cytotoxicity and anti-inflammatory efficacy of FD and non-FD particles on human keratinocytes indicated no differences.

Keywords: lyophilization; freeze drying; dexamethasone; lipomers; ethyl cellulose; nanoparticles; drug release; skin permeation; keratinocytes; topical; corticoid



Citation: Pena-Rodríguez, E.; Mata-Ventosa, A.; Garcia-Vega, L.; Pérez-Torras, S.; Fernández-Campos, F. The Physicochemical, Biopharmaceutical, and In Vitro Efficacy Properties of Freeze-Dried Dexamethasone-Loaded Lipomers. *Pharmaceutics* **2021**, *13*, 1322. <https://doi.org/10.3390/pharmaceutics13081322>

Academic Editor: Anna Angela Barba

Received: 28 July 2021

Accepted: 17 August 2021

Published: 23 August 2021

Publisher's Note: MDPI stays neutral with regard to jurisdictional claims in published maps and institutional affiliations.



Copyright: © 2021 by the authors. Licensee MDPI, Basel, Switzerland. This article is an open access article distributed under the terms and conditions of the Creative Commons Attribution (CC BY) license (<https://creativecommons.org/licenses/by/4.0/>).

1. Introduction

Nanoparticles have a high surface-to-volume ratio, which is very interesting for topical applications as they increase skin–nanoparticle contact and improve drug diffusion into the skin [1]. In addition, the rigid structure of the nanoparticles facilitates penetration into skin appendages, such as the hair follicles. This follicular targeting acts as a drug reservoir [2], and it is especially interesting to treat diseases related with hair follicles and sebaceous glands, as a result of the accumulation and direct interaction of the drug in the site of action. The high concentration and size of scalp hair follicles (up to 10% of the skin surface), which increase permeability [3], makes this surface very interesting for treatment with these particles.

Alopecia areata is an inflammatory disease that affects between 1% and 2% of the general population [4]. It involves hair loss in different patterns (patches of different sizes; alopecia totalis, in which the hair loss affects the entire scalp; and alopecia universalis, involving the loss of body hair), pain, and has a strong emotional impact on the patient. The disease is usually associated with other immunological-related conditions, such as asthma, atopic dermatitis, vitiligo, etc. [5]. Current treatments involve the use of immunosuppressants, for example, topical corticosteroids and minoxidil. When patients are refractory to topical treatment, corticosteroids could be administered intralesionally or

systemically [6], but these routes of administration are associated with a higher incidence of adverse effects and patient discomfort. With the aim of improving the therapeutic index of the corticoid topical treatment, a dexamethasone (DEX)-lipomers formulation was developed as a promising tool to treat alopecia areata as a result of its accumulation in the hair follicles [7]. The follicular targeting was demonstrated by confocal fluorescence microscopy and immunohistofluorescence. After ex vivo hair follicle imaging, an increase in drug accumulation in the desired site of action was demonstrated and compared with a free DEX solution. This fact could reduce the frequency of administration, increase drug delivery, and, consequently, enhance the efficacy of the topical treatment, improving patient compliance. The produced nanoparticles were made of ethyl cellulose (a biocompatible and low-cost excipient) with a hydrophobic core (medium-chain triglyceride oil), which allows the drug-loading capacity to be increased. The physicochemical properties of the nanoparticles were characterized, obtaining a particle size around 120 nm with a polydispersity index below 0.25, a zeta potential around +30 mV, and an encapsulation efficiency higher than 95%.

Polymeric lipid hybrid nanoparticles, also called lipomers, are promising vehicles for the topical administration of hydrophobic drugs. The lipomers contain a polymeric matrix, which can control drug release by diffusion, erosion, or swelling (depending on the polymer type used) and lipids, which are able to increase the loading capacity of hydrophobic drugs. These particles are stabilized by amphiphilic compounds on the nanoparticle surface. Nanoparticle suspensions could have different instability issues, such as drug leakage in aqueous medium, particle aggregation, polymer hydrolysis, issues related with the chemical stability of the entrapped drug [8], etc. A common technique used to reduce nanoparticle long-term instability is freeze drying (FD). This technique involved water removal by sublimation after freezing of the sample. Special care must be taken as large ice crystals can appear during the freezing step. To avoid this issue, the addition of cryoprotectants is recommended, for example sugars, such as trehalose, sucrose, mannitol, and glucose, among others. These compounds surround the particle surface through hydrogen bonding and also prevent nanoparticle aggregation [9]. On occasion, a high percentage of cryoprotectant is required, e.g., up to 20%, but these amounts can increase the viscosity and modify the sensorial properties, which has a high impact on topical formulations. In addition, this can have an impact on the final drug dose being administrated, because the addition of 20% of excipients may involve the use of 20% less water for the reconstitution of the same dose, thus affecting the nanoparticle redispersibility. Therefore, an adequate balance between these aspects needs to be considered. Finally, FD can not only affect the physicochemical properties and stability of nanoparticles but can also modify the biopharmaceutical and pharmacokinetic profile of the drug delivery systems, which should also be evaluated. The most studied polymeric nanoparticles are polylactic-polyglycolic (PLGA) [10–12] derivatives (at different lactic-to-glycolic ratios and molecular weights) and polycaprolactone polymers [13–15], such as nanoparticles or nanocapsules with an oil nucleus. Studies are scarce regarding the lyophilization of ethyl cellulose nanoparticles [16] or ethyl cellulose microcapsules with an oil core [17], but any of these authors used in their formulation cryoprotectants.

The aim of this research was to study the impact of the FD process (with different cryoprotectants) of ethyl cellulose DEX-lipomers on the physicochemical, biopharmaceutical (drug release and ex vivo skin permeation), and in vitro anti-inflammatory properties (on human keratinocytes) of the obtained particles.

2. Materials and Methods

2.1. Materials and Lipomer Formulation

Nanoparticles were produced with ethyl cellulose (EC) (Ashaland Industries Europe GmbH, Rheinweg, Switzerland) and medium-chain triglycerides (MCT) (Oxi-Med Expres S.A., Barcelona, Spain); Tween 80 and Span 60 (Croda Iberica S.A., Barcelona, Spain) were used as stabilizers, and benzalkonium chloride (Sigma Aldrich, Madrid, Spain) was chosen

as preservative. DEX (Fagron Ibérica, Barcelona, Spain) was the active pharmaceutical ingredient, and the selected solvents were ethyl acetate (EA), ethanol absolute (ET) (Scharlab S.L., Barcelona, Spain), and purified water (Inhouse). The cryoprotectants used in the freeze-drying process were sucrose (Acor, Valladolid, Spain), trehalose, and mannitol (Pfanstiehl, Zug, Switzerland).

The DEX-lipomer formulation was previously developed by an emulsion solvent evaporation method [7]. Briefly, EC, MCT, span 60, and DEX (2.33% *w/w*, 0.2% *w/w*, 0.16%, and 1% *w/w*, respectively) were dissolved in EA:ET (5:1) and emulsified with purified water with tween 80 and the preservative benzalkonium chloride (1.5% *w/w* and 0.2% *w/w*, respectively) with a UP400st ultrasonic device (Hielscher Ultrasonics, Teltow, Germany) with an amplitude of 40% for 5 min. The organic solvent of the emulsion was evaporated under vacuum at 40 °C for 5 min. Cryoprotectants were added after nanoparticle production. A schematic representation of the lipomers is presented in Figure 1.

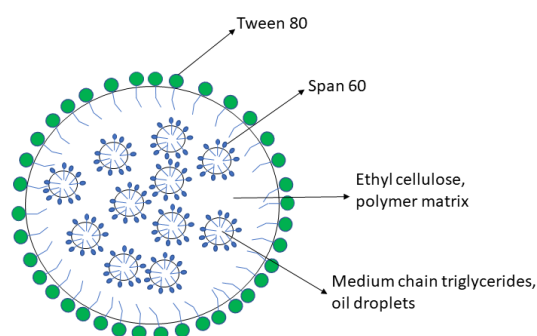


Figure 1. Schematic representation of lipomers.

2.2. Freeze Drying

Freeze-Drying Microscopy (FDM) was carried out to determine the temperature at which the different thermal events occur in the formulation of lipomers and thus define the optimal lyophilization cycle. The system used was an Olympus BX51 Lyophilization Microscope (Olympus Iberia S.A.U., Hospitalet Llobregat, Spain), a PixeLINK camera, with a liquid nitrogen cooling system, a Linkam temperature controller TMS 94, a liquid nitrogen pump (Linkam Scientific Instruments, Surrey, UK), a 10× magnifications objective, a Linkam FDCS 196 Freeze-Drying Stage (Linkam Scientific Instruments, Surrey, UK) attached to the Freeze-Drying Stage system, and a Pirani Gauge pressure controller (Linkam Scientific Instruments, Surrey, UK).

A drop of 10 µL of freshly prepared placebo lipomers, DEX-lipomers, DEX-lipomers with 6% trehalose, DEX-lipomers with 6% sucrose, and DEX-lipomers with 6% mannitol were added, and a cooling ramp was carried out from 25 to −80 °C at a rate of 10 °C/min. The temperature was stabilized at −80 °C for 3 min, and finally, a temperature ramp was applied from −80 to −5 °C at a rate of 2 °C/min; 600 photographs were taken throughout the event. Three different lyoprotectants (Sucrose, Trehalose, and Mannitol at a concentration of 6% *w/w*) were added to the DEX-lipomers and subjected to a lyophilization cycle together with the nanoparticles without lyoprotectant to compare their effect on the reconstitution of the particles.

A Lyobeta20 freeze-dryer (Telstar, Terrasa, Spain) was used for the lyophilizer. From the information obtained in the Lyophilization Microscope studies, the parameters of temperature, pressure, and time were established for each freeze-drying cycle.

2.3. Physicochemical Characterization

2.3.1. Z-Average, Pdl, and Z-Potential before and after Freeze Drying

Dynamic Light Scattering (DLS) (Malvern Zetasizer Nano ZS (Malvern Panalytical, Malvern, UK)) was used to study the Hydrodynamic size (Z-ave), Polydispersity Index

(PDI), and Zeta-potential (Z-pot) of the produced nanoparticles. Prior to measurements, a 1:10 dilution of nanoparticles in milliQ water was carried out.

2.3.2. Transmission Electron Microscopy before and after Freeze Drying

Transmission Electron Microscopy (TEM) (Jeol JEM 1010 100 kv; Jeol, Tokyo, Japan) was employed to study the size and morphology of the nanoparticles before and after the lyophilization process. A dilution of 1:10 non-freeze-dried (non-FD) DEX-lipomers and water resuspended FD DEX-lipomers was prepared in milliQ water, placed in TEM grids, and stained for 1 min with Uranyl Acetate solution 2% *w/w* at 25 °C until samples were dried.

2.3.3. Differential Scanning Calorimetry before and after Freeze Drying

Differential Scanning Calorimetry (DSC) analyses were performed in a DSCq20 (Waters corporation, TA Instruments, Barcelona, Spain) to observe the thermal events taking place in the formulations before and after the lyophilization process. Samples of 3 mg DEX, freeze-dried DEX-lipomers (FD DEX-lipomers), and non-FD DEX-lipomers were placed in Tzero Aluminum pans and sealed with Tzero hermetic aluminum lids with a Tzero press (Water corporation, TA instruments, Barcelona, Spain). Temperature ramps were applied from 0 to 200 °C at 10 °C/min for the formulations containing sucrose and from 20 to 277 °C at 10 °C/min for the formulations without sucrose. This was because sucrose degrades at approximately 210 °C [18] and, in DSC, it is advisable to avoid degradation temperatures.

2.4. Gel Formulations

Xanthan Gum was added at a concentration of 0.75% *w/w* under magnetic stirring at 500 rpm for 1 h at room temperature to solutions of DEX-lipomer, placebo hydrogel, and DEX-hydrogel formulations.

Formulation rheology studies were performed at 25 °C, 24 h after formulation production. Measurements were performed with a Bohlin VOR rheometer (Malvern Instruments limited, Worcestershire, UK). Studies were performed with parallel plate-plate geometry (PP30) with a 0.5 mm gap. A strain sweep test was performed with a strain range of 1–100% and a 1 Hz oscillation rate. Approximately 3.5 g was placed on the plates. The viscosity was measured with a shear rate of 0.1–6.3·s⁻¹.

The following rheological parameters were determined: storage modulus (*G'*), loss modulus (*G''*), delta angle (δ), viscosity (η), thixotropy, and rheological behavior. The obtained rheological behavior experimental data were fit to different equations (Table 1).

Table 1. Rheological equations used to evaluate the prepared formulations.

Rheological Model	Equation	
Newton	$\tau = \eta \cdot \dot{\gamma}$	(1)
Bingham	$\tau = \tau_0 + (\eta_0 \cdot \dot{\gamma})$	(2)
Ostwald–de Waele	$\tau = K \cdot \dot{\gamma}^n$	(3)
Herschel–Bulkley	$\tau = \tau_0 + K \cdot \dot{\gamma}^n$	(4)
Casson	$\tau = \sqrt[n]{\tau_0^n + (\eta_0 \cdot \dot{\gamma})^n}$	(5)
Cross	$\tau = \dot{\gamma} \cdot (\eta_\infty + (\eta_0 - \eta_\infty) / (1 + (\dot{\gamma} / \dot{\gamma}_0)^n))$	(6)

Here, τ denotes the shear stress (Pa), η denotes the viscosity (Pa·s), $\dot{\gamma}$ denotes the shear rate (1/s), τ_0 denotes the yield stress (Pa), η_0 denotes the zero-shear viscosity (Pa·s), η_∞ denotes the infinite-shear viscosity, K denotes the consistency index, n denotes the flow index, and $\dot{\gamma}_0$ denotes the zero-shear rate (1/s).

Model fitting was performed with Python software (module scipy, submodule optimize; Python Software Foundation; Python Language Reference, version 2.7; available at

<http://www.python.org>, accessed on 23 July 2021), and the best fit was selected based on the lowest equation cost (Equation (7)).

$$\sum_{i=1}^N \frac{1}{2} (f(p, x_i) - y_i)^2 \quad (7)$$

where p denotes the equation parameters, x_i denotes the empirical shear rate, and y_i denotes the empirical shear stress.

2.5. High-Performance Liquid Chromatography (HPLC)

A previously described HPLC method [7] was employed to quantify the DEX concentration in the release and permeation experiments (Sections 2.5 and 2.6, respectively). Briefly, an isocratic elution with a mobile phase composed by acetonitrile:KH₂PO₄ 0.05M (60:40) passed at 1.8 mL/min through a C18 HPLC column (250 × 4.6 mm, 3 μm) at 25 °C. The detection wavelength was 208 nm, and the injection volume was 20 μL. The assay was performed with an HPLC instrument (Waters 2695 and detector Waters 2996, Waters Corporation, Milford, MA, USA). In addition, this method was used to estimate the encapsulation efficiency (%EE) according to Equation (8), where W_T denotes the total content of DEX in the formulation and W_{NE} denotes the DEX obtained in the filtrate (not encapsulated) after centrifugation of the amicon ultra device (Merck Millipore, Barcelona, Spain) with a membrane cut-off of 100 KDa at 4500 rpm for 30 min.

$$\%EE = \frac{W_T - W_{NE}}{W_T} \times 100 \quad (8)$$

2.6. In Vitro Release Tests

The in vitro release of DEX from non-FD DEX-lipomers, FD-DEX-lipomers, FD-DEX-lipomers hydrogel, and Free-DEX hydrogel was studied using 12 mL vertical Franz Cells (Vidrafoc, Barcelona, Spain) with a diffusional area of 1.54 cm². Experimental variables were the same as previously used [7]: briefly, receptor medium (ethanol:purified water 50:50) at 32 °C, 60 mg of DEX placed in the donor compartment, and 0.3 mL of sample volume obtained at regular time intervals of up to 24 h. A 12–14 KDa dialysis membrane (Spectrum Chemical, New Brunswick, NJ, USA) was placed between the donor and receptor compartments. Model fitting to several kinetic equations (Table 2) was performed with the DD-solver Excel add-in [19] using the lowest Akaike Information Criteria (AIC) as the model selection criteria.

Table 2. Release equations used to evaluate the prepared formulations.

Kinetic Model	Equation
First Order	$F = F_{max} (1 - e^{-K_1 t})$ (9)
Higuchi	$F = K_H \cdot t^{\frac{1}{2}}$ (10)
Korsmeyer–Peppas	$F = K_{KP} \cdot t^n$ (11)
Weibull	$F = 1 - e^{-(\frac{t}{T_d})^\beta}$ (12)

Here, F denotes the drug fraction released at time t ; F_{max} denotes the maximum released amounts at infinite time; K_1 , K_H , and K_{KP} denote the release constant of the first-order, Higuchi, and Korsmeyer–Peppas (KP) functions, respectively; T_d denotes the time required to dissolve the 63.2% of the drug dose; and β denotes the shape parameter of the Weibull function. The value of exponent n of KP describes the release mechanism ($n < 0.43$ represents a Fickian diffusion; $0.43 \leq n \leq 0.85$ corresponds to anomalous transport; $n > 0.85$ corresponds to a case II transport).

2.7. Pig Skin In Vitro Permeation Tests

Pig skin was obtained at the time of sacrifice from a local abattoir (Barcelona, Spain). The skin was cleaned with sterile saline solution and transported to the laboratory at 4 °C in saline solution. Then, subcutaneous fat was removed with a scalpel, dermatomized at 0.5 mm with an electrical dermatome (GA630, Aesculap, Tuttlingen, Germany), and frozen

at $-20\text{ }^{\circ}\text{C}$ for a maximum period of 6 months or until use. On the day of the experiment, skin pieces were thawed and placed between the donor and receptor compartments of Franz cells, with the same characteristics as described in Section 2.5. In this case, the receptor medium was a solution of PBS pH 7.4 and 5% of bovine serum albumin, to maintain sink conditions through the experiment. Skin integrity was checked (by evaluating the TEWL (transepithelial water loss)) before carrying out the experiment with a TEWL Vapometer (SWL4549, Delfin Technologies Ltd., Kuopio, Finland). Samples from the receptor compartment (0.3 mL) were taken at regular time intervals of up to 24 h and replenished with the same volume of fresh receptor medium. Samples were analyzed with the method described in Section 2.4. Once obtained, the permeated drug quantities per square centimeter and the skin permeation parameters were obtained, according to the following equations:

$$J_{sup} = \frac{\Delta Q_t}{(\Delta t \cdot s)} \quad (13)$$

$$K_p = \frac{J_{sup}}{C_d} \quad (14)$$

$$K_p = P_1 \cdot P_2 \quad (15)$$

$$t_{lag} = \frac{1}{6 P_2} \quad (16)$$

where J_{sup} denotes the transdermal flux in a steady state, Q_t denotes the permeated amount at time t , t denotes the time, s denotes the diffusional area, K_p denotes the permeability coefficient, C_d denotes the concentration of the drug in the donor compartment, P_1 denotes the diffusion parameter, P_2 denotes the partitioning parameter, and t_{lag} denotes the lag time.

t_{lag} was estimated as the extrapolation in the x-axis (x-intercept) of the plot cumulative amounts vs. time.

2.8. In Vitro Cytotoxicity/Anti-TNF α Efficacy

HEK001 cells (ATCC, Promochem Partnership, Manassas, VA, USA) and HaCaT cells (DKFZ, Heidelberg, Germany) were grown in cell culture plates at $37\text{ }^{\circ}\text{C}$ and 5% CO_2 . The HEK001 cell medium was a Keratinocyte Serum Free supplemented with Epidermal Growth Factor (EGF; $100\text{ }\mu\text{g}/\text{mL}$) (Life Technologies, Carlsbad, CA, USA), penicillin ($20\text{ U}/\text{mL}$), and streptomycin (Life Technologies; $20\text{ }\mu\text{g}/\text{mL}$). HaCaT was maintained in Dulbecco's modified Eagle's medium (DMEM; Life Technologies) supplemented with 10% fetal bovine serum (FBS), 2 mM L-glutamine (Gln) (Life Technologies), 20 U/mL penicillin, and $20\text{ }\mu\text{g}/\text{mL}$ streptomycin (Life Technologies). A PCR amplification was carried out every 14 days to confirm the absence of Mycoplasma contamination. Both cell lines, HEK001 and HaCaT, were used to test the cytotoxicity and the anti-inflammatory effect of the formulations.

Cell viability was tested before the anti-inflammatory experiment. A total of 5000 cells/well were seeded in 96-well plates. Dilutions of the different lipomers (non-FD DEX-lipomers, FD DEX-lipomers, and sucrose) equivalent to DEX doses of 5, 1, 0.5, 0.25, and $0.1\text{ }\mu\text{M}$ were added to the cell culture for 24 h. After 48 h, MTT (3-[4,5-dimethylthiazol-2-yl]-2,5 diphenyl tetrazolium bromide; Sigma-Aldrich, St. Louis, MO, USA) was added to evaluate the cell viability by colorimetric assay. Cell survival was calculated considering the 100% viability of the untreated control cells.

To study the anti-inflammatory effect of the DEX-formulations, 700,000 cells/well were seeded in 6-well culture plates. DEX, non-FD DEX-lipomers, and FD DEX-lipomers at a DEX concentration equivalent to $0.1\text{ }\mu\text{M}$ were added to the cells, after a pretreatment with LPS (lipopolysaccharide) at $10\text{ }\mu\text{g}/\text{mL}$ for 1 h. TNF α RNA and GAPDH (endogenous control, used as normalization of gene expression) were quantified by RT-PCR (TaqMan Gene Expression Assays (Applied Biosystems)). RNA was isolated with an EZNA Total RNA kit I (Omega Bio-Tek, Norcross, GA, USA) according to supplier recommendations. M-MLV Reverse Transcriptase (Life Technologies) and random hexamers (Life Technologies)

were used for the reverse transcription of RNA (1 µg) to cDNA. Gene expression was determined using the $\Delta\Delta\text{CT}$ method (TaqMan user's manual. User Bulletin no. 2; Applied Biosystems). The concentration of mRNA was reported as arbitrary units.

2.9. Statistical Analysis

The statistical evaluation was carried out using GraphPad Prism (8.0.2, 2019, La Jolla, San Diego, CA, USA). Firstly, the data distribution and homoscedasticity were studied in order to apply a parametric or nonparametric test. If a normal distribution and homoscedasticity were obtained, an ANOVA test was carried out to compare the groups. If these prerequisites were not achieved, a Kruskal–Wallis test was applied. The significance level (α) was 5% in all cases.

3. Results and Discussion

3.1. Freeze Drying

Freeze drying is a stabilization process in which water is extracted by the sublimation of ice at controlled temperatures and pressures. It is a complex process that requires a good understanding of the product characteristics. In order to obtain a redispersible product and protect the formulation from the freezing and lyophilization processes, different cryoprotectants are used.

Mannitol, trehalose, and sucrose are three of the most commonly used excipients for protecting the sample during the lyophilization process. They have a cryoprotective and lyoprotective effect. Their ability to form hydrogen bonds around the samples creates an amorphous matrix and allows the aqueous structure to be maintained after the dehydration process during primary and secondary drying [20]. Mannitol is also widely used as a bulking agent, as it provides mechanical support and improves the appearance of the formulation once lyophilized [21].

The type and concentration of cryoprotectant used were based on results from the literature. Several authors concluded that high concentrations of cryoprotectant could cause nanoparticle agglomeration. Almalik et al. investigated the effect of different cryoprotectants (including sucrose, trehalose, and mannitol) at different concentrations (from 5% to 50% *w/w*) on the physicochemical characteristics of different polymeric nanoparticles. It was observed that trehalose and sucrose adequately protected at all concentrations and provided the lowest polydispersity index results [22]. Bonaccorso et al. studied the effect of sucrose at different concentrations (from 0% to 5%) during the lyophilization of Poly-Lactic-co-Glycolic-Acid-Polyethylene-Glycol nanoparticles. The lowest hydrodynamic diameter after redispersing the lyophilized nanoparticles was obtained using the 5% *w/w* sucrose concentration [23]. Kannan et al. determined that a 1:3 ratio was adequate to obtain a protective effect during nanoparticle lyophilization and to minimize active ingredient leakage [24]. In our study, the recommended cryoprotectant concentration was between 6% and 7% of cryoprotectant. Therefore, low cryoprotectant concentrations (<6% *w/w*) were ruled out, since a lower ratio could cause an increase of DEX leakage. In addition, a high concentration of sugars increases the formulation stickiness, which could lead into user rejection due to the lack of cosmetic attributes, considering a topical administration. The sensorial properties of the formulations are growing as an important fact in formulation development because they could determine the patient therapeutic compliance. Then, 6% *w/w* cryoprotectant concentration was chosen trying to obtain a balance between formulation cosmetic attribute (to assure patient compliance) and adequate nanoparticle properties.

Studies were conducted using FDM to compare five different formulations: placebo lipomers, DEX-lipomers, DEX-lipomers 6% sucrose, DEX-lipomers 6% trehalose, and DEX-lipomers 6% mannitol. The FDM system consists of an optical microscope coupled to a lyophilization system to freeze-dry and observe images. The system has a heater, a vacuum system, and a liquid nitrogen vapor cooling system. It allows one to analyze a small sample and control the lyophilization cycle conditions in order to later observe the different thermal events, such as the collapse temperature, sublimation front, crystallization, eutectic melting,

and nucleation temperature. FDM is the best technique to accurately determine the collapse temperature and thus design freeze-drying cycles that avoid these thermal events [25–27].

The collapse temperature is the temperature at which a glassy solute phase begins to soften, resulting in a loss of structural rigidity. In crystalline materials, when the collapse temperature is exceeded, the frozen sample melts (the melting back phenomenon), with consequent puffing [28].

In Figure 2, the different thermal events that occurred in the DEX-lipomers with no cryoprotectant droplet are shown. In Figure 2A, the sample of DEX-lipomers is in liquid state at $-13.6\text{ }^{\circ}\text{C}$. Upon reaching $-14.5\text{ }^{\circ}\text{C}$, the freezing process can be observed, and the sample becomes darker.

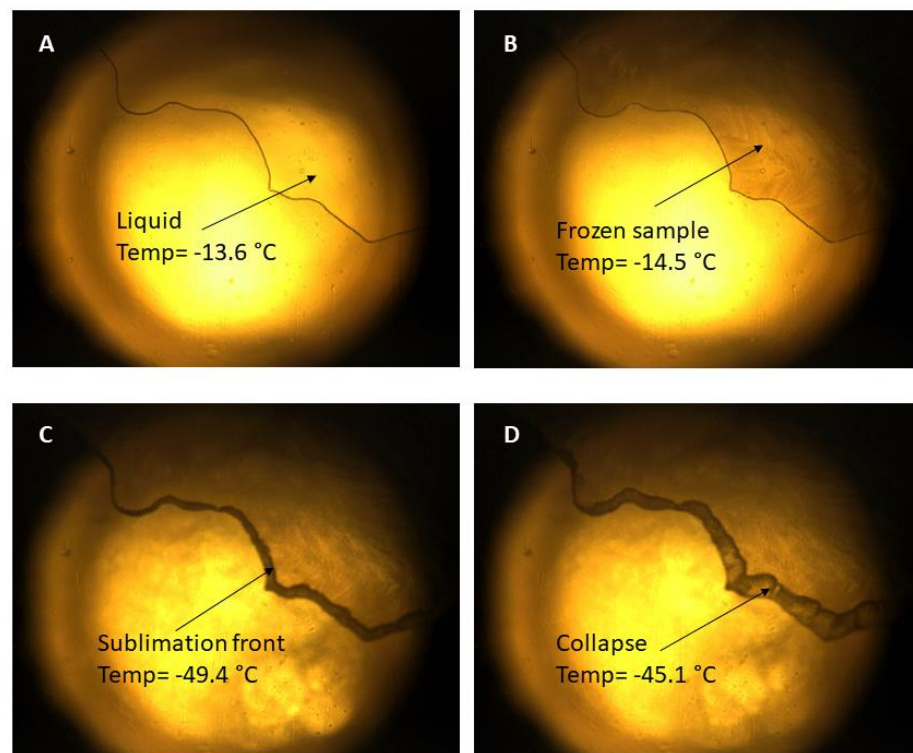


Figure 2. FDM pictures of a drop of DEX-lipomers (no cryoprotectant) showing different thermal events: (A) liquid sample; (B) freezing; (C) sublimation front; (D) collapse temperature.

Sublimation occurs at the interface between the frozen and dry layers, which is called the sublimation front. The black band that borders the sample (Figure 2C) is the sublimation front, which advances as the temperature rises. At approximately $-45\text{ }^{\circ}\text{C}$, we begin to observe small drops (Figure 2C,D), which indicates the sample collapse temperature. The rest of the formulations (placebo lipomers, DEX-lipomers 6% sucrose, DEX-lipomers 6% trehalose, and DEX-lipomers 6% mannitol) showed similar results, with freezing temperatures of approximately $-15\text{ }^{\circ}\text{C}$ and collapse temperatures between -50 and $-40\text{ }^{\circ}\text{C}$. Videos of the FDM of the different samples are available in the Supplementary Material (video S1: FDM video of placebo lipomers, DEX-lipomers 6% sucrose, DEX-lipomers 6% trehalose, and DEX-lipomers 6% mannitol).

After the FDM analysis, a lyophilization cycle (Table 3) was designed. It was necessary to adapt the results from the FDM (conducted with one drop of each formulation) to the real lyophilization process (with a higher formulation volume). For example, the mass and heat flux cause the most superficial part of the product to dry before the product in the bottom of the vial. It is necessary to adjust the heat and mass flow throughout the process to avoid unwanted events such as back melting, puffing, or collapse [29].

Table 3. Freeze-drying cycle conditions.

FD Cycle	Temperature	Time
Soak	10 °C	1 h
Freezing	−55 °C	4 h
Primary Drying	−30 °C	72 h
Secondary Drying ramp	−30 °C to 30 °C	4 h
Secondary Drying	30 °C	4 h

The first step in the cycle was to condition the vials at a temperature of 10 °C for 1 h. Regarding the freezing process, a cooling ramp at 0.27 °C/min was established for 4 h at atmospheric pressure with a temperature setpoint of −55 °C in order to remain at least 30 °C below the freezing temperature observed in FDM and to assure that the sample was completely frozen.

On the basis of the collapse temperature observed by FDM at low temperatures (approximately −45 °C), a thermal fluid temperature of −30 °C, combined with a pressure slightly below the collapse temperature, was established for primary drying.

During primary drying, ice was removed by sublimation using a vacuum. As the sublimation front advanced to the base of the vial, an almost dry product was obtained. After primary drying, there was still around 10% of aqueous residues, which were eliminated by desorption during secondary drying [30]. A temperature ramp was performed to 30 °C at 0.25 °C/min for 4 h, and it was maintained at 30 °C for another 4 h at the minimum pressure achievable with the equipment.

3.2. Physicochemical Characterization before and after Freeze Drying

After lyophilization, the physicochemical characteristics of DEX-lipomers were studied and compared with the characteristics obtained before the lyophilization process.

As it can be seen in Table 4, there were no significant differences ($p > 0.05$) as regards the lipomer properties (size, PDI, Z-pot and EE) before lyophilization, with respect to the cryoprotectant employed. The EE before FD was the same for all formulations, because the cryoprotectants were added after nanoparticle production. After the FD process, significant differences were observed, mainly in particle size, when nanoparticles were reconstituted in water. According to the obtained particle size after lyophilization, sucrose DEX-lipomers were selected for further experiments, as they were characterized by the lowest hydrodynamic diameter.

Table 4. Particle size, polydispersion (PDI), zeta potential, and encapsulation efficiency (EE) of nanoparticles before and after lyophilization with different cryoprotectants.

Formulation	Before Freeze Drying				After Freeze Drying			
	Hydrodynamic Diameter (nm)	PDI	Z-Pot (mV)	EE (%)	Hydrodynamic Diameter (nm)	PDI	Z-Pot (mV)	EE (%)
DEX-lipomers (no cryo)	185.23 ± 5.24	0.360 ± 0.019	39.0 ± 0.1	98.60 ± 0.01	1850.00 ± 188.75	0.313 ± 0.051	35.9 ± 2.0	98.94 ± 0.01
DEX-lipomers (trehalose 6%)	186.87 ± 2.68	0.361 ± 0.015	36.3 ± 0.4		446.70 ± 3.21	0.355 ± 0.013	34.3 ± 0.5	98.97 ± 0.01
DEX-lipomers (sucrose 6%)	185.67 ± 4.92	0.349 ± 0.016	37.3 ± 0.5		374.33 ± 7.60	0.229 ± 0.011	34.7 ± 0.4	98.87 ± 0.01
DEX-lipomers (mannitol 6%)	183.97 ± 1.27	0.334 ± 0.008	37.4 ± 0.4		749.53 ± 26.49	0.435 ± 0.013	34.9 ± 1.7	94.63 ± 6.22

Figure 3B shows the TEM ultrastructure of nanoparticles after the freeze-drying (FD) process. Similar to the non-FD particles (Figure 3A, taken from Pena-Rodriguez et al. [7]), a dark area corresponding to the polymer shell and an internal bright area corresponding to the lipids could be observed. In addition, the particle size observed in the TEM analysis corresponds to the diameter observed in the DLS analysis (Table 4), which is larger than

that seen in the non-FD-particles. Regarding the internal structure of the particles, in the non-FD formulation, small oil droplets in the polymer matrix can be observed, whereas in the FD particles, a continuous oil structure can be seen, with no isolated droplets within the nanoparticle core. A possible explanation for the size increase and the modification of the internal structure is the crystallization of the oil droplets (miglyol melting point of approximately $-12\text{ }^{\circ}\text{C}$) within the nanoparticle structure. Choi et al. [15] evaluated the effect of FD on polycaprolactone nanoparticles with an oil core. They concluded that the crystallization of miglyol caused a nanoparticle leak and the modification of their structure. They recommended slow cooling during FD to reduce the crystal size in the oil core. The FD was carried out at a slow cooling rate to reduce the oil crystal growth as suggested. Despite an increase in particle size being observed, nanoparticle damage (Figure 3B) and drug leakage (this can be seen in the high encapsulation efficiency in Table 4) were not observed, which was possibly due to the relatively low concentration of oil inside the polymer matrix.

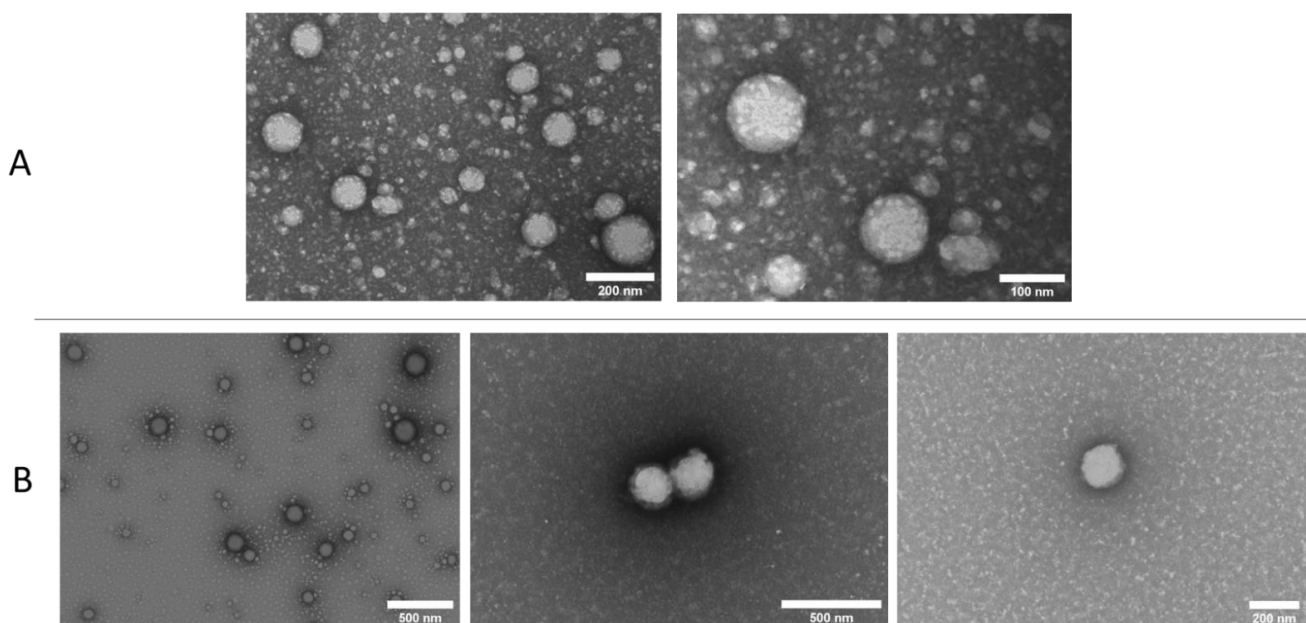


Figure 3. TEM picture of lipomers after negative staining with uranyl acetate. Panel (A) corresponds to non-FD lipomers (image reproduced from [7], MDPI, 2021). Panel (B) corresponds to FD lipomers.

DSC is an interesting tool for analyzing polymer–drug interactions. It allows one to demonstrate whether the polymer and drug are molecularly dispersed.

Figure 4 shows the thermograms of pure DEX (red curve), non-FD DEX-lipomers (blue curve), and FD DEX-lipomers (green curve). When comparing non-FD DEX-lipomers and pure DEX, it can be seen that the endothermic peak at $271.47\text{ }^{\circ}\text{C}$, corresponding to the fusion of DEX, is not present in the thermogram of lipomers. This indicates that the drug is in a noncrystalline state encapsulated within the polymer–lipid matrix of the nanoparticles, corroborating the results obtained by ultrafiltration with amicon and quantification in HPLC (Table 4).

The endothermic peak at $106.21\text{ }^{\circ}\text{C}$ in the non-FD formulation corresponds to water evaporation. The absence of the water evaporation peak in the FD DEX-lipomers curve shows that the chosen lyophilization cycle was adequate and that it was possible to completely sublime the water and avoid the presence of water residues [31]. The endothermic peak at $187.82\text{ }^{\circ}\text{C}$ shows the melting of the sucrose. The FD DEX-lipomer curve ends at $200\text{ }^{\circ}\text{C}$ so that sucrose thermal decomposition at $220\text{ }^{\circ}\text{C}$ was avoided.

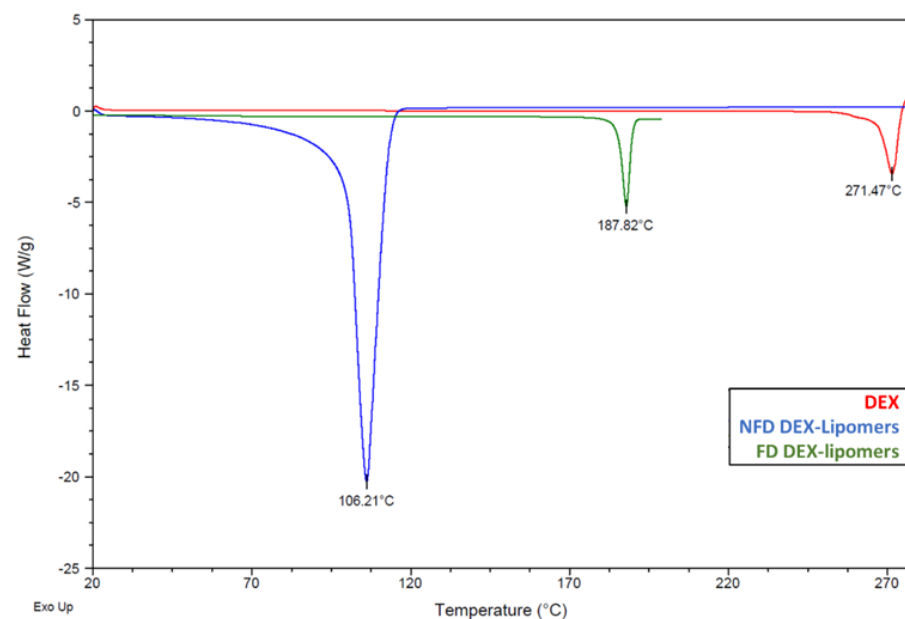


Figure 4. DSC thermogram of non-FD DEX-lipomers (blue curve), FD DEX-lipomers (green curve), and DEX (red curve).

3.3. Gel Formulations Rheology Studies

The incorporation of nanoformulations to cream or gel-type formulations is a common approach to improve certain cosmetic properties (e.g., spreadability, emolency); however, the manner in which they affect the microstructure of the formula has been scarcely studied.

Figure 5 shows the thixotropic behavior of the tested formulations. Placebo hydrogel exhibited a low hysteresis loop (area 1.278 ± 0.82), and the sample required a short time to recover its initial structure after the end of the shear stress application. The same characteristics were observed in a DEX hydrogel but with a lower thixotropic area (0.79 ± 0.05). When DEX-lipomers were loaded in the hydrogel, the rheology profile changed, and thixotropy was only observed at low shear rates and disappeared at shear rates of around 5 s^{-1} (area 0.92 ± 0.38). In addition, when shear stress ended, the internal structure did not completely recover, probably because more time was required for this to occur. To ascertain the rheology behavior, experimental data were fit to different equations. The equation costs are shown in Table 5. The lower cost represents the best fit.

Table 5. Rheological model fitting of hydrogel placebo, dexamethasone hydrogel, and freeze-dried dexamethasone lipomers hydrogel.

Rheological Model	Hydrogel Placebo (Cost)	FD-DEX-Lipomers Hydrogel (Cost)	DEX Hydrogel (Cost)
Newton	904.563	137.743	768.095
Bingham	59.985	19.360	44.060
Ostwald–de Waele	23.138	0.665	13.814
Herschel–Bulkley	2.721	0.656	3.372
Casson	4.952	0.791	4.883
Cross	2.080	0.142	2.529

The Cross equation is a versatile equation that is able to estimate different models that converge in more simple models based on different assumptions. Although it usually improves model fitting, this equation contained four parameters, which caused overparameterization. The model that best fit the experimental data of three formulations is the Herschel–Bulkley equation, which is usually employed to describe the rheological behavior of pseudoplastic material with yield stress values [32].

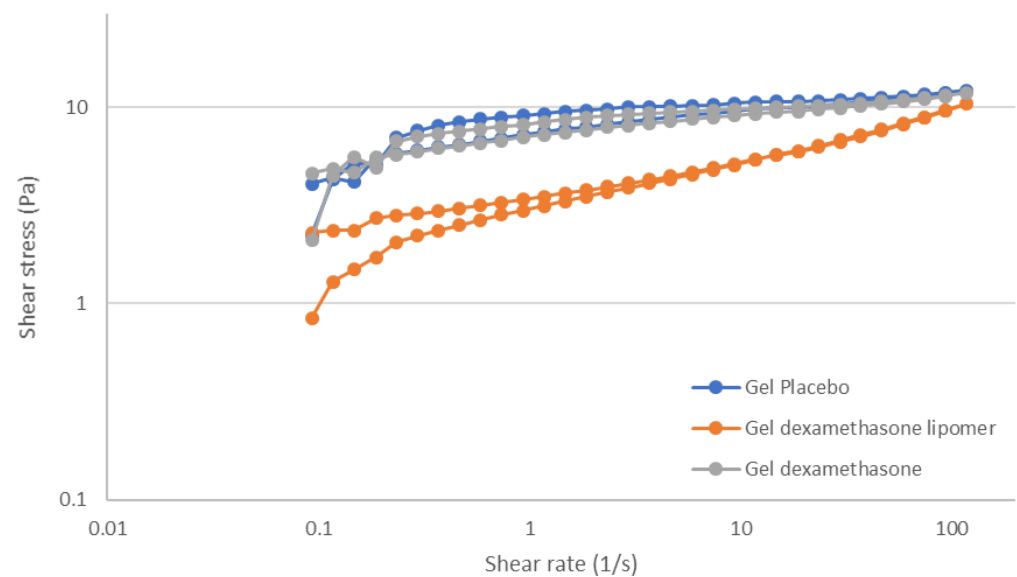


Figure 5. Shear stress vs. shear rate curves of the hydrogel formulations.

Table 6 shows the Herschel–Bulkley equation parameters of the hydrogel placebo, DEX-lipomers hydrogel, and DEX hydrogel. A minimal level of stress (τ_0) was required to start the flow, below which the value the formulation acted like a solid. The flow behavior changed when lipomers were loaded into the hydrogel. Yield stress was almost null. A similar cost function value was also observed for the Herschel–Bulkley and Ostwald–de Waele models (which is the same model but without yield stress). The n value was lower than 1 in all cases, which represents a pseudoplastic profile. This profile was less predominant in the DEX-lipomer hydrogel, followed by the DEX hydrogel.

Table 6. Rheological parameters of the Herschel–Bulkley equation of hydrogel placebo, DEX hydrogel, and FD DEX-lipomers hydrogel (mean \pm standard deviation). (*) denoted statistical differences $p < 0.05$.

Herschel–Bulkley Equation Parameter	Hydrogel Placebo	DEX-Lipomers Hydrogel	DEX Hydrogel
τ_0 (Pa)	11.312 \pm 1.990	−0.120 \pm 0.250 *	11.283 \pm 0.189
K	−2.040 \pm 0.957	2.971 \pm 0.523 *	−2.935 \pm 0.196
n	−0.611 \pm 0.076 *	0.259 \pm 0.019 *	−0.411 \pm 0.025 *

Figure 6 shows the viscoelasticity parameters (storage modulus: G' and loss modulus: G''), related with the product microstructure.

In addition, Table 7 shows the mean and standard deviation of G' , G'' , G^* (complex modulus) and $\tan \delta$ (tangent of the phase angle). There were no statistical differences between the placebo hydrogel and DEX hydrogel for any parameter. The formulations behaved as solid-like products ($G' > G''$), and when DEX was loaded into the gel, no alteration in the microstructure was observed. When the DEX-lipomers were loaded in the gel, the viscoelastic properties were significantly modified. The value of both storage and complex moduli decreased. Furthermore, the linearity of G' decreased as the strain increased (around 0.07 Pa). The formulation maintained its solid-like properties ($G' > G''$) but reduced compared with the hydrogel without nanoparticles. Moreover, the loss modulus exhibited a slight increase compared with the formulations with no lipomers.

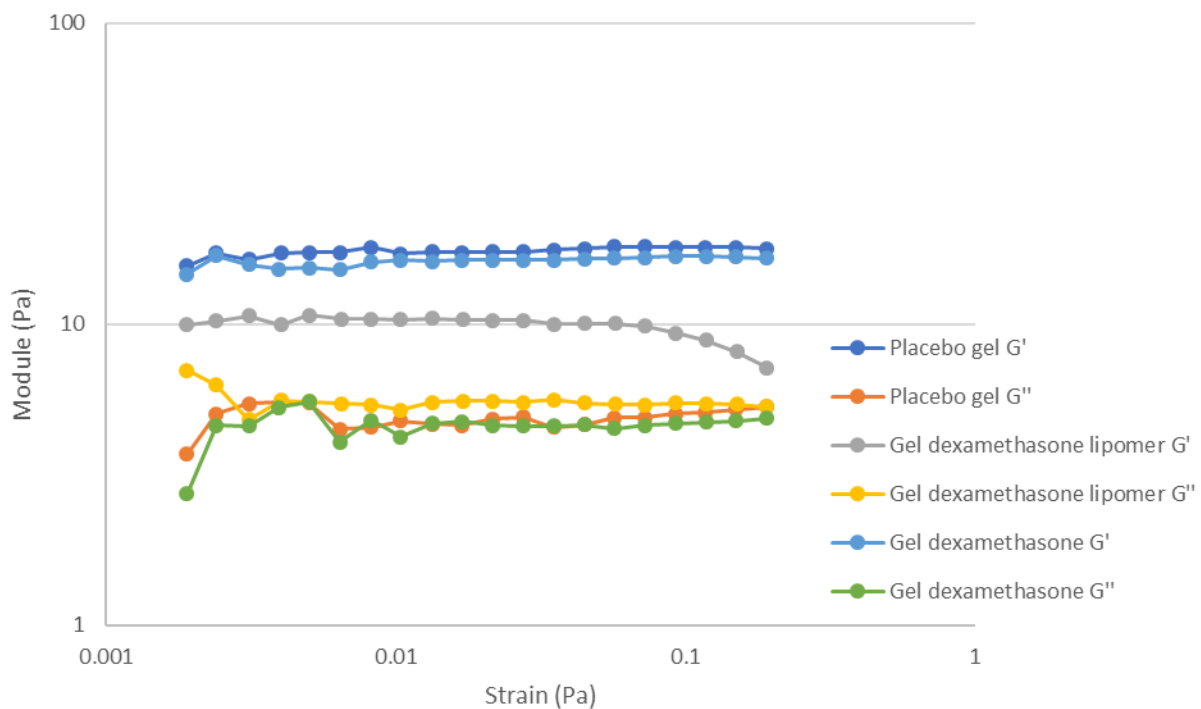


Figure 6. Storage and loss modulus of the hydrogel formulations.

Table 7. Viscoelasticity parameters of hydrogel placebo, dexamethasone hydrogel, and freeze-dried dexamethasone lipomers hydrogel (mean \pm standard deviation (SD)). (*) denoted statistical differences $p < 0.05$.

Parameter	Formulation	Mean \pm SD
G'	Placebo gel	17.48 ± 0.44 Pa
	Gel DEX-lipomer	9.97 ± 0.35 Pa (*)
	Gel DEX	16.19 ± 0.13 Pa (*)
G''	Placebo gel	4.88 ± 0.09 Pa
	Gel DEX-lipomer	5.55 ± 0.24 Pa (*)
	Gel DEX	4.60 ± 0.03 Pa
G^*	Placebo gel	18.16 ± 0.43 Pa
	Gel DEX-lipomer	11.35 ± 0.42 Pa (*)
	Gel DEX	16.84 ± 0.12 Pa
$\tan \delta$	Placebo gel	$15.6 \pm 0.64^\circ$
	Gel DEX-lipomer	$29.4 \pm 0.09^\circ$ (*)
	Gel DEX	$15.8 \pm 0.25^\circ$

DEX-lipomers had a positive z-potential (+39 mV) and could interact with the negatively charged xanthan gum polymer chain, reducing the intra- and interpolymer chain repulsion in the formulations with no lipomers. This caused the reduction in G' and G^* . Although there were statistical differences in G'' , the magnitude of the differences was low, and the interactions between the polymer/lipomers with the continuous phase (water) were essentially preserved. These interpolymer modifications when lipomers were loaded into the hydrogel may also explain the previously observed decrease in yield stress and the higher value of exponent “ n ” in the Herschel–Bulkley equation.

3.4. In Vitro Release Tests

To study the impact of FD and the consequent modification of the lipomer structure on the release profile, an in vitro release test was performed under the same conditions as previously stated [7]. In addition, the release profile of the freeze-dried lipomer-loaded hydrogel was analyzed.

Figure 7 shows the release patterns of the tested formulations. The release profile of the nanosystems before FD was previously studied [7] and is included in the figure for ease of understanding.

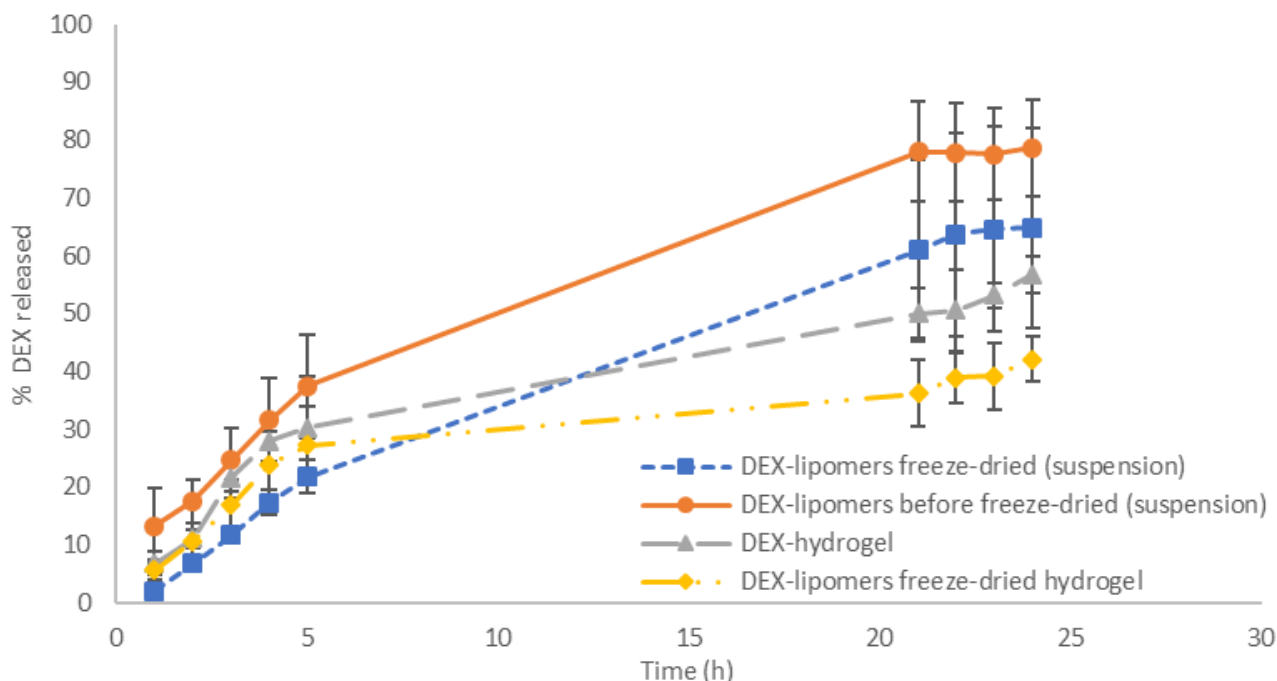


Figure 7. DEX release percentages of the tested formulations ($n = 6$). Results shown mean and standard deviation values.

Table 8 shows that the FD process significantly modified the release pattern of DEX from the delivery system. The maximum percentage of DEX released decreased by approximately 14% compared with non-FD particles. Although the release equation followed a Weibull function as was the case before FD, the exponent β increased (1.008 vs. 0.82). This indicates that the release mechanism changed from a combined release to a Fickian diffusion mechanism. This may be explained by the modification of the internal structure and/or the increase in particle size of the nanoparticles observed in the TEM analysis.

The free DEX hydrogel followed the Higuchi equation, which is typically used to describe the behavior of semisolid formulations in which the drug release follows a pseudo-steady state [33]. When FD nanoparticles were included in the hydrogel, DEX release was slower. This was expected due to the increase in viscosity of the formulation as a result of the addition of xanthan gum. The higher viscosity usually reduces the drug release rate. In this case, the drug release followed a Fickian diffusion pattern, which was confirmed by the exponent n of the Korsmeyer–Peppas equation ($n < 0.43$) and the value of β in the Weibull equation ($\beta < 0.75$) [7]. This modification was probably caused by the interaction between the positive charged lipomers and the anionic polymer chain. This reduced the formulation microstructure, as was described in the rheological characterization, and it reduced the effect of the polymer matrix on the DEX release mechanism, which is very similar to the release mechanism of the FD nanoparticles not included in the hydrogel.

Table 8. Results of model fitting of DEX drug release for the prepared formulations. AIC in bold corresponds to the model that best fit the experimental data. “*n*” corresponds to the release exponent of Korsmeyer–Peppas (KP) equation.

Formulation	Model	AIC	Parameters	Value
Freeze-dried DEX-lipomers	First order	28.59	k (h^{-1})	0.046
	Higuchi	57.87	k_H ($\% \text{h}^{-1/2}$)	12.579
	Korsmeyer–Peppas	35.48	n	0.800
			k_{KP} ($\% \text{h}^{-n}$)	5.261
	Weibull	28.57	t_d (h)	22.75
		β	1.008	
Freeze-dried DEX-lipomers hydrogel	First order	44.988	k (h^{-1})	0.155
	Higuchi	46.539	k_H ($\% \text{h}^{-1/2}$)	44.196
	Korsmeyer–Peppas	49.847	n	0.383
			k_{KP} ($\% \text{h}^{-n}$)	10.960
	Weibull	48.870	t_d (h)	11.960
		β	0.601	
DEX hydrogel	First order	48.877	k (h^{-1})	0.133
	Higuchi	44.710	k_H ($\% \text{h}^{-1/2}$)	11.277
	Korsmeyer–Peppas	52.096	n	0.590
			k_{KP} ($\% \text{h}^{-n}$)	9.060
	Weibull	48.484	t_d (h)	10.965
		β	0.700	

3.5. In Vitro Permeation Tests

An in vitro permeation test was performed with dermatomed pig skin on fresh non-FD DEX-lipomers, FD DEX-lipomers, hydrogel-loaded FD DEX-lipomers, and free DEX hydrogel.

Figure 8 shows the permeation profile of the tested formulations. No concentrations were found in the receptor compartment in the Franz cells in the hydrogel formulations (free DEX hydrogel and the FD-lipomer-loaded hydrogel). This was probably due to the slower drug release observed (see Section 3.3) as the formulation viscosity increased. The drug permeation in the nanoparticle suspension showed a similar pattern as the previously studied drug release, i.e., non-FD nanoparticles had a higher release rate and a higher skin absorption, whereas the FD formulation exhibited a lower release and permeation. Therefore, the drug release rate is the limiting factor for skin permeation. It is possible that the lipomer structure alteration throughout the FD process and/or the increase in particle size had a dramatic impact on the biopharmaceutical behavior.

Additionally, the permeation parameters were estimated (Table 9). No statistical differences were found between formulations, for K_p or J_{sup} . Although there were differences in the maximum permeated drug concentration, the slope of both formulations was similar, and the same transdermal flux was obtained. The significance of P_1 (diffusion-related parameter) was borderline ($p = 0.08$), which was probably related with the differences in drug release; however, the power of the statistical test was not enough to discriminate between both formulations. Clear statistical differences were found in lag time and related parameters (diffusion related parameter, P_2). The FD process increased the lag time, which was probably caused by the increase in particle size (double that of non-FD particles) and the modification of nanoparticle structure. The greater particle size can affect the number of nanoparticles that are stored in the hair follicles and may reduce the packaging of the particles in the skin surface, i.e., the greater the size, the lower the

surface-to-volume ratio. The modification of the lag time brings about the modification of P_2 (the partitioning-related parameter), which is reduced compared with the non-FD formulation. This could be caused by the reduced amount of intimate contact between both systems (due to the increase in particle size and the reduction in the surface-to-volume ratio), which may lead to a decrease in P_2 . Another possibility is that the cryoprotectant modifies the formulation/skin partitioning, because these compounds can form hydrogen bonds with the nanoparticle surface and alter the interaction with the skin.

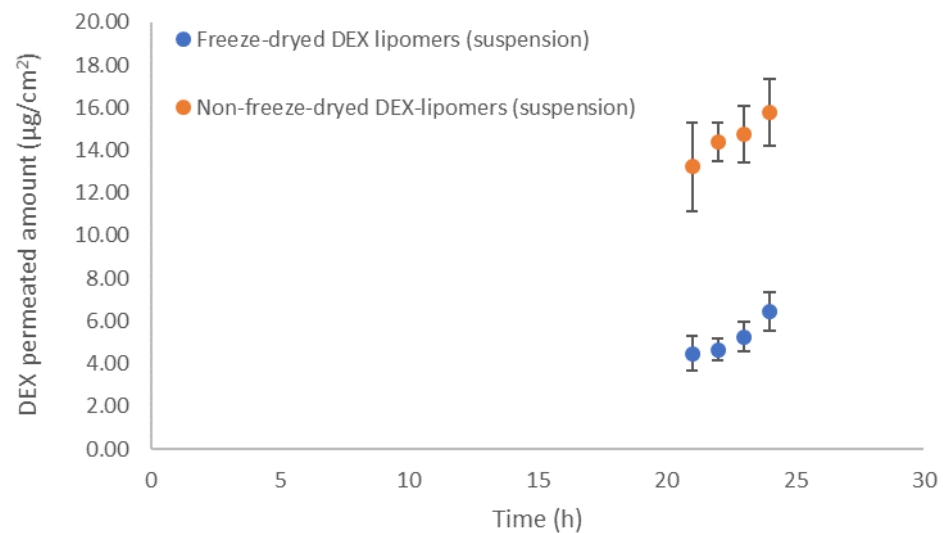


Figure 8. Transdermal DEX (lipomers before and after lyophilization) profile in dermatomed pig skin ($n = 6$). The results show the mean and standard deviation.

Table 9. Permeation parameters of nanoparticles before and after lyophilization.

Parameter	Non-Freeze-Drying DEX-Lipomers (Mean \pm SD)	Freeze-Drying DEX-Lipomers (Mean \pm SD)
J_{sup} ($\mu\text{g}/\text{h}\cdot\text{cm}^2$)	0.4759 ± 0.1123	0.3789 ± 0.2093
K_p (cm/h)	$7.9316 \times 10^{-5} \pm 1.900 \times 10^{-5}$	$6.3148 \times 10^{-5} \pm 5.156 \times 10^{-5}$
P_2 (1/h)	0.0385 ± 0.0011	0.0117 ± 0.0039 (*)
P_1 (cm)	0.0020 ± 0.0006	0.0073 ± 0.0067
t_{lag} (h)	4.213 ± 0.064	11.978 ± 4.776 (*)

(*) statistical differences $p < 0.05$.

3.6. Cytotoxicity and Anti-TNF α Efficacy

Human-transformed normal epidermal keratinocytes (HEK001) and human immortalized keratinocytes (HaCaT) were chosen to determine the cytotoxic effect of FD DEX-lipomers compared to the non-FD DEX-lipomers. Non-loaded non-FD lipomers with sucrose (sucrose) were tested as controls. HEK001 cell viability profiles exhibited the same pattern as that previously observed in non-FD DEX-lipomers [7] (Figure 9A). However, the results showed less cytotoxic effect related to FD DEX-lipomers at the lowest dilutions (indicated by the inverse dilution factors 5000 and 25,000), which correspond to the DEX concentrations of 5 and 1 μM . Lyophilization seems to confer a little protection to cytotoxicity in HEK001 cells. The cytotoxicity of the tested non-FD lipomers was attributed to the benzalkonium chloride (BAK), as was previously studied by our research group. The zeta potential of the nanoparticles after lyophilization was a little lower (although not significantly) compared with the non-FD particles. This was probably caused by the strong interaction between sucrose and the positively charged BAK after lyophilization. This could reduce the toxicity of FD lipomers. In contrast, no cytotoxic effects were detected in HaCaT cells after any of the treatments (Figure 9B). The differences in the cytotoxic profile

of both cell lines were possibly due to the immortalization procedure, which can modify the cell sensibility to xenobiotics.

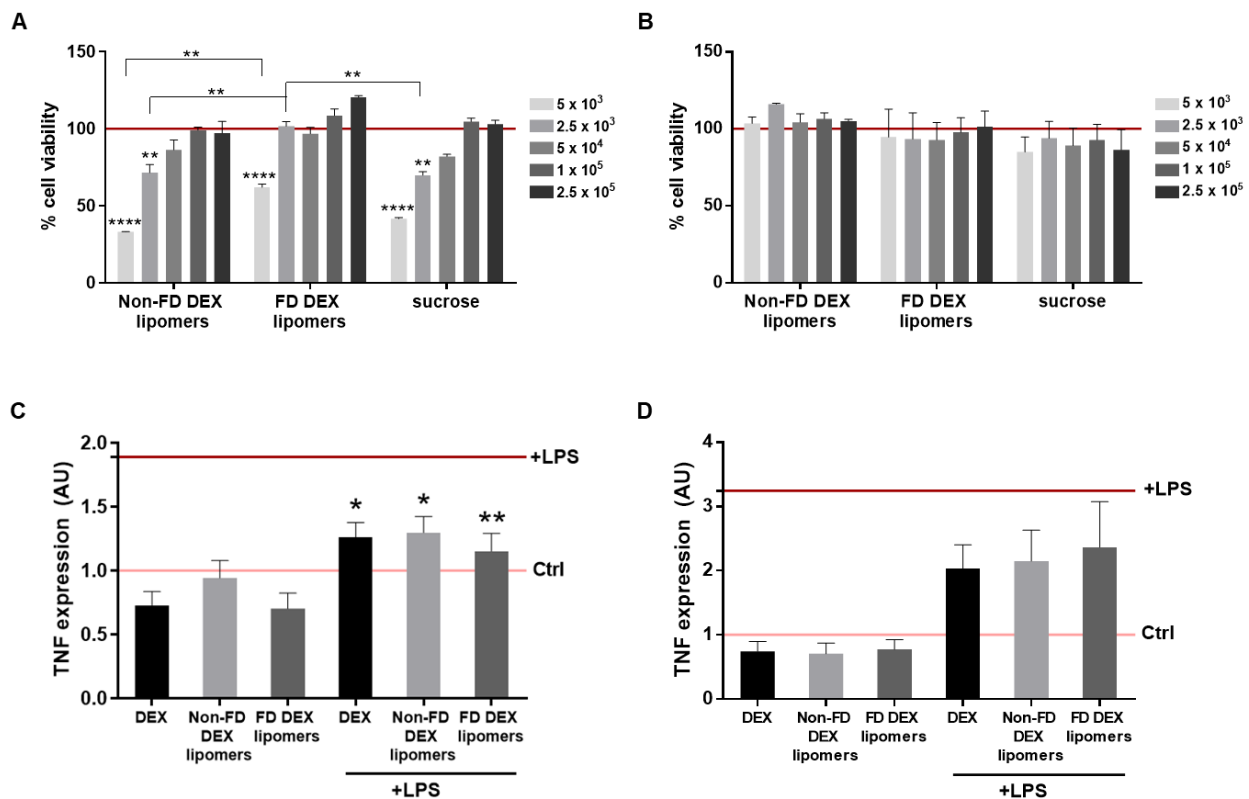


Figure 9. Cytotoxicity and anti-TNF α efficacy studies in HEK001 (A,C) and HaCaT cells (B,D). (A,B) Cell viability analyzed by MTT. The indicated numbers represent the inverse dilution factors, referring to the synthesized lipomers. Dilution factors for DEX-loaded lipomers correspond to concentrations of 5, 1, 0.5, 0.25, and 0.1 μ M of DEX. Data are represented as the mean \pm SEM ($n = 3$) of the cell viability percentage, referring to untreated controls (horizontal lane). Statistical significance was assessed by two-way ANOVA ** $p < 0.01$; **** $p < 0.0001$. (C,D) TNF α mRNA expression was determined after a 24 h treatment of free DEX 0.1 μ M (black), non-FD DEX-lipomers (gray), or FD DEX-lipomers (dark gray), without (left) or with (right) a 1 h pretreatment with LPS (10 μ g/mL). TNF α expression is represented as the mean \pm SEM ($n = 4$ HEK001; $n = 3$ HaCaT); horizontal pink and red lanes represent TNF α expression under control and LPS conditions, respectively. Statistical significance was evaluated by one-way ANOVA compared to LPS; * $p < 0.05$, ** $p < 0.01$.

To ascertain the *in vitro* anti-inflammatory efficacy of DEX-loaded lipomers, we selected the cytokine TNF α as a marker, considering its role in most inflammatory alterations, including those related to the skin such as alopecia areata [34,35]. The results showed an increase in TNF α mRNA expression, indicating an inflammatory induction after 10 μ g/mL of LPS treatment in HEK001 and HaCaT cell lines (Figure 9C,D). Given the cytotoxic effect at the highest doses of lipomers in HEK001, we next chose the lower dose assay for the anti-TNF α efficacy assays in both cell lines to avoid harmful consequences. Thus, an equivalent to 0.1 μ M of DEX was the lipomer test condition, and the same amount of free DEX was used as control. TNF α expression decreased in both cell lines after treatment with free DEX, with non-FD DEX, and with FD DEX-lipomers (Figure 9C,D), although this difference was not significant in HaCaT cells (Figure 9D). Moreover, no significant differences were observed in the three conditions as regards the anti-TNF α effect of dexamethasone.

4. Conclusions

Previously developed DEX-lipomers composed of ethyl cellulose and medium chain triglycerides were freeze-dried. The lyophilization process significantly modified the nanoparticle internal structure and size, which was probably caused by the crystallization of

the oil core. This significantly modified the drug release characteristics and the permeation profile of dermatomed pig skin compared with the non-freeze-dried particles. Xanthan gum hydrogel was loaded with DEX-lipomers, which significantly changed the rheological behavior compared with the placebo (free DEX) hydrogel. Regarding the in vitro anti-TNF α analyses, no significant differences were observed between the freeze-dried and the non-freeze-dried particles. The most interesting biopharmaceutical properties were achieved with the non-freeze-dried formulation in suspension. An adequate balance between stability, efficacy, patient texture preference, and biopharmaceutical properties must be established to obtain a successful drug delivery system.

Supplementary Materials: The following are available online at <https://www.mdpi.com/article/10.3390/pharmaceutics13081322/s1>, Video S1: Freeze-Drying Microscopy (FDM) video of placebo lipomers, DEX-lipomers 6% sucrose, DEX-lipomers 6% trehalose, and DEX-lipomers 6% mannitol.

Author Contributions: Conceptualization, E.P.-R., F.F.-C. and S.P.-T.; methodology, E.P.-R., F.F.-C., S.P.-T., A.M.-V. and L.G.-V.; software, E.P.-R., A.M.-V. and L.G.-V.; formal analysis, E.P.-R., F.F.-C., S.P.-T., A.M.-V. and L.G.-V.; investigation, E.P.-R., F.F.-C., S.P.-T., A.M.-V. and L.G.-V.; resources, F.F.-C. and S.P.-T.; data curation, E.P.-R., F.F.-C., S.P.-T., A.M.-V. and L.G.-V.; writing—original draft preparation, E.P.-R., F.F.-C. and S.P.-T.; writing—review and editing, E.P.-R., F.F.-C. and S.P.-T.; supervision, F.F.-C. and S.P.-T.; project administration, F.F.-C. and S.P.-T.; funding acquisition, F.F.-C. and S.P.-T. All authors have read and agreed to the published version of the manuscript.

Funding: This research received funding from the Generalitat de Catalunya Industrial Doctorate program of the candidate Eloy Pena Rodríguez, expedient number 2019 DI 1989691.

Institutional Review Board Statement: Not applicable.

Informed Consent Statement: Not applicable.

Data Availability Statement: The data presented in this study are available on request from the corresponding author. The data are not publicly available due to industrial property restrictions.

Acknowledgments: We thank Manuel Pena-Rodriguez for his collaboration in the rheological model fitting. We also give thanks to Anna Anglada, Laia Garcia Uceda, and Sasha Nikolic from the Center of Excellent of Lyophilization of Reig Jofre Laboratories for their support in the freeze-drying process. Furthermore, we thank Trond Aasen from the research institute of Vall d'Hebron (Barcelona) for sharing the HaCaT cells.

Conflicts of Interest: F.F.-C. and E.P.-R. are employees of Reig Jofre. The authors are not involved in any commercial or marketing activities of the developed product. Other authors declare no conflicts of interest. The funders and Reig Jofre had no role in the design of the study; in the collection, analyses, or interpretation of data; in the writing of the manuscript; or in the decision to publish the results.

References

1. Kaul, S.; Gulati, N.; Verma, D.; Mukherjee, S.; Nagaich, U. Role of Nanotechnology in Cosmeceuticals: A Review of Recent Advances. *J. Pharm.* **2018**, *2018*, 420204. [[CrossRef](#)]
2. Fang, C.-L.; Aljuffali, I.A.; Li, Y.-C.; Fang, J.-Y. Delivery and targeting of nanoparticles into hair follicles. *Ther. Deliv.* **2014**, *5*, 991–1006. [[CrossRef](#)]
3. Wosicka, H.; Cal, K. Targeting to the hair follicles: Current status and potential. *J. Dermatol. Sci.* **2010**, *57*, 83–89. [[CrossRef](#)] [[PubMed](#)]
4. Juárez-Rendón, K.J.; Rivera Sánchez, G.; Reyes-López, M.Á.; García-Ortiz, J.E.; Bocanegra-García, V.; Guardiola-Avila, I.; Altamirano-García, M.L. Alopecia areata. Actualidad y perspectivas. *Arch. Argent. Pediatr.* **2017**, *115*, e404–e411. [[PubMed](#)]
5. Hordinsky, M.K. Overview of Alopecia Areata. *J. Investig. Dermatol. Symp. Proc.* **2013**, *16*, S13–S15. [[CrossRef](#)]
6. Lee, S.; Lee, W.-S. Management of alopecia areata: Updates and algorithmic approach. *J. Dermatol.* **2017**, *44*, 1199–1211. [[CrossRef](#)] [[PubMed](#)]
7. Pena-Rodríguez, E.; Lajarin-Reinares, M.; Mata-Ventosa, A.; Pérez-Torras, S.; Fernández-Campos, F. Dexamethasone-Loaded Lipomers: Development, Characterization, and Skin Biodistribution Studies. *Pharmaceutics* **2021**, *13*, 533. [[CrossRef](#)] [[PubMed](#)]
8. Abdelwahed, W.; Degobert, G.; Stainmesse, S.; Fessi, H. Freeze-drying of nanoparticles: Formulation, process and storage considerations. *Adv. Drug Deliv. Rev.* **2006**, *58*, 1688–1713. [[CrossRef](#)] [[PubMed](#)]

9. Mohammady, M.; Mohammadi, Y.; Yousefi, G. Freeze-Drying of Pharmaceutical and Nutraceutical Nanoparticles: The Effects of Formulation and Technique Parameters on Nanoparticles Characteristics. *J. Pharm. Sci.* **2020**, *109*, 3235–3247. [[CrossRef](#)]
10. Holzer, M.; Vogel, V.; Mäntele, W.; Schwartz, D.; Haase, W.; Langer, K. Physico-chemical characterisation of PLGA nanoparticles after freeze-drying and storage. *Eur. J. Pharm. Biopharm.* **2009**, *72*, 428–437. [[CrossRef](#)]
11. Fonte, P.; Soares, S.; Sousa, F.; Costa, A.M.M.M.; Seabra, V.; Reis, S.; Sarmiento, B. Stability Study Perspective of the Effect of Freeze-Drying Using Cryoprotectants on the Structure of Insulin Loaded into PLGA Nanoparticles. *Biomacromolecules* **2014**, *15*, 3753–3765. [[CrossRef](#)] [[PubMed](#)]
12. Srihaphon, K.; Lamlerthon, S.; Pitaksuteepong, T. Influence of stabilizers and cryoprotectants on the characteristics of freeze-dried plga nanoparticles containing morus alba stem extract. *Songklanakarin J. Sci. Technol.* **2021**, *43*, 72–79.
13. Gajra, B.; Dalwadi, C.; Patel, R. Formulation and optimization of itraconazole polymeric lipid hybrid nanoparticles (Lipomer) using box behnken design. *DARU J. Pharm. Sci.* **2015**, *23*, 1–15. [[CrossRef](#)] [[PubMed](#)]
14. Ramesh, G.; Sathesh Kumar, S. Lyophilization and stability study of noscapine-loaded polycaprolactone nanoparticles. *Drug Invent. Today* **2019**, *12*, 2516–2521.
15. Choi, M.J.; Briancon, S.; Andrieu, J.; Min, S.G.; Fessi, H. Effect of Freeze-Drying Process Conditions on the Stability of Nanoparticles. *Dry. Technol.* **2004**, *22*, 335–346. [[CrossRef](#)]
16. Pan-In, P.; Banlunara, W.; Chaichanawongsaroj, N.; Wanichwecharungruang, S. Ethyl cellulose nanoparticles: Clarithromycin encapsulation and eradication of *H. pylori*. *Carbohydr. Polym.* **2014**, *109*, 22–27. [[CrossRef](#)]
17. Mirabedini, S.; Dutil, L.; Farnood, R. Preparation and characterization of ethyl cellulose-based core-shell microcapsules containing plant oils. *Colloids Surf. A Physicochem. Eng. Asp.* **2012**, *394*, 74–84. [[CrossRef](#)]
18. Abd-Elrahman, M.I.; Ahmed, S.M. Thermal Degradation Kinetics and Geometrical Stability of D-Sucrose. *Int. J. Polym. Mater.* **2009**, *58*, 322–335. [[CrossRef](#)]
19. Zhang, Y.; Huo, M.; Zhou, J.; Zou, A.; Li, W.; Yao, C.; Xie, S. DDSolver: An Add-In Program for Modeling and Comparison of Drug Dissolution Profiles. *AAPS J.* **2010**, *12*, 263–271. [[CrossRef](#)]
20. Starciuc, T.; Malfait, B.; Danede, F.; Paccou, L.; Guinet, Y.; Correia, N.T.; Hedoux, A. Trehalose or Sucrose: Which of the Two Should be Used for Stabilizing Proteins in the Solid State? A Dilemma Investigated by In Situ Micro-Raman and Dielectric Relaxation Spectroscopies During and After Freeze-Drying. *J. Pharm. Sci.* **2020**, *109*, 496–504. [[CrossRef](#)]
21. Kumar, K.N.; Mallik, S.; Sarkar, K. Role of freeze-drying in the presence of mannitol on the echogenicity of echogenic liposomes. *J. Acoust. Soc. Am.* **2017**, *142*, 3670–3676. [[CrossRef](#)]
22. Almalik, A.; Alradwan, I.; Kalam, M.A.; Alshamsan, A. Effect of cryoprotection on particle size stability and preservation of chitosan nanoparticles with and without hyaluronate or alginate coating. *Saudi Pharm. J.* **2017**, *25*, 861–867. [[CrossRef](#)]
23. Bonaccorso, A.; Musumeci, T.; Carbone, C.; Vicari, L.; Lauro, M.R.; Puglisi, G. Revisiting the role of sucrose in PLGA-PEG nanocarrier for potential intranasal delivery. *Pharm. Dev. Technol.* **2017**, *23*, 265–274. [[CrossRef](#)]
24. Kannan, V.; Balabathula, P.; Thoma, L.A.; Wood, G.C. Effect of sucrose as a lyoprotectant on the integrity of paclitaxel-loaded liposomes during lyophilization. *J. Liposome Res.* **2014**, *25*, 270–278. [[CrossRef](#)]
25. Nail, S.L.; Jiang, S.; Chongprasert, S.; Knopp, S.A. Fundamentals of Freeze-Drying. *Pharm. Biotechnol.* **2002**, *14*, 281–360. [[CrossRef](#)]
26. Meister, E.; Sasić, S.; Gieseler, H. Freeze-Dry Microscopy: Impact of Nucleation Temperature and Excipient Concentration on Collapse Temperature Data. *AAPS PharmSciTech* **2009**, *10*, 582–588. [[CrossRef](#)]
27. Ward, K.R.; Matejtschuk, P. The use of microscopy, thermal analysis, and impedance measurements to establish critical formulation parameters for freeze-drying cycle development. In *Freeze-Drying/Lyophilization of Pharmaceutical and Biological Products*, 3rd ed.; CRC Press: London, UK, 2016; pp. 112–135. [[CrossRef](#)]
28. Meister, E.; Gieseler, H. Freeze-Dry Microscopy of Protein/Sugar Mixtures: Drying Behavior, Interpretation of Collapse Temperatures and a Comparison to Corresponding Glass Transition Data. *J. Pharm. Sci.* **2009**, *98*, 3072–3087. [[CrossRef](#)] [[PubMed](#)]
29. Pikal, M.J.; Shah, S. The collapse temperature in freeze drying: Dependence on measurement methodology and rate of water removal from the glassy phase. *Int. J. Pharm.* **1990**, *62*, 165–186. [[CrossRef](#)]
30. Pauline, M.D. *Chapter 11—Unit Operations, Bioprocess Engineering Principles*, 2nd ed.; Academic Press: Amsterdam, The Netherlands, 2013; pp. 445–595; ISBN 9780122208515. [[CrossRef](#)]
31. Talik, P.; Piwowarczyk, J.; Muszyńska, B.; Hubicka, U. DSC study of hydration and water-holding behaviour of cultured in vitro mycelium and naturally grown fruiting bodies of freeze-dried *Boletus badius*, *Agaricus bisporus* and *Cantharellus cibarius*. *J. Therm. Anal. Calorim.* **2021**, *143*, 3525–3532. [[CrossRef](#)]
32. Osswald, T.; Rudolph, N. Generalized Newtonian Fluid (GNF) Models. In *Polymer Rheology: Fundamentals and Applications*; Strohm, C., Ed.; Hanser Publications: München, Germany, 2014; pp. 59–99.
33. Fernández-Campos, F.; Obach, M.; Moreno, M.; García, A.; González, J. Pharmaceutical development of a generic corticoid semisolid formulation. *J. Drug Deliv. Sci. Technol.* **2017**, *42*, 227–236. [[CrossRef](#)]
34. Tauber, M.; Buche, S.; Reygagne, P.; Berthelot, J.-M.; Aubin, F.; Ghislain, P.-D.; Cohen, J.-D.; Coquerelle, P.; Goujon, E.; Jullien, D.; et al. Alopecia areata occurring during anti-TNF therapy: A national multicenter prospective study. *J. Am. Acad. Dermatol.* **2014**, *70*, 1146–1149. [[CrossRef](#)] [[PubMed](#)]
35. Pratt, C.H.; King, L.E.; Messenger, A.G.; Christiano, A.M.; Sundberg, J.P. Alopecia areata. *Nat. Rev. Dis. Primers* **2017**, *3*, 17011. [[CrossRef](#)]

Chapter 6. Nanostructured lipid carriers

Resumen

Se desarrollaron NLCs y mostraron ser unas de las nanoformulaciones más interesantes. Debido a su alto contenido en lípidos (hasta un 18% p/p), las NLCs permiten encapsular una mayor cantidad de compuestos hidrofóbicos en su interior, en comparación con las nanopartículas poliméricas o liposomas.

Se realizaron diseños de experimento de screening (DoE) y diseños de superficie de respuesta, y fue posible obtener un modelo predictivo preciso para el tamaño y el Pdl de las NLCs. También se realizó un escalado de las NLCs mediante un DoE con un procesador industrial de ultrasonidos y no se encontraron diferencias significativas entre el volumen de lote y el tamaño y Pdl de las NLCs. Esto significa que la escalabilidad de las NLCs es viable ya que el aumento del volumen del lote no afecta las propiedades de las NLCs. También fue posible obtener un modelo matemático para determinar la cantidad de energía de cavitación necesaria por L de lote (Ws/L) para obtener NLCs menores de 260 nm y monodispersas (Pdl<0.3).

Los NLCs mostraron un efecto significativo en cuanto al aumento de la absorción percutánea frente a un control de XXXXXXXXXX no encapsulado mediante IVPTs en piel de cerdo dermatomizada. Debido a su geometría y mayor rigidez en comparación con los liposomas, se cree que este tipo de nanopartículas se acumulan en los diferentes anejos cutáneos y folículos pilosos. En los estudios realizados mediante microscopía confocal de fluorescencia, no sólo se verificó el targeting folicular logrado con las NLCs, sino que también fue posible observar una acumulación en las glándulas sebáceas al marcar las NLCs con LRB. El fluoróforo C6 se encapsuló dentro de las NLC y se comprobó que la biodistribución cutánea de C6 y de las NLC marcadas con LRB fue diferente. Mientras que la C6 se acumuló en la epidermis y en las zonas más superficiales de la dermis y los folículos pilosos (aproximadamente hasta unos 400 µm de profundidad), las nanopartículas marcadas con LRB se acumularon en las zonas de las glándulas sebáceas y en las zonas más profundas de los folículos pilosos.

6.1. Introduction

The first generation of solid lipid nanoparticles was discovered in the early 1990s. These nanoparticles have several advantages, such as the lack of requirement of organic solvents, the promotion of absorption into different biological membranes and the high biocompatibility of the commonly used lipids. However, they also have limitations such as drug leakage during storage and a limited loading capacity due to the crystalline structure of the solid lipid.

In the 2000s, the next generation of lipid nanoparticles called nanostructured lipid carriers (NLCs) was developed. By adjusting the amount and ratio of solid to liquid lipids, the crystalline structure of the nanoparticles can be modified. The core of the NLCs is made up of an amorphous lipid structure instead of the crystalline one seen in solid lipid nanoparticles. Consequently, the loading capacity of these particles is improved, with decreased drug leakage during storage [Iti Chauhan et al 2020].

Due to its scalability, hot homogenisation is one of the most widely used methods. This method consists of heating the lipid and aqueous phases separately at a temperature about 5-10°C above the melting temperature of the solid lipid. The lipid phase usually consists of a mixture of solid lipids, liquid lipids, and active ingredients. The aqueous phase usually contains purified water, surfactants, preservatives, and pH buffers. The aqueous phase is then added over the lipid phase under vigorous agitation. This agitation can be achieved by high shear mixing or probe sonication. At the level of industrial scale-up, the high cavitation energy provided by probe sonication allows more homogeneous, smaller, and more reproducible size distributions batch by batch [Chia-Lang Fang et al 2013].

To avoid the possible degradation of the active ingredient when heating the lipid phase, cold methods have been developed. One of them is cold homogenisation, which consists of melting the lipid phase and then cooling it to form microparticles. Once cold, the active ingredient is added before the homogenisation is performed, breaking the microparticles into NLCs. Although this method avoids the need for heating, the encapsulation yields are usually lower, and the size of the nanoparticles obtained is higher. Finally, there is also the microemulsion method, which consists of adjusting the amount of molten lipids, surfactants, and water at the correct ratio to achieve a thermodynamically stable dispersion. Once obtained, it is diluted in water, causing the precipitation of the lipid phase in the nanoparticles. Although it is an easily scalable method, it usually requires concentration methods such as lyophilisation or ultrafiltration, which increase production costs and difficulties [Chia-Lang Fang et al 2013].

The possibility of selective drug delivery to hair follicles is particularly interesting in hair follicle-related diseases like alopecia areata and androgenetic alopecia. Despite high demand, there are currently only two drugs authorised on the European market for the treatment of [REDACTED] [Areej Adil et al 2017].

[REDACTED] is a drug that was originally intended for the treatment of hypertension (through oral administration) due to its ability to open adenosine triphosphate-sensitive potassium channels in vascular smooth muscle cells, inducing vasodilation. Nowadays, [REDACTED] solution is the most widely used drug for topical administration for the treatment of [REDACTED] [Martina Bienova et al 2005].

[REDACTED] has low aqueous solubility. Hence, it is currently formulated in hydroalcoholic solutions with a high propylene glycol content, causing mild to moderate adverse effects on the

scalp (itching, irritation, dermatitis and moderate adverse effects on the scalp (pruritus, desquamation, irritation, contact dermatitis, erythema and dryness)) [Rathnayake D et al 2010].

██████████ is a highly selective irreversible inhibitor of ██████████ (5AR) with low aqueous solubility that blocks the conversion of ██████████ to ██████████, decreasing serum and skin ██████████ concentrations [Drake L et al 1999]. ██████████ is a potent androgen that mediates the appearance of secondary sexual characteristics such as hair growth. DHT is formed due to the action of two isoforms of 5AR. Type 1 5AR is found in sebaceous glands, hair follicles, the epidermis, sweat glands, Schwann cells and endothelial cells, while type 2 5AR is mainly localised in hair follicles. The pathogenesis of AGA seems to be connected to the genetically based sensitivity of hair follicles to DHT concentration and their varied response to androgen activity.

██████████ was originally administered orally (5 mg/day) as an anti-androgen in benign prostate hyperplasia due to the expression of 5AR in the prostate. Its clinical effectiveness for the treatment of androgenic alopecia was subsequently demonstrated in clinical trials after oral administration at 1 mg/day. Oral treatment with 1 mg/day of ██████████ presents adverse effects at the systemic level due to the partial conversion of testosterone to oestradiol by the aromatase enzyme. This can lead to adverse effects such as water retention, adipose tissue modification and gynaecomastia, while low levels of DHT can lead to sexual dysfunction such as a loss of libido, erectile dysfunction, and reduced ejaculation [Rossi A et al 1998].

According to a very large prospective study, the effect of ██████████ on sexual function is low for most men, but may worsen quality of life or even reduce compliance with treatment. This makes many patients reluctant to undergo this treatment. To reduce these systemic adverse effects, topical administration of this drug to locally inhibit the 5AR enzyme may be of particular interest. Although there are several approaches in the literature with promising preliminary results, the low aqueous solubility of ██████████ forces the use of hydroalcoholic solutions or solutions with a high cosolvent content, which can lead to scalp irritation or contact dermatitis. There is currently no formulation of topical ██████████ on the market that has demonstrated efficacy and the absence of adverse effects in randomised clinical studies [Mysore V et al 2012, Caserini M et al 2019, Hajheydari et al 2009].

In this work, extensive optimisation was performed for the development of a lipid nanoparticle formulation encapsulating the active ingredient ██████████ for topical administration in patients with androgenetic alopecia.

6.2. Materials

██████████ and purified water (in-house) were used to formulate the NLCs. Coumarin 6 (C6) (Sigma Aldrich, St. Louis, MO, USA) and 1,2-dioleoyl-3-[16-N-(lissamine rhodamine B sulfonyl) amino]palmitoyl-sn-glycerol (LRB) (Avanti Polar Lipids, Alabaster, AL, USA) were used as fluorochromes. Paraformaldehyde (Scharlab S.L., Barcelona, Spain), sucrose (Acor, Valladolid, Spain), optimal cutting temperature (OCT) compound (Tissue-Tek Sakura Finetek, Torrance, CA, USA), rabbit anti-DEX IgG antibody (Abcam, Cambridge, UK), anti-cytokeratin 14 mouse monoclonal IgG_{2a} antibody (Santa Cruz Biotechnology, California, USA), goat anti-mouse IgG1 cross-adsorbed secondary antibody, Alexa Fluor 594 (Thermo Fisher Scientific, Barcelona, Spain), goat anti-rabbit secondary antibody, Alexa Fluor 488 (Life Technologies, Carlsbad, CA, USA), ProLong™ Gold Antifade

mounting medium (Thermo Fisher Scientific, Barcelona, Spain) and Tween 20 (Sigma-Aldrich, St. Louis, MO, USA) were used to prepare samples for microscopic visualisation.

6.3. Methods

6.3.1. Production of [REDACTED]-loaded NLCs

The encapsulation of [REDACTED] in NLCs was carried out using the hot homogenisation method [Eman Gomaa et al 2022] and a laboratory-scale UP400st ultrasonic device (Hielscher Ultrasonics, Teltow, Germany). In this method, a lipid phase composed of [REDACTED] was warmed up to 71°C in a thermostatic bath. An aqueous phase containing [REDACTED], Tween 80 (3% w/w) and milli-Q water (qsp 100% w/w) was also warmed up to 71°C. Both phases were mixed by vortexing and then sonicated to an energy limit of 3729 Ws, with an amplitude of 20%. Formulations were produced with the different levels of the factors studied during the subsequent factorial designs.

Once the composition of the [REDACTED] NLCs was optimised at the laboratory scale, the laboratory-scale UP400st ultrasonic processor (batch size 200 mL) was replaced by the UIP1000HdT industrial ultrasonic processor (batch size 8 L).

The industrial sonication system consists of an ultrasonic processor UIP1000HdT (consisting of a transducer and ultrasonic generator), a sonotrode (BS4d22; diameter 22 mm) and a flow cell (FC100L1K-1S; Figure 13). The UIP1000HdT processor produces longitudinal mechanical oscillations through the electrical stimulation of a piezoelectric material (a material that produces mechanical movements in response to electrical stimuli). This electrical power can be regulated from 20 to 100%, thus regulating the oscillation amplitude. With this configuration, a maximum amplitude (peak to peak) of 57 µm is achieved by selecting the 100% amplitude. These oscillations of the sonotrode cause cavitation of the medium. The high time pressures generated allow this technology to be applied to different top-down processes. The flow cell allows the recirculation of the formulation to be sonicated, keeping the sonication volume constant. This facilitates the scaling process and improves the reproducibility of the manufacturing processes.



Figure 13 The UIP1000HdT system consisting of a transducer (1), ST2 support (2), booster (3), sonotrode (4) and flow cell (5). Image obtained from [https://www.hielscher.com/es/i1000_p.htm].

The compositions of the organic and aqueous phases were the same as those described for the laboratory scale. Briefly, a 10-L beaker with the aqueous phase and a 5-L beaker with the organic phase were placed in a thermostatic bath at 71°C. Both phases were subjected to mechanical agitation at 500 rpm with a paddle stirrer until complete homogenisation. Then, the organic phase was added to the aqueous phase, maintaining the agitation at room temperature. A 1-mL aliquot was taken to measure the particle size, polydispersity index (PDI) and Z-potential of the premix by DLS. A peristaltic pump was connected to the flow cell with a flow rate of 1 mL/min through rubber tubing and the formulation was recirculated through the system. In addition, the flow cell jacket was connected to a water-cooling system. Aliquots were taken after each sonication cycle to monitor the size, PDI and Z-potential of the formulation and to estimate the amount of energy required per L of the batch to obtain adequate size, PDI and Z-potential.

6.3.2. Physicochemical characterisation

Dynamic light scattering (DLS) (Malvern Zetasizer Nano ZS (Malvern Panalytical, Malvern, UK)) was used to study the hydrodynamic diameter (Z-average), PDI and zeta-potential of the produced nanoparticles. Prior to obtaining the measurements, a 1:10 dilution of nanoparticles in milli-Q water was carried out.

Transmission electron microscopy (TEM) (Jeol JEM 1010 100 kv; Jeol, Tokyo, Japan) was employed to study the size and morphology of the nanoparticles. A dilution of 1:10 of NLCs was prepared in milli-Q water, before being placed in TEM grids and stained for 1 min with uranyl acetate solution (2% w/w) at 25°C until the samples were dried.

The possible formation of drug crystals was analysed by optical microscopy to determine the maximum concentration of the active ingredient to be encapsulated in NLCs. A drop of the placebo formulation or drug formulation (between 0.1 and 0.30%) was placed on a slide and analysed under 40x magnification on an Eclipse E400 Ci-L microscope (Nikon Europe BC, the Netherlands).

6.3.3. High Performance Liquid Chromatography

An isocratic elution with a mobile phase composed of (60:40) acetonitrile:KH₂PO₄ (0.05 M) was passed at a flow rate of 1.8 mL/min through a C18 HPLC column (250 × 4.6 mm, 3 μm) at 25°C. The detection wavelength was 208 nm and the injection volume was 20 μL. The assay was performed with an HPLC instrument (Waters 2695 and detector Waters 2996, Waters Corporation, Milford, MA, USA). This method was also used to estimate the encapsulation efficiency (%EE) according to Equation (1), where W_T denotes the total content of drug in the formulation and W_{NE} the drug obtained in the filtrate (not encapsulated) after centrifugation in an Amicon ultra device (Merck Millipore, Burlington, US) with a membrane cut-off of 100 kDa at 4500 rpm for 30 min.

$$\%EE = \frac{W_T - W_{NE}}{W_T} \times 100 \quad (1)$$

The amount of total drug entrapped per weight of nanoparticle or loading capacity (% LC) was calculated using Equation (2):

$$\%LC = \%EE \times \frac{W_{drug}}{W_{NLCs}} \quad (2)$$

where W_{drug} is the amount of active ingredient initially added to the formulation and W_{NLCs} the mass of the nanoparticle components.

6.3.4. Design of experiments and response surface regression at the laboratory scale

A design of experiments was performed to optimise the hydrodynamic diameter or Z-average (nm), the Pdl, the surface charge or Z-potential (mV) and the encapsulation efficiency (%EE) of the NLCs produced at the laboratory scale, using the Minitab 17 statistical software (Minitab, Inc., 2010, State College, PA, USA). The factors % cationic surfactant, % drug, % Tween 80 and sonication energy (Ws) were selected as possible significant factors. A fractional factorial design (FFD) with 4 factors, 8 runs and a class IV resolution was performed. The factors and levels chosen are shown in Table 1.

Table 1 FFD factors for [redacted]-loaded NLCs.

Factors			
% cationic surfactant	% drug	% Tween 80	Sonication energy (Ws)
0.2	0.1	5	2000
0.2	0.2	5	4000
0.1	0.2	1	4000
0.1	0.1	1	2000
0.2	0.2	1	2000
0.1	0.1	5	4000
0.1	0.2	5	2000
0.2	0.1	1	4000

The high positive charge of the quaternary ammonium salt makes % cationic surfactant an interesting factor to study, since it can influence the electrostatic stability of the nanoformulations. In the same way, % Tween 80 may influence the amount of surfactant that stabilises and coats the nanoparticles and may influence their final characteristics. To determine the drug-encapsulation capacity of the NLCs, % drug was also included. Finally, sonication energy (Ws) was included in the design as it is the factor that most directly influences particle size during top-down processes.

The first design of experiments carried out was a screening, with the aim of finding the significant factors. Once the significant factors had been determined, response surface values for the Z-average and Pdl were obtained by adding central and axial values to the significant factors of the design of experiments: % Tween 80 and sonication energy (Ws). The factors and levels chosen in the response surface regression are shown in Table 2.

Table 2 Response surface regression design with the factors for XXXXXXXXXX-loaded NLCs.

Factors	
% Tween 80	Sonication energy (Ws)
1.00000	4000.00
5.00000	2000.00
0.17157	3000.00
5.00000	4000.00
3.00000	3000.00
5.82843	3000.00
1.00000	2000.00
3.00000	3000.00
3.00000	4414.21
3.00000	1585.79
3.00000	3000.00

In a response surface design, a low level and a high level are designated to each factor. These factor levels define the proportions of the "cube" around which the design is built. The Minitab software determines the central and axial values to ensure that all design points fall between the defined maxima and minima for each factor. In this case, the response surface design was a central composite design with 11 runs, 5 central points, 2 axial points and 4 cube points. To obtain a more accurate model, quadratic interactions between the factors were included in the response surface design. This enabled the determination of the curvature of the response as well as the minimum or maximum values to optimise size and/or the Pdl.

6.3.5. Design of experiments during the scale-up of Finasteride-loaded NLCs

A Plackett-Burman FFD with a class III resolution, 12 runs, 4 factors and a significance set at $\alpha = 0.05$ was performed using Minitab to obtain the maximum information about scaling while producing the minimum number of batches. The responses to be optimised were the Z-average and Pdl. The factors selected were: % amplitude, batch volume (L), number of sonication cycles and flow cell jacket temperature ($^{\circ}\text{C}$).

Table 3 shows the levels of the selected factors for the scale-up Plackett-Burman FFD.

Table 3 Scale-up FFD design of experiments: factors and responses for [redacted]-loaded NLCs

Amplitude (%)	Batch volume (L)	Sonication cycles	Jacket temperature (°C)
100	1	10	45
20	8	10	45
20	1	10	45
100	8	4	30
20	1	4	45
100	1	4	30
100	1	10	30
20	8	10	30
100	8	4	45
100	8	10	45
100	8	10	30
20	1	4	30

In this case, factors were chosen to help design the set-up of the scaling process after the optimisation of the formula at the laboratory scale. The amplitude and number of sonication cycles are related to the sonication energy input. The flow cell temperature was also included to control the temperature stability during the production process. Finally, to test the scalability of the formulation, batch volume (L) was included.

6.3.6. Stability studies

Optimised 8-L scaled-up placebo NLCs were packaged in 8-mL sealed glass vials and subjected to stability studies in chambers at $25 \pm 2^\circ\text{C}/60 \pm 5\% \text{RH}$ (long-term conditions) and $40 \pm 2^\circ\text{C}/75 \pm 5\% \text{RH}$ (accelerated conditions). Samples were analysed at times 0, 15 days, 1 month, 3 months and 6 months for the studies at 40°C , and at times 0, 15 days, 1 month, 3 months, 6 months, 9 months and 12 months for the studies at 25°C . The Z-average (nm), Pdl and Z-potential (mV) of the nanoparticles were analysed following the method described in section 6.3.2. by DLS. The [redacted] content and %EE of the nanoformulations were analysed at 0, 3 and 6 months and characterised by HPLC, according to the method described in section 6.3.3.

6.3.7. *In vitro* permeation tests in dermatomised pig skin

Pig skin was obtained at the time of sacrifice from a local abattoir (Barcelona, Spain). The skin was cleaned with sterile saline solution and transported to the laboratory at 4°C in saline solution. Subcutaneous fat was removed with a scalpel, and the skin was dermatomised at 0.5 mm with an electrical dermatome (GA630, Aesculap, Tuttlingen, Germany) and frozen at -20°C for a maximum period of 6 months or until use. On the day of the experiment, skin pieces were thawed and placed between the donor and receptor compartments of Franz cells (Vidrafoc,

Barcelona, Spain), with a 12-mL receptor compartment and an effective diffusion area of 1.54 cm². The receptor medium was an ethanol:water (50:50) solution to maintain sink conditions throughout the experiment. Skin integrity was checked (by evaluating transepithelial water loss (TEWL)) with a TEWL Vapometer (SWL4549, Delfin Technologies Ltd., Kuopio, Finland) before carrying out the experiment. Infinite dose formulation amounts of 600 mg were applied to the donor compartment for each one of the replicates. Samples from the receptor compartment (0.3 mL) were taken at times 1, 2, 3, 4, 5, 21, 22, 23 and 24 h and replenished with the same volume of fresh receptor medium [European Commission 2018]. Samples were analysed with the method described in section 6.3.4. The permeated drug quantities per square centimetre and the skin permeation parameters were determined, according to the following equations:

$$J_{sup} = \frac{\Delta Q_T}{\Delta t \cdot s} \quad (3)$$

$$K_p = \frac{J_{sup}}{C_d} \quad (4)$$

$$K_p = P_1 \cdot P_2 \quad (5)$$

$$t_{lag} = \frac{1}{6 \cdot P_2} \quad (6)$$

where J_{sup} denotes the transdermal flux in a steady state, Q_t the permeated amount at time t , t the time, s the diffusional area, K_p the permeability coefficient, C_d the concentration of the drug in the donor compartment, P_1 the diffusion parameter (it is related to the Fick's laws of diffusion), P_2 the partitioning parameter between the stratum corneum and the formulation, and t_{lag} the lag time or the time necessary for the active ingredient to achieve a steady state of permeation.

t_{lag} was estimated from the extrapolation in the x-axis (x-intercept) of the cumulative amounts vs. time plot.

6.3.8. *In vitro* penetration tests with full-thickness pig skin and human scalp

Human scalp was purchased from Biopredic (Saint Grégoire, France), which has authorisation for the collection, processing, and transfer of human biological samples for research purposes (Figure 14). Samples were remnants from surgeries complying with the French law CSP1245-2, with informed consent provided by the patient, who was anonymous and did not receive financial reward or publicity. The donor was a 58-year-old Caucasian female. Pig skin was obtained at the time of sacrifice from a local abattoir (Barcelona, Spain). The skin was cleaned with sterile saline solution and transported to the laboratory at 4°C in saline solution. Full-thickness skin pieces of human and pig were defatted (with a scalpel) and frozen at -20°C until use. The permeation experiment was performed in a similar manner to that described in section 6.3.7. in terms of temperature, TEWL reading, agitation and Franz cells. In this case, the skin pieces were mounted in Franz cells with an effective diffusion area of 0.196 cm². The objective was not to analyse the permeated amount, but the amount penetrating the tissue. For this reason, it was not necessary to comply with sink conditions and, therefore, PBS was chosen as the receptor medium. A solution dose of 76 mg of each of the formulations was given in infinite dose in non-occluded conditions.

Sections 6.3.9. and 6.3.10. describe the formulas tested for the pig and human full-thickness skin penetration experiments.



Figure 14 Human scalp remnants from surgery.

6.3.9. Confocal fluorescence microscopy to study NLC biodistribution

The biodistribution of NLCs in the skin was studied using confocal fluorescence microscopy. To this end, coumarin 6 (C6) was encapsulated at a concentration of 0.1% w/w in the nanoparticles to simulate the biodistribution of a hydrophobic small molecule. Lissamine rhodamine B (LRB) was used as a fluorophore covalently bound to a lipid (palmitic acid) at a concentration of 0.0003% w/w and included in the lipid core of the NLCs to track the nanoparticles. Fluorescent nanoparticles were purified using Visking dialysis tubing with a cut-off of 12,000–14,000 Dalton (Visking, London, United Kingdom). Free C6 (0.1% w/w) and LRB (0.0003% w/w) aqueous solution was also prepared with 3% w/w Tween 80 as a solubiliser. Full-thickness pieces of human scalp and pig skin were warmed and placed in Franz cells (see section 6.3.8). After 18 h of permeation, the diffusion surface was washed with PBS, cut with a scalpel into pieces of about 0.5 cm², and fixed in 4% w/w paraformaldehyde solution for 5 min. Then, the skin samples were incubated in aqueous solutions of increasing sucrose concentration (5%, 15% and 25% w/w) for 15 min in each solution. They were then placed in plastic moulds and embedded in OCT compound to aid sectioning in a Leica CM 3050 S cryostat (Leica Biosystems, Barcelona, Spain) to a thickness of 50 μm. The slices were collected on poly-lysine-coated slides and washed with PBS and 0.05% Tween 20 (TPBS) for 5 min to remove the OCT compound and permeabilise the samples. On the day of observation, sections were incubated with 15 μL of Hoechst solution (2 μg/mL) for 10 min and washed with TPBS to stain the cell nuclei. The samples were analysed under a confocal microscope (Leica Microsystems, Wetzlar, Germany). The emission laser wavelengths were 570, 500 and 525 nm and the excitation wavelengths were 561, 488 and 405 nm for LRB, C6 and Hoechst, respectively. About 20 planes were obtained per image, separated by a 3-μm step. Composites of the different planes were created in terms of the brightest point for each pixel, using the ImageJ tool Z-stack (ImageJ2 v2.35, National Institutes of Health, Bethesda, MD, USA). A skin blank was processed in the same way as the test samples to quantify skin autofluorescence. The mean intensity was measured with the ImageJ software and was subtracted from the intensity of the red and green channels of the samples.

6.3.10. Immunohistofluorescence to study NLC biodistribution

To directly track the biodistribution of the active ingredient, the drug under study was immunolocalised using a specific antibody. Unfortunately, antibodies against this drug are not yet available. Considering the structural similarity (Figure 15) between the drug under study and dexamethasone (DEX), both compounds were expected to show comparable cutaneous biodistributions. Since antibodies against DEX are available, the biodistribution of DEX loaded into NLCs was studied.

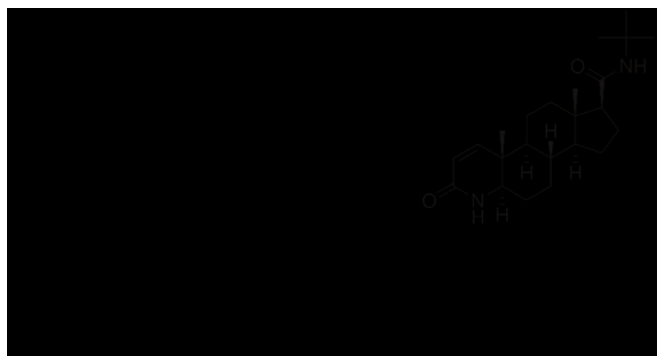


Figure 15 Molecular structure of Dexamethasone and [REDACTED]

Permeation and skin slices were obtained in the same way as that described in section 6.3.9., but the slices were 10 μm thick in this case. Then, 15 μL of a 1/300 dilution of the rabbit polyclonal primary anti-DEX IgG and 15 μL of a 1/300 dilution of the anti-cytokeratin 14 mouse monoclonal IgG_{2a} antibody were added, before incubating the samples in a humid environment overnight at 4°C. The samples were then washed with TPBS and incubated with a 1/300 dilution of the Alexa Fluor 594 goat anti-mouse IgG1 secondary antibody and the Alexa Fluor 488 goat anti-rabbit IgG secondary antibody for 2 h under the same incubation conditions. Figure 16 shows a visual scheme of the immunohistofluorescence experiment, demonstrating that the Alexa Fluor 594 antibody binds specifically to the anti-cytokeratin 14 antibody while the Alexa Fluor 488 antibody binds to the anti-DEX antibody. Finally, ProLong Gold Antifade mounting medium was added. Samples were visualised with a Leica DMIRB wide-field fluorescence and transmitted light microscope. To study the possible non-specific interactions of the skin, the same process was carried out with untreated skin samples and processed in the same way as the test samples. The resulting intensity was subtracted from the profiles of the samples using the ImageJ software.

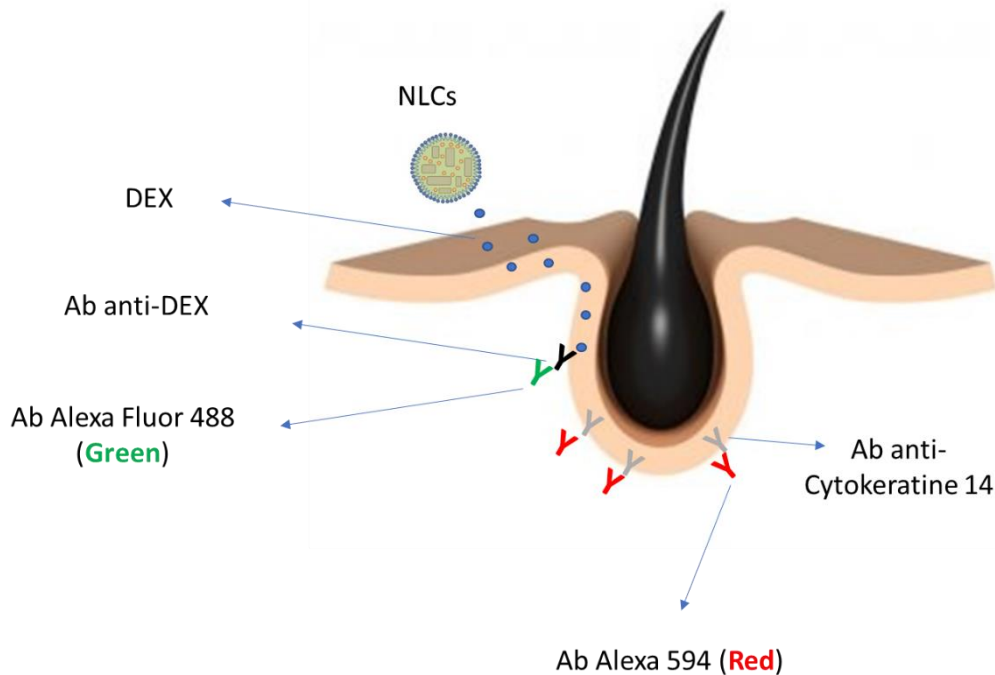


Figure 16 Visual scheme of the immunohistofluorescence experiment against DEX after the skin permeation of DEX-loaded NLCs.

6.4. NLCs Results and discussion

6.4.1. Design of experiments and response surface regression at the laboratory scale
Size, surface charge and the PDI affect the bioavailability and biodistribution of nanomedicines. It is therefore important to study them to optimise formulations. Design of experiments (DoE) is a statistical tool commonly used to evaluate significant variables and to optimise drug delivery systems. The relevant independent variables and their range (or levels) (called design space) are selected based on the knowledge of the specific system and/or on a risk assessment management system. DoE reduces the number of independent experiments, without the need for extensive information or statistical power loss. This is useful to avoid extensive development work and a high number of different development batches. It can be used to optimise the combination of independent variables. This reduced experimental design is called a fractionated factorial design (FFD).

Depending on the number of independent variables and the reduction in the number of experiments, different resolutions are obtained. A proper balance between statistical resolution and the number of experiments should be considered. Class III resolutions are usually employed for screening purposes due to the high reduction in the number of experiments. In this case, the main effects are aliased with 2-way interactions. Thus, it is not possible to distinguish between the factors. On the other hand, in class IV resolutions, the main effects are not aliased with any 2-way interactions and the main factors (which are variables of high interest) are estimated without uncertainty, being more precise than class III resolutions and not requiring a high increase in the number of experiments.

Thus, an FFD with a class IV resolution, 4 factors, 8 runs and a significance level of $\alpha = 0.05$ was performed using Minitab for the optimisation of drug-loaded NLCs. Table 4 shows the levels established for each factor and the obtained responses.

Table 4 FFD DoE factors and responses for drug loaded NLCs.

Factors				Responses			
% cationic surfactant	% API	% Tween 80	Sonication Energy (Ws)	Z-average (nm)	Pdl	Z-potential	%EE
0.2	0.1	5	2000	173.2	0.185	43.4	98.87
0.2	0.2	5	4000	138.2	0.197	44.3	99.11
0.1	0.2	1	4000	188.0	0.203	46.5	99.20
0.1	0.1	1	2000	200.7	0.222	43.0	99.57
0.2	0.2	1	2000	185.0	0.188	55.6	98.36
0.1	0.1	5	4000	137.2	0.166	37.4	98.90
0.1	0.2	5	2000	166.1	0.154	44.5	96.22
0.2	0.1	1	4000	167.5	0.191	40.8	99.07

In the case of the Z-average, % Tween 80 and sonication energy were found to be significant ($p < 0.05$).

$$Z - average (nm) = 228.5 - 7.91\% Tween 80 - 0.01176 Sonication Energy (Ws) (7)$$

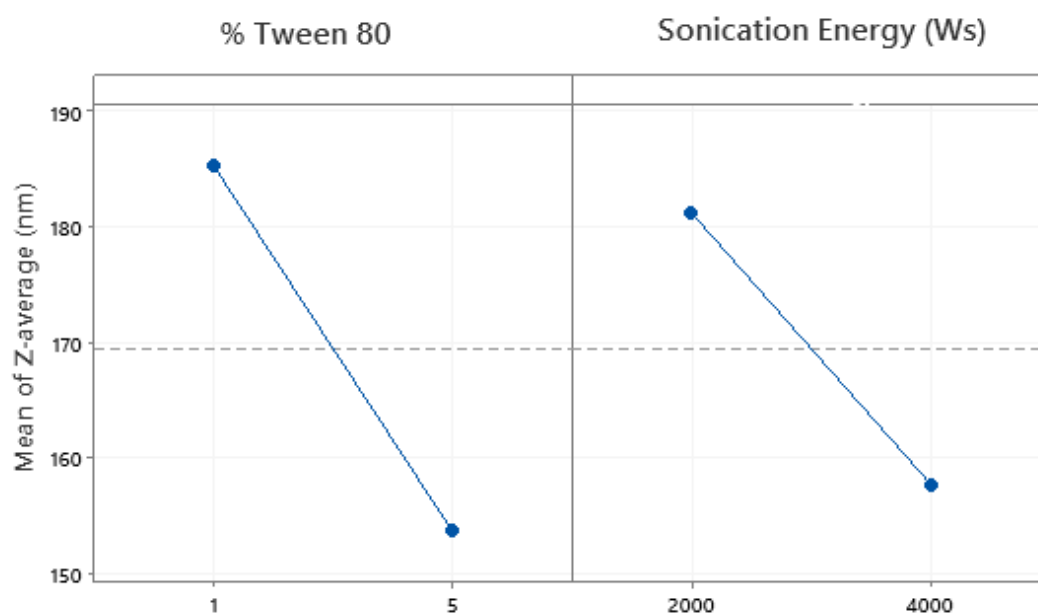


Figure 17 Factorial plot for the significant factors % Tween 80 and sonication energy (Ws) for the Z-average.

Figure 17 shows that both % Tween 80 and sonication energy (Ws) affected the Z-average in the same direction. As the % Tween 80 and sonication energy increased, particle size decreased. The increase in % Tween 80 stabilised the nanoparticle droplets, which had a high surface-to-volume ratio. Similarly, the higher the sonication energy supplied to the system, the smaller the droplets produced.

To evaluate the fit of the model to the empirical data, both R^2 and $R^2(\text{adjusted})$ were analysed. R^2 assumes that every single variable explains the variation in the response, while $R^2(\text{adjusted})$ describes the percentage of variation by only the factors that significantly affect the response. $R^2(\text{adjusted})$ penalises the model when factors that are not significant are added to the model. In this way, the simplest model is chosen. The regression equation for the Z-average response

(equation 7) had an $R^2(\text{adjusted})$ value of 80.56%. Therefore, 80.56% of the variability of the Z-average response was explained by % Tween 80 and the sonication energy.

The only significant variable for Pdl (Figure 18) was % Tween 80 ($p < 0.05$). The regression model (equation 8) for the Pdl had an $R^2(\text{adjusted})$ value of 31.97%. The variability in the Pdl values was not properly explained by the Tween 80 concentration. Therefore, there could be other experimental variables that could increase the model predictability, or the number of experiments was not enough to properly explain the response variability.

$$Pdl = 0.2074 - 0.00638\% \text{ Tween } 80 \quad (8)$$

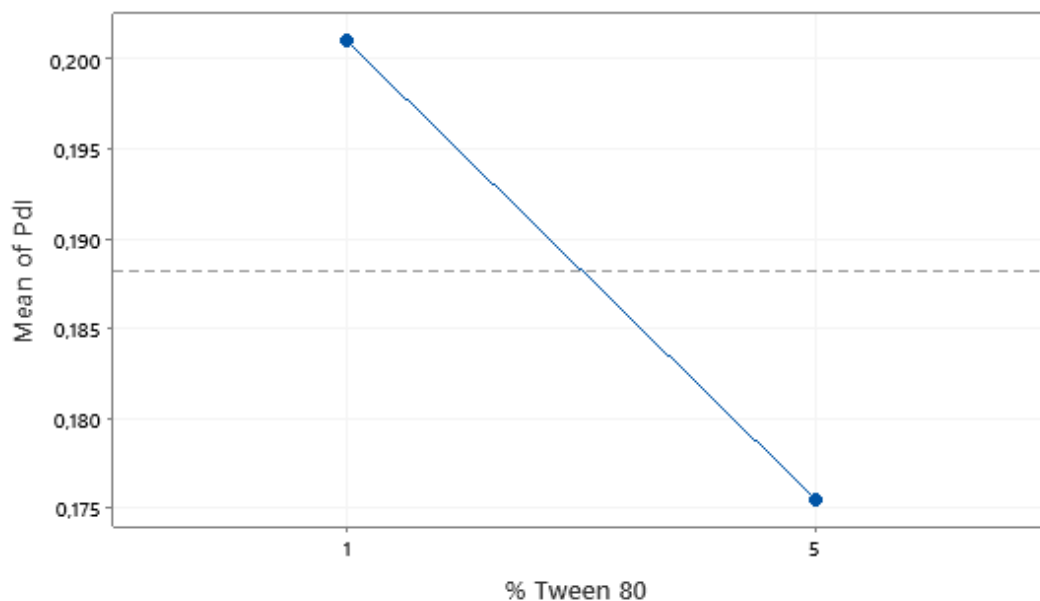


Figure 18 Factorial plot for the significant factor % Tween 80 for the Pdl.

Finally, the significant variable for Z-potential (Figure 19) was the % of API. The regression equation (Equation 9) for the Z-potential response had an $R^2(\text{adjusted})$ value of 35.12%.

$$Z - \text{potential (mV)} = 34.5 + 65.8 \% \text{ API} \quad (9)$$

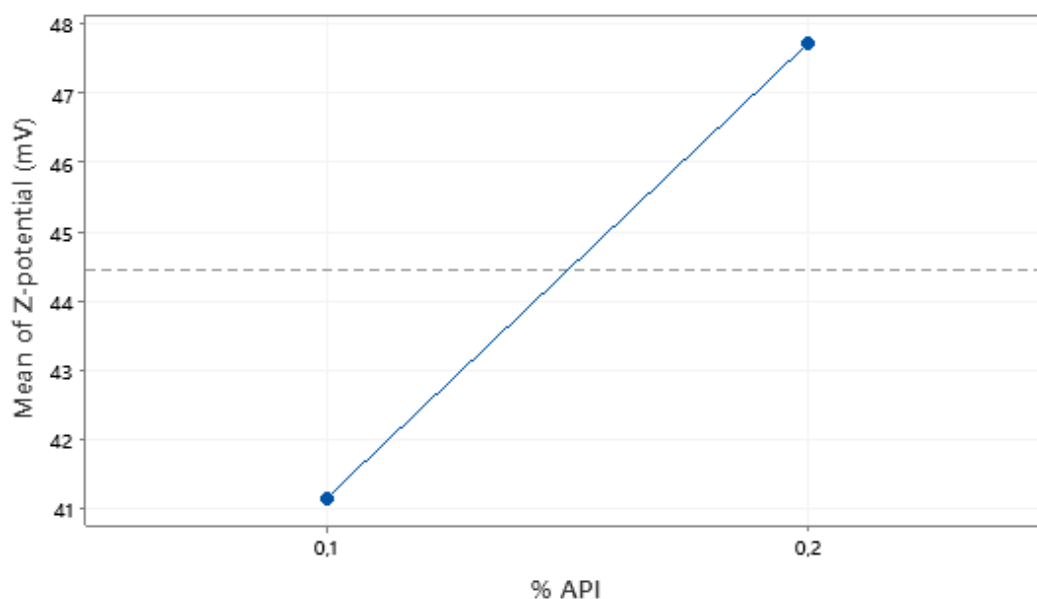


Figure 19 Factorial plot for the significant factor % API for the Z-potential.

Figure 19 shows the direction of influence of the % API on the Z-potential of the particles. As the amount of active ingredient increased, it was placed on the surface of the particles, increasing their positive charge due to the protonated amines.

After finding the significant factors during the FFD, a response surface study was carried out by adding quadratic interactions of the significant factors as well as the central and axial levels by means of a response surface regression for the Z-average and the Pdl. The objective for the Z-potential response optimisation was to obtain nanosystems stable against aggregation in suspension. A net value higher than 30 mV on the surface of the nanoparticles provides stability through electrostatic repulsion. In all cases, the Z-potential was found to be above this value. Thus, it was not necessary to further optimise this response.

A response surface regression was performed for the Z-average and the Pdl. The two significant factors % Tween 80 and sonication energy were chosen. For the Pdl, the significant factor % Tween 80 was chosen. The response surface regression design was a central composite design with 11 runs, 5 central points, 2 axial points, and 4 cube points. Quadratic interactions between the factors were included to analyse the curvature of the response.

Table 5 shows the levels of the response surface factors.

Table 5 Response surface regression design with factors and responses for [redacted]-loaded NLCs.

Factors		Responses	
% Tween 80	Sonication Energy (Ws)	Z-average (nm)	Pdl
1.00000	4000.00	183.9	0.222
5.00000	2000.00	157.0	0.160
0.17157	3000.00	183.5	0.230
5.00000	4000.00	145.5	0.161
3.00000	3000.00	166.4	0.178
5.82843	3000.00	143.9	0.154
1.00000	2000.00	201.3	0.230

3.00000	3000.00	159.8	0.169
3.00000	4414.21	162.4	0.171
3.00000	1585.79	180.3	0.166
3.00000	3000.00	164.6	0.201

The regression equation (10) obtained after the Z-average surface response was the following:

$$Z - \text{average (nm)} = 252.8 - 8.669\% \text{ Tween 80} - 0.0346 \text{ Sonication Energy (Ws)} + 0.000005 \text{ Sonication Energy (Ws)} * \text{ Sonication Energy (Ws)} \quad (10)$$

As expected, the influence of % Tween 80 on the Z-average obtained was confirmed. As the surfactant concentration increased, the particle diameter decreased (Figure 20).

The quadratic effect of the sonication energy on particle size can be seen in the regression equation 10. This quadratic effect can be visualised as a curvature on the contour plot of Figure 20, where the minimum of the curve corresponds to the sonication energy value at which the minimum particle size is obtained.

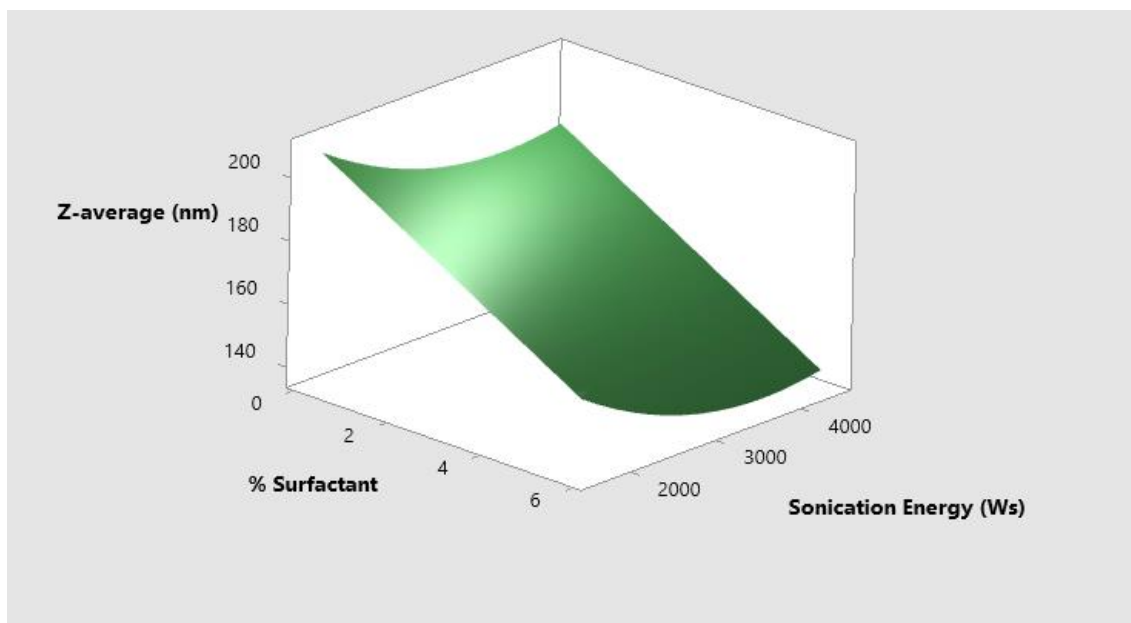


Figure 20 Z-average contour plot for [redacted] loaded NLCs.

The addition of quadratic interactions between the factors and more levels per factor makes the response surface model a more exhaustive model than the FFD. This can be corroborated by looking at the R^2 (adjusted) values for the Z-average response. The R^2 (adjusted) value was 92.15% and the R^2 (predicted) value was 84.84%, indicating the great predictive capacity of the model.

The regression equation obtained after the PDI response was the following:

$$PDI = 0.2441 - 0.02847\% \text{ Surfactant} + 0.00226\% \text{ Surfactat} * \% \text{ Surfactant} \quad (11)$$

As can be seen in the main effects plot in Figure 21, the % of surfactant affected the PDI, producing more monodisperse nanoparticles as the percentage of the surfactant increased.

Colloidal suspensions of NLCs can undergo destabilisation processes such as Ostwald ripening. By incorporating surfactants such as Tween 80, it is possible to reduce the probability of particle aggregation through steric stabilisation. During sonication, collisions between particles can occur and lead to aggregation into larger particles. Therefore, the more the % surfactant is increased, the greater the number of particles that are coated by Tween 80 molecules, consequently leading to a smaller and more monodisperse hydrodynamic diameter of the formulation.

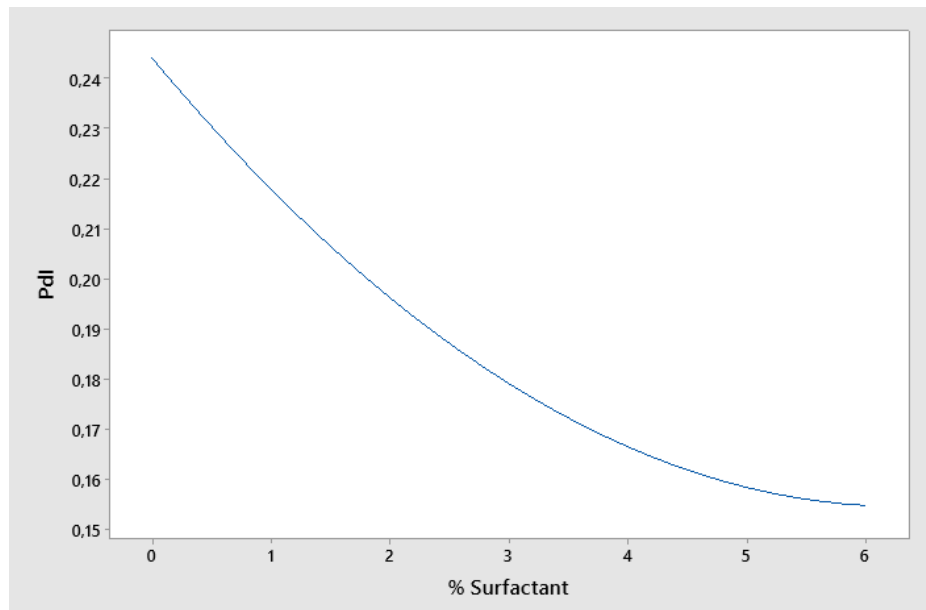


Figure 21 Pdl main effects plot of [redacted]-loaded NLCs.

For the Pdl surface response, the R^2 (adjusted) value was 84.48% and the R^2 (predicted) value was 76.38%, indicating the great predictive capacity of the model. When comparing the R^2 (adjusted) value of the FFD and the response surface for the Pdl, the response surface, being a more exhaustive model, explained a much higher percentage of the variability of the response. It increased from 31.97% in the FFD to 84.48%.

Once the predictive models were obtained, an optimisation was performed to obtain the minimum values of the Pdl and Z-average within the design space. A limit of 3% Tween 80 was established since the rheological characteristics of the formulation obtained at higher concentrations of Tween 80 are not desirable (viscosity is too high to be sprayed).

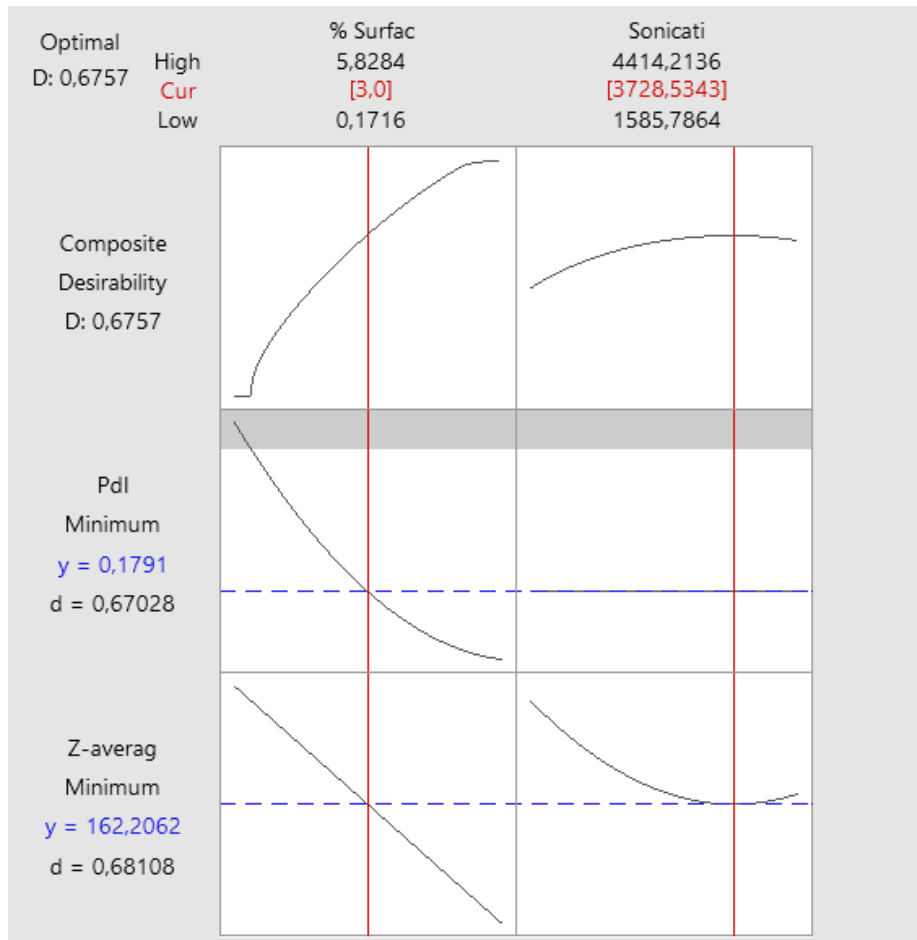


Figure 22 Desirability functions after the optimisation to obtain minimum Pdl and Z-average responses with a 3% surfactant limit.

Figure 22 shows the desirability functions for the optimisation performed. The red lines mark the 3% Tween 80 limit and the minimum of the effect plot for the Z-average as a function of the sonication energy. The predicted values from the model are shown in blue. Table 6 shows the predicted values as well as the empirical values after the production of a batch with 3% Tween 80 subjected to 3729 Ws of sonication energy. The BIAS calculated between the predicted and empirical values was 22.87 and 8.94% for the Z-average and Pdl, respectively, further corroborating the good predictive ability of the model.

Table 6 Predicted and empirical data comparison.

	Z-average (nm)	Pdl
Empirical Batch (LP0309-199)	125.1 ± 1.4	0.163 ± 0.006
Predicted values	162.2	0.179
BIAS	22.87%	8.94%

Once optimised, the size and morphology of the nanoparticles were analysed by TEM. Due to the high resolution of this technique, it was possible to differentiate between the structure of the solid and liquid lipids at the core of the nanoparticles (Figure 23 B). Compared with the results obtained by DLS, the size obtained by TEM was significantly smaller. In DLS, the hydrodynamic diameter is observed, i.e., the diameter of a perfect solid sphere exhibiting the same hydrodynamic friction as the particle of interest. In TEM, the actual size and morphology

are observed at a much higher resolution, which is why the nanoparticles were more accurately observed to be of a smaller size.

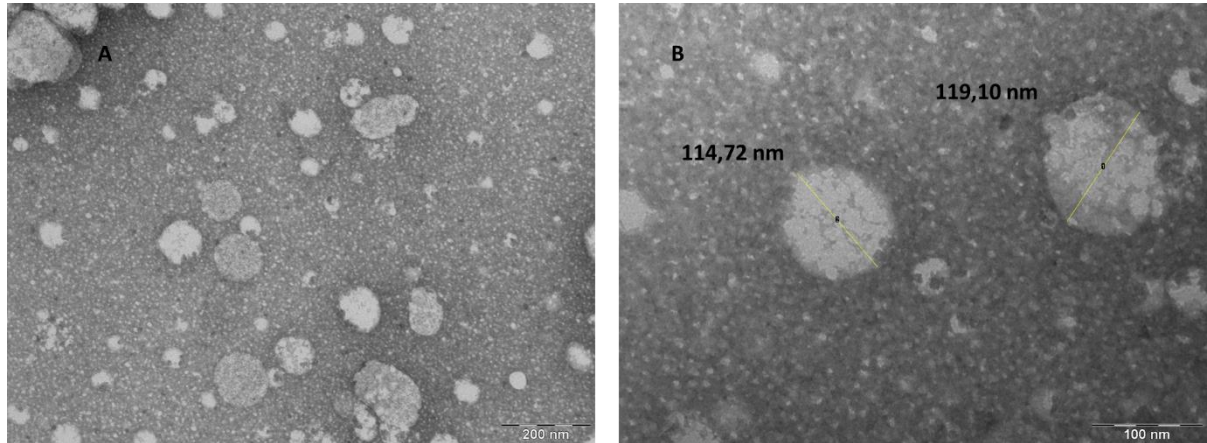


Figure 23 TEM images of NLCs. (A) Scale bar, 200 nm. (B) Scale bar, 100 nm. Diameters of two representative nanoparticles of 114.72 nm and 119.19 nm are shown.

6.4.2. Pilot plant scale-up production of [redacted]-loaded NLCs

Once the formulation parameters were fixed at the compositional level, another factorial design was performed to optimise the scaling process with UIP1000HdT. Table 7 shows the levels of the selected factors as well as the responses obtained for each factor with the Plackett-Burman FFD.

Table 7 Scale-up FFD factors and responses for [redacted]-loaded NLCs.

Amplitude (%)	Batch Volume (L)	Sonication cycles	Jacket Temperature (°C)	Z-average (nm)	PDI
100	1	10	45	222.0	0.212
20	8	10	45	234.1	0.269
20	1	10	45	427.8	0.703
100	8	4	30	250.9	0.264
20	1	4	45	728.0	0.899
100	1	4	30	255.0	0.265
100	1	10	30	211.9	0.221
20	8	10	30	497.1	0.674
100	8	4	45	265.4	0.311
100	8	10	45	214.1	0.205
100	8	10	30	218.9	0.223
20	1	4	30	677.2	0.853

The regression equation (11) obtained after the Z-average FFD was the following:

$$Z - average (nm) = 778,7 - 3.540\% Amplitude - 25.66 Sonication cycles \quad (11)$$

The R²(adjusted) value was 70.92% and the R²(predicted) value was 55.67%.

The regression equation (12) obtained after the Pdi FFD was the following:

$$Pdi = 1.009 - 0.00552\% Amplitude - 0.0288 Sonication cycles \quad (12)$$

The $R^2(\text{adjusted})$ value was 79.18% and the $R^2(\text{predicted})$ value was 61.86%.

After regression, different conclusions were drawn. The % amplitude factor had a significant influence on particle size and the Pdl. A higher amplitude in the sonotrode oscillation caused a higher cavitation energy and, consequently, smaller particle sizes. The number of sonication cycles also proved to be a significant factor for the Z-average and Pdl. Logically, the more times the formulation passes through a flow cell under sonication, the more the particle hydrodynamic diameter is reduced and the more monodisperse the particle population is.

A file from the memory card of UIP1000HdT can be obtained that contains information on temperatures, sonication energies (Ws) and powers during the whole sonication process. From the sonication energy data and the characterisation performed with the aliquots taken in the premix and after each cycle, it was possible to perform non-linear regression and obtain a mathematical model (Figures 24 and 25) to predict the size and the Pdl as a function of the sonication energy normalised by the batch volume (Ws/L).

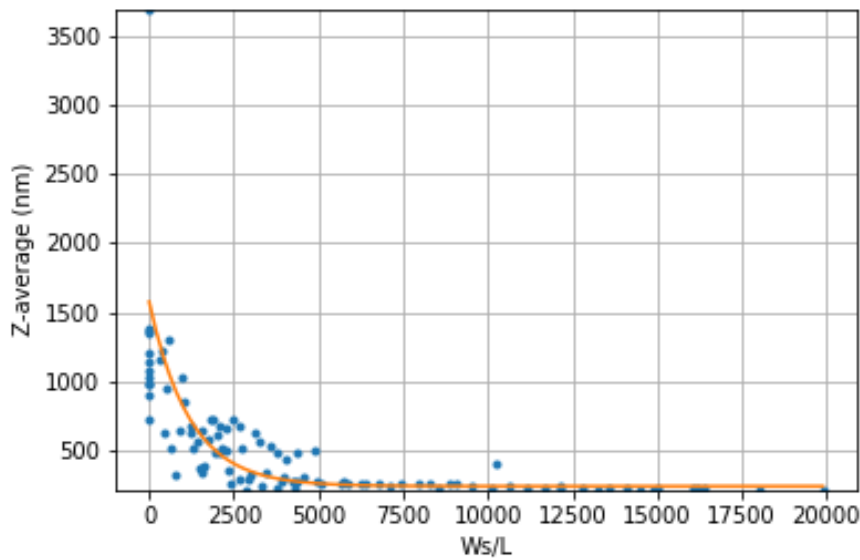


Figure 24 Z-average data modelling from the sonication energy (Ws/L) record and the aliquots characterised by DLS.

From the modelling of the data obtained for the Z-average as a function of the sonication energy (Ws/L), the following equation was obtained:

$$Z - average (nm) = 1335.43e^{\frac{(-Ws)}{1991}} + 239.82 \quad (13)$$

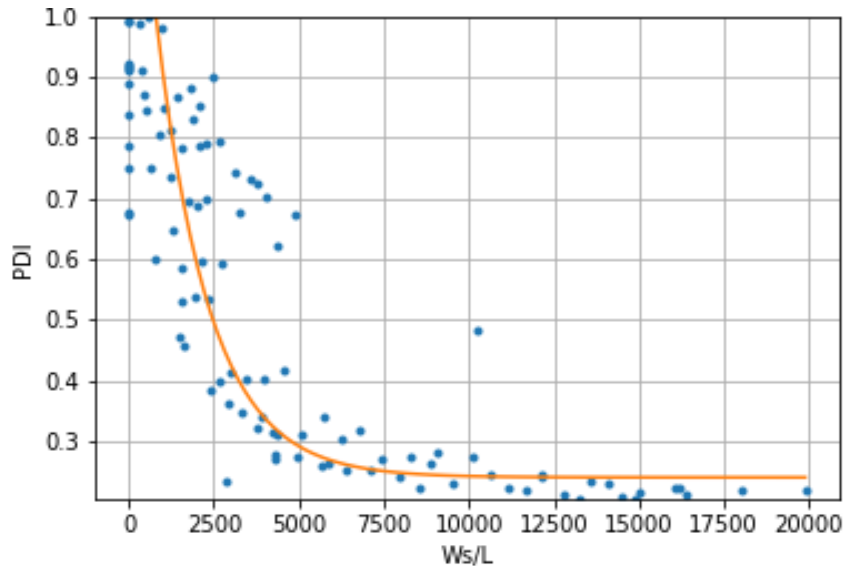


Figure 25 PDI data modelling from the sonication energy (Ws/L) record and the aliquots characterised by DLS.

From the modelling of the data obtained for the PDI as a function of the sonication energy (Ws/L), the following equation was obtained:

$$PDI = 1.260e^{\frac{(-Ws)}{1560}} + 0.241 \quad (14)$$

Once the equations for the Z-average and PDI were obtained, different values of energy/L were simulated to estimate the energy range necessary to obtain a hydrodynamic diameter less than 250 nm and a PDI < 0.3. Table 8 shows the simulation results for both responses. For an energy of 6000 Ws/L, a PDI of 0.268 and a Z-average of 248.48 nm would be obtained, i.e., about 48000 Ws of sonication would be needed for a batch size of 8 L.

Table 8 PDI and Z-average prediction of [redacted]-loaded NLCs as a function of the sonication energy per L of formulation.

Sonication Energy (Ws/L)	Predicted PDI	Predicted Z-average (nm)
1000	0.905	816.55
2000	0.591	488.89
3000	0.425	347.39
4000	0.338	286.27
5000	0.292	259.88
6000	0.268	248.48
7000	0.255	243.56
8000	0.248	241.43
9000	0.245	240.52
10000	0.243	240.12
11000	0.242	239.95
12000	0.242	239.87

6.4.3. Stability studies

Except for the PDI, after 1 year at 25°C/60% RH, the p-values of the regression slope were above 0.05. Thus, the regression lines were statistically equal to zero, which means that the NLCs kept

their hydrodynamic diameter, Z-potential, ██████████ content, %EE and Pdl stable under these conditions (Figure 26, Table 9).

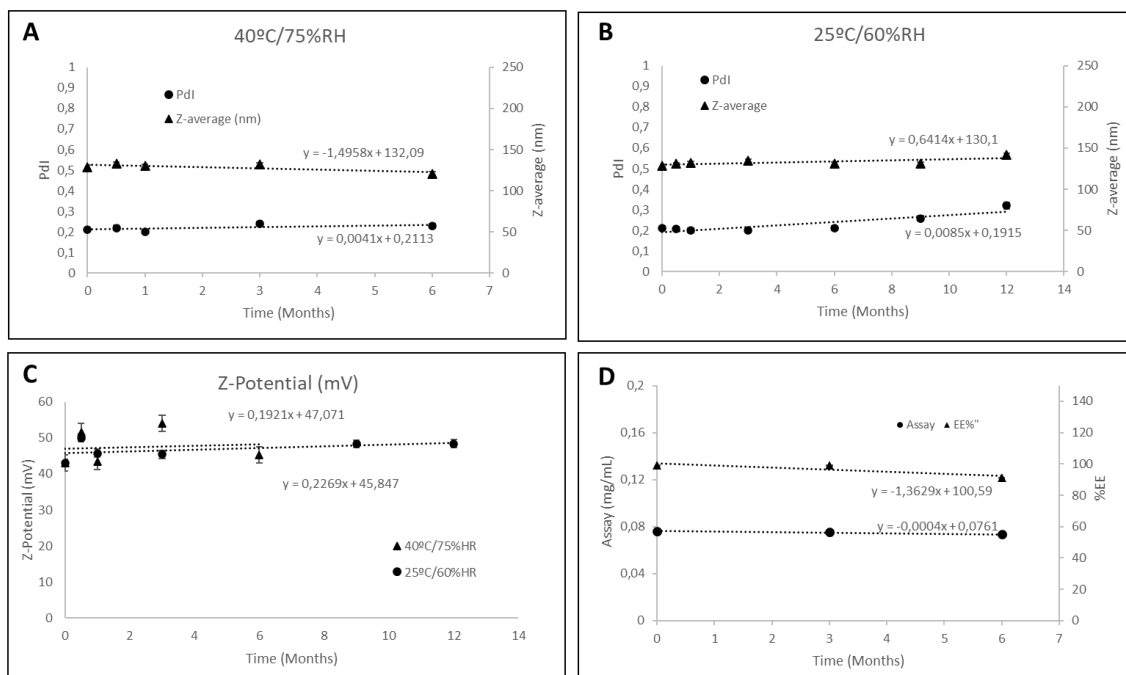


Figure 26 Stability studies. (A) Placebo NLC Z-average and Pdl stability plot during 6 months at $40 \pm 2^\circ\text{C}/75 \pm 5\% \text{RH}$. (B) Placebo NLC Z-average and Pdl stability plot during 12 months at $25 \pm 2^\circ\text{C}/60 \pm 5\% \text{RH}$. (C) Placebo NLC Z-potential stability plot during 6 and 12 months at $40 \pm 2^\circ\text{C}/75 \pm 5\% \text{RH}$ and at $25 \pm 2^\circ\text{C}/60 \pm 5\% \text{RH}$, respectively. (D) ██████████ loaded NLC assay and %EE stability plot during 6 months at $40 \pm 2^\circ\text{C}/75 \pm 5\% \text{RH}$.

The Pdl increased to a value of 0.32 after 12 months at 25°C and the p-value of the regression slope was 0.0041, indicating that the slope was not equal to zero. The nanoparticles remained as a monodisperse population. Hence, technically it was a stable formulation, and the applicable acceptance limit would be < 0.35 . The lack of significant variations under accelerated conditions, according to ICH Q1E [European Commission ICH Q1E Evaluation of stability data, 2003], means that the estimated product shelf-life can be extended up to two times, but should not be more than 12 months beyond the period covered by the long-term data, which is up to 24 months in this case.

Table 9 NLCs stability regression slopes.

Condition	12 months at $25^\circ/60\% \text{RH}$			6 months at $40^\circ\text{C}/75\% \text{RH}$			HPLC assay (mg/mL)	%EE
	Z-average (nm)	Pdl	Z-potential (mV)	Z-average (nm)	Pdl	Z-potential (mV)		
Slope	0.6414	0.0085	0.2269	-1.4956	0.0041	0.1921	0.0004	1.3629
p-value	0.090	0.009	0.376	0.118	0.242	0.881	0.139	0.338

In the first process, the microscopic structure of NLCs was not characterised. The %EE was characterised along with the rest of the physicochemical parameters and if they were compliant, the lot was tested by IVPT.

Batches were produced at a concentration higher than 0.40% w/w. Surprisingly, although the %EE was close to 100% when IVPT was performed, ██████████ permeated even less than at the

lowest dose (0.10% w/w). It was then that the microscopic aspect was characterised and crystal formation was observed. These microcrystals were artefacts that separated NLCs from the free [REDACTED], since they did not pass through the filter in the crystal form and the %EE values were therefore false. It was then that the highest encapsulable dose was determined. From this moment on, the microscopic structure was always characterised alongside the %EE assays.

To determine the maximum concentration for incorporation into the nanoformulations, NLCs with increasing concentrations of [REDACTED] were analysed by optical microscopy to observe crystal formation. They were also observed after 3 months in the 25°C/60% RH chamber.

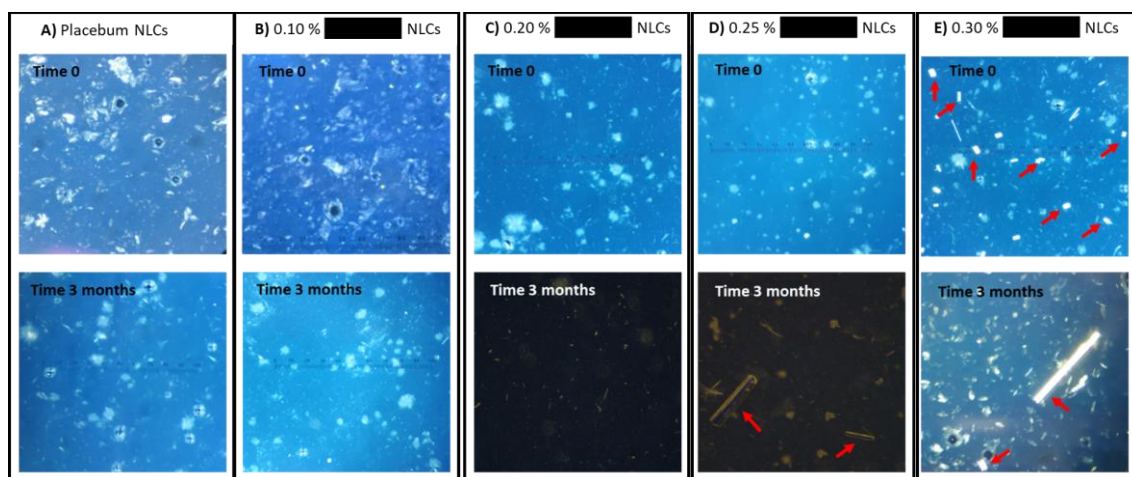


Figure 27 Optical microscope images at time 0 and after 3 months at 25°C/60% RH. (A) Placebo NLCs. (B) 0.10% [REDACTED]-NLCs. (C) 0.20% [REDACTED]-NLCs. (D) 0.25% [REDACTED]-NLCs. (E) 0.30% [REDACTED]-NLCs. [REDACTED] crystals are marked with red arrows. Images were captured using 40x magnifications.

After 3 months, there was no [REDACTED] crystal formation for concentrations up to 0.20% (Figure 27). However, for concentrations of 0.25%, some crystals were observed (red arrows in Figure 27). The 0.30% [REDACTED]-NLC formulation showed [REDACTED] crystals both at time 0 and after 3 months. Based on these results, the 0.20% dose was established as the maximum dose to be encapsulated into the NLCs.

6.4.4. *In vitro* permeation tests on dermatomised pig skin

An *in vitro* permeation test was performed with dermatomised pig skin using fresh 0.1% w/w [REDACTED]-loaded NLCs, 0.20% w/w [REDACTED]-loaded NLCs, 0.10% w/w ethanol:water (40:60) formulation and 0.20% w/w ethanol:water (40:60) formulation.

The amount of permeated [REDACTED] after 24 h for the 0.20% w/w formulation of NLCs was approximately twice that of the 0.1% formulation (Figure 28). When comparing the 0.20% dose formulated in the NLCs and the hydroalcoholic solution, the absorption-promoting effect of the NLCs was verified, since both the slope and the amount permeated after 24 h were considerably higher. As for the 0.1% dose, no significant differences between the NLCs and ethanol solution were observed. However, it is remarkable that the NLCs had an absorption-promoting effect at this dose that was in the same order as that of the ethanol solution.

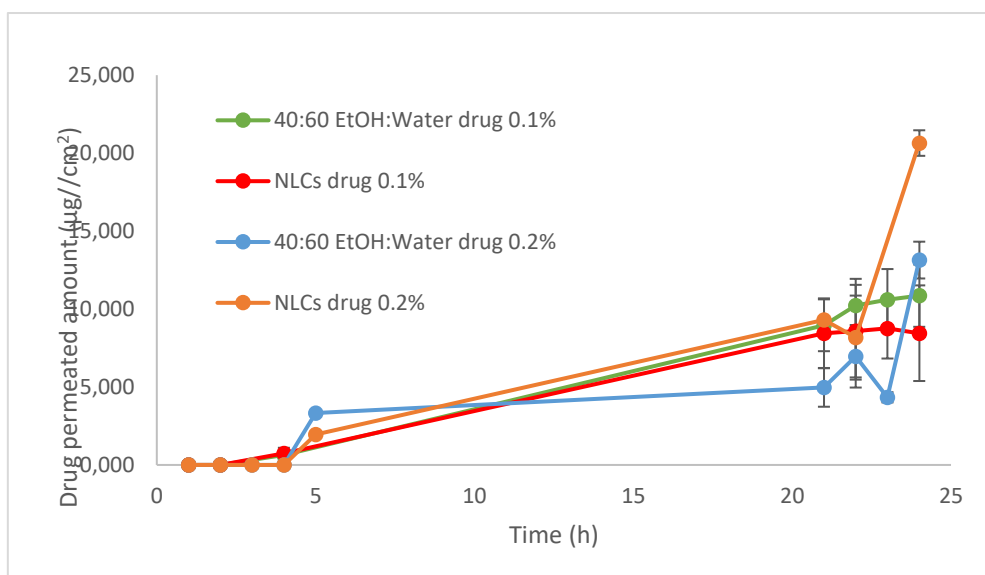


Figure 28 Transdermal XXXXXXXXXX NLCs and EtOH:water formulations in dermatomised pig skin at 0.1% and 0.2% w/w doses. The results show the median and interquartile coefficient. $n = 5$ replicates.

The estimation of the different permeation parameters indicates the mechanisms that most influence the skin permeation process (Table 10). When analysing the transdermal flux (J_{sup}) and the permeation coefficient (K_p) of the different formulations, it can be observed that they were higher for the NLCs than for the hydroalcoholic solution at the same XXXXXXXXXX concentration. The same occurred with the 0.10% dose, where the parameters of the NLCs were higher than those of the hydroalcoholic solution due to the absorption-promoting effect of the vehicle. The parameter related to P_2 partitioning was also higher for the NLCs than for the hydroalcoholic formulations at the same concentration. This parameter is proportional to the solubility of the drug in the stratum corneum and inversely proportional to the solubility of the drug in the vehicle. In other words, P_2 is the differential solubility of XXXXXXXXXX between the vehicle and the skin. Due to the high solubility of XXXXXXXXXX in ethanol, this parameter was lower for control hydroalcoholic solutions and higher for the NLCs. As for the P_1 parameter, no significant differences were observed between the alcoholic solution and NLCs for the 0.10% dose. When the dose was increased to 0.20%, the P_1 parameter was higher for the NLCs than the hydroalcoholic solution, probably due to the increase in the concentration difference in the skin layers when the dose of XXXXXXXXXX was increased. Finally, as for the T_{lag} , i.e., the time required for XXXXXXXXXX permeation to reach steady state (steady flow), it was lower in the case of the NLCs, but there was a large difference between the 0.10% and 0.20% doses. As the dose of API increased, the flux increased and as it was constant, more time was required to reach steady state.

Table 10 Permeation parameters of nanoparticles before and after lyophilisation of XXXXXXXXXX NLCs and EtOH:water formulations in dermatomised pig skin at 0.1 and 0.2% w/w doses. The results show the median and interquartile coefficient.

Parameter	0.1% w/w EtOH:water (40:60)	0.1% w/w XXXXXXXXXX loaded NLCs	0.2% w/w EtOH:water (40:60)	0.2% w/w XXXXXXXXXX loaded NLCs
$J_{sup}(\mu\text{g}/\text{h}\cdot\text{cm}^2)$	0.405 ± 0.098	0.420 ± 0.132	2.544 ± 1.477	3.989 ± 1.1799

K_p (cm/h)	0.0004 ± 0.0001	0.0004 ± 0.0001	0.0015 ± 0.0007	0.0020 ± 0.0006
P₂ (1/h)	0.046 ± 0.020	0.084 ± 0.002	0.008 ± 0.002	0.009 ± 0.001
P₁ (cm)	0.008 ± 0.005	0.005 ± 0.001	0.155 ± 0.103	0.219 ± 0.075
t_{lag} (h)	3.637 ± 0.850	1.983 ± 0.036	20.273 ± 5.456	19.496 ± 1.2470

6.4.5. Confocal Fluorescence Microscopy NLCs Biodistribution

After the permeation experiment with the fluorochrome nanoformulations, the skin was observed under a confocal microscope to evaluate the skin distribution of both fluorochromes. The literature has described a large number of fluorochromes that are included in nanoparticles for localisation in the skin. Usually, the selection of the tracking compound is based on the aim of the experiment. In this case, C6 was selected as the fluorescent small molecule model and LRB was selected as the lipid covalently bound to the fluorophore Rhodamine B to track the NLCs. To improve visualisation, cell nuclei were stained with Hoechst (blue colour). The autofluorescence value in the red channel (corresponding to LRB) was 5.5 AU and 4.6 AU for human scalp and pig skin, respectively, while that of the green channel (corresponding to C6) was 0.7 and 0.6 AU, respectively. These values were subtracted from the mean intensity of the samples. Using ImageJ, linear segments were drawn to analyse the intensity profile as a function of the depth (in μm). The yellow colour corresponds to the co-localisation of both fluorochromes.

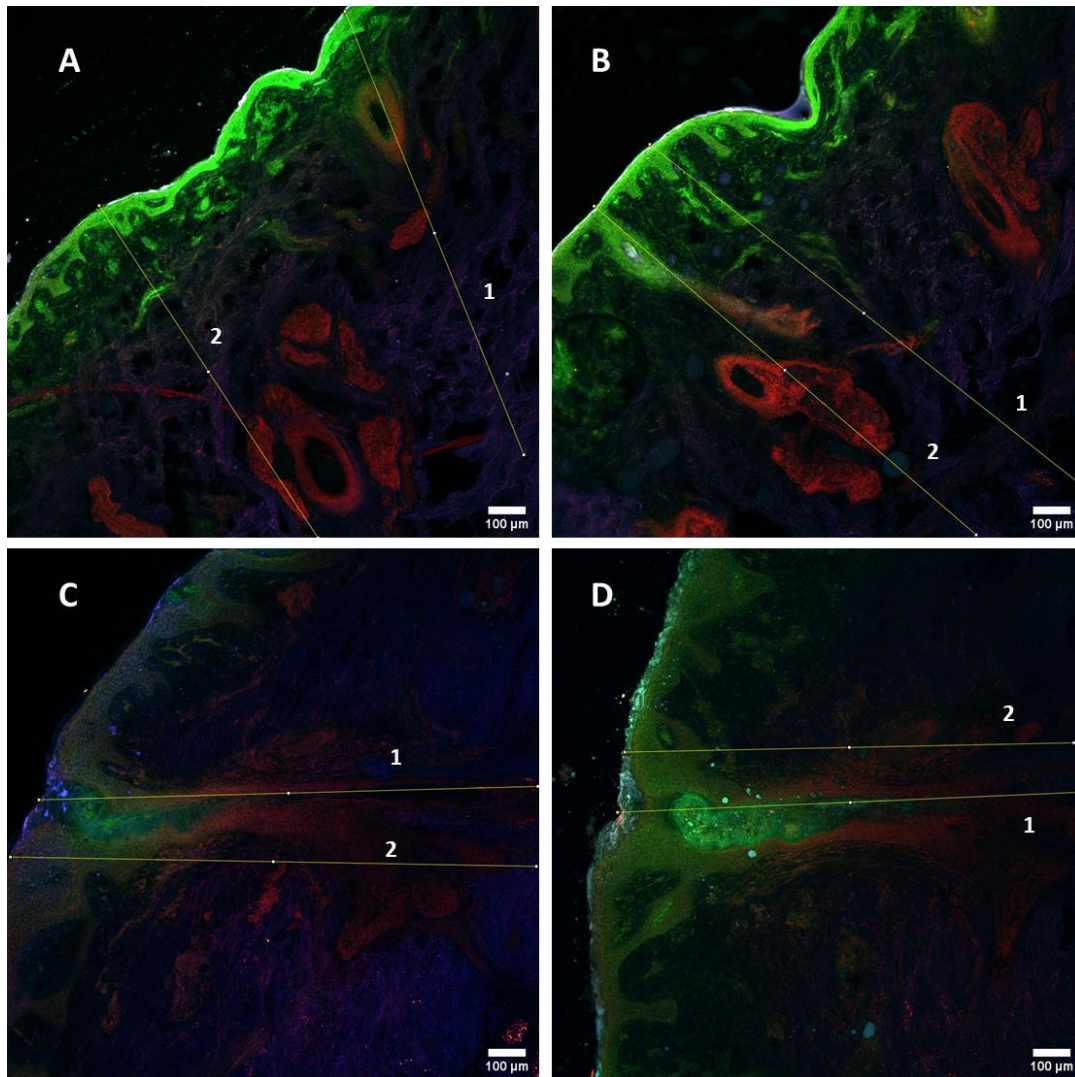


Figure 29 Confocal fluorescence microscopy images of human scalp cross-sections. Green colour corresponds to C6 and red to LRB fluorescence. (A, B) C6-loaded LRB-labelled NLCs. (C, D) Free C6 and LRB control solution. Lines numbered 1–2 in Figure 29 A, B, C and D correspond to multichannel intensity plot profiles as a function of the depth (μm) (see Figure 30). The images were captured using 10 \times magnifications.

Figure 29 A, B shows the biodistribution patterns of the C6 and LRB fluorophores vehiculated in NLCs (C6-LRB-NLCs) in the human scalp. Figure 29 C, D shows the biodistribution patterns of free-C6 and free-LRB in the human scalp. In the images, two lines were drawn from the stratum corneum to the deeper layers of the skin.

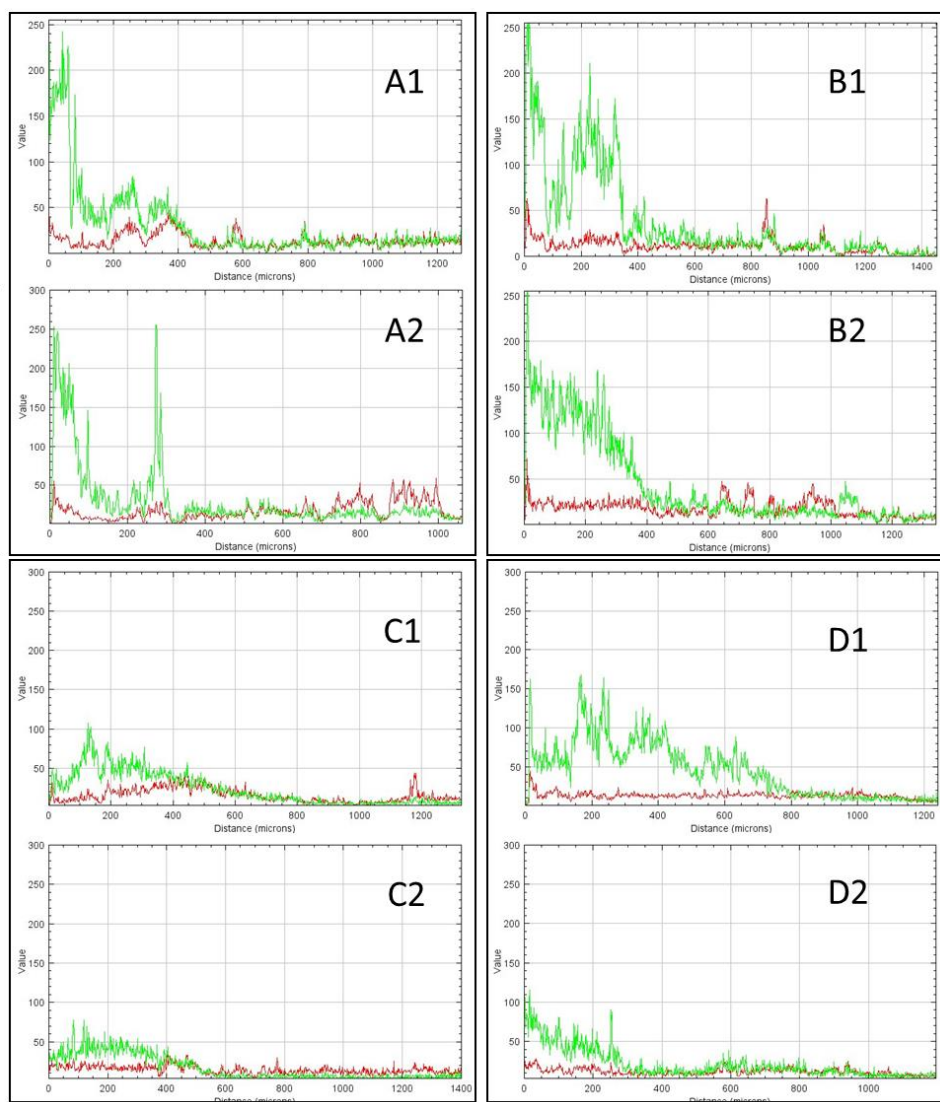


Figure 30 Confocal fluorescence microscopy plot intensity profiles of human scalp cross-sections corresponding to the lines drawn in the images of Figure 29.

As can be seen in Figure 30 A1 and B1 corresponding to superficial hair follicles (lines A1 and B1), the intensity of C6 was between 50 and 200 AU (depth < 400 μm). Below the follicle, at depths beyond 400 μm , the intensity of C6 was low (around 10AU), indicating that C6 did not reach the deeper dermis regions. Regarding the intensity of the red fluorescence corresponding to the localisation of LRB, a similar behaviour was observed. The superficial hair follicles showed an intensity value between 25 and 50 AU from the surface to a depth of 400 μm . As for the spectrums in Figure 30 A2 and B2, the accumulation in the sebaceous gland was verified by the increase in the intensity of the red fluorescence signal at around 600-1000 μm .

The biodistribution of the Free-C6-LRB control solution was different (Figure 29 C and D). As can be seen in spectrums C1 and D1 (Figure 30), the intensity in the superficial follicles was not more than 50 AU for C6 and not more than 25 AU for LRB, significantly below the values observed for the C6-LRB-NLCs. When the fluorophores were not delivered in the nanoparticles, the accumulation in the hair follicles was much lower. Furthermore, accumulation in the sebaceous glands was not observed (Figure 30 C2 and D2). When observing the stratum corneum and epidermis (thickness approximately 100 μm), an intense green colouration was observed, produced by the accumulation of C6 when vehiculated in the NLCs. If the intensities at this depth

are compared between images A, B and C, D, it can be observed that the green intensity is about 3 to 4 times higher in the case of C6-loaded NLCs (150-200 vs. 50 AU). This also corroborates the possibility of using these nanosystems as delivery systems targeting the epidermis.

Analysis on pig skin showed a biodistribution similar to that observed in the human scalp. Although pig skin has a thicker stratum corneum and does not contain sebaceous glands, differences were also observed between the cutaneous biodistribution of the fluorophore vehicle and the control solution (Figures 31 and 32).

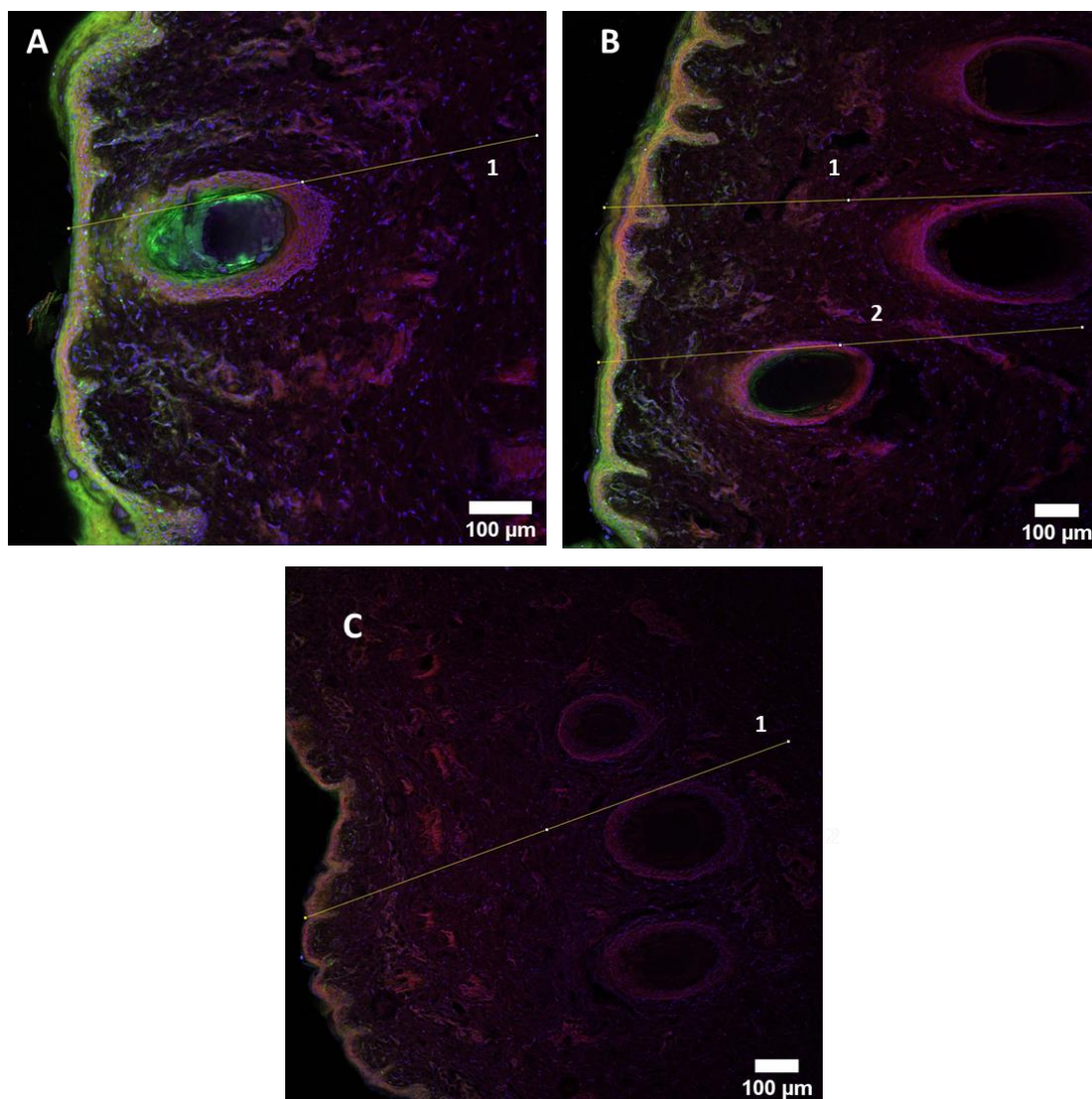


Figure 31 Confocal fluorescence microscopy images of pig skin cross-sections. Green colour corresponds to C6 and red to LRB fluorescence. (A, B) C6-loaded LRB-labelled NLCs. (C, D) Free C6 and LRB control solution. Lines numbered 1–2 in Figure 31 A, B, and C correspond to multichannel intensity plot profiles as a function of the depth (μm) (see Figure 32). The images were captured using 10 \times magnifications.

Figure 31 A, B shows the biodistribution patterns of the C6 and LRB fluorophores vehiculated in NLCs (C6-LRB-NLCs) in pig skin. Figure 31 C, D shows the biodistribution patterns of free-C6 and free-LRB in pig skin. In the image, a line was drawn from the stratum corneum to the deeper regions of the skin. In Figure 31 B, two lines were drawn: line 1, corresponding to a superficial

hair follicle, and line 2, corresponding to deeper hair follicles. All the lines crossed a section of the outer root sheath, including in Figure 31 A, B and C.

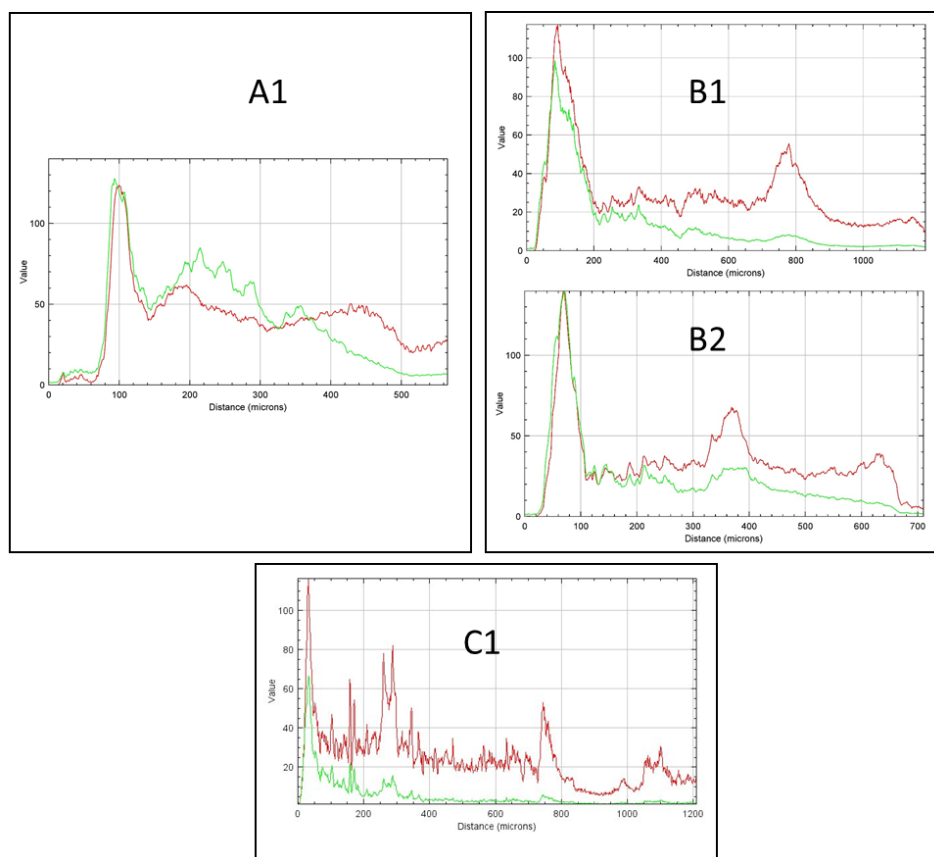


Figure 32 Confocal fluorescence microscopy plot intensity profiles of pig skin cross-sections corresponding to the lines drawn in the images of Figure 31.

As can be seen in Figure 32 A1 and B2 corresponding to superficial hair follicles (lines A1 and B2), the intensity of C6 was between 50 and 100 AU (depth < 400 μm). Below the follicle, at depths beyond 400 μm , the intensity of C6 dropped to 10 AU, indicating that C6 did not reach the deeper dermis regions. Regarding the intensity of the red fluorescence corresponding to the localisation of LRB, a different behaviour was observed. The superficial hair follicles showed an intensity value between 50 and 100 AU from the surface to a depth of 400 μm . This intensity was maintained below the hair follicle. When comparing the profiles in Figure 31 B, a difference in the biodistribution of C6 was observed. In the superficial follicle (Figure 32 B2) at a depth of about 350 μm , an LRB peak with an intensity of more than 50 AU was observed, coinciding with a C6 peak of about 30 AU. As for the deeper follicle (Figure 32 B1) at about 800 μm , an LRB peak with an intensity between 40 and 60 AU was observed, but not for C6, which remained at about 10 AU. This indicated that after the permeation of C6-LRB-NLCs in the pig skin, C6 accumulated in follicles up to a depth of 350 μm , but not in the deeper follicles.

Looking at the biodistribution of free-C6 and free-LRB, Figure 31 C shows the promoter effect of NLCs in pig skin too. Although there was an intensity peak for the red fluorescence signal, indicating some LRB accumulation in the follicle at 800 μm , comparison of the intensities with those in Figure 31 A and B showed that the intensities were lower. These intensities were around 20 AU for LRB and < 10 AU for C6 at depths greater than 200 μm .

These results explain the biodistribution of these two hydrophobic fluorophores carried in the NLCs both in the human scalp and pig skin. The intensity of the green fluorescence signal, corresponding to the accumulation of C6, was greater in the epidermis and in the upper part of the hair follicle, decreasing with increasing depth in the skin. The images obtained by confocal microscopy indicated that the *in vitro* skin penetration by C6 in the NLCs accumulated in the epidermis and hair follicle infundibulum, but did not penetrate into the deepest parts of the hair follicles. This suggested that C6 is released when it comes into contact with the lipids of the stratum corneum due to its hydrophobic nature, leading to greater accumulation in the less deep areas.

The intensity of the fluorescence signal corresponding to LRB was less than that of C6 in the epidermis, but greater than that of C6 in the deeper parts of the hair follicle. The fact that an accumulation of LRB was observed at these depths suggests that this fluorophore is found in the lipid nucleus of the nanoparticles and travels with them towards the bulb of the follicle. As described in the literature, lipid nanoparticles accumulate in skin annexes due to their geometry and size. Thus, they can deliver small molecules to hair follicles through the transfollicular route, limiting distribution to the rest of the skin and to the systemic circulation [**Ghasemiyeh P et al. 2019**].

The greater presence of sebaceous glands in the human scalp compared to pig skin allowed us to observe the accumulation of LRBs vehiculated in NLCs, probably due to the lipid nature of the nanoparticles and the hydrophobicity of the sebocyte environment.

6.4.6. Immunohistofluorescence to study NLC biodistribution

Confocal laser microscopy is usually employed to study the biodistribution of nanoparticles in different tissues. Unfortunately, this is an indirect measurement, as there is no direct tracking of the API. There are other techniques to study topical biodistribution, such as skin layer separation [**Eloy Pena et al. 2020**], cyanoacrylate tape stripping [**Pin Dong et al 2020**] and dermatopharmacokinetics [**Herkenne C et al 2006**]. Techniques such as cyanoacrylate stripping can be used to study hair follicle targeting, but usually have a lower spatial resolution than immunohistofluorescence (IHF) and could have problems such as analytical interferences, quantification limit issues, a lack of complete recovery and matrix effects. IHF can be used to visualise any accumulation in different anatomical regions of a hair follicle.

Thus, to confirm the data obtained in the previous section, an IHF experiment was carried out. Rabbit anti-DEX IgG and Alexa Fluor 488 goat anti-rabbit antibodies were employed so that direct visualisation of the drug in the green channel could be performed. Mouse anti-cytokeratin 14 IgG_{2a} and Alexa Fluor 594 goat anti-mouse antibodies were used to visualise the biodistribution of the highly expressed cytokeratin 14 in the epidermis and hair follicles in the red channel. The yellow channel corresponded to the co-localisation of cytokeratin 14 and DEX.

After the IHF experiment, a different behaviour was observed with respect to DEX-loaded NLCs (Figure 33) and DEX-FREE (Figure 34). The green colour indicated the localisation of DEX, while the red colour indicated the localisation of cytokeratin 14. In the same way as in the previous section, different lines were drawn to compare the intensity profiles. Surface plots were obtained to compare the intensities in a more visual way.

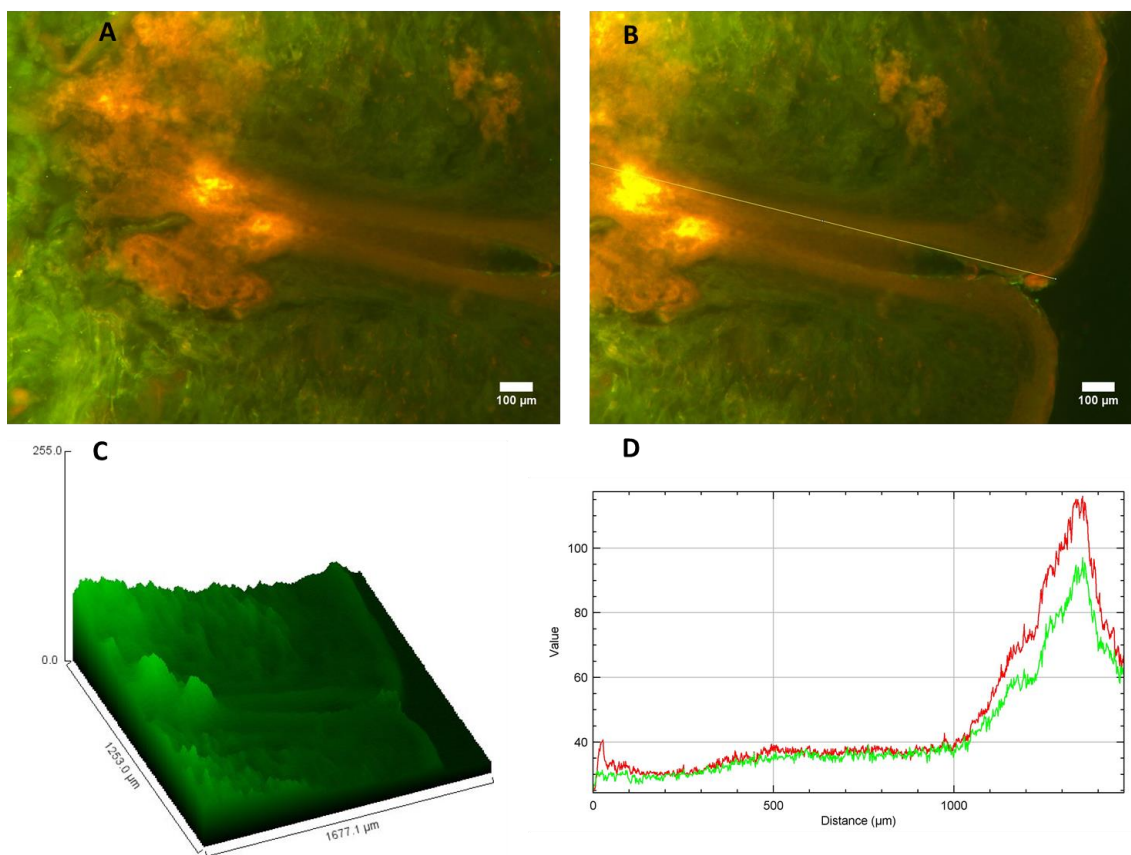


Figure 33 IHF images of a human scalp cross-section. The green colour indicates the localisation of DEX, while the red colour indicates the localisation of cytochrome 14. (A, B) Fluorescence images of the DEX-loaded NLCs. (C) Surface plot of DEX green fluorescence intensity. (D) Red and green fluorescence intensity plot profiles as a function of the depth (μm). The images were captured using 10 \times magnifications.

Line 1 in Figure 33 A and B corresponds to the intensity across the lateral zone of a hair follicle. In this case, an accumulation of DEX was observed (intensity around 100 AU at a depth of 1400 μm). Figure 33 C shows a surface plot for DEX intensity, where the accumulation at a depth of 1400 μm can be observed. The peak at the depth of 1400 μm corresponds to the sebaceous gland of the follicle. In the spectrum of Figure 33 D, the co-localisation of cytochrome 14 (highly expressed in hair follicles and the epidermis) and DEX can be observed as they show coinciding peaks.

Regarding the permeation of FREE-DEX, the behaviour was different. Line 1 in Figure 34 C shows low intensity (about 20 AU) and no follicular targeting was observed when DEX was formulated in solution. This behaviour is also shown in the surface plots of Figure 34 B. In this case, the reagents necessary to perform cytochrome 14 staining were not available. Therefore, this staining was not performed.

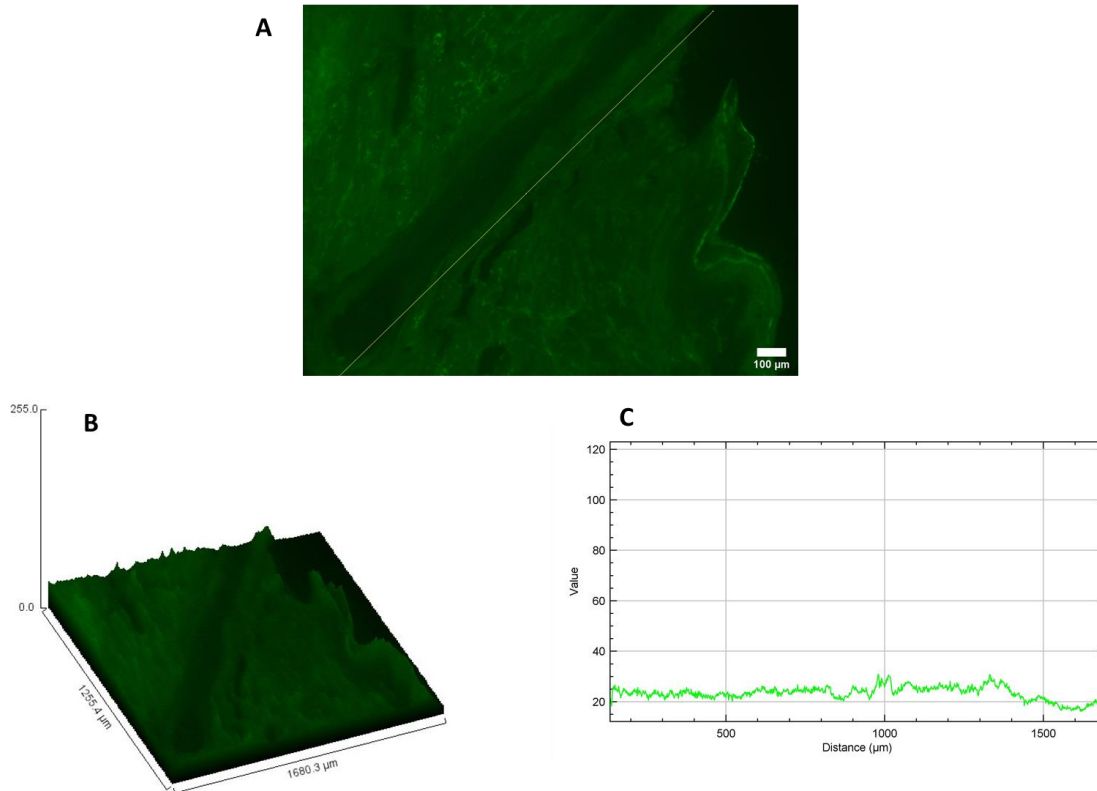


Figure 34 IHF images of a human scalp cross-section. Green colour indicates the localisation of DEX. (A) Fluorescence image of Free-DEX control solution. (C) Surface plot of DEX green fluorescence intensity. (D) Green fluorescence intensity plot profiles as a function of the depth (μm). The images were captured using 10 \times magnifications.

When comparing these results with those obtained by confocal microscopy, it can be observed that the biodistribution of DEX was similar to that of LRB, as it accumulated in the deep areas of the follicles ($> 400 \mu\text{m}$). These findings corroborate the high encapsulation efficiency results and suggest that it is possible to achieve a targeted release in the hair follicle by encapsulation in NLCs. As a result, a depot effect in the pilosebaceous unit is expected. This effect could, on the one hand, reduce the frequency of administration (from the 12 h usually used for topical corticosteroids to 24 h), decreasing associated adverse effects. On the other hand, a depot effect and the release of the drug at the site of action could improve treatment efficacy and reduce or avoid the systemic or intralesional administration of the drug, reducing systemic adverse effects (which are usually worse than the adverse effects arising from topical administrations) and patient discomfort caused by injections (for intralesional therapy). These facts should be evaluated in future clinical trials.

6.5. Conclusions

NLCs with a high drug loading capacity were successfully developed and optimised through a design of experiments for the active ingredient [REDACTED]. In addition, a response surface regression was used to obtain an accurate predictive model for the size and PDI of NLCs. The results of the design of experiments applied to the scale-up by means of the industrial ultrasonic processor UIP1000HdT were satisfactory since no significant differences of the batch volume were found in the size and PDI of the NLCs. Furthermore, it was possible to develop mathematical models to establish the amount of energy needed per L of batch (Ws/L) to obtain NLCs smaller than 260 nm that were monodisperse (PDI < 0.3). The NLCs were shown to be stable, with a shelf-life of 36 months. After the analysis of crystals by optical microscopy, the maximum concentration of [REDACTED] at 0.20% w/w was determined. The [REDACTED]

absorption-promoting effect of the NLCs was demonstrated by the increased permeation parameters when compared to a control of hydroalcoholic [REDACTED] solution after IVPT.

Confocal microscopy confirmed the accumulation of the nanoparticles in hair follicles and cutaneous annexes, thus proving their ability to achieve follicular targeting. These results were confirmed by the biodistribution of DEX, as observed with immunohistofluorescence, where DEX-loaded NLCs showed increased accumulation in hair follicles compared to FREE-DEX. Its high %EE, good physicochemical properties and localised release in hair follicles make this nanoformulation a very interesting candidate to improve the efficacy and reduce the adverse effects of [REDACTED]. Thus, a promising formulation for the topical administration of [REDACTED] was developed, which could reduce the adverse effects seen with the administration of oral [REDACTED] (e.g., decreased libido, ejaculatory disturbances and breast enlargement). Furthermore, due to the follicular targeting, a depot effect within the pilosebaceous unit might be possible, which could reduce the frequency of administration compared to classical formulations. The safety and efficacy profiles of the loaded NLCs should be verified in clinical trials to compare side effects.

6.6. Bibliography

Adil A, Godwin M. The effectiveness of treatments for androgenetic alopecia: A systematic review and meta-analysis. *J Am Acad Dermatol.* 2017 Jul;77(1):136-141.e5. DOI: 10.1016/j.jaad.2017.02.054. Epub 2017 Apr 7.

Bienová M, Kucerová R, Fiurásková M, Hajdúch M, Kolář Z. Androgenetic alopecia and current methods of treatment. *Acta Dermatovenerol Alp Pannonica Adriat.* 2005 Mar;14(1):5-8. PMID: 15818439.

Caserini M, Radicioni M, Leuratti C, Terragni E, Iorizzo M, Palmieri R. Effects of a novel finasteride 0.25% topical solution on scalp and serum dihydrotestosterone in healthy men with androgenetic alopecia. *Int J Clin Pharmacol Ther.* 2016 Jan;54(1):19-27. DOI: 10.5414/CP202467.

Chauhan I, Yasir M, Verma M, Singh AP. Nanostructured Lipid Carriers: A Groundbreaking Approach for Transdermal Drug Delivery. *Adv Pharm Bull.* 2020;10(2):150-165. doi:10.34172/apb.2020.021.

Drake L, Hordinsky M, Fiedler V, Swinehart J, Unger WP, Cotterill PC, Thiboutot DM, Lowe N, Jacobson C, Whiting D, Stieglitz S, Kraus SJ, Griffin EI, Weiss D, Carrington P, Gencheff C, Cole GW, Pariser DM, Epstein ES, Tanaka W, Dallob A, Vandormael K, Geissler L, Waldstreicher J. The effects of finasteride on scalp skin and serum androgen levels in men with androgenetic alopecia. *J Am Acad Dermatol.* 1999 Oct;41(4):550-4. PMID: 10495374.

Eman Gomaa, Heba A. Fathi, Noura G. Eissa, Mahmoud Elsabahy, Methods for preparation of nanostructured lipid carriers, *Methods*, Volume 199, 2022, Pages 3-8, DOI: 10.1016/j.ymeth.2021.05.003.

European Centre for the Validation of Alternative Methods (CVAM). Test Guideline for Skin Absorption: *In Vitro* Method; Official Journal of the European Union Method B.45 of Annex to 440/2008/EC; European Commission: Paris, France, 2008.

European Commission, ICH Q1E Evaluation of stability data, August 2003CPMP/ICH/420/02.

Fang Chia-Lang, A. Al-Suwayeh Saleh, Fang Jia-You, Nanostructured Lipid Carriers (NLCs) for Drug Delivery and Targeting, Recent Patents on Nanotechnology, Volume 7, Number 1, 2013, pp. 41-55(15), Bentham Science Publishers, DOI: 10.2174/187221013804484827.

Ghasemiyeh P, Azadi A, Daneshamouz S, Heidari R, Azarpira N, Mohammadi-Samani S. Cyproterone acetate-loaded nanostructured lipid carriers: effect of particle size on skin penetration and follicular targeting. *Pharm Dev Technol.* 2019 Sep;24(7):812-823. DOI: 10.1080/10837450.2019.1596133. Epub 2019 Apr 26. PMID: 30889371.

Hajheydari Z, Akbari J, Saeedi M, Shokoohi L. Comparing the therapeutic effects of finasteride gel and tablet in treatment of the androgenetic alopecia. *Indian J Dermatol Venereol Leprol.* 2009 Jan-Feb;75(1):47-51. DOI: 10.4103/0378-6323.45220.

Mysore V. Finasteride and sexual side effects. *Indian Dermatol Online J.* 2012;3(1):62-65. DOI:10.4103/2229-5178.93496.

Pena-Rodríguez, E.; Moreno, M.C.; Blanco-Fernandez, B.; González, J.; Fernández-Campos, F. Epidermal Delivery of Retinyl Palmitate Loaded Transfersomes: Penetration and Biodistribution Studies. *Pharmaceutics* 2020, 12, 112. DOI: 10.3390/pharmaceutics12020112.

Pin Dong, Viktor Nikolaev, Marius Kröger, Christian Zoschke, Maxim E. Darvin, Christian Witzel, Jürgen Lademann, Alexa Patzelt, Monika Schäfer-Korting, Martina C. Meinke, Barrier-disrupted skin: Quantitative analysis of tape and cyanoacrylate stripping efficiency by multiphoton tomography, *International Journal of Pharmaceutics*, Volume 574, 2020, 118843, ISSN 0378-5173, DOI:/10.1016/j.ijpharm.2019.118843.

Rathnayake D, Sinclair R. Male androgenetic alopecia. *Expert Opin Pharmacother.* 2010 Jun;11(8):1295-304. DOI: 10.1517/14656561003752730.

Rossi R, Zatelli MC, Valentini A, Cavazzini P, Fallo F, del Senno L, degli Uberti EC. Evidence for androgen receptor gene expression and growth inhibitory effect of dihydrotestosterone on human adrenocortical cells. *J Endocrinol.* 1998 Dec;159(3):373-80. DOI: 10.1677/joe.0.1590373.

Chapter 7 - *In vitro* cell culture research

7.1. Introduction

Hair follicles are organs containing a wide variety of cell types. The high demand for pharmacological and dermocosmetics therapies to promote new hair growth makes it necessary to develop pre-clinical screening tools to accelerate research in this field. Hair follicles consist of epithelial and dermal components. Dermal papilla cells (DPCs) are mesenchymal cells that are deeply involved in hair development and growth as they act as a reservoir for growth factors, multipotent stem cells and other molecules that promote hair growth. For this reason, DPCs are one of the most commonly used cell lines to study the mechanisms of action of therapies for alopecia as well as to test their efficacy and safety and to look for synergies [Alka Madaan et al]. Hair follicles also have a very high level of proliferation and differentiation of keratinocytes, which ultimately leads to the production of hair fibres. Androgenic Alopecia (AGA) is characterised by miniaturised hair follicles with shortened growth cycles. Hence, it is believed that the ratio between the proliferation and differentiation of keratinocytes may be an important factor in AGA [Boyera et al].

In parallel to the studies of [REDACTED] encapsulation in NLCs, *in vitro* cell methods were developed to compare the efficacy of different active ingredients. To do this, immortalised human epidermal keratinocytes (HEK001) and immortalised human hair follicle DPCs were selected as the cell types mainly involved in the development of hair follicles.

The current treatment of AGA is based on two drugs: minoxidil and finasteride. Minoxidil was originally intended for the treatment of hypertension (after oral administration) due to its ability to block potassium channels and, thus, and subsequently induce vasodilatation. It was originally thought that the mechanism of action of this drug in the treatment of AGA (male or female) was related to its ability to induce vasodilation, which would improve irrigation and nutrient supply to the hair follicle. It has since been observed that this may not be the only mechanism responsible for the effect against AGA. Therefore, its mechanism of action is not fully understood. There is scientific evidence regarding the proliferative effect of minoxidil on keratinocytes [Howard P. Baden et al], but the concentrations differ in the different investigations and there is very little information regarding its effect on DPCs. As for finasteride, its inhibitory effect on 5AR is known, but it is not clear whether it can also influence other mechanisms of cell proliferation in both keratinocytes and DPCs. Furthermore, the influence of the combination of testosterone and finasteride on the growth of DPCs has not been described to date. That is why the different *in vitro* proliferation assays were performed.

7.2. Materials

Immortalised human hair follicle dermal papilla cells – hTERT (DPCs) (Abm Good, Richmond, Canada), Applied Cell Extracellular Matrix (Abm Good, Richmond, Canada), Prigrow III medium (Abm Good, Richmond, Canada), minoxidil (Sigma-Aldrich, St. Louis, MO, USA), testosterone (Fagron Ibérica, Barcelona, Spain), immortalised human epidermal keratinocytes (HEK001 cells) (ATCC Promochem Partnership, Manassas, VA, USA), Dulbecco's Modified Eagle Medium (DMEM, Life Technologies, Carlsbad, CA, USA) supplemented with 5% foetal bovine serum (FBS) (Life Technologies, Carlsbad, CA, USA), trypsin (Life Technologies, Carlsbad, CA, USA), MTT (3-[4,5-dimethylthiazol-2-yl]-2,5 diphenyl tetrazolium bromide) colorimetric assay (Sigma-Aldrich, St. Louis, MO, USA), keratinocyte serum-free (KSF) media supplemented with 100 µg/mL epidermal growth factor (EGF) and 20 µg/mL streptomycin (Life Technologies) were purchased to perform *in vitro* proliferation studies.

7.3. Methods

7.3.1. DPCs and HEK cell maintenance

HEK001 cells and DPCs were cultured in monolayer in 100-mm Petri dishes at 37°C in a humidified atmosphere with 5% CO₂. In the case of HEK001 cells, KSF media supplemented with 100 µg/mL of EGF, 20 U/mL of penicillin and 20 µg/mL of streptomycin were used to grow the cells. In the case of DPCs, an applied extracellular matrix composed mainly of type 1 collagen isolated from rat tail was incubated for 2 h at 37°C in a Petri dish at a concentration of 5 µg/cm². PBS from the collagen solution was aspirated and cells were grown using the Prigrow III medium. Mycoplasma-free maintenance was confirmed in all the cases every two weeks by PCR amplification.

7.3.2. HEK001 cells and DPCs proliferation set up

To test the influence of the active ingredients on keratinocytes, it was necessary to find the optimal culture settings. Conditions that are too favourable for proliferation would not allow the detection of the additional effects of the molecules being tested, while conditions that are too unfavourable for proliferation would prevent the desired effects from being observed.

HEK001 cells: Three different concentrations of cells per well were seeded (2500, 5000 and 7500 cells/well). The effect of the absence of EGF on the HEK001 cells was also studied. The starvation process consisted of incubating the cells in the absence of a nutrient (in this case EGF) for a given time interval (in this case for 24 h). This reduced the possible interference of the proliferative effect of EGF with the effects of the active ingredients to be tested. Cells were seeded in DMEM supplemented with 5 ng/mL of EGF, 5% FBS and 10% FBS. Table 11 shows the factors studied during the HEK001 cell proliferation setup.

Table 11 HEK001 cell proliferation setup factors and levels studied.

Factors	Levels
Seeding concentration	2500, 5000 and 7500 cells/well
DMEM supplementation	5 ng/mL EGF, 5% FBS and 10% FBS
Method	72 h of proliferation with and without starvation

DPCs: DPCs grow faster than HEK001 cells. Therefore, lower cell concentrations were chosen. Three different concentrations of cells per well were seeded (1500, 3000 and 6000 cells/well). Two concentrations (5 and 10 µg/cm²) of the applied extracellular collagen matrix were studied. The effect of testosterone (between 0 and 0.10 µM) on DPCs was also studied. Table 12 shows the factors studied during the DPC proliferation setup.

Table 12 DPC proliferation setup factors and levels studied.

Factors	Levels
Seeding concentration	1500, 3000 and 6000 cells/well

Applied Extracellular collagen matrix concentration	5 and 10 $\mu\text{g}/\text{cm}^2$
Testosterone concentration	0, 0.01 and 0.10 μM

7.3.3. *In vitro* HEK001 cell viability assays with finasteride, minoxidil and ebastine.

Once the appropriate setup for the *in vitro* HEK001 cell proliferation experiments was determined, the effects of different concentrations of finasteride, minoxidil and ebastine on HEK001 cell proliferation were studied. Cells were seeded at a density of 5000 cells/well in 96-well plates with KSF-EGF media. Untreated cells were also assessed and 5 ng/mL of EGF (1 nM) was included as a positive proliferation control. After 24 h, cells were treated with increasing doses of the compounds diluted in DMEM supplemented with 5% FBS. Table 13 shows the concentrations tested for each of the active ingredients.

Table 13 Finasteride, ebastine and minoxidil tested conditions on HEK001.

Finasteride	Minoxidil	Ebastine
10 μM	10 μM	10 μM
1 μM	5 μM	5 μM
100 nM	1 μM	1 μM
10 nM	100 nM	100 nM
5 nM	10 nM	10 nM
1 nM	5 nM	5 nM

Sextuplicates of each condition were performed. After 72 h of proliferation, cell viability was assessed using the MTT colorimetric assay. Cell survival for all the experiments was expressed as the percentage of viable cells relative to that of the untreated cells (defined as 100%).

7.3.4. *In vitro* DPCs viability assays with finasteride, minoxidil and testosterone.

Similarly, the effect of different concentrations of finasteride, minoxidil and testosterone on DPCs was studied. In this case, the wells were treated with collagen at a concentration of 5 $\mu\text{g}/\text{cm}^2$ and the density of the seeded cells was 3000 cells/well in 96-well plates containing Prigrow III media. After 24 h, cells were treated with increasing doses of the compounds diluted in DMEM supplemented with 5% FBS. Untreated cells were also assessed and testosterone was included as a negative proliferation control. Table 14 shows the concentrations tested for each of the active ingredients.

Table 14 Finasteride, testosterone, and minoxidil on DPCs.

Finasteride	Minoxidil	Testosterone
50 μM	20 μM	20 μM

10 μ M	10 μ M	10 μ M
1 μ M	1 μ M	
100 nM	100 nM	

Sextuplicates of each condition were performed. After 72 h of proliferation, cell viability was assessed using the MTT colorimetric assay. Cell survival for all the experiments was expressed as the percentage of viable cells relative to that of the untreated cells (defined as 100%).

7.4. Results

7.4.1. HEK001 and DPCs proliferation set up

In vitro cell proliferation assays are used to determine whether or not cells are triggered to divide after exposure to a certain stimulus. To observe these proliferative effects, optimal conditions have to be established. Analysis of cell viability showed differences depending on the assayed conditions.

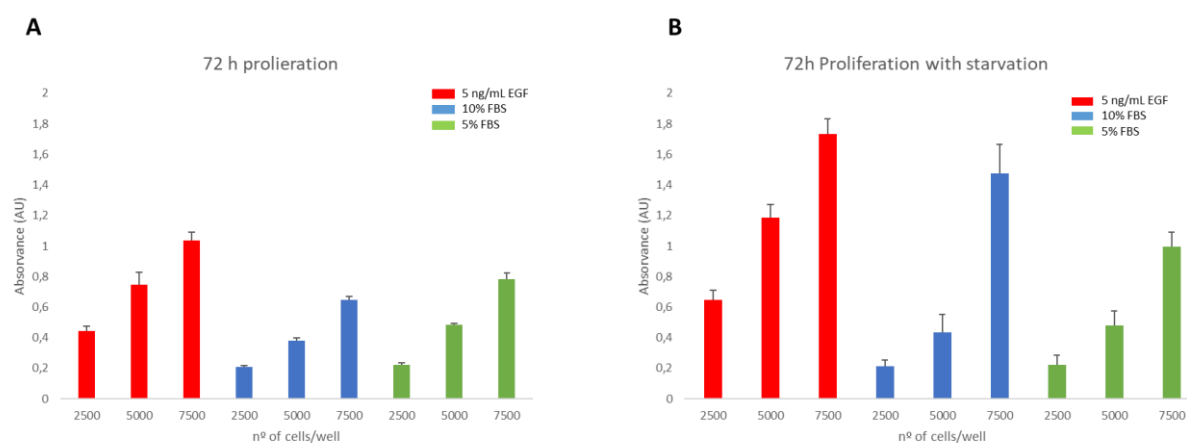


Figure 35 HEK001 cell proliferation setup. Red bars correspond to 5 ng/mL of EGF supplementation, blue bars correspond to 10% FBS supplementation and green bars correspond to 5% w/w FBS supplementation. (A) 72 h of HEK cell proliferation assays and (B) 72 h of proliferation assays with a 24-h starvation process.

Regarding growth medium supplementation, as expected, cell proliferation was higher in the presence of 5 ng/mL of EGF than in the presence of 5% and 10% FBS. In the absence of starvation (Figure 35 A), the results for the cells grown with 10% and 5% FBS, respectively, were very similar. The starvation process consisted of maintaining the cells without substrate (no EGF nor FBS) for the first 24 h of proliferation. This process (Figure 35 B) increased the differences between the cells grown with 10% and 5% FBS, respectively, especially at the highest cell density (7500 cells/well).

To find the basal conditions where proliferation was not highly induced and the margin to test the active ingredients was increased to be able to observe possible proliferative inductions, the definitive setup was chosen. Therefore, the concentration of 5000 cells/well seemed to be the most appropriate to work with in subsequent tests. The starvation process did not seem to cause significant differences in proliferation. Hence, this process was avoided. The 5% FBS supplementation was chosen as it was sufficient for the cells to proliferate at an adequate rate when seeded at a density of 5000 cells/well.

Once the conditions for the proliferation assays were determined for the HEK001 cells, the setup for the DPCs was established. Cell proliferation assays were performed under different conditions (Figure 36).

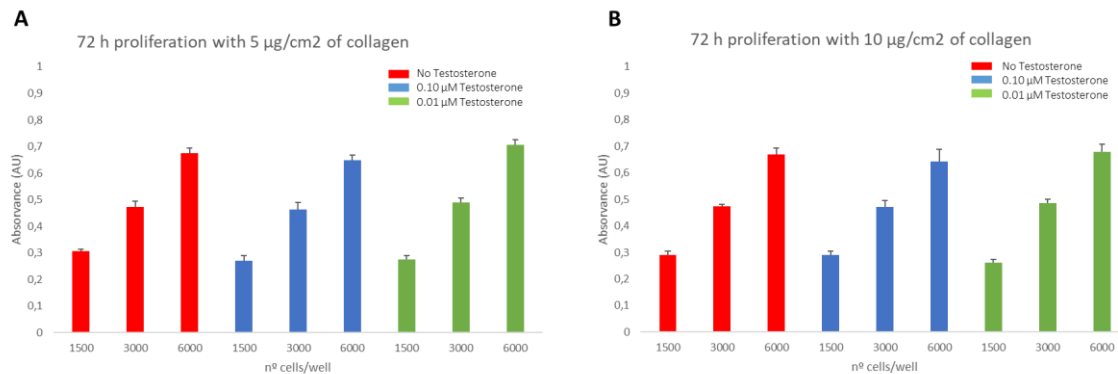


Figure 36 DPCs proliferation setup. Red bars correspond to proliferation in the absence of testosterone, blue bars correspond to incubation with 0.10 µM testosterone and green bars correspond to incubation with 0.01 µM testosterone. (A) 72 h of DPC proliferation assays with 5 µg/cm² of the applied collagen extracellular matrix and (B) 72 h of DPC proliferation assays with 10 µg/cm² of the applied collagen extracellular matrix. N = 1 experiment was performed in sextuplicate.

Comparing Figure 36 A and B, it can be seen that there was no difference between the collagen extracellular matrix concentrations. A concentration of 5 µg/cm² was sufficient for the cells to adhere adequately to the base of the well. As for the presence of testosterone, the proliferation of DPCs was neither positively nor negatively affected at the indicated concentrations (up to 0.10 µM). Finally, the appropriate cell density for future proliferation assays appeared to be 3000 cells/well as it provided absorbance results of approximately 0.5 AU.

In summary, after the proliferation setup for subsequent assays in DPCs, it was decided to increase the concentration of testosterone and seed 3000 cells/well after applying 5 µg/cm² of the collagen extracellular matrix.

7.4.2. *In vitro* HEK001 cell viability assays with finasteride, minoxidil and ebastine.

Once the conditions for the proliferation experiments were set up, HEK001 cell viability tests were performed after treatment with minoxidil, finasteride or ebastine. A positive control with 1 nM EGF was also added.

As seen in Figure 37, both minoxidil and ebastine as well as EGF showed a proliferation-promoting trend in HEK001 cells. As for finasteride, only the highest concentration showed a slight proliferative effect.

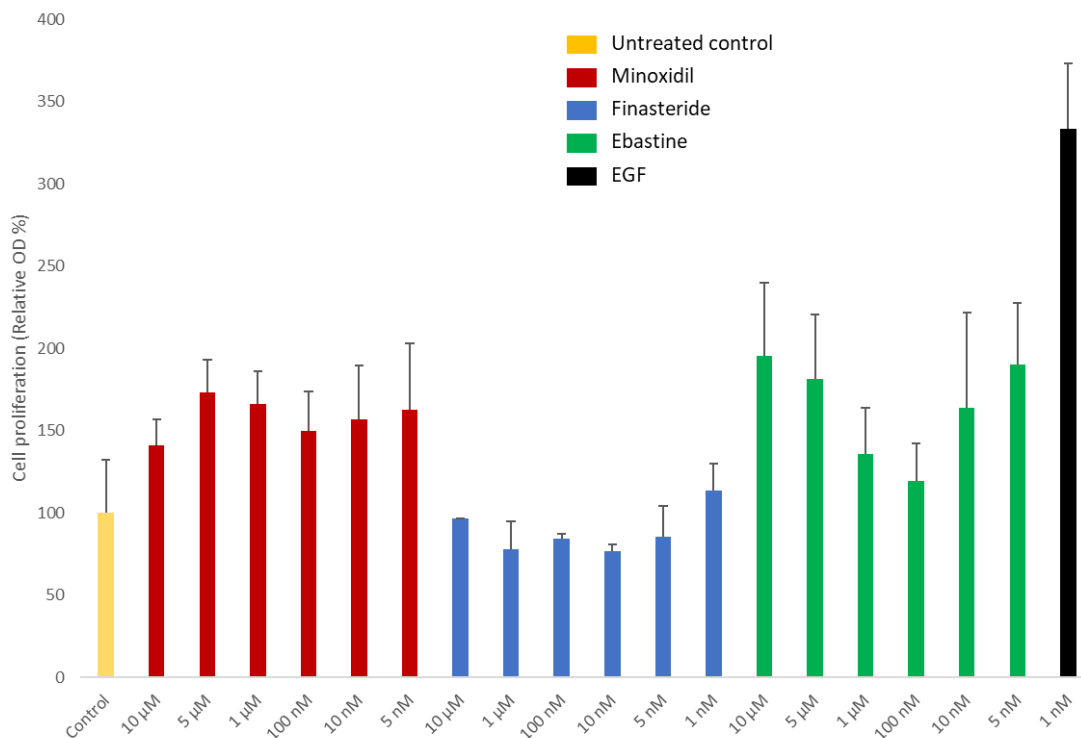


Figure 37 HEK001 cell proliferation results: $n = 5$ experiments for minoxidil (red), $n = 2$ experiments for finasteride (blue), $n = 1$ experiment for ebastine (green), $n = 1$ experiment for EGF (black), and $n = 5$ experiments for untreated control (yellow). Each condition was tested in sextuplicate. In the case of minoxidil and finasteride, the bars show the mean \pm standard deviation of the replicates and of the different experiments. In the case of ebastine and EGF, the mean and standard deviation of the replicates are shown since only a single experiment was performed.

The increase in hair length produced by minoxidil may be due in part to the prolongation of the anagen phase of the hair cycle. This could be caused by a slowing of the senescence of the matrix cells and a lengthening of the time during which cells can divide. Although the ageing of cells in culture and the conversion of hairs from anagen to telogen are different events, it is very likely that both are caused by some type of metabolic signal. A possible mechanism of action of minoxidil might be to prevent the release of this signal or block the response to it [Howard P. Baden et al]. Another explanation for the effect of minoxidil on keratinocytes could be that minoxidil has an EGF-like effect in that it delays cell senescence. Indeed, previous studies comparing minoxidil and EGF observed that cell behaviour was identical [Rheinwald and Green et al]. As for finasteride, no significant differences were observed between the control and the treatments. Due to the different mechanisms of action of 5AR inhibitors, a proliferative effect on HEK was not expected for finasteride.

7.4.3. *In vitro* DPCs viability assays with finasteride, minoxidil and testosterone.

DPCs are one of the most important cells in hair growth and regeneration. Different types of chemical and physical stimuli (e.g., hormones, platelet-rich plasma, peptides, electrical impulses and electromagnetic impulses, among others) have been studied for their effects on hair growth in DPCs [Alka Madaam et al 2018]. DPCs express androgen receptors and their proliferation is usually sensitive to testosterone. For this reason, DPCs were incubated with different concentrations of testosterone, finasteride, minoxidil, and finasteride + testosterone.

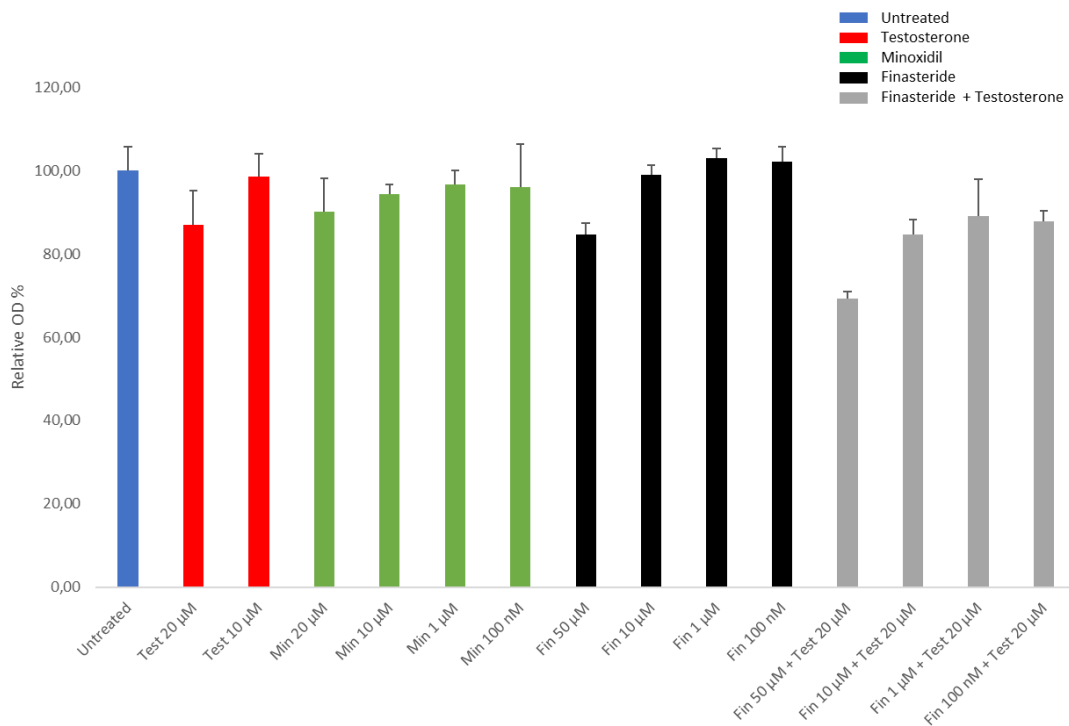


Figure 38 DPCs proliferation results after an untreated control (blue), and treatments with increasing concentrations of: Testosterone (red), Minoxidil (green), Finasteride (black) and Finasteride + 20 µM Testosterone (grey). The mean and standard deviation of the replicates are shown since only a single experiment was performed. Conditions were sextuplicated.

As seen in Figure 38, DPCs showed no change in proliferation in the presence of 10 µM testosterone. When the testosterone concentration was increased to 20 µM, an antiproliferative effect was observed. This was also observed at the highest dose of finasteride (50 µM). As for the combination of finasteride and testosterone, there was a trend of lower proliferation in all cases. **Franklin Kieseewetter et al.** demonstrated that DPCs and keratinocytes from the outer root sheath show significantly inhibited proliferation when treated with testosterone and dihydrotestosterone (345 nM). In their studies, they worked with primary cultures isolated from androgen-sensitive scalp areas. In this thesis, the work was performed with immortalised cell cultures. Immortalised cells have been engineered to proliferate indefinitely so that they can be cultured for long periods of time. Depending on the region and the patient from which these cells have been isolated, their sensitivity to androgens can be highly variable [**S. Itami et al 1994**]. In addition, due to the nature of DPCs, the expression of androgen receptors decreases when the number of cell passages increases. Although it is less cost effective, further studies could be performed with immortalised DPCs with intact chromosomes and androgen receptor expression in order to avoid this problem. Another strategy could be to use primary DPCs isolated from patients with androgen-sensitive scalp areas to study the efficacy of 5AR inhibitors like finasteride; however, the reproducibility of the results could be affected [**Tomokazu Fukuda et al 2020**].

7.5. Conclusions

The seeding concentration, medium supplementation, method (starvation process) and extracellular matrix concentration were established to test the effects of different active ingredients on the proliferation of HEK001 cells and DPCs.

We found a proliferation-promoting effect of minoxidil and ebastine on HEK001 cells. However, due to the variability found, it is necessary to increase the number of experimental replicates before drawing a conclusion.

Regarding the DPCs, the inhibitory effect on proliferation observed with testosterone was lower than that described in the literature for the same dose. It would be advisable to perform these experiments in an androgen-sensitive line of DPCs. Furthermore, it would be interesting to perform this test in primary DPCs to compare their results with those of the immortalised line.

7.6. Bibliography

Boyera N, Galey I, Bernard BA. Biphasic effects of minoxidil on the proliferation and differentiation of normal human keratinocytes. *Skin Pharmacol.* 1997;10(4):206-20. DOI: 10.1159/000211506. PMID: 9413895.

Fukuda, T., Takahashi, K., Takase, S., Orimoto, A., Eitsuka, T., Nakagawa, K., & Kiyono, T. (2020). Human Derived Immortalized Dermal Papilla Cells With a Constant Expression of Testosterone Receptor. *Frontiers in cell and developmental biology*, 8, 157. DOI: 10.3389/fcell.2020.00157

Howard P. Baden, Joseph Kubilus, Effect of Minoxidil on Cultured Keratinocytes, *Journal of Investigative Dermatology*, Volume 81, Issue 6, 1983, Pages 558-560, ISSN 0022-202X, DOI: 10.1111/1523-1747.ep12523220.

Itami S, Sonoda T, Kurata S, Takayasu S. Mechanism of action of androgen in hair follicles. *J Dermatol Sci.* 1994 Jul;7 Suppl:S98-103. DOI: 10.1016/0923-1811(94)90040-x. PMID: 7999680.

Kiesewetter F, Arai A, Schell H. Sex hormones and antiandrogens influence *in vitro* growth of dermal papilla cells and outer root sheath keratinocytes of human hair follicles. *J Invest Dermatol.* 1993 Jul;101(1 Suppl):98S-105S. DOI: 10.1111/1523-1747.ep12363015. PMID: 8326159.

Madaan A, Verma R, Singh AT, Jaggi M. Review of Hair Follicle Dermal Papilla cells as *in vitro* screening model for hair growth. *Int J Cosmet Sci.* 2018 Oct;40(5):429-450. DOI: 10.1111/ics.12489. Epub 2018 Oct 4. PMID: 30144361.

Rheinwald JG, Green H. Epidermal growth factor and the multiplication of cultured human epidermal keratinocytes. *Nature.* 1977 Feb 3;265(5593):421-4. DOI: 10.1038/265421a0. PMID: 299924.

Chapter 8 - Latanoprost-loaded nanotransfersomes for scalp administration: Scale-up and biopharmaceutical studies

Resumen

Los nanotransfersomas son un subtipo de liposoma que aumenta la absorción cutánea de los principios activos gracias a las propiedades ultraflexibles de su membrana. En estas vesículas flexibles se encapsuló el principio activo Latanoprost, un análogo de la prostaglandina, y dos fluorocromos (uno hidrofílico y otro lipofílico). Se estudió la biodistribución cutánea *ex vivo* tanto en el cuero cabelludo humano como en piel de cerdo. La microscopía láser confocal mostró que ambos fluorocromos aumentan su penetración, con un patrón similar en ambas especies, en comparación con las soluciones de fluorocromos sin nanotransfersomas. Se comprobó que los nanotransfersomas fueron estables en condiciones aceleradas (40°C/75% HR) y a largo plazo (25°C/60% HR) durante un año,. No se observaron diferencias en el tamaño de las vesículas ni en la polidispersidad al encapsular Latanoprost. Se realizó un estudio de escalado, mediante el método de ultrasonidos, para evaluar las variables significativas y se descubrió que la energía de cavitación suministrada por el sistema se correlaciona directamente con las propiedades de los nanotransfersomas.

Asian Journal of Pharmaceutical Sciences

Latanoprost-loaded nanotransfersomes for scalp administration. Scale-up and biopharmaceutical studies

--Manuscript Draft--

Manuscript Number:	
Article Type:	Research Paper
Keywords:	Nanotransfersomes; scale-up; latanoprost; sonication; confocal laser microscopy; biodistribution.
Corresponding Author:	Francisco Fernandez-Campos Laboratory Reig Jofre SPAIN
First Author:	Eloy Pena-Rodríguez
Order of Authors:	Eloy Pena-Rodríguez Francisco Fernandez-Campos Sandra Perez-Torras Maria Lajarin-Reinares
Abstract:	<p>Nanotransfersomes are a subtype of liposomes that increase the skin absorption of active ingredients due to their ultraflexible membrane properties. Latanoprost, a prostaglandin analog, and two fluorochromes (hydrophilic and lipophilic) were loaded into these flexible vesicles. Ex vivo skin biodistribution was studied both in human scalp and pig skin. Confocal laser microscopy showed that both fluorochromes increased their penetration, with similar patterns in both species, compared with fluorochrome solutions containing no nanotransfersomes. Nanotransfersomes were stable under accelerated conditions (40°C/75% RH) and long-term conditions (25°C/60% RH) for up to one year, with no differences in vesicle size and polydispersity when latanoprost was loaded. A scale-up study with the ultrasonication method was carried out to evaluate the significant variables. The cavitation energy supplied by the system strongly correlated with the properties of the nanotransfersomes.</p>
Suggested Reviewers:	Ana Cristina Calpena Campmany anacalpena@ub.edu Francisco Javier Otero Espinar francisco.otero@usc.es Joaquim Amela Navarro jamela@mesoestetic.com
Opposed Reviewers:	

Cover letter

Dear Editor of AJPS,

I am writing to submit a manuscript for consideration for publication in the *Asian Journal of Pharmaceutical Sciences*. The title of the article is "Latanoprost-loaded nanotransfersomes for scalp administration: Scale-up and biopharmaceutical studies". This research has not been published elsewhere nor has it been simultaneously submitted for publication elsewhere.

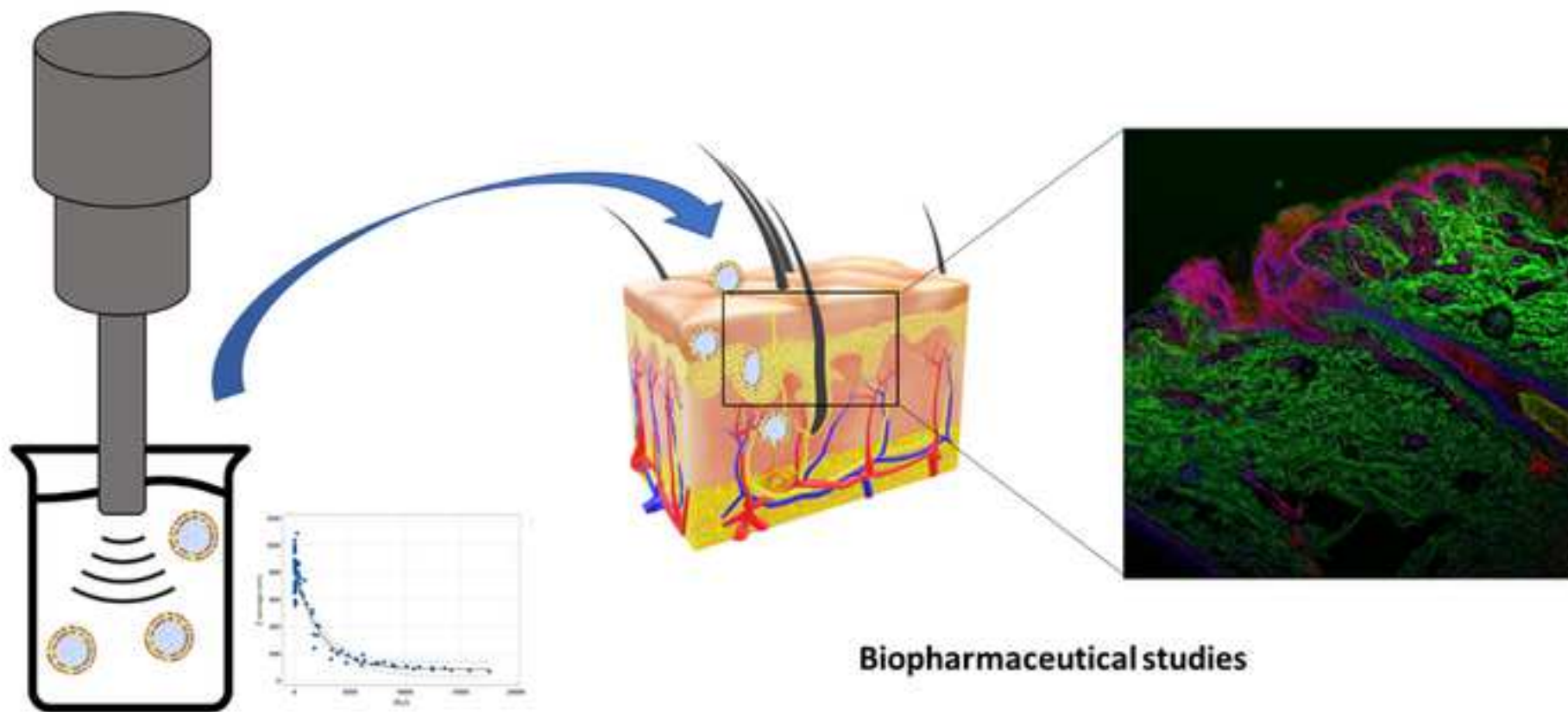
This contribution is aimed at shedding light on the use of nanotransfersomes for scalp administration. The tiny size and deformability of nanotransfersomes make them very interesting systems for topical drug delivery. However, for these nanosystems to reach the patient, extensive physicochemical characterization, optimization of the scale-up process and stability are needed. In addition, there is very little information about the processes that these particles undergo once they come into contact with the skin environment.

The results reported in this manuscript will help the scientific community bring this type of nanosystems closer to the patient.

Thank you very much for your consideration.

Yours faithfully,

Dr. Francisco Fernandez-Campos



Nanotransferomes Scale-up

Biopharmaceutical studies

**Latanoprost-loaded nanotransfersomes for scalp administration.
Scale-up and biopharmaceutical studies.**

Eloy Pena-Rodriguez^a, Maria Lajarin Reinares^a, Sandra Perez-Torras^{b,c,d}, Francisco
Fernandez-Campos^{a,*}

^aLaboratory Reig Jofre, R&D Department, 08970 Sant Joan Despi, Barcelona, Spain

^bMolecular Pharmacology and Experimental Therapeutics, Department of Biochemistry
and Molecular. Biomedicine, Institute of Biomedicine (IBUB), University of Barcelona
(IBUB), 08028 Barcelona, Spain

^cBiomedical Research Networking Center in Hepatic and Digestive Diseases
(CIBEREHD),

Carlos III Health Institute, 28029 Madrid, Spain

^dSant Joan de Déu Research Institute (IR SJD-CERCA) Esplugues de Llobregat, 08950
Barcelona, Spain

*Corresponding author.

Tel.: +34 93 480 67 10

E-mail: ffernandez@reigjofre.com (F. Fernandez-Campos)

Latanoprost-loaded nanotransfersomes for scalp administration.

Scale-up and biopharmaceutical studies

Abstract:

Nanotransfersomes are a subtype of liposomes that increase the skin absorption of active ingredients due to their ultraflexible membrane properties. Latanoprost, a prostaglandin analog, and two fluorochromes (hydrophilic and lipophilic) were loaded into these flexible vesicles. Ex vivo skin biodistribution was studied both in human scalp and pig skin. Confocal laser microscopy showed that both fluorochromes increased their penetration, with similar patterns in both species, compared with fluorochrome solutions containing no nanotransfersomes. Nanotransfersomes were stable under accelerated conditions (40°C/75% RH) and long-term conditions (25°C/60% RH) for up to one year, with no differences in vesicle size and polydispersity when latanoprost was loaded. A scale-up study with the ultrasonication method was carried out to evaluate the significant variables. The cavitation energy supplied by the system strongly correlated with the properties of the nanotransfersomes.

Keywords: Nanotransfersomes; scale-up; human skin; pig skin; latanoprost; hair follicle; sonication; confocal laser microscopy; biodistribution.

1. Introduction

Nanoliposomes are self-assembling vesicular systems with a diameter below 100 nm. They encapsulate hydrophilic molecules in their aqueous core as well as hydrophobic or amphiphilic molecules, which are intercalated in their lipid membrane. Their small size allows them to permeate across different biological membranes and barriers, increasing the bioavailability of different drugs. Transfersomes are a subtype of liposomes that contain edge activators (usually surfactants) in their membranes, which increase their deformability compared with traditional liposomes. This deformability increases dermal penetration as they can extrude across skin pores. In addition, the edge activators can act as permeation enhancers, since they can modify the solubility and packaging of skin lipids [1]. Transfersomes with a diameter below 100 nm are also called nanotransfersomes [2].

There are different techniques for the production of liposomes. The Bangham method [3], also known as the thin-film hydration method, consists of dissolving lipids in an organic phase, removing the organic solvent by evaporation to form a lipid layer, and rehydrating the layer with an aqueous medium under agitation. Sometimes an additional step is required, such as sonication or extrusion, to reduce size and/or vesicle lamellarity [4]. The use of classic organic solvents, such as chloroform or dichloromethane, limits its scalability and sustainability and could give rise to toxicological concerns. The microfluidic method developed by Jahn et al. [5] consists of mixing ethanolic phases with dissolved lipids and aqueous phases, resulting in the formation of liposomes at the liquid interface between the two phases under a laminar flow. This technique usually produces a more reproducible particle size and enables the control of polydispersity. It also allows for continuous manufacturing. However, the encapsulation efficiency is usually low. It also requires the use of microfluidic consumable materials, which increase production costs and waste products, and necessitates strict control of different process variables. In addition, the small diameter of the chips limits the lipid phase viscosity, restricting the loading capacity (derived from the amount of lipid material used) [6]. Ultrasonication methods produce liposomes of different sizes and with higher polydispersity indexes (PDI), which limit their use in injectable systems that require monodispersion. However, they have acceptable values

for topical application. The sonication energy supplied by the system produces cavitation [7]. When liquids are sonicated at high intensities, the acoustic waves propagating through the liquid medium produce alternating cycles of high and low pressures at a frequency-dependent rate. During the low-pressure cycle, high-intensity ultrasonic waves create small vacuum bubbles within the liquid. When the bubbles reach a volume where they can no longer absorb energy, they collapse violently during a high-pressure cycle. This phenomenon is called cavitation. The implosion of cavitation bubbles generates microturbulence and a microjet. With an adequate recirculation of the formulation through the ultrasonic device, particle size and PDI can be reduced to achieve product requirements. Microfluidics and ultrasonication are the most promising techniques for the industrial scale-up of liposomes, but this scale-up process has not been sufficiently explored to date in the literature.

Latanoprost (LAT) is a prostaglandin analog that binds to the receptor F2 α , leading to vasodilation. It is used to reduce ocular hypertension and glaucoma [8]. The described adverse effects after eye drop administration include eyelash hypertrichosis [9]. Due to this fact, LAT has been investigated as a possible treatment against androgenic and areata alopecia [10], [11], [12], [13], [14]. As well as for minoxidil, another drug used topically for both pathologies, the hypothesized mechanism of action is based on the vasodilation of the area and the subsequent increase in blood supply and nutrient uptake by the pilosebaceous unit. However, additional molecular mechanisms could be involved in the proliferation of the pilosebaceous unit and hair growth [15], [16], [17]. Several studies have encapsulated LAT into liposomes to extend drug release and improve the therapeutic index in glaucoma and related diseases [18], [19], [20], [21]. However, there is no information about LAT encapsulation in nanotransfersomes for topical administration as a potential tool to treat hair disorders. Nanotransfersomes were selected to increase the skin absorption of the drug and deliver it to the deep terminal hair follicles of the human scalp in the dermis.

The aim of this work was to produce, with an ultrasonic device, LAT-loaded nanotransfersomes for skin application. The scale-up parameters were studied to evaluate its industrializability. In addition, drug release and nanotransfersome biodistribution in the human scalp were studied.

2. Materials and methods

2.1. Materials

α -tocopherol (Merck Chemicals and Life Sciences, Barcelona, Spain), phosphatidylcholine (Lipoid, Ludwigshafen, Germany), cholesterol (Merck KGaA, Darmstadt, Germany), LAT (Fagron, Barcelona, Spain), Tween 80 (Croda Iberica S.A., Barcelona, Spain), ethanol absolute (Scharlab S.L., Barcelona, Spain) and purified water (inhouse) were used to formulate the nanotransfersomes. Methanol (Scharlab S.L., Barcelona, Spain), 1,2-dioleoyl-3-[16-N-(lissamine rhodamine B sulfonyl) amino]palmitoyl-sn-glycerol (LRB) (Avanti Polar Lipids, Alabaster, AL, USA), Hoechst, phosphate buffered saline (PBS), paraformaldehyde (Merck KGaA, Darmstadt, Germany), sodium fluorescein (Merck KGaA, Darmstadt, Germany), uranyl acetate (Electron Microscopy Sciences, Hatfield, England) and optimal cutting temperature (OCT) compound (IESMAT S.A., Barcelona, Spain) were used to perform the different analyses.

2.2. Formulations

Nanotransfersomes were manufactured by the sonication method [22], [23]. For the placebo nanotransfersomes, α -tocopherol (0.01% w/w), cholesterol (0.01% w/w), phosphatidylcholine (0.73% w/w), hydrogenated phosphatidylcholine (0.20% w/w) and Tween 80 (0.05% w/w) were dissolved in ethanol (10% w/w). Then, milli-Q water (qs 100% w/w) was added to the organic phase at 500 rpm (paddle stirring) until complete homogenization. LAT-nanotransfersomes were produced in the same way, by adding LAT (0.005% w/w) to the ethanolic solution.

Fluorescent nanotransfersomes were produced to study skin biodistribution. Fluorescein (0.1% w/w) was selected as the hydrophilic fluorochrome, which was encapsulated in the aqueous core of the vesicle. It was added to the water phase. LRB (0.0003% w/w) was added to the ethanolic phase, with this hydrophobic fluorochrome inserted into the lipid bilayer of the nanotransfersome. After its production, the formulation was dialysed overnight (Slide-A-Lyzer™ 10-kDa cut-off cassettes (Thermo Fisher Scientific, Barcelona, Spain)) to remove and quantify (section 2.5) the unloaded fluorescein. Free fluorochrome solution was produced at equivalent concentrations of

LRB and the encapsulated fluorescein with the addition of 0.05% Tween 80 to solubilize LRB.

To produce laboratory-scale batches (around 30 ml), a UP400st ultrasonicator (Hielscher Ultrasonics, Germany) was used with an amplitude of 40% for 5 min.

For scale-up batch production, a UIP1000HdT device (consisting of a transducer and ultrasonic generator), a sonotrode (BS4d22; diameter 22 mm) and a flow cell (FC100L1K-1S; Hielscher Ultrasonics, Teltow, Germany) were used. A peristaltic pump was connected to the flow cell with a flow rate of 2 l/min through rubber tubing and the formulation was recirculated through the system. The cell jacket was connected to a water-cooling system. Aliquots were taken after each sonication cycle to monitor the particle size and Pdl. Finally, the sonication was stopped and the suspension of nanotransfersomes was left to settle at room temperature.

2.3. Physicochemical characterization

Hydrodynamic size (Z-average) and the Pdl were studied with dynamic light scattering (DLS) using a Zetasizer Nano ZS system (Malvern Panalytical, Malvern, UK). Dilutions of 1:10 in water were used for the measurements.

Nanotransfersome particle size of the selected formulation after scale-up was studied with transmission electron microscopy (TEM) using a Jeol JEM 1010 100 kv electron microscope (Jeol, Tokyo, Japan). TEM grids were coated with formvar of a 1:10 nanotransfersome dilution in milli-Q water and incubated for 1 min at room temperature. The grids were then washed with water and stained with a 2% w/w uranyl acetate solution for 1 min at room temperature. Afterwards, nanotransfersomes were dried overnight and analyzed.

2.4. Nanotransfersomes stability studies

Nanotransfersomes were subjected to stability studies in chambers at $25 \pm 2^\circ\text{C}/60 \pm 5\%$ relative humidity (RH) (long-term conditions) or $40 \pm 2^\circ\text{C}/75 \pm 5\%$ RH (accelerated conditions) and packaged in hermetically sealed glass vials. The Z-average and Pdl were characterized by DLS, according to section 2.3, at time points 0, 0.5, 1, 3 and 6 months

for accelerated conditions (40°C/75% RH) and at 0, 0.5, 1, 3, 6, 9 and 12 months for long-term conditions (25°C/60% RH).

2.5. Drug analysis and encapsulation efficiency

LAT was analyzed by high-performance liquid chromatography (HPLC). Briefly, a mobile phase (acetonitrile:water, 60:40 v/v) flowed isocratically through a C18 HPLC column (250 x 4.6 mm, 5 µm) at a flow rate of 1 ml/min. The injection volume was 20 µl and the wavelength was 210 nm. The sample and column were maintained at 25°C. The limit of quantification (LOQ) of the analytical technique was set at 0.1 ng/ml.

Fluorescein was quantified with a UV spectrophotometer (VICTOR Multilabel Plate Reader, Perkin Elmer, Massachusetts, USA) at the wavelength of 485 nm.

Encapsulation efficiency, according to the indirect method, was calculated according to Equation 1.

$$\%EE = \frac{W_{NE} - W_T}{W_T} \times 100 \quad (1)$$

where W_{NE} is the amount of drug quantified in the filtrate (drug not encapsulated) and W_T the drug quantified in the total formula. Liposomes were centrifuged in 100-kDa Amicon Ultra units (Merck Millipore, Barcelona, Spain) at 4500 rpm for 30 min.

2.6. Latanoprost drug release

In vitro LAT release ($n = 6$) from nanotransfersomes was studied in vertical Franz diffusion cells (Vidrafoc, Barcelona, Spain) with an effective diffusional area of 1.54 cm². The receptor compartment was filled with a PBS solution, pH 7.4, and 5% hydroxypropyl-beta-cyclodextrin (to maintain sink conditions) and kept at 32°C and continuous stirring at 500 rpm. 1 ml of LAT nanotransfersomes was loaded in the donor compartment, which was separated from the receptor compartment by a dialysis membrane (Spectrum Chemical, New Brunswick, USA) with a pore size cut-off value of 12-14 kDa. Samples of 300 µl were taken regularly for up to 24 h and analyzed by the HPLC method, as described in section 2.5.

2.7. In vitro penetration tests with full-thickness pig and human scalp

Human scalp was purchased from Biopredic (Saint Grégoire, France), which has authorization for the collection, processing and sectioning of human biological samples for research purposes. Samples were remnants from surgeries complying with the French law CSP1245-2, with informed consent provided by the patient, who remained anonymous and did not receive financial reward or publicity. The donor was a 58-year-old Caucasian female.

Pig skin was obtained at the time of sacrifice from a local abattoir (Barcelona, Spain). The skin was cleaned with sterile saline solution and transported to the laboratory at 4°C in saline solution. Both human and pig full-thickness skin pieces were defatted (with a scalpel) and frozen at -20°C until use.

The permeation experiment was performed in Franz diffusion cells with an effective diffusion area of 0.196 cm². Skin pieces were placed between the donor compartment and receptor compartment, which was filled with PBS, pH 7.4, and 4% albumin at 32°C and stirred at 500 rpm. Transepidermal water loss (TEWL) was recorded with a vaporimeter device (Delfin Technologies, Kuopio, Finland) to check skin integrity before the experiment. 76 mg of each formulation were placed into the donor compartment (fluorescent nanotransfersomes and free fluorescent solutions).

After 18 h of permeation, the skin sections treated with the fluorescent formulations were washed with PBS, cut with a scalpel into pieces of about 0.5 cm², and fixed in 4% w/w paraformaldehyde solution for 5 min. Then, the skin samples were incubated in aqueous solutions of increasing sucrose concentration (5%, 15% and 25% w/w) for 15 min in each solution. They were then placed in plastic moulds and dipped in OCT to cut on a Leica CM 3050 S cryostat (Leica Biosystems, Barcelona, Spain) into 50-µm thicknesses. The slices were collected on poly-lysine-coated slides and washed with PBS and 0.05% Tween 20 (TPBS) for 5 min to remove the OCT and permeabilize the samples. On the day of observation, sections were incubated with 15 µl of Hoechst solution (2 µg/ml) for 10 min and washed with TPBS to stain the cell nuclei.

2.8. Confocal laser microscopy

The samples were analyzed under a confocal microscope (Leica Microsystems, Wetzlar, Germany). The emission laser wavelengths were 570, 500 and 525 nm and the

excitation wavelengths were 561, 488 and 405 nm for LRB, fluorescein and Hoechst, respectively. About 20 Z-planes were obtained per image, separated by a 3- μ m step. Composites of the different planes were created, in terms of the brightest point for each pixel, through the ImageJ tool Z-stack (ImageJ2 v2.35, National Institutes of Health, Bethesda, MD, USA). A skin blank was processed in the same way as the test samples to quantify skin autofluorescence. The mean intensity was measured with the ImageJ software and was subtracted from the intensity of the red and green fluorescence of the samples.

2.9. Scale-up variables

Using the Minitab software (Minitab 17 Statistical Software), a class III resolution Plackett-Burman screening design of experiments (DoE) with 11 runs, 4 factors and a significance level of $\alpha = 0.05$ was performed to obtain the maximum information about scaling while producing the minimum number of batches. The responses to be optimized were the Z-average and Pdl. The factors selected were: % amplitude, batch volume (l), number of sonication cycles and flow cell jacket temperature ($^{\circ}$ C). The amplitude and the number of sonication cycles are related to the cavitation energy input. The flow cell temperature was also included to control the temperature stability during the production process. Finally, to test the scalability of the formulation, batch size (l) was included.

Table 1 shows the levels of the selected factors for the scale-up Plackett-Burman design. Due to the high cost of LAT, scale-up activities were carried out with placebo nanotransfersomes.

3. Results and discussion

3.1. Formulations and stability studies

Table 2 shows the size and Pdl of the placebo nanotransfersomes, LAT nanotransfersomes and fluorescent nanotransfersomes (LRB-fluorescein-loaded) after production of the laboratory-scale formulations. The inclusion of LAT into the nanotransfersomes did not affect either size or the Pdl. Nanotransfersome size and Pdl remained below 100 nm and was 0.3, respectively, in all cases.

The encapsulation efficiency for LAT was 100% since the WNE values were below the LOQ after ultrafiltration. On the other hand, the %EE of fluorescein was low (24.11%), as would be expected for hydrophilic compounds. The free fluorescein solutions for the confocal experiments were produced at the same concentration (0.024% w/w).

Placebo nanotransfersomes were subjected to long-term conditions (25°C/60% RH) for one year and accelerated conditions (40°C/75% RH) for six months in the stability studies. The Z-average and Pdl values are shown in Fig. 1. Regression slopes and the statistical significance were also obtained. The p-values of the regression slope for the Z-average were above 0.05 in both conditions, with the regression lines statistically equal to zero, indicating that the nanotransfersomes kept their hydrodynamic diameter stable under these conditions. The regression slope for the Pdl showed a significant increase over time (at 25°C/60% RH, $p < 0.05$) that was not observed under the accelerated conditions (40°C/75% RH, $p > 0.05$), although the final value (around 0.3) was acceptable for topical applications. Therefore, the liposomes could be considered stable in solution during the studied time. Modified PEG-phospholipids are usually added to the liposome structure to improve stability in solution, preventing vesicle aggregation [24]. The presented formulation exhibited very good stability without the introduction of PEG-phospholipids, showing a reduced particle size (compared to pegylated systems) and maintaining its flexibility to improve drug delivery to the skin.

3.2. Latanoprost drug release

Fig. 2 shows the release profile of LAT nanotransfersomes after 24 h of analysis. During the first hours, no LAT was observed in the receptor medium (< LOQ). Only after 20 h, small amounts of LAT were found, with a very low increase over time. The slow release could be related to the high lipophilicity of LAT, which probably is a structural part of the nanotransfersome membrane. Vesicles could act as a drug reservoir, which could be useful in reducing the administration frequency. Drug release over time showed a linear pattern, compatible with a controlled release profile, with a release constant equivalent to 0.3993 $\mu\text{g}/\text{cm}^2/\text{h}$. The total LAT released at 24 h corresponded to 23.46% of the loading dose in the donor compartment.

3.3. Confocal fluorescence microscopy to study the skin biodistribution of nanotransfersomes

The skin penetration-promoting effect of nanotransfersomes has been described in the literature. Many of these studies were performed on pig skin, which is one of the more similar models compared to human skin. Even so, there are several differences between pig and human skin, such as the different thicknesses of the stratum corneum and epidermis and the lack of sebaceous and sweat glands in pig skin. This could be important in follicular targeting studies, especially for products applied to the scalp. To evaluate the possible differences in permeability between the two species and to demonstrate the higher permeability properties of the studied nanotransfersomes, penetration studies of fluorescent vesicles were performed.

Two different fluorophores were co-encapsulated, sodium fluorescein (NaFl) and LRB. NaFl (green fluorophore) simulates the behavior of a hydrophilic drug and was encapsulated in the aqueous core of the nanotransfersomes. Due to the C16 hydrocarbon tail of LRB (red fluorophore), it was inserted into the lipid membrane of the nanotransfersomes. LRB simulates the behavior of a lipophilic drug loaded into nanotransfersomes. Free solutions of both fluorophores were used as controls. Hoechst staining was performed on the histological sections to observe the cell nuclei (in blue) and improve visualization.

After the skin permeation assays, histological cryosections were analyzed by confocal fluorescence microscopy. The biodistribution results are shown in Fig. 3 (human scalp) and 4 (pig skin). The autofluorescence intensities in the red and green channels were subtracted from the mean intensity of the samples using ImageJ. Linear segments were drawn to analyze the intensity profiles as a function of the depth (in μm). The yellow color corresponds to the co-localization of NaFl and LRB. Lines were drawn across the slices to obtain plot profiles of red and green fluorescence intensities. Representative images of each permeation are reported.

The images shown in Fig. 3A correspond to cryosections of human scalp permeated with NaFl-loaded LRB-labeled nanotransfersomes. The images in Fig. 3B correspond to human scalp slices permeated with the control free NaFl and LRB solution. Comparing

the images and the intensity profiles of the lines plotted in Fig. 3, differences were observed in the biodistribution of the fluorophores. Non-vehiculated NaFl (Fig. 3B) showed very low skin penetration, with its fluorescence intensity remaining below 50 AU even in the most superficial layers of the skin. However, a clear absorption-promoting effect of the nanotransfersomes for NaFl was observed (Fig. 3A). The intensity, even in the deepest layers of the skin, reached levels above 150 AU at depths of up to 2500 μm , i.e., an increase of 300% compared to the NaFl control solution. The absorption of LRB was also higher in the presence of nanotransfersomes. In the intensity profile in Fig. 3A, values above 100 AU can be observed at depths of 1250 and 1750 μm . Non-vehiculated LRB (Fig. 3B) showed lower intensities that were below 50 AU.

The same effect was found after experiments on pig skin (Fig. 4). Although there are no sebaceous glands in pig skin, clear differences were also observed in the cutaneous biodistribution between the vehiculated fluorophores and the control solution. As for NaFl, similar to that observed in the human scalp, the control solution (Fig. 4B) showed no signs of NaFl penetration into the stratum corneum or the epidermis, nor in the deeper layers. However, Fig. 4A shows strong coloration corresponding to NaFl from the superficial layers to the dermis. When comparing the intensities, the intensity was below 25 AU practically throughout the whole tissue for the control solution (Fig. 4B), while it was between 50 and 100 AU at depths of up to 400 μm for the NaFl vehiculated in the nanotransfersomes.

Comparing the permeation in pig and human skin, the intensity of both fluorochromes was similar in the control and test samples. Pig skin remained a good substitute of human scalp skin despite the lack of sebaceous glands. This is an important feature to consider when lipophilic drugs are studied, as can be seen in Fig. 3A showing the accumulation of LRB in the sebaceous glands. These glands play an important role in the physiology of the skin and pilosebaceous units. They are responsible for the hydro-lipidic layer of the skin, regulating skin pH and the follicular microbiome. They are also attracting growing interest due to the stem cells they contain. These all illustrate the increasing importance of this organ as a drug target site.

3.4. Nanotransfersome scale-up variables

The good results regarding the particle size and PDI (stable over time) and the good permeation profile of the nanotransfersomes suggested that the formulation was a good candidate for further development. A scale-up study was carried out. Scale-up of nanomedicines is one of the most critical steps. Methods such as sonication usually provide low control over particle size and polydispersity. Therefore, it is advisable to study this process to understand the characteristics of the nanoformulation. Placebo nanotransfersomes were used for the screening design to study the scaling process with a UIP1000HdT sonicator. Amplitude (%), batch volume (l), sonication cycles and jacket temperature (°C) were the process parameters selected. Table 3 shows the levels of the selected factors as well as the responses obtained for each factor after the Plackett-Burman screening design.

The parameters amplitude (%) and batch size (l) were found to be significant for the Z-average (nm). The regression equation (2) obtained after the Z-average screening design was as follows.

$$\text{Z-average (nm)} = 728.20 - 5.922 \text{ Amplitude (\%)} - 8.39 \text{ batch volume (l)} \quad (2)$$

As can be observed from Equation 2, as the amplitude and batch size increase, the particle size decreases. The higher the amplitude, the more the cavitation that is produced in the system, resulting in smaller nanoparticles. The R²(adjusted) value was 97.57% and the R²(predicted) value was 96.47%. This indicated that virtually all the variability in the results of the nanotransfersome size within this design space was correctly explained by amplitude (%) and batch volume (l).

The parameters amplitude (%), batch volume (l) and sonication cycles were found to significantly influence the PDI of the vesicles. The regression equation (3) obtained after the PDI factorial design was as follows.

$$\text{PDI} = 0.6267 - 0.000904 \text{ amplitude (\%)} + 0.000586 \text{ batch volume (l)} - 0.01817 \text{ sonication cycles} \quad (3)$$

The R²(adjusted) value was 86.33% and the R²(predicted) value was 77.62%. The model had good predictability and most of the variability found in the data could be explained by the selected variables.

Amplitude (%) had a significant influence both on the particle size and Pdl. A higher amplitude of the sonotrode oscillation causes a higher cavitation energy and, consequently, smaller and narrower particles. The number of sonication cycles also proved to be a significant factor for the Pdl. The more times the formulation passes through the flow cell under sonication, the more the particle size is reduced and the more monodisperse the particle population is (lower Pdl). Regarding the Pdl, the larger the batch scale produced, the higher the Pdl. This is in the opposite direction when compared to the particle size.

The presented models explained the results obtained at the end of the sonication process, but it is also important to understand how the particles behave during the process. In addition, the presented equations had a different number of significant parameters in the analysis of particle size (two variables: amplitude and batch size) and the Pdl (three variables: amplitude, batch size and cycles). Batch size had the smallest effect among the studied variables on particle size and the Pdl, while amplitude and sonication cycles had the largest effect and correlated with the cavitation energy ($w s$) applied to the formulation. All these facts made us evaluate alternative models to predict the particle size and Pdl as a function of the cavitation energy normalized per batch size. This model, with only one variable to study, is simpler to use for scale-up activities. Previous studies also identified cavitation energy as a critical variable in liposome production [25]. During the sonication process, different aliquots were taken from the pre-mix (before sonication) and after each sonication cycle. In this way, it was possible to obtain the sonication energy value needed to produce nanotransfersomes with the desired size and Pdl values for a given batch volume.

Fig. 5A shows the sizes obtained for each batch and for each aliquot as a function of the cavitation energy normalized per batch volume ($w s/l$).

The following regression equation (Equation 4) was obtained using the Minitab software:

$$\text{Size (nm)} = 83.29 + 742.12 e^{-0.00044 \text{ energy}} \quad (4)$$

Both the empirical data on the particle size and the non-linear regression with a 95% confidence interval (CI) are presented in Fig. 5B. The R²(adjusted) value of the presented model was 0.8999, indicating a good fit to the empirical data.

Fig. 6A shows the Pdl values obtained for each batch and for each aliquot as a function of the cavitation energy.

The DLS software was optimized for monodisperse populations of one or two different population sizes. When the sample is very polydisperse, the Pdl results are not very accurate. This was observed since the increase in the Pdl between 0 and 4000 w s/l did not agree with the direction of the influence of the sonication cycles and the amplitude correlated with the Pdl. For this reason, to perform a non-linear regression, cavitation energy values > 4000 w s/l were chosen from the aliquot in which the slope started to be negative. In this way, the predictive model was more accurate and relevant for the final Pdl of the manufactured formulation.

The following regression equation (Equation 5) was obtained using the Minitab software:

$$\text{Pdl} = 0.353 + 0.924 e^{-4713.93 \text{ energy}} \quad (5)$$

Both the empirical data of the Pdl and the non-linear regression with a 95% CI are presented in Fig. 6B. The R²(adjusted) value of the presented model was 0.8379, indicating a good fit to the empirical data.

After obtaining the non-linear regression equations for size and the Pdl, different values of cavitation energy were simulated to observe the predicted values of both responses. As can be seen in Table 4, to obtain a Pdl value < 0.5 and a Z-average < 90 nm, 11000 w s/l would be needed. That is, for a batch size of 8 l, 88000 w s of sonication energy would be required.

Finally, an additional batch with the final configuration (100% amplitude, 11000 w s/l and 8 l batch size) was produced and analyzed by TEM (Fig. 7), according to section 2.3, to corroborate the predictability of the model.

Fig. 7 shows two TEM images of the nanotransfersomes and a histogram representing the size distribution. The size of the vesicles obtained was very similar to

the hydrodynamic diameter obtained by DLS. The average diameter was 91.34 nm for a sample size of $n = 72$, obtained using the ImageJ software after TEM analysis. The mean difference between the TEM diameter (91.34 nm) and the predicted Z-average of the model (89.36 nm) for an energy of 11000 w s/l was 2.22%. This low bias value demonstrated the high quality and accuracy of the model in predicting the Z-average obtained within the design space described.

4. Conclusion

Nanotransfersomes were successfully developed as encapsulation systems of both hydrophilic and lipophilic drugs (LAT and NaFl and LRB). The vesicles had a particle size below 100 nm and a Pdl value below 0.3. The formulation was stable under long-term conditions (25°C/60% RH) for one year and under accelerated conditions (40°C/75% RH) for up to six months. The vesicle showed a slow-release pattern. Furthermore, the nanotransfersomes promoted the skin penetration of the loaded fluorochromes in both human scalp and pig skin, with similar results for both species. Statistical models explaining the particle size and Pdl of the nanotransfersomes as a function of the manufacturing parameters were obtained. They were mainly influenced by the cavitation energy. These results showed that the formulation was scalable, reproducible and suitable for future industrial development.

Conflicts of interest

E. Pena-Rodriguez, M. Lajarin-Reinares and F. Fernandez-Campos work at Laboratory Reig Jofre. The authors work in the R&D department and are not involved in marketing or commercial activities. The authors alone are responsible for the content and the writing of this article. The research was conducted under a quality management system to obtain reliable results.

References

- [1] Opatha SAT, Titapiwatanakun V, Chutoprapat R. Transfersomes: A Promising Nanoencapsulation Technique for Transdermal Drug Delivery. *Pharm* 2020, Vol 12, Page 855 2020;12:855. <https://doi.org/10.3390/PHARMACEUTICS12090855>.

- [2] Ahad A, Aqil M, Kohli K, Sultana Y, Mujeeb M, Ali A. Formulation and optimization of nanotransfersomes using experimental design technique for accentuated transdermal delivery of valsartan. *Nanomedicine* 2012;8:237–49. <https://doi.org/10.1016/J.NANO.2011.06.004>.
- [3] Bangham AD, Hill MW, Miller NGA. Preparation and Use of Liposomes as Models of Biological Membranes. *Methods Membr Biol* 1974;1–68. https://doi.org/10.1007/978-1-4615-7422-4_1.
- [4] Zhang H. Thin-Film Hydration Followed by Extrusion Method for Liposome Preparation. *Methods Mol Biol* 2017;1522:17–22. https://doi.org/10.1007/978-1-4939-6591-5_2.
- [5] Jahn A, Vreeland WN, Devoe DL, Locascio LE, Gaitan M. Microfluidic directed formation of liposomes of controlled size. *Langmuir* 2007;23:6289–93. https://doi.org/10.1021/LA070051A/ASSET/IMAGES/LA070051A.SOCIAL.JPEG_V03.
- [6] Carugo D, Bottaro E, Owen J, Stride E, Nastruzzi C. Liposome production by microfluidics: potential and limiting factors. *Sci Reports* 2016 61 2016;6:1–15. <https://doi.org/10.1038/srep25876>.
- [7] Richardson ES, Pitt WG, Woodbury DJ. The Role of Cavitation in Liposome Formation. *Biophys J* 2007;93:4100–7. <https://doi.org/10.1529/BIOPHYSJ.107.104042>.
- [8] Perry CM, McGavin JK, Culy CR, Ibbotson T. Latanoprost. *Drugs Aging* 2003;20:597–630. <https://doi.org/10.2165/00002512-200320080-00005>.
- [9] Demitsu T, Manabe M, Harima N, Sugiyama T, Yoneda K, Yamada N. Hypertrichosis induced by latanoprost. *J Am Acad Dermatol* 2001;44:721–3. <https://doi.org/10.1067/MJD.2001.111625>.
- [10] Blume-Peytavi U, Lönnfors S, Hillmann K, Garcia Bartels N. A randomized double-blind placebo-controlled pilot study to assess the efficacy of a 24-week topical treatment by latanoprost 0.1% on hair growth and pigmentation in healthy

- volunteers with androgenetic alopecia. *J Am Acad Dermatol* 2012;66:794–800. <https://doi.org/10.1016/J.JAAD.2011.05.026>.
- [11] Bloch LD, Escudeiro CC, Sarruf FD, Valente NYS. Latanoprost e minoxidil: Estudo duplocego comparativo, placebo-controlado no tratamento da queda de cabelos. *Surg Cosmet Dermatology* 2018;10:39–43. <https://doi.org/10.5935/SCD1984-8773.20181011015>.
- [12] Uno H, Zimbric ML, Albert DM, Stjernschantz J. Effect of latanoprost on hair growth in the bald scalp of the stump-tailed macaque: a pilot study. *Acta Derm Venereol* 2002;82:7–12. <https://doi.org/10.1080/000155502753600803>.
- [13] Razi-Khosroshahi M, Sobhani ; Soheila, Yousefi KM, Harooni G, Mashayekhi F, Balasi1 J, et al. Latanoprost in treatment of alopecia areata and androgenic alopecia: A comprehensive review 2021;15:1535.
- [14] Bhat S, Handa S, De D, Bhat S, Handa S, De D. A randomized comparative study of the efficacy of topical latanoprost versus topical betamethasone dipropionate lotion in the treatment of localized alopecia areata. *Indian J Dermatol Venereol Leprol* 2021;87:42–8. https://doi.org/10.25259/IJDVL_787_19.
- [15] Messenger AG, Rundegren J. Minoxidil: mechanisms of action on hair growth. *Br J Dermatol* 2004;150:186–94. <https://doi.org/10.1111/J.1365-2133.2004.05785.X>.
- [16] Johnstone MA, Albert DM. Prostaglandin-Induced Hair Growth. *Surv Ophthalmol* 2002;47:S185–202. [https://doi.org/10.1016/S0039-6257\(02\)00307-7](https://doi.org/10.1016/S0039-6257(02)00307-7).
- [17] Wolf R, Matz H, Zalish M, Pollack A, Orion E. Prostaglandin analogs for hair growth: Great expectations. *Dermatol Online J* 2003;9:107–13. <https://doi.org/10.5070/D34HZ1F3RR>.
- [18] Natarajan J V., Ang M, Darwitan A, Chattopadhyay S, Wong TT, Venkatraman SS. Nanomedicine for glaucoma: liposomes provide sustained release of latanoprost in the eye. *Int J Nanomedicine* 2012;7:123–31. <https://doi.org/10.2147/IJN.S25468>.

- [19] Fahmy HM, Saad EAEMS, Sabra NM, El-Gohary AA, Mohamed FF, Gaber MH. Treatment merits of Latanoprost/Thymoquinone – Encapsulated liposome for glaucomatus rabbits. *Int J Pharm* 2018;548:597–608. <https://doi.org/10.1016/J.IJPHARM.2018.07.012>.
- [20] Development and in vitro/in vivo Evaluation of Liposomal Gels for the Sustained Ocular Delivery of Latanoprost n.d. <https://www.longdom.org/open-access/development-and-in-vitroin-vivo-evaluation-of-liposomal-gels-for-the-sustained-ocular-delivery-2155-9570.1000390.pdf> (accessed April 12, 2022).
- [21] Natarajan J V., Chattopadhyay S, Ang M, Darwitan A, Foo S, Zhen M, et al. Sustained Release of an Anti-Glaucoma Drug: Demonstration of Efficacy of a Liposomal Formulation in the Rabbit Eye. *PLoS One* 2011;6:e24513. <https://doi.org/10.1371/JOURNAL.PONE.0024513>.
- [22] Woodbury DJ, Richardson ES, Grigg AW, Welling RD, Knudson BH. Reducing liposome size with ultrasound: bimodal size distributions. *J Liposome Res* 2006;16:57–80. <https://doi.org/10.1080/08982100500528842>.
- [23] Jesorka A, Orwar O. Liposomes: technologies and analytical applications. *Annu Rev Anal Chem (Palo Alto Calif)* 2008;1:801–32. <https://doi.org/10.1146/ANNUREV.ANCHEM.1.031207.112747>.
- [24] Anabousi S, Kleemann E, Bakowsky U, Kissel T, Schmehl T, Gessler T, et al. Effect of PEGylation on the stability of liposomes during nebulisation and in lung surfactant. *J Nanosci Nanotechnol* 2006;6:3010–6. <https://doi.org/10.1166/JNN.2006.461>.
- [25] Silva R, Ferreira H, Little C, Cavaco-Paulo A. Effect of ultrasound parameters for unilamellar liposome preparation. *Ultrason Sonochem* 2010;17:628–32. <https://doi.org/10.1016/J.ULTSONCH.2009.10.010>.

Figure and Table legends

Fig. 1. Size and the Pdl of placebo nanotransfersomes under long-term (25°C/60% RH) and accelerated conditions (40°C/75% RH).

Fig. 2. Release profile of LAT from nanotransfersomes and the regression equation. Points represent the empirical mean and standard deviation. Line is the estimated regression line.

Fig. 3. Panel A. Confocal fluorescence microscopy images of human scalp cross-sections after permeation of fluorescent nanotransfersomes. Green color corresponds to NaFl and red to LRB. Panel B. Free NaFl and LRB control solution. Lines correspond to multichannel intensity plot profiles as a function of the depth (μm). The images were captured using 10 \times magnifications.

Fig. 4. Confocal fluorescence microscopy images of pig skin cross-sections. Panel A. Green color corresponds to NaFl and red to LRB in NaFl-loaded LRB-labeled nanotransfersomes. Panel B. Free NaFl and LRB control solution. Lines correspond to multichannel intensity plot profiles as a function of the depth (μm). The images were captured using 10 \times magnifications.

Fig. 5. Size of the formulations studied at scale-up as a function of the cavitation energy. Panel A shows the individual values of each formulation. Panel B shows the fit to a non-linear model.

Fig. 6. The Pdl of the formulations studied at scale-up as a function of the cavitation energy. Panel A shows the individual values of each formulation. Panel B shows the fit to a non-linear model.

Fig. 7. TEM images of nanotransfersomes after scale-up. (A) Scale bar, 500 nm. (B) Scale bar, 200 nm. (C) Nanotransfersome diameter histogram.

Table 1. Scale-up fractioned factorial design factors and levels for placebo nanotransfersomes.

Table 2. Nanotransfersome size and Pdl values of the different formulations.

Table 3. Scale up screening design of experiments factors and responses for each Nanotransfersomes batch.

Table 4. Pdl and size prediction of nanotransfersomes as a function of the sonication energy per liter of formulation.

Figures:

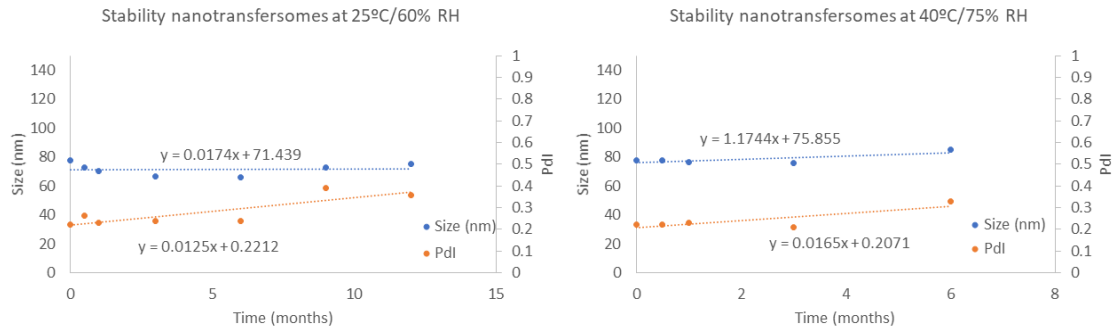


Fig. 1. Size and the Pdl of placebo nanotransfersomes under long-term (25°C/60% RH) and accelerated conditions (40°C/75% RH).

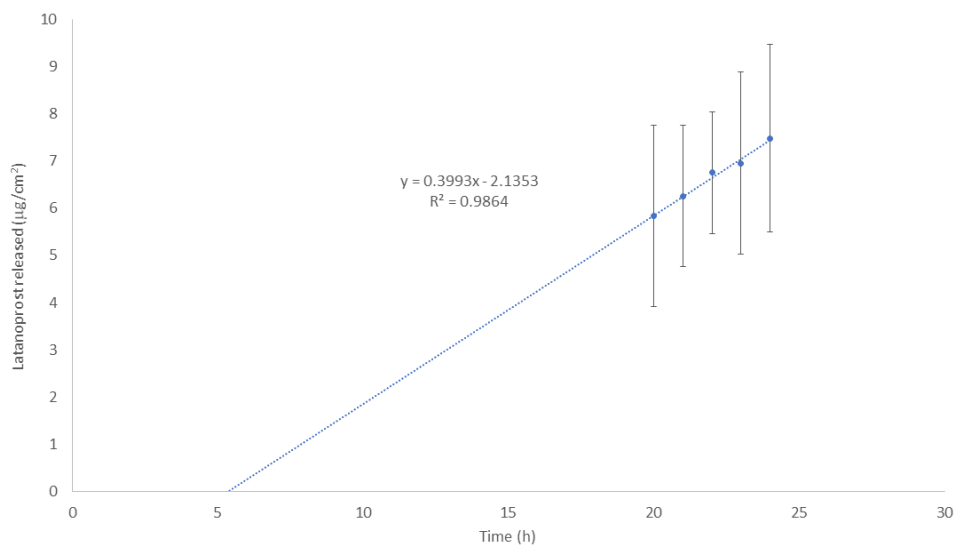


Fig. 2. Release profile of LAT from nanotransfersomes and the regression equation. Points represent the empirical mean and standard deviation. Line is the estimated regression line.

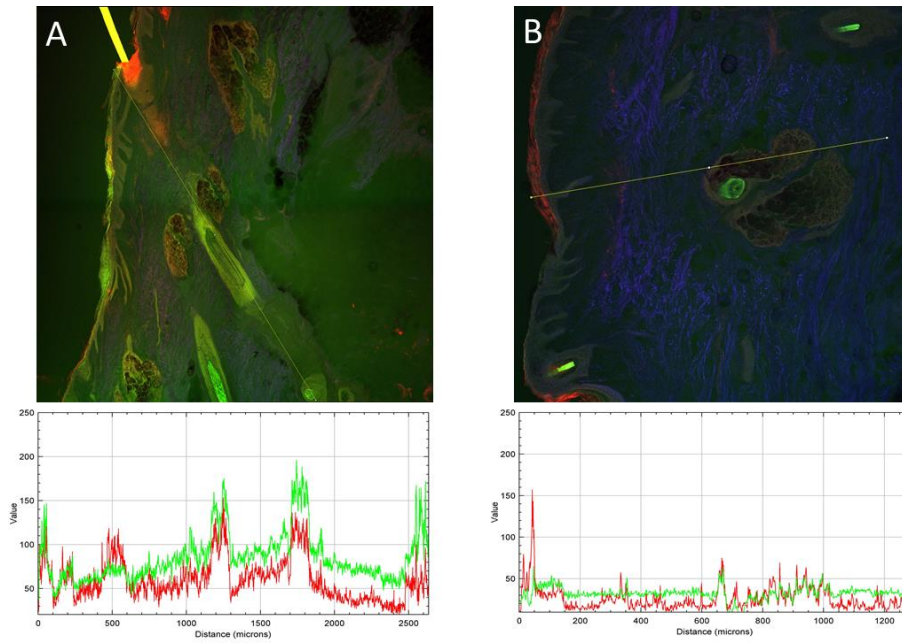


Fig. 3. Panel A. Confocal fluorescence microscopy images of human scalp cross-sections after permeation of fluorescent nanotransfersomes. Green color corresponds to NaFI and red to LRB. Panel B. Free NaFI and LRB control solution. Lines correspond to multichannel intensity plot profiles as a function of the depth (μm). The images were captured using 10 \times magnifications.

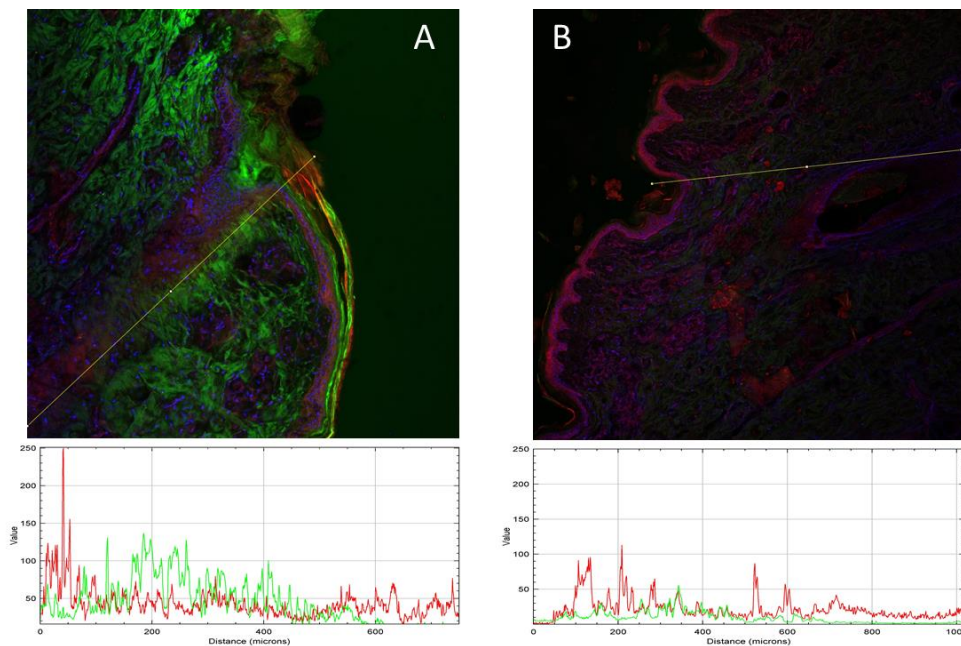


Fig. 4. Confocal fluorescence microscopy images of pig skin cross-sections. Panel A. Green color corresponds to NaFl and red to LRB in NaFl-loaded LRB-labeled nanotransfersomes. Panel B. Free NaFl and LRB control solution. Lines correspond to multichannel intensity plot profiles as a function of the depth (μm). The images were captured using 10 \times magnifications.

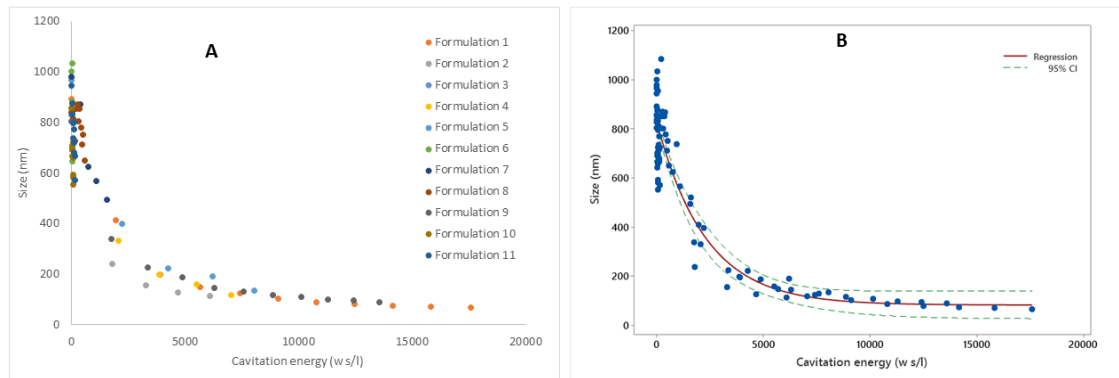


Fig. 5. Size of the formulations studied at scale-up as a function of the cavitation energy. Panel A shows the individual values of each formulation. Panel B shows the fit to a non-linear model.

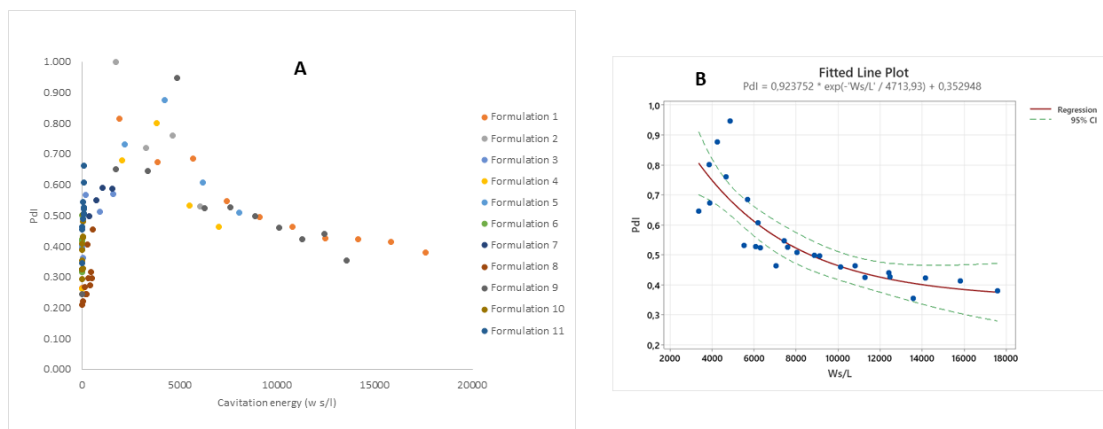


Fig. 6. The Pdl of the formulations studied at scale-up as a function of the cavitation energy. Panel A shows the individual values of each formulation. Panel B shows the fit to a non-linear model.

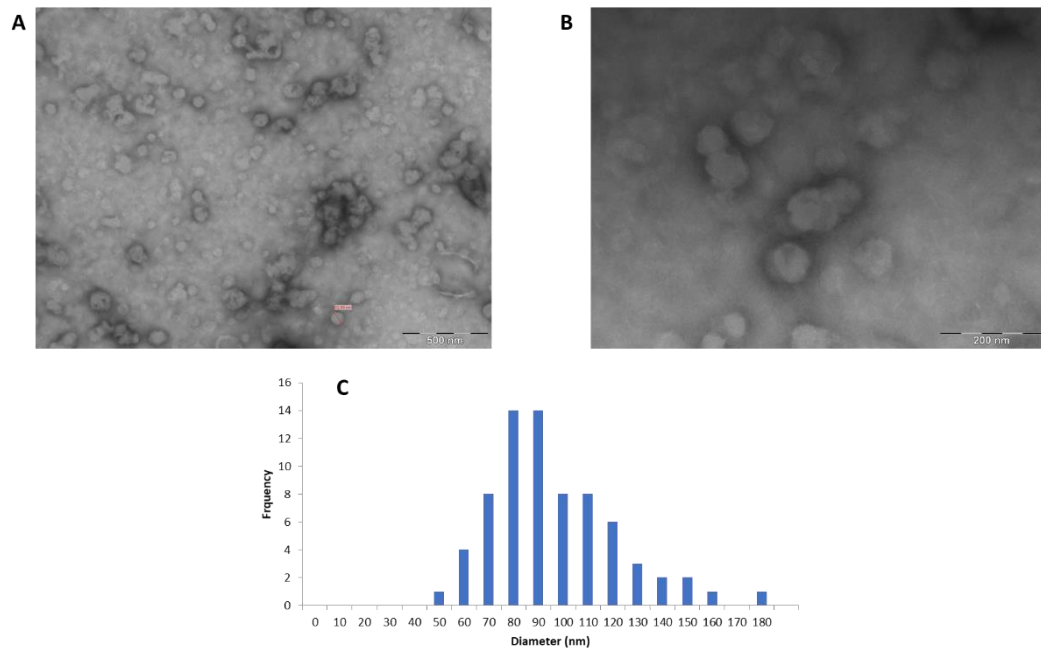


Fig. 7. TEM images of nanotransfersomes after scale-up. (A) Scale bar, 500 nm. (B) Scale bar, 200 nm. (C) Nanotransfersome diameter histogram.

Tables:

Table 1. Scale-up fractioned factorial design factors and levels for placebo nanotransfersomes.

Formula	Amplitude (%)	Batch Volume (l)	Sonication cycles	Jacket Temperature (°C)
1	100	8	10	30

2	100	8	4	45
3	20	8	4	30
4	100	1	4	30
5	100	1	4	45
6	20	1	4	30
7	20	8	4	45
8	20	1	10	30
9	100	1	10	45
10	20	1	10	45
11	20	8	10	45

Table 2. Nanotransfersome size and Pdl values of the different formulations.

Formulation	Size (nm)	Pdl	%EE
Placebo	60.48	0.206	NP
LAT nanotransfersomes	67.22	0.181	100%
Fluorescent nanotransfersomes	71.92	0.190	24.11%

Table 3. Scale up screening design of experiments factors and responses for each Nanotransfersomes batch.

Formula	Amplitude (%)	Batch size (l)	Sonication cycles	Jacket Temperature (°C)	Size (nm)	PdI
1	100	8	10	30	67.11	0.380
2	100	8	4	45	114.00	0.528
3	20	8	4	30	521.70	0.571
4	100	1	4	30	118.00	0.463
5	100	1	4	45	134.30	0.508
6	20	1	4	30	643.40	0.500
7	20	8	4	45	494.10	0.587
8	20	1	10	30	650.30	0.453
9	100	1	10	45	88.96	0.354
10	20	1	10	45	551.90	0.429
11	20	8	10	45	570.50	0.507

Table 4. PdI and size prediction of nanotransfersomes as a function of the sonication energy per liter of formulation.

Sonication Energy (w s/l)	Predicted PdI	Predicted size (nm)
1000	1.100	562.68
2000	0.958	392.96

3000	0.842	283.33
4000	0.749	212.51
5000	0.673	166.76
6000	0.612	137.21
7000	0.562	118.12
8000	0.522	105.79
9000	0.490	97.83
10000	0.464	92.68
11000	0.443	89.36

Chapter 9 - *Ex vivo* MALDI-TOF Mass Spectrometry Imaging and Confocal Raman spectroscopy quantitative skin biodistribution of dexamethasone loaded nanoparticles.

Chapter 9 - *Ex vivo* MALDI-TOF mass spectrometry imaging and confocal Raman spectroscopy for the quantitative analysis of the skin biodistribution of dexamethasone-loaded nanoparticles

Eloy Pena-Rodríguez^a, Teresa García-Berrococo^{b,†}, Ezequiel Vázquez Fernández^{c,†}, Francisco J. Otero-Espinar^{d,e,f,+}, J. Abian^{b,+}, Francisco Fernández-Campos^{a,*}

^aLaboratory Reig Jofre, R&D Department, 08970 Sant Joan Despi, Barcelona, Spain

^bProteomics Facility, Institut d'Investigacions Biomèdiques de Barcelona (IIBB), Consejo Superior de Investigaciones Científicas/Universitat Autònoma de Barcelona (CSIC/UAB), Institut d'Investigacions Biomèdiques August Pi i Sunyer (IDIBAPS), Barcelona, Spain.

^cUnidade de Espectroscopía IR-Raman, Rede de Infraestruturas de Apoio á Investigación e ao Desenvolvemento Tecnolóxico (RIAIDT) Universidade de Santiago de Compostela, Edificio CACTUS, Campus VIDA.

^dPharmacology, Pharmacy and Pharmaceutical Technology Department, Faculty of Pharmacy, University of Santiago de Compostela (USC), Santiago de Compostela, Spain

^eParquasil Group, Health Research Institute of Santiago de Compostela (FIDIS), Santiago de Compostela, Spain.

^fInstitute of Materials (iMATUS), University of Santiago de Compostela (USC), Santiago de Compostela, Spain.

[†]These authors have contributed equally to this work.

⁺These authors have contributed equally to this work.

Chapter 9 - *Ex vivo* MALDI-TOF Mass Spectrometry Imaging and Confocal Raman spectroscopy quantitative skin biodistribution of dexamethasone loaded nanoparticles.

9.1. Introduction

Transdermal drug delivery systems are an interesting alternative for many molecules that are currently administered orally or parenterally [RH Guy et al 2003]. Specifically, the vectorization in nanoparticles capable of crossing the stratum corneum and accumulating in skin appendages is a strategy currently used in both the pharmaceutical and cosmetic industries [Silpa Raj et al 2012].

However, the mechanisms undergone by encapsulated active ingredients and nanoparticles have not yet been fully understood.

One of the most common obstacles that researchers encounter when developing topical drugs is the difficulty in knowing the amount of drug in the different layers and regions of the skin. There are different techniques such as fluorescence confocal microscopy or immunohistofluorescence that allow to obtain qualitative images of the biodistribution of drugs or fluorophores.

It is also possible to quantify the non-permeated active ingredient by separation of the skin layers, extraction and HPLC analysis. Due to the complexity of this technique the error is usually quite high and it only gives an idea of the amount penetrated in each layer, but it is not possible to observe the cutaneous biodistribution of the active ingredient.

Regulatory authorities are becoming increasingly stringent in studying the biodistribution of topical active ingredients, whether for bioequivalence studies, for safety reasons and/or to demonstrate the efficacy of formulations. Advanced analytical techniques that allow selective detection and quantification are needed by the scientific community. One of the most promising techniques in skin drug delivery research today is confocal Raman microscopy [L. Franzen et al 2016].

Many of the techniques currently used to analyse the biodistribution of drug treatments require the use of molecular labeling (e.g. fluorescent or radiological). Among the label free techniques. Matrix Assisted Laser Desorption Ionisation - Time Of Flying Mass Spectrometry Imaging (MALDI-TOF MSI) and Confocal Raman are two of the techniques with the greatest potential for biomedical analysis of biological tissues.

MALDI-MSI is a technique that allows the analysis of multiple molecules in biological tissues. Although in the past this technique has been used to analyse specific substances such as lipids or proteins [Fitzgerald et al 1993] in a qualitative manner, in recent years it has gained interest in terms of the possibility of quantitatively analysing the biodistribution of different molecules [Anne Mette Handler 2021].

Raman spectroscopy is a non-invasive spectroscopic technique with high spatial resolution. It is commonly used to study the biodistribution of different compounds within formulations and in different biological tissues. Devices have also been developed to quantify both skin intrinsic compounds and the penetration of different compounds in a non-invasive way by *In vivo* Confocal Raman [Caspers PJ et al 2001, Caspers PJ et al 2003].

In previous studies, lipomers encapsulating DEX were developed and optimised. During these studies an extensive physicochemical characterization was performed in addition to studying the *ex vivo* cutaneous biodistribution by Confocal Fluorescence Microscopy and by Immunohistofluorescence, in pig skin. The DEX penetration promoting effect of the Lipomers was proven and it was possible to qualitatively study the biodistribution of the fluorescently

Chapter 9 - *Ex vivo* MALDI-TOF Mass Spectrometry Imaging and Confocal Raman spectroscopy quantitative skin biodistribution of dexamethasone loaded nanoparticles.

labelled lipomers as well as DEX by immunohistofluorescence. Both techniques seem to indicate the accumulation of these nanoparticles (size, 115 nm; polydispersity, 0.24; zeta-potential (Z-potential), +30 mV) in hair follicles and skin appendages [Eloy Pena-Rodríguez et al 2021a].

Figure 1 shows an illustrative scheme summarising the steps necessary to study the cutaneous biodistribution of DEX and BAK by Confocal Raman and MALDI-TOF IMS. The first step was to permeate the formulations in human scalp explants using Franz Cells. Once permeated, skin cryosections were obtained for histology, Confocal Raman and MALDI-TOF IMS. Calibrators were deposited on tissue and outside of tissue to try to quantify the amount of DEX and BAK by Confocal Raman and MALDI-TOF IMS. In the case of MALDI samples, DEX was derivatized to increase the sensitivity of the technique to detect DEX. Finally, calibrators and tissues were analysed to obtain quantitative biodistribution maps.

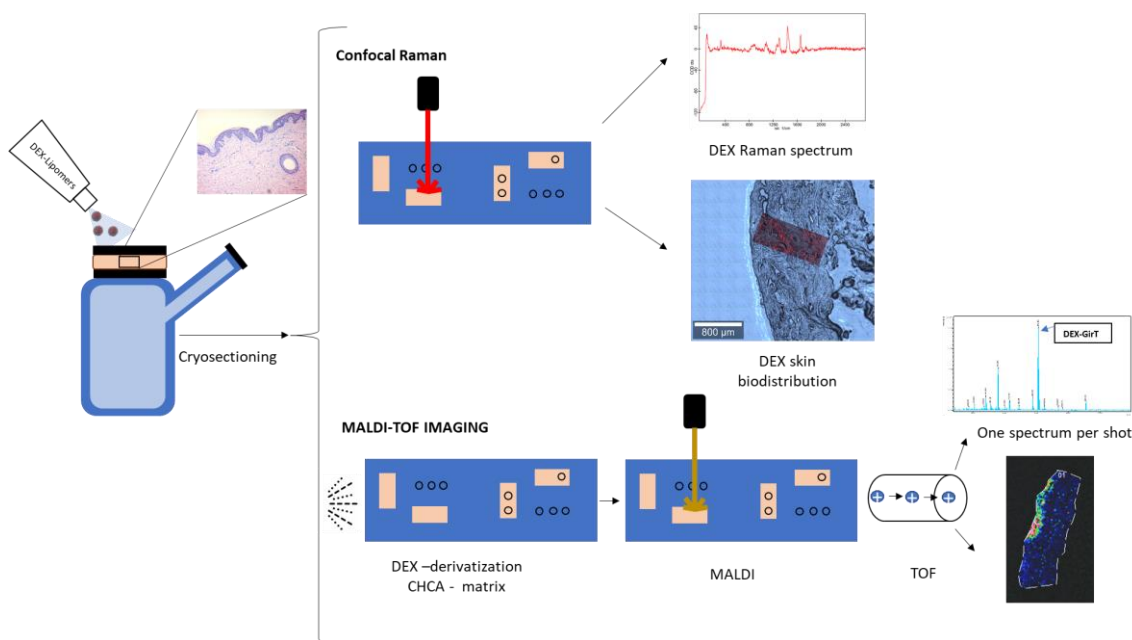


Figure 1. Illustrative workflow showing the steps performed to study the cutaneous biodistribution of DEX and BAK by confocal Raman spectroscopy and MALDI-TOF MSI.

The aim of this research was to fine-tune and compare two of the most promising techniques for the quantitative study of topically administered active ingredients (confocal Raman spectroscopy and MALDI-TOF MSI) in *ex vivo* studies on human scalp permeated with the formulations previously studied (Free-DEX and DEX-lipomers) [Eloy Pena-Rodríguez et al 2021a].

9.2. Materials

Ethyl cellulose with an 49% ethoxyl substitution, 215000 Da average molecular weight and 100 mPa viscosity (EC) (Ashland Industries Europe GmbH, Rheinweg, Switzerland), medium-chain triglycerides (MCT) (Oxi-Med Expres S.A., Barcelona, Spain); Tween 80 and Span 60 (Croda Iberica S.A., Barcelona, Spain), and benzalkonium chloride (Sigma Aldrich, St. Louis, MO, USA) were used to produce the nanoparticles. DEX (Fagron Ibérica, Barcelona, Spain) was the active pharmaceutical ingredient, and the selected solvents were ethyl acetate (EA), ethanol absolute (ET) (Scharlab S.L., Barcelona, Spain), and purified water (Inhouse). A-Cyano-4-hydroxycinnamic acid (CHCA) (Sigma Aldrich, St. Louis, MO, USA), Girard's reagent T (Sigma Aldrich, St. Louis, MO, USA), Methanol (Sigma Aldrich, St. Louis, MO, USA), Acetic acid (Sigma Aldrich, St. Louis, MO, USA), Trifluoroacetic acid (TFA) (Sigma Aldrich, St. Louis, MO, USA), Acetonitrile (Sigma

Chapter 9 - *Ex vivo* MALDI-TOF Mass Spectrometry Imaging and Confocal Raman spectroscopy quantitative skin biodistribution of dexamethasone loaded nanoparticles.

Aldrich, St. Louis, MO, USA), Phosphate buffer saline (Sigma Aldrich, St. Louis, MO, USA), Optimal Cutting Temperature Compound (OCT) (Fisher Scientific, Waltham, USA), Hematoxylin (Sigma Aldrich, St. Louis, MO, USA), Eosin (Sigma Aldrich, St. Louis, MO, USA), Xylene (Sigma Aldrich, St. Louis, MO, USA).

9.3. Methods

9.3.1. Manufacturing of DEX- loaded lipomers

The encapsulation of DEX in EC and MCT lipomers was performed by the emulsion solvent evaporation method, as previously described [Eloy Pena-Rodríguez et al 2021a]. Briefly, the polymer EC (2.33% w/w), MCT (0.20% w/w), DEX (1.00% w/w) and the surfactant Span 60 (0.16% w/w) were dissolved in a mixture of ethanol:ethyl acetate (1:5) (3% and 12% w/w respectively). In parallel, an aqueous phase composed of the surfactants Tween 80 (1.50% w/w) and benzalkonium chloride (0.20% w/w) was prepared. Both phases were mixed and emulsified using a UP400st sonicator at an amplitude of 40% for 5 min. Finally, the organic solvent was evaporated under a vacuum at 40°C for 5 min.

9.3.2. Physicochemical characterisation

Dynamic light scattering (DLS) (Malvern Zetasizer Nano ZS (Malvern Panalytical, Malvern, UK)) was used to study the hydrodynamic diameter (Z-average), polydispersity index (PDI), and zeta-potential of the nanoparticles produced. Previously described DEX-lipomers with a hydrodynamic diameter of 185.23 ± 5.24 nm, a PDI of 0.360 ± 0.019 , a Z-potential of 39.0 ± 0.1 mV and an encapsulation efficiency (%EE) of 98.60 ± 0.01 were used for skin permeation assays and MALDI-MSI analysis [Eloy Pena-Rodríguez et al 2021a].

9.3.3. Full thick human scalp *In vitro* penetration tests

Human scalp was purchased from Biopredic (Saint Grégoire, France), which has authorisation for the collection, processing and sectioning of human biological samples for research purposes. Samples were remnants from surgeries complying with the French law CSP1245-2, with informed consent provided by the patient, who remained anonymous and did not receive financial reward or publicity. The donor was a 58-year-old Caucasian female. The skin was cleaned with sterile saline solution and transported to the laboratory at 4°C in saline solution. Skin pieces were defatted (with a scalpel) and frozen at -20°C until use. On the day of the experiment, skin pieces were warmed and mounted in Franz cells with an effective diffusion area of 0.196 cm² and around 12 mL of receptor volume capacity (PBS at 32°C and stirred at 500 rpm). TEWL measurements were performed to check the integrity of the skin samples (TEWL Vapometer SWL4549, Delfin Technologies Ltd., Kuopio, Finland). 76 mg of each of the formulations were given in infinite doses in non-occluded conditions.

9.3.4. Cryosectioning

After 18 h of permeation, the diffusion surface was washed with PBS, cut with a scalpel into pieces of about 0.5 cm², frozen in dry ice and transported to a Leica CM 3050 S cryostat (Leica Biosystems, Barcelona, Spain). Using a drop of the OCT compound, the skin slices were attached to the cryostat holder. 12-µm cross-sections were obtained from the part of the skin that did not come into contact with the OCT. The temperature of the cryostat chamber was -25°C and that of the sample was -27°C. The skin sections were collected on three different types of slides. The samples for confocal Raman spectroscopy were deposited on CaF₂ slides (Crystan Ltd, Poole, United Kingdom), since it is a material that only emits one peak at 321 cm⁻¹ and, thus, the interference with the sample signal is minimal. Skin sections for MALDI-MSI were collected on superconductive glass slides with an ITO coating (Bruker Daltonics, Germany). Contiguous slices

Chapter 9 - *Ex vivo* MALDI-TOF Mass Spectrometry Imaging and Confocal Raman spectroscopy quantitative skin biodistribution of dexamethasone loaded nanoparticles.

were obtained and collected on Superfrost® poly-lysine-coated slides for histology. Skin cryosections were then dried with a vacuum pump in a silica gel desiccator overnight.

9.3.5. H&E Staining

Haematoxylin & eosin staining was performed on slices contiguous to those analysed by MALDI-MSI to observe the biodistribution of DEX and BAK in the skin structure. Superfrost® slides were immersed for 2 min in 100%, 90%, 80% and 70% ethanol consecutively. Then, the samples were washed in purified water for 5 min. The slides were then immersed in haematoxylin for 8 min and washed with purified water. The next step was to dehydrate the samples for 3 min in increasing 70%, 80% and 90% ethanol solutions. The slides were submerged for 2 min in an eosin solution and washed for 3 min in a 90% ethanol solution. Finally, the slides were immersed two times in a xylene solution for 5 min each time. Optical images were obtained with a Leica Z16 APO vertical fluorescence stereomicroscope under a 1x magnification (Leica Microsystems, Wetzlar, Germany).

9.3.6. MALDI-TOF set up

To optimise the experimental conditions for DEX detection by MALDI-TOF as a preliminary step to the MSI experiments, different ionisation tests were first performed. These ionisation tests consisted of studying the feasibility of analysing DEX and BAK, checking the effect of derivatisation with GirT and making sure that there were no interferences between the different compounds. Underivatised samples of 2 µg/µL of DEX crystals, 100 pg/µL of the GirT reagent, 0.2% w/w BAK and a 1:1 mixture of GirT (100 pg/µL):BAK (2 µg/µL) were tested to obtain the individual spectra of each spectrum and to study possible interferences. Crystals of derivatised DEX-GirT (2 µg/µL) were also analysed and the corresponding peaks of both DEX and DEX-GirT were assessed to check the completeness of the reaction.

9.3.7. On tissue and out of tissue DEX and BAK Calibrators for MALDI and Confocal Raman quantification

To obtain a quantitative biodistribution of DEX and BAK, calibrators were prepared. Calibrators were deposited on-tissue and out-of-tissue to compare the DEX and BAK intensities and calculate the matrix effect for each compound (Figure 2). The matrix effect was calculated by the signal-based method (Equation 1):

$$\text{Matrix effect \%} = \frac{\text{Analyte signal}_{\text{matrix extracted}}}{\text{Analyte signal}_{\text{solvent}}} \times 100 \quad (1)$$

Chapter 9 - *Ex vivo* MALDI-TOF Mass Spectrometry Imaging and Confocal Raman spectroscopy quantitative skin biodistribution of dexamethasone loaded nanoparticles.

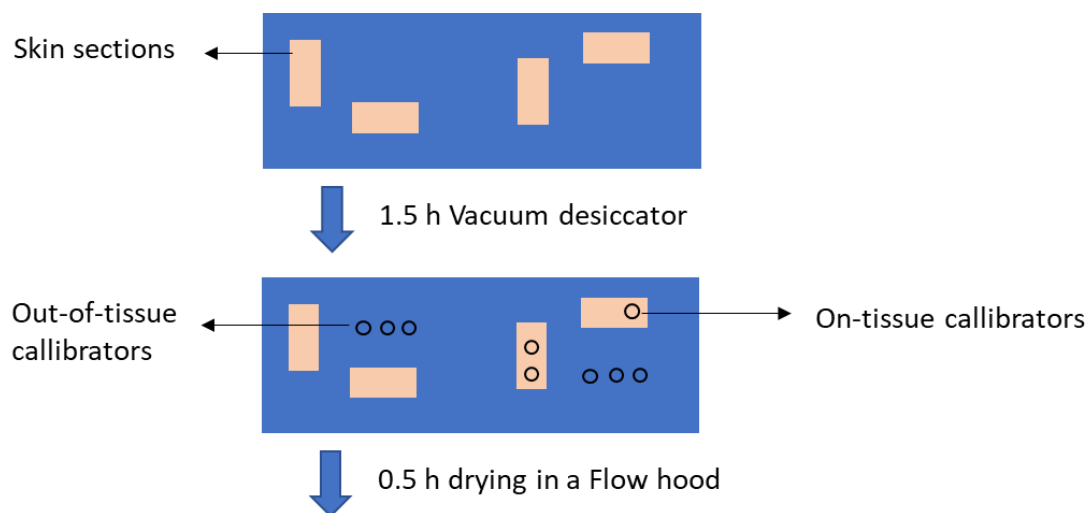


Figure 2. Illustrative scheme showing the steps performed to prepare the out-of-tissue and on-tissue calibrators.

On-tissue calibrators: Mixtures of DEX and BAK were prepared in 80% w/w methanol and 0.2% w/w TFA for the on-tissue calibrators at four different concentrations (Table 1). A 0.5- μ L drop of the mixture was placed on non-permeated skin cross-sections. Once the drops were deposited, they were left to dry for 20 min in a fume hood.

Out-of-tissue calibrators: To calculate the matrix effect, the same concentrations of calibrators were prepared in skin homogenates with 0.2% w/w TFA for the out-of-tissue calibrators. In this case, skin homogenates were obtained by grinding with zirconium beads in the MagNA Lyser device (Roche Diagnostics GmbH, Mannheim, Germany). Briefly, pieces of skin were cut with a scalpel and 10 replicates of 15 mg were weighed into Eppendorf tubes with the zirconium beads. A 600- μ L volume of a 20% w/w methanol solution was poured into each Eppendorf tube and centrifuged for 90 seconds at 7500 rpm. Finally, the skin homogenate was collected from each tube and pooled.

Table 1 DEX and BAK concentrations and corresponding amounts in a 0.5- μ L drop for each of the calibrators.

DEX (ng/ μ L)	BAK (% w/w)	DEX (ng)	BAK (ng)
2000	0.002	1000	10
200	0.0002	100	1
20	0.00002	10	0.1
2	0.000002	1	0.01

These quantities (Table 1) were chosen by estimating the expected amount of DEX that could be found in a skin cross-section. 76 μ L of DEX lipomers were applied at a concentration of 10 mg/mL of DEX. This corresponded to a total applied amount of 0.76 mg for DEX. The skin surface area where they were applied was 0.196 cm^2 (see section 3.3). The skin samples were approximately 0.2 cm thick. The corresponding volume of the skin cylinder where the nanoparticles were applied (V_{skin}) is shown in Equation 2:

$$V_{skin} = S_{skin} \times h_{skin} = 0.19600 \text{ cm}^2 \times 0.20000 \text{ cm} = 0.00392 \text{ cm}^3 \quad (2)$$

where S_{skin} is the surface area of the skin and h_{skin} the skin thickness.

Chapter 9 - *Ex vivo* MALDI-TOF Mass Spectrometry Imaging and Confocal Raman spectroscopy quantitative skin biodistribution of dexamethasone loaded nanoparticles.

The volume of an average histological slice (see section 4.3), V_{hist} , is shown in Equation 3:

$$V_{hist} = A_{hist} \times B_{hist} \times C_{hist} = 0.5 \text{ cm} \times 0.2 \text{ cm} \times 0.0012 \text{ cm} = 0.00012 \text{ cm}^3 \quad (3)$$

where A_{hist} is the width of the histological slice, B_{hist} the height of the slice, C_{hist} the depth of the slice, S_{skin} the surface area of the skin and h_{skin} the skin thickness.

The percentage volume of a 12- μm slice ($V\%$) is shown in Equation 4:

$$V\% = \frac{V_{hist}}{V_{skin}} \times 100 = 0.30\% \quad (4)$$

As for BAK, the original formulation contained BAK at 0.1% w/w, 10 times more diluted than DEX. Therefore, applying the calculated $V\%$, the maximum penetrated amount per skin cryosection of both molecules after a 76- μL administration of the Free-DEX formulation or DEX-lipomer formulation is shown in Table 2.

Table 2 Maximum estimated amounts of DEX and BAK after a 76- μL administration of the Free-DEX or DEX-lipomer formulation.

	Total amount applied (μg)	Maximum estimated amount in an histological slice (μg)
DEX	760	2.280
BAK	76	0.228

Taking into account the difficulty of penetration into the skin barrier, the concentrations shown in Table 1 were chosen to interpolate the intensity obtained by MALDI-MSI and confocal Raman spectroscopy for both DEX and BAK. Dilutions were made up to a DEX quantity of 1 ng and a BAK quantity of 0.01 ng, which were determined as the limit of quantification for both molecules.

MALDI-TOF MSI was internally calibrated by the crystallisation of a mixture of an already derivatised 2000 ng/ μL of GirT-DEX and 10 mg/mL of CHCA (1:1) that were administered in a 1- μL drop deposited on the slide after spraying the matrix on the slide.

9.3.8. Confocal Raman spectroscopy

Samples were analysed with the Alpha 300R confocal Raman microscope (WITec, Ulm, Germany) using a 20x Zeiss EC Epiplan-Neofluar objective. The equipment has two lasers of 785 and 633 nm. Each laser source has its benefits and limitations. The 785-nm laser has a greater ability to penetrate the sample since more photons penetrate the tissue. Due to the pigmented nature of skin, the fluorescence of the tissue has to be taken into account. This fluorescence interferes with the Raman signal and should be minimised. The Raman intensity is inversely proportional to the fourth order of the excitation wavelength. For this reason, the use of a shorter wavelength (633 nm) improves sensitivity since the ratio between the Raman signal and the skin fluorescence is higher. In addition, the quantum efficiency of the detectors decreases rapidly for longer wavelengths [Ali Jaafar et al 2021]. For these reasons, the 633-nm wavelength was chosen to analyse the different tissues and improve the spectral resolution of the assay.

The microscope is equipped with a 50 x 50 mm² motorised table and an electric piezo table. It is equipped with two lens spectrometers (UHT S300 for visible light and UHTS400 for near infrared)

Chapter 9 - *Ex vivo* MALDI-TOF Mass Spectrometry Imaging and Confocal Raman spectroscopy quantitative skin biodistribution of dexamethasone loaded nanoparticles.

with their corresponding back-illuminated CCD detectors and two back-illuminated Peltier cooled charge-coupled detectors with a quantum efficiency greater than 90% that are optimised for visible and near infrared light. The spatial X-Y resolution of the equipment is 350 nm. The lasers are connected to the microscope and the microscope is linked to the spectrometers by fibre optics. The spectrometers are equipped with two diffraction gratings. In the case of the visible one, which was used, it has gratings of 600 and 1800 lines/mm. The grating of 600 lines/mm was used. A white light source with Köhler illumination and a high-quality visualisation camera were used. The results were treated with the Project Five Plus 5.3 software. The visible light spectrometer used was previously calibrated in each of its diffraction gratings with an Ar/Hg lamp.

Optical images of the tissues were obtained. The regions of interest (ROI) to be scanned were selected to obtain the Raman spectra. Scanned areas were composed of 100 lines per area and 1000 points per line with a laser power of 10 mW. The duration of each scanning was 1 h and 15 min. The integration time was 0.4 s and the scan speed was 43.371 lines/s. Table 3 shows the scanned areas. The Live Auto Focus tool was selected to follow the sample topography in real time.

Table 3. Scanned areas corresponding to each analysed region for each formulation using confocal Raman spectroscopy. Figure 6 shows all the regions except the DEX-lipomer 4 region, although it was also used for quantification.

Formulation	Region	Area (μm^2)
DEX-lipomers	1	300000
	2	427500
	3	405000
	4	600000
Free-DEX	1	300000
	2	400000

Once the data were obtained, a cosmic ray was removed for each analysis with a filter size of 3 and a dynamic factor of 8. A background subtraction was performed with a polynomial of degree 6, making sure that no band was detrended. After the correction of the spectrum, a true component analysis was performed. All these data processing steps were performed using WITec Suite Five 5.3 (WITec, Ulf, Germany). This method considers the full Raman spectra rather than single bands. This tool is based on an algorithm that describes each measured spectrum of a hyperspectral dataset by a linear combination of reference spectra [Isaac Benito-González et

al. 2020]. The biodistribution map of the component of interest was superimposed onto the optical image of the tissue using the “overlay” tool of the software.

9.3.9. DEX derivatisation for MALDI-TOF detection

DEX was derivatised with GirT in two different ways.

The derivatisation in solution was performed as follows. A stock solution of DEX at a concentration of 4 $\mu\text{g}/\mu\text{L}$ was prepared in a 10% w/w acetic acid solution in methanol, while a stock solution of GirT at 2 $\mu\text{g}/\mu\text{L}$ was prepared in purified water. In a 1.5-mL Eppendorf tube, 200 μL of the DEX stock and 10 μL of the GirT stock were pipetted and incubated at 37°C in an oven for 5 min.

GirT derivatisation on the ITO slide was also performed. Figure 3 shows a schematic of the steps required for this process. To obtain correct crystallisation, water condensation in the sample must be avoided. For this purpose, the slide was placed in a vacuum desiccator after each step to keep the sample as dry as possible.

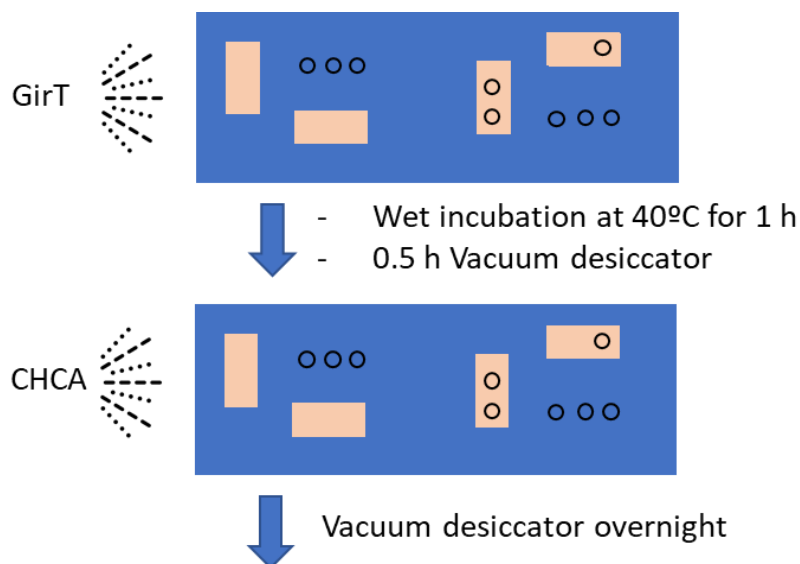


Figure 3. Illustrative scheme showing the steps performed for the on-tissue DEX derivatisation.

A volume of 5 mL of a 5 mg/mL solution of GirT in 80% methanol, 20% purified water and 0.2% TFA was sprayed using the ImagePrep device (Bruker Daltonics, Bremen, Germany). The optimised set-up for derivatisation was 40 cycles at 40% power, with 2.2-second spray pulses, as well as a 30-second incubation and a 60-second drying per cycle. The amount of derivatising agent per mm^2 of sample was calculated by weight difference before and after spraying.

Samples were dried again inside the desiccator for 30 min under a vacuum. Then, the samples were covered with CHCA (10 mg/mL in 80% acetonitrile, 20% purified water and 0.2% TFA) as a MALDI matrix sprayed using the ImagePrep device. The amount of deposited matrix per mm^2 of sample was calculated by weight difference before and after spraying.

9.3.10. MALDI-TOF spectrometry.

After derivatisation on an ITO slide and matrix deposition, samples were finally mounted onto the MTP slide adapter (Bruker Daltonics, Bremen, Germany) and placed into the MALDI-TOF mass spectrometer. Mass spectrometry imaging data were obtained in the reflector positive ion mode in an UltrafleXtreme MALDI-TOF/TOF mass spectrometer (Bruker Daltonics, Bremen, Germany). The spectra were averaged from 500 laser shots per spot. The mass accuracy was <

Chapter 9 - *Ex vivo* MALDI-TOF Mass Spectrometry Imaging and Confocal Raman spectroscopy quantitative skin biodistribution of dexamethasone loaded nanoparticles.

50 ppm. The calibrator analysis was performed in the fast-scanning mode and the permeated skin cryosection analysis was performed in the random spot scanning mode. Laser intensity was set at 85%. The laser diameter was set to the medium size, which corresponded to the spatial raster resolution of 50 μm . The analysis of the spectra focused on the mass range 240-800 m/z . Ion extraction was set at 100 ns.

9.3.11. MALDI -TOF MSI

High-resolution (6400 dpi) scanning of the samples was undertaken with an Epson Perfection V600 scanner (Epson Ibérica, Barcelona, Spain). The FlexImaging 3.0 software (Bruker Daltonics, Bremen, Germany) was used to obtain ion density maps on biological tissues. Using this software, ROIs were defined inside and outside the tissue.

To avoid oversampling, the raster width distance of the selected laser diameter in FlexControl was set to 50 μm . To match the triangulation coordinates (previously marked with a marker pen on the ITO slide), the laser pointer in FlexControl was positioned in the same place as each mark selected in the FlexImaging software until there were 3 teach points around the tissue and calibrator drops. The image was scaled so that the correspondence with the holder was adequate. ROIs around each tissue and each calibrator drop were defined and the random spot scanning method was selected. A total ion count (TIC) normalisation was performed by dividing the intensities of each m/z by the mean intensity for each mean spectrum. In this way, the distribution of each selected m/z (DEX, BAK C₁₂ and BAK C₁₄) in each sample was obtained.

9.4. Results and discussion

9.4.1. Confocal Raman microscopy

First, the individual spectra of DEX, BAK, human scalp, DEX-lipomers and a mixture of DEX and BAK (1:1) deposited on the human scalp were obtained by confocal Raman spectroscopy (Figure 4). The objective of this first step was to test the feasibility of tracing DEX and BAK in different matrices. Possible band overlaps with both human scalp and lipomer excipients were checked. As can be seen in Figure 4, the spectrum of DEX showed an intense peak at 1657 cm^{-1} , while that of BAK showed one at 1007 cm^{-1} . By comparing the spectra of human scalp and that of human scalp with the mixture of DEX and BAK, it was possible to corroborate the possibility of tracing the DEX peak in the skin. For BAK, it was not possible to identify the characteristic peak at 1007 cm^{-1} when depositing the DEX:BAK (1:1) mixture on the skin.

Chapter 9 - *Ex vivo* MALDI-TOF Mass Spectrometry Imaging and Confocal Raman spectroscopy quantitative skin biodistribution of dexamethasone loaded nanoparticles.

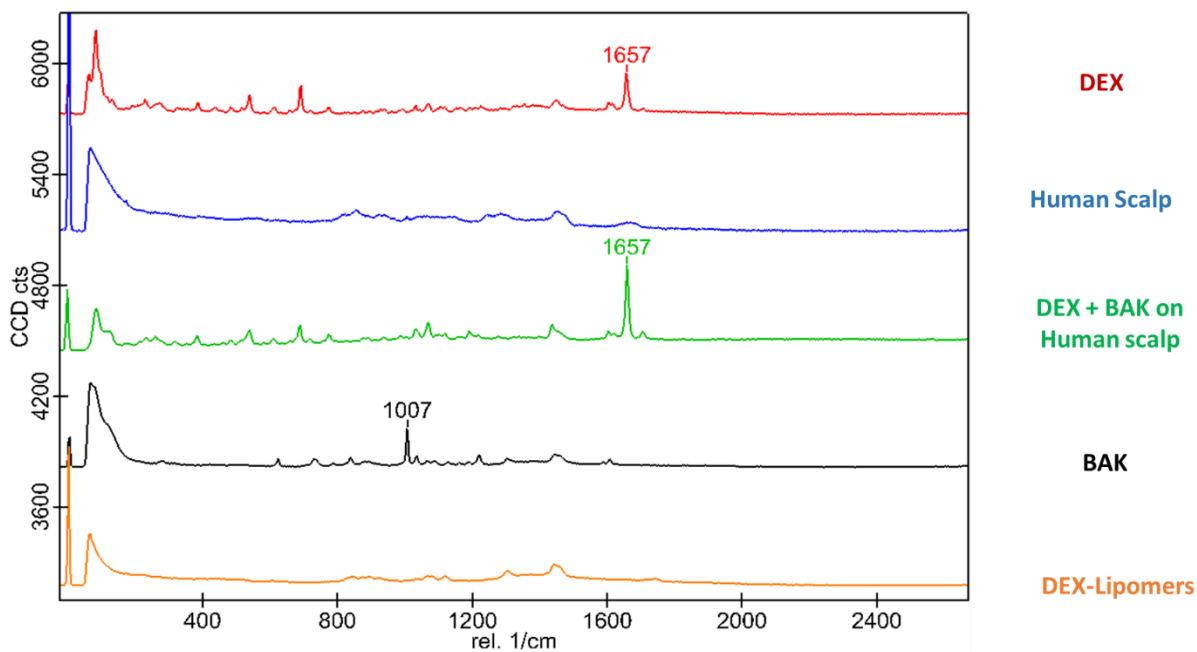


Figure 4. Individual Raman average spectra of pure DEX (red), pure BAK (black), human scalp (blue), DEX-lipomers (orange) and a mixture of DEX and BAK (1:1) deposited on human scalp (green).

Figure 5 A shows the amounts of on-tissue calibrators (DEX and BAK) deposited on each skin region.

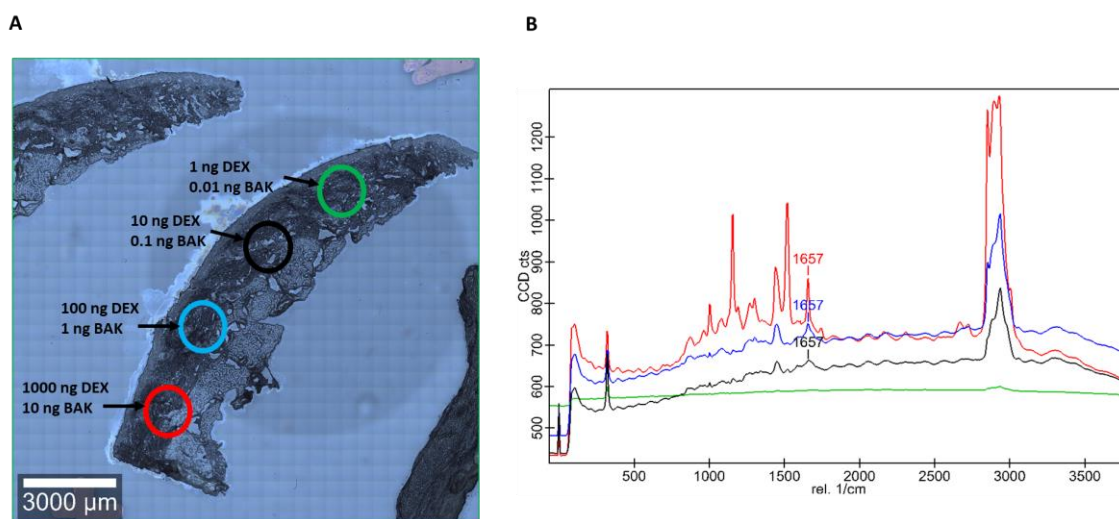


Figure 5 On-tissue calibrators for confocal Raman analysis. (A) Human scalp cryosection showing the regions where 0.5- μ L drops were deposited of the different calibrator concentrations: 1000 ng of DEX, 10 ng of BAK (red); 100 ng of DEX, 1 ng of BAK (blue); 10 ng of DEX, 0.1 ng of BAK (black); and 1 ng of DEX, 0.01 ng of BAK (green). (B) Raman average spectra of the regions scanned for each calibrator (same colours as before) showing the characteristic DEX Raman peak at 1657 cm^{-1} .

Figure 5 B shows the average spectra for each concentration. The dependence between the DEX peak intensity (1657 cm^{-1}) and the amount of DEX deposited on the skin can be observed.

The BAK peak at 1007 cm^{-1} was not identified in any of the calibrators so it was not possible to study its biodistribution by confocal Raman spectroscopy.

A filter was created at 1657 cm^{-1} with a peak width of 50 cm^{-1} and 4 points were taken on each side to obtain the average intensity sum of each calibrator. A regression was performed between

Chapter 9 - *Ex vivo* MALDI-TOF Mass Spectrometry Imaging and Confocal Raman spectroscopy quantitative skin biodistribution of dexamethasone loaded nanoparticles.

the known amount of the calibrator (ng of DEX) and the average peak intensity obtained. An exponential fitting was chosen because the intensity of electromagnetic waves undergoes an exponential decay when they penetrate the skin [Lutz Franzen et al. 2012]. To avoid possible overfitting, simple exponential models were chosen. In this way, it was possible to obtain the equation that was used to interpolate the amount of DEX as a function of the intensity obtained after permeation assays with DEX-lipomers or the Free-DEX control solution. Equation 23 shows the regression of the quantification curve and the equation obtained:

$$y = 2.504e^{0.9931x} \quad R^2 = 0.9931 \quad (5)$$

where “y” is the DEX amount in ng and “x” the sum of the 1657 cm⁻¹ Raman band intensity.

Once the calibrators were analysed on the tissue, different regions of the skin cryosections were analysed after permeation with DEX-lipomers (Figure 6 A) or the Free-DEX control solution (Figure 6 B). After cosmic ray removal and background subtraction, the true component analysis tool of the WITec software was used to analyse the different components present in the tissue. The epidermis and hair follicles are marked with white arrows. Raman spectra of the on-tissue DEX calibration component (green), the DEX component of the lipomers (red) and the DEX component of the control solution (blue) are shown in Figure 6 C. The biodistribution maps (in red) of the 1657 cm⁻¹ Raman band intensity were overlaid on the corresponding skin regions (Figure 6 A 1, 2, 3 and Figure 6 B 1, 2).

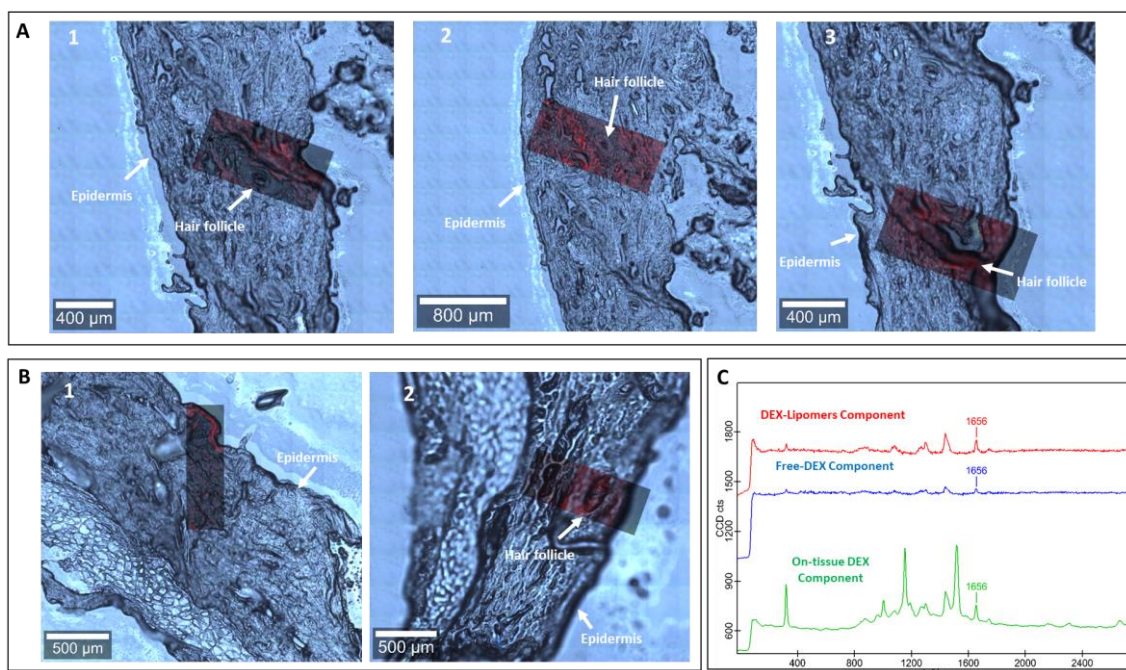


Figure 6. Cryosections of human scalp permeated with DEX-lipomers or Free-DEX analysed by confocal Raman microscopy. (A) DEX-lipomer-permeated cryosections, showing the overlay of the DEX distribution map on the scanned regions number A.1, A.2 and A.3. (B) Free-DEX-permeated cryosections, showing the overlay of the DEX distribution map on the scanned regions B.1 and B.2. (C) Average DEX Raman component spectra of the on-tissue DEX calibrator component (green), the DEX component of the lipomers (red) and the DEX component of the control solution (blue). White arrows indicate the localisation of the epidermis and hair follicles in the cryosections.

Even at depths of > 1000 μm, DEX accumulations could be observed in the human scalp after encapsulation in lipomers. In the hair follicles, DEX accumulation was observed in the outer root sheath. In previous studies [Eloy Pena-Rodríguez et al 2021a], the accumulation of DEX in hair

Chapter 9 - *Ex vivo* MALDI-TOF Mass Spectrometry Imaging and Confocal Raman spectroscopy quantitative skin biodistribution of dexamethasone loaded nanoparticles.

follicles and sebaceous glands was also observed by immunohistofluorescence when loaded in lipomers. In addition, the accumulation of fluorescently labelled lipomers has also been verified by confocal microscopy.

The Free-DEX control showed lower skin permeability, with an accumulation of DEX in some regions of the epidermis (Figure 6 B.1). However, in the dermis, the accumulation of DEX was qualitatively lower when compared to the DEX-lipomers (Figure 6 A 1, 2, 3).

Due to the autofluorescence of skin and the interference with the Raman signals of the different components present in this tissue, it is difficult to obtain quantitative data. In addition to the qualitative analysis of biodistributions, an attempt was made to obtain a quantitative estimate of the amount of DEX present in the scanned regions.

Table 4 shows the DEX quantities interpolated from Equation 5, which was obtained after regression of the on-tissue calibrators (Figure 5) normalised by the skin mass in μg .

The factors to convert from skin volume to skin mass in μg , assuming a skin density of 1 g/cm^3 , are shown in Equation 6, where “ M_{scanned} ” is the mass of the scanned region, “ A ” the area of the scanned region and “ T ” the thickness of the skin sample.

$$M_{\text{scanned}} (\mu\text{g}) = A \times T \times \frac{10^{-12} \text{ cm}^3}{1 \mu\text{m}^3} \times \frac{1 \text{ g}}{1 \text{ cm}^3} \times \frac{10^6 \mu\text{g}}{1 \text{ g}} \quad (6)$$

Table 4 Average DEX AUC and estimated interpolated DEX amounts (ng) after the quantitative approach of confocal Raman spectroscopy for Free-DEX and DEX-lipomers. P-value represents the $\alpha = 0.05$ significance when comparing the results between DEX-lipomers and Free-DEX.

Formulation	DEX Raman band intensity (AU)	Interpolated DEX amount (ng)	Skin mass normalised DEX amount (ng/ μg)	P-value ($\alpha=0.05$)
DEX-lipomers	198.34 \pm 38.64	53.82 \pm 29.29 ng	10.82 \pm 5.87	0.13
Free-DEX	159.13 \pm 7.41	27.42 \pm 2.61 ng	6.30 \pm 1.47	

Although there were no significant differences ($p > 0.05$, Table 4), a trend towards a higher permeate concentration was observed for DEX when loaded into the lipomers. It must be noted that this was a quantitative approach. When qualitatively comparing the amounts of DEX in the different scanned regions of the skin, it was found that the active ingredient mainly accumulated in the superficial layers (the epidermis and stratum corneum) when in the Free-DEX control solution, while accumulation of DEX was observed around the follicles and in the dermis at a depth of up to approximately 1000 μm when encapsulated in the lipomers.

Thus, confocal Raman spectroscopy was proven to be a very useful technique to study and compare the cutaneous biodistributions of DEX in a quantitative manner.

9.4.2. MALDI-TOF set up

At the beginning of the experiments, underivatized DEX crystals were analysed. The spectrum obtained (Figure 7 A) shows very low intensity peaks at $m/z = 393.2 \text{ Da}$ corresponding to the mass of protonated DEX ($M+H^+$). The low-intensity peaks of $\text{DEX} + \text{Na}^+$ and $\text{DEX} + \text{K}^+$ are also

Chapter 9 - *Ex vivo* MALDI-TOF Mass Spectrometry Imaging and Confocal Raman spectroscopy quantitative skin biodistribution of dexamethasone loaded nanoparticles.

shown. This indicated the need to derivatise DEX so that the signal obtained from the compound would be higher (Figure 8 B).

As for BAK, being a quaternary ammonium salt, the signal obtained was much more intense and suitable for tracing lipomers by MALDI MSI (Figure 7 B). The peaks corresponding to the BAK C_{12} analogue ($m/z = 304.3$ Da) and the BAK C_{14} analogue ($m/z = 332.3$ Da) were observed.

GirT is a charged quaternary ammonium salt that reacts with ketones and aldehydes to yield hydrazone derivatives. It is used in MALDI-MS to conjugate steroids, peptides and other molecules to improve the sensitivity of the analysis [Haizheng Hong et al 2007]. The spectrum in Figure 7 C shows the GirT peak at $m/z = 132.1$ Da.

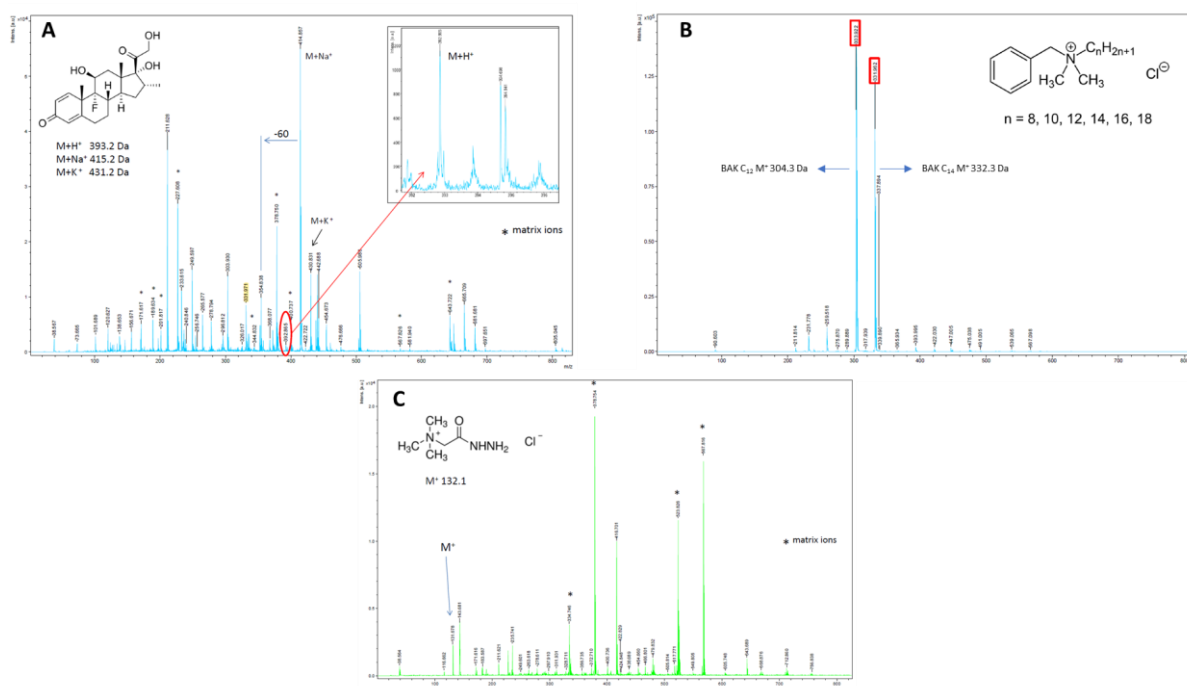


Figure 7 MALDI-MS spectra: (A) 2 μ g of DEX showing an $M+H^+$ peak at $m/z = 392.8$ Da; (B) 0.2% w/w BAK showing M^+ peaks of BAK C_{12} at $m/z = 304.3$ Da and of BAK C_{14} at $m/z = 332.3$; and (C) 50 μ g of GirT showing an M^+ peak at $m/z = 131.7$ Da.

Once individual spectra were obtained, a 1:1 mixture of GirT (50 μ g) with 0.2% w/w BAK (Figure 8 A) and a 2- μ g sample of a GirT-DEX conjugate (Figure 8 B) were analysed. As can be seen in Figure 8 A, there were no changes in the spectrum when mixing GirT and BAK; hence, no reaction seemed to be possible between these two molecules. The method was considered to be selective, as there were no interferences between the reagents or different compounds.

Chapter 9 - *Ex vivo* MALDI-TOF Mass Spectrometry Imaging and Confocal Raman spectroscopy quantitative skin biodistribution of dexamethasone loaded nanoparticles.

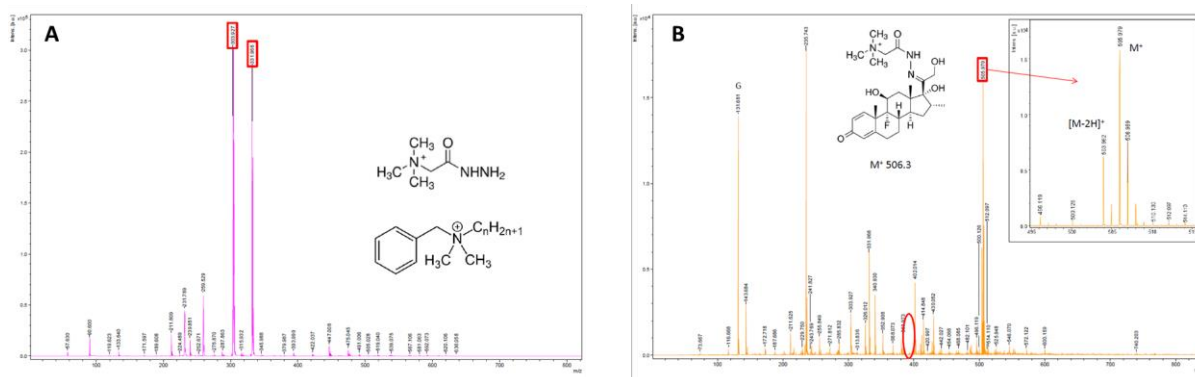


Figure 8 MALDI-MS spectra: (A) A 1:1 mixture of 50 pg of GirT and 0.2% w/w BAK; (B) 2 µg of GirT-DEX showing an M⁺ peak at m/z = 506.3 Da. Red ellipse shows the absence of the DEX peak at 393.2 Da, suggesting full derivatisation with GirT.

To check the correct reaction of GirT with DEX, the spectrum of a 2-µg sample was analysed after derivatisation. GirT added 114 Da to the DEX molecule. Consequently, the derivatised DEX peak was observed at 506.3 Da. The ellipse marked in red shows the absence of the DEX peak at m/z = 393.2 Da, suggesting a complete reaction with GirT (Figure 8 B).

9.4.3. MALDI-MSI and quantification

On-tissue derivatisation methods that consist of depositing derivatisation reagents onto the tissue by spraying or sublimation have been developed to improve the sensitivity of the mass spectrometry imaging of different molecules [Hua Zhang et al 2020].

On-tissue DEX derivatisation for skin worked properly, with human scalp not showing any interfering peaks with the DEX or BAK peaks. Once the individual spectra were obtained, the on-tissue and off-tissue calibrators were analysed, with the signal ratio between both samples used to obtain the matrix effect. A calibration curve was obtained for the on-tissue DEX, BAK C₁₂ and BAK C₁₄ calibrators by performing exponential regressions of the DEX and BAK amounts (ng) as a function of the mean corresponding peak intensities.

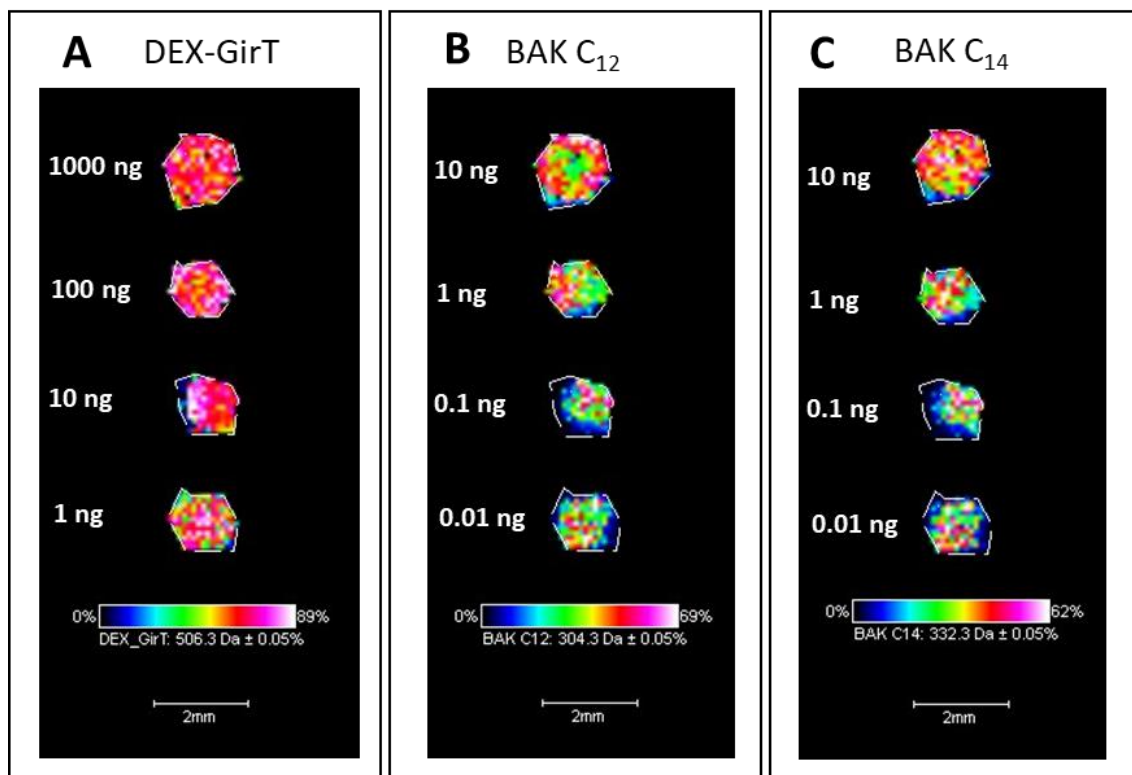


Figure 9 MALDI-TOF MSI: (A) Intensity maps and exponential regression for the outside-of-tissue 506.3-Da DEX-GirT calibrator; (B) intensity maps and logarithmic regression for the outside-of-tissue 304.3-Da BAK C₁₂ calibrator; and (C) intensity maps and logarithmic regression for the outside-of-tissue 332.3-Da BAK C₁₄ calibrator. Scale bar, 2 mm.

Figure 9 shows the MALDI-MSI results of the ROIs for the out-of-tissue DEX, BAK C₁₂ and BAK C₁₄ calibrators.

On-tissue calibrators

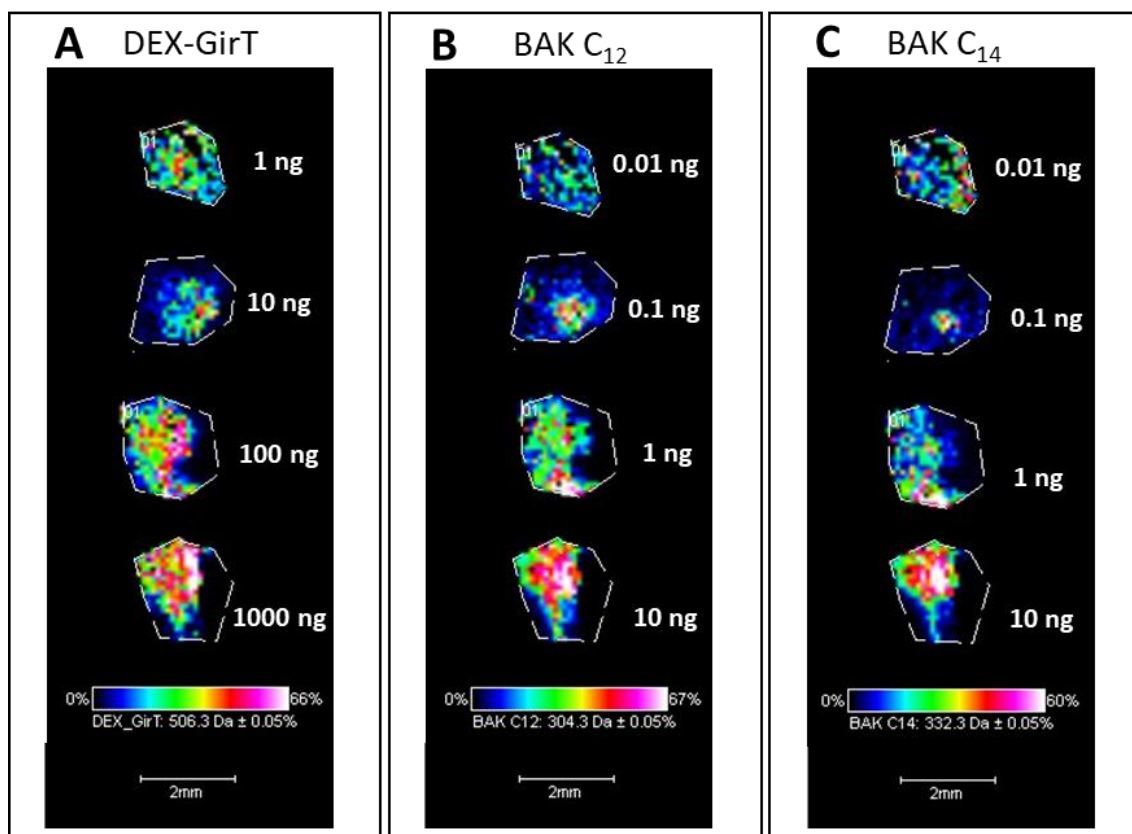


Figure 10 Intensity maps after MALDI-MSI analysis for: (A) on-tissue 506.3-Da DEX-GirT calibrator; (B) on-tissue 304.3-Da BAK C₁₂ calibrator; and (C) on-tissue 332.3-Da BAK C₁₄ calibrator. Scale bar, 2 mm. Intensity colour scale bar is shown. White text indicates the corresponding amount of each calibrator.

Out-of-tissue (Figure 9) and on-tissue (Figure 10) derivatisation were successful, as the dependence of DEX-GirT on the 506.3-Da peak was clearly observed in both cases. Even at the lowest amount (Figure 10 - 1 ng of DEX), it was possible to observe the distribution of the 0.5- μ L drop on the tissue.

The on-tissue exponential regressions (Equations 7-9) showed good correlations between the on-tissue Dex-GirT, BAK C₁₂ and BAK C₁₄ calibrator amounts and the mean intensity of the corresponding peaks.

The exponential equations obtained were the following:

$$\text{DEX-GirT: } y = 2.3398e^{0.1404x} \quad R^2 = 0.9996 \quad (7)$$

$$\text{BAK C}_{12}: y = 0.0503e^{0.1045x} \quad R^2 = 0.9934 \quad (8)$$

$$\text{BAK C}_{14}: y = 0.0542e^{0.1463x} \quad R^2 = 0.9930 \quad (9)$$

where “y” is the on-tissue calibrator amount in ng, “x” the mean intensity of the corresponding peaks and R² the correlation factor between the two variables.

By visually comparing the on-tissue colour scale and comparing it with that of the out-of-tissue calibrators, the matrix effect could be observed whereby the on-tissue intensities were slightly lower. In this way, it was possible to calculate the matrix effect in the skin. The matrix effect for

Chapter 9 - *Ex vivo* MALDI-TOF Mass Spectrometry Imaging and Confocal Raman spectroscopy quantitative skin biodistribution of dexamethasone loaded nanoparticles.

DEX-GiT, BAK C₁₂ and BAK C₁₄ was calculated according to Equation 1 (see section 3.7) for each amount of the calibrator. The results are shown in Table 5.

Table 5 DEX-GiT, BAK C₁₂ and BAK C₁₄ % matrix effect after signal-based comparison of the on-tissue and out-of-tissue calibrators.

DEX (ng)	Out-of-tissue signal (AU)	On-tissue signal (AU)	Matrix effect (%)	BAK C12 (ng)	Out-of-tissue signal (AU)	On-tissue signal (AU)	Matrix effect (%)	BAK C14 (ng)	Out-of-tissue signal (AU)	On-tissue signal (AU)	Matrix effect (%)
1	10.92	0.46	4.17	0.01	25.91	0.43	1.64	0.01	16.23	0.41	2.55
10	34.21	3.07	8.96	0.1	17.07	1.03	6.01	0.1	11.39	0.94	8.28
100	92.80	27.65	29.80	1	30.18	14.56	48.24	1	19.64	8.68	44.20
1000	130.10	43.03	33.07	10	67.79	54.42	80.28	10	48.93	38.17	78.01
Average			19.00	Average			34.04	Average			33.26
Standard deviation			14.55	Standard deviation			37.30	Standard deviation			35.07

If the matrix effect was minimal, the on-tissue signals would be very similar to the out-of-tissue signals and the % matrix effect would remain close to 100% (Equation 1). In other words, the lower the percentage, the greater the matrix effect. As expected, as the concentration of the analyte increased, the % matrix effect decreased (Table 5) due to the higher signal of the analyte. The matrix effect was directly proportional to the concentration of the analyte. It maintained a linear relationship. The results showed high standard deviations. However, in this study, the matrix effect was not applied to the results since the data were quantified with on-tissue calibrators. Nevertheless, an attempt was made to estimate the value of the matrix effect for each of the compounds to obtain more information from the assay.

The next step was to analyse the *ex vivo* permeated human scalp and determine if it was possible to derivatise on-tissue the accumulated DEX *in vitro* in a Franz cell. It was also determined whether it was possible to trace the lipomers by assessing BAK biodistribution.

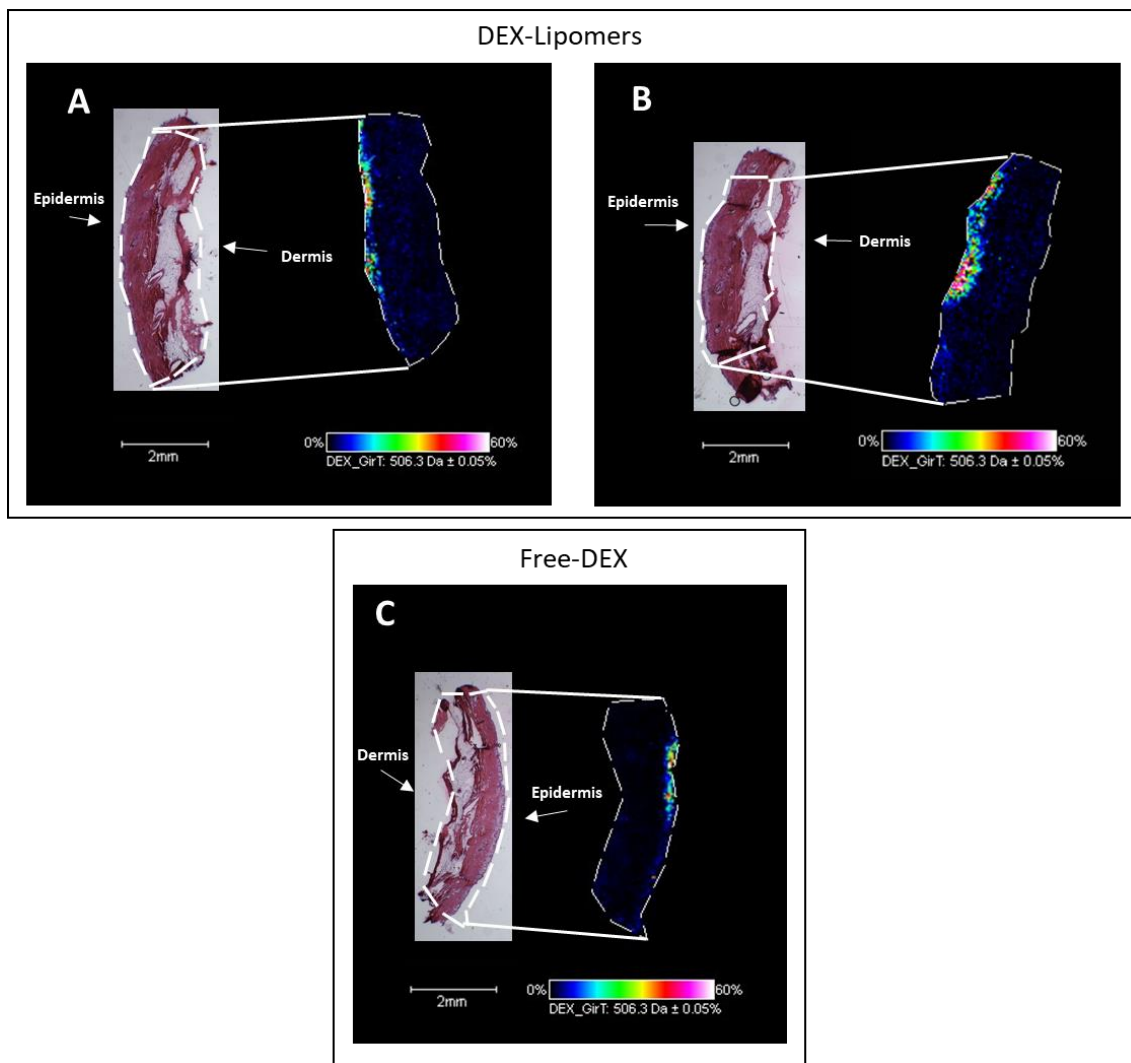


Figure 11 MALDI images and spectra: (A, B) cryosections of human scalp permeated with DEX-lipomers; (C, D) cryosections of human scalp permeated with Free-DEX. White arrows show the epidermis and dermis orientation. Scale and intensity bars are shown. The overlaying of the ROIs on the corresponding histological cryosections is also shown.

Figure 11 A-B shows two skin cryosections after permeation with the DEX-lipomers. The presence of the 506.3-Da peak showed the correct derivatisation of DEX in the permeated samples. As can be seen by the white arrows, DEX accumulated in the more superficial layers (epidermis), while the amount of DEX in the dermis and deeper layers was lower. Figure 11 C shows a less intense accumulation that was restricted to the most superficial layers of the skin (the epidermis and stratum corneum).

Table 6 shows the areas of the analysed ROIs and the corresponding mass in μg calculated by Equation 6 (see section 4.1). In this case, the areas were measured with ImageJ (ImageJ2 v2.35, National Institutes of Health, Bethesda, MD, USA).

Table 6 MALDI-MSI analysis of the skin ROIs (areas, volume, and mass).

ROI	Area (μm^2)	Volume (μm^3)	Mass (μg)
Figure 11 A	10686523	133898604	133.90
Figure 11 B	11158217	128238276	128.24

Figure 11 C	8721085	104653020	104.65
-------------	---------	-----------	--------

As observed in previous immunohistofluorescence studies [Eloy Pena et al 2021a], skin penetration was lower when DEX was not loaded in the lipomers but free in the control solution.

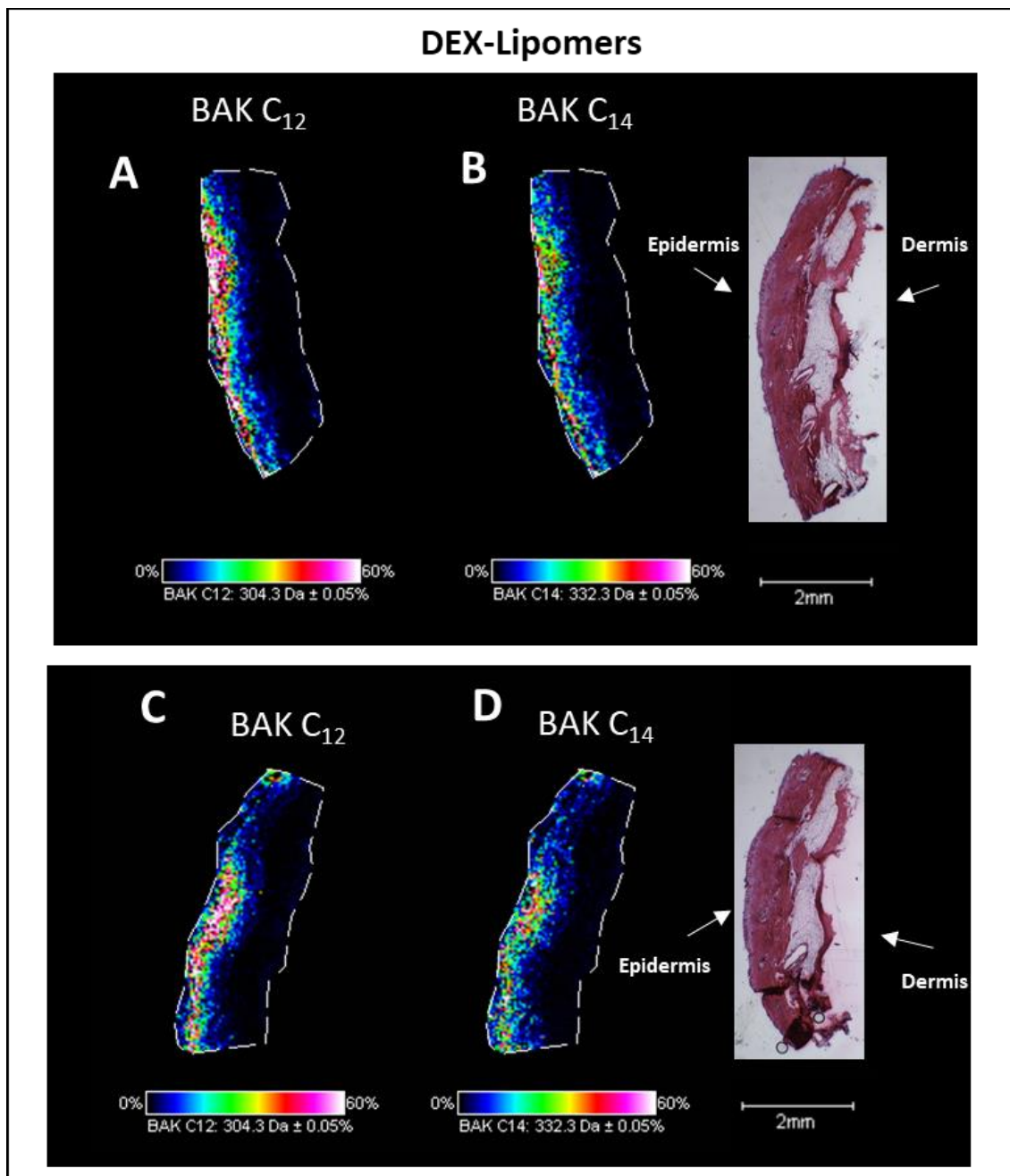


Figure 12 MALDI images and spectra for cryosections of human scalp permeated with DEX-lipomers: (A, C) biodistribution of BAK C₁₂; (B, D) biodistribution of BAK C₁₄. White arrows show the epidermis and dermis orientation.

Simultaneously, the biodistributions of BAK C₁₂ and BAK C₁₄ in skin tissues permeated with DEX-lipomers were analysed. Figure 12 A, C shows the skin biodistribution of BAK C₁₂, while Figure 12 B, D shows the skin biodistribution of BAK C₁₄. The biodistribution results indicated that the lipomers were able to permeate beyond the epidermis (up to a depth of about 800 μ m). This

Chapter 9 - *Ex vivo* MALDI-TOF Mass Spectrometry Imaging and Confocal Raman spectroscopy quantitative skin biodistribution of dexamethasone loaded nanoparticles.

would be in agreement with the results obtained in previous studies [Eloy Pena et al 2021a]. In those studies, by encapsulating a hydrophobic fluorophore (coumarin 6) and labelling the lipomers with LRB, the lipomers were observed to penetrate deep layers, releasing the encapsulated active ingredient into the epidermis and hair follicles.

Table 7 shows the results of the interpolation of the average DEX and BAK intensities obtained with the on-tissue calibrators using Equations 7, 8 and 9.

Table 7 Estimated average interpolated DEX and BAK amounts (ng) for Free-DEX and DEX-lipomers using the MALDI-MSI quantitative approach.

	DEX Intensity (AU)	DEX (ng)	DEX (ng/ μ g skin)	BAK C ₁₂ Intensity (AU)	BAK C ₁₂ (ng)	BAK C ₁₂ ng/ μ g skin)	BAK C ₁₄ Intensity (AU)	BAK C ₁₄ (ng)	BAK C ₁₄ (ng/ μ g skin)
DEX-Lipomers	3.261	3.70	0.029	26.74	8.22	0.064	11.91	0.31	0.002
	3.184	3.66	0.036	26.37	7.91	0.062	10.67	0.26	0.002
Free-DEX	4.803	4.59	0.035	NP	NP	NP	NP	NP	NP

By observing the results in Table 7, different conclusions can be drawn. The total amount of DEX-GiT extracted from the skin tissues was similar for DEX-lipomers and Free-DEX. When studying the qualitative data, the biodistributions were different. Although the amount of penetrated DEX was the same, DEX-lipomers were distributed more in the deeper layers when compared to Free-DEX. This is in agreement with the results obtained by confocal Raman spectroscopy.

As for the BAK results in Table 7, BAK C₁₂ penetrated in greater quantities than BAK C₁₄. However, the relative abundance of the BAK C₁₂ homologue in bulk BAK was higher than that of BAK C₁₄, which might explain the differences found.

9.4.4. Confocal Raman and MALDI-MSI comparison

When comparing the results obtained with confocal Raman spectroscopy and MALDI-MSI, the amounts of DEX detected were lower with MALDI-MSI. A possible explanation is the fact that quantification in this case was performed indirectly through on-tissue derivatisation with GiT. Since these were permeated samples, it is possible that the derivatisation yield was lower than that for the calibrators, where DEX was more accessible when deposited on the cross-section. In addition, the spatial resolution of confocal Raman spectroscopy is higher; thus, it may be possible to detect more DEX present in the tissue with this technique.

A summary table (Table 8) comparing the different techniques applied to the quantitative analysis of the biodistributions of DEX and BAK after permeation in the human scalp is shown below.

Table 8 MALDI-MSI versus confocal Raman spectroscopy for skin imaging analysis.

	MALDI-TOF MSI	Confocal Raman
Spatial resolution	Aproximately 5 μ m	350 nm spatial resolution
Sampling time	Faster	Slower
Setting-up complexity	Harder	Easier

Chapter 9 - *Ex vivo* MALDI-TOF Mass Spectrometry Imaging and Confocal Raman spectroscopy quantitative skin biodistribution of dexamethasone loaded nanoparticles.

Analysis type	Destructive	Non-destructive
Interferences	Matrix effect	Skin autofluorescence
DEX sensitivity	Lower	Higher
BAK sensitivity	Higher	Lower

One of the major differences between the characteristics of the two techniques is the spatial resolution. Raman spectroscopy has a high spatial resolution, which can even highlight subcellular features [**Kong et al 2015**].

With the equipment used in this work, spatial resolutions of 350 nm and 50 μm were achieved with confocal Raman spectroscopy and MALDI-MSI, respectively. It was possible to reduce the diameter of the MALDI-MSI laser to 30 μm , but the intensities obtained were too low. Therefore, the intermediate laser diameter of 50 μm was used. There is currently a new generation of MALDI-MSI equipment that can achieve better spatial resolutions (of up to 5 μm) [**Bin Li et al 2016**].

Due to low scattering efficiency, Raman spectroscopy is a time-consuming technique with a rather slow sampling rate [**Oleg Ryabchykov et al 2018**]. For this reason, the ROIs analysed in this work using MALDI-MSI covered practically 100% of the tissue (Figures 11 and 12), while the ROIs analysed with confocal Raman spectroscopy were considerably smaller (Figure 6). The setup of MALDI-MSI is more complex than that for confocal Raman spectroscopy. Although the sampling time once the technique was set up was shorter in MALDI-MSI, the time and complexity required to prepare the samples were greater due to the need to set up the different steps described in sections 3.9, 3.10 and 3.11.

Another difference was the type of signal interferences encountered in each technique. Skin autofluorescence is the main interference in Raman spectroscopy, while the sensitivity of detecting biomolecules in MALDI-MSI can vary depending on the different MALDI matrices used [**Perry WJ et al 2020**].

Unlike MALDI-MSI, Raman spectroscopy is a non-destructive technique, which has allowed the development of devices for *in vivo* skin analysis [**Caspers PJ et al 1998**].

In terms of sensitivity, the sensitivity for DEX was higher in Raman spectroscopy, while the sensitivity for BAK was higher in MALDI-MSI.

However, both techniques were complementary when analysing biological tissues. MALDI-MSI can provide a lot of information about the lipid content of a sample, while Raman spectroscopy provides information about the overall chemical composition of a tissue.

9.5. Conclusions

Two techniques (MALDI-MSI and confocal Raman spectroscopy) were used to obtain quantitative data on the cutaneous biodistributions of DEX and BAK after permeation of DEX-lipomers or a Free-DEX control solution [**Eloy Pena-Rodríguez et al 2021a**]. The data obtained are in agreement with the findings of previous studies demonstrating the penetration-promoting effect of lipomers on DEX by qualitative immunohistofluorescence techniques. A

Chapter 9 - *Ex vivo* MALDI-TOF Mass Spectrometry Imaging and Confocal Raman spectroscopy quantitative skin biodistribution of dexamethasone loaded nanoparticles.

detailed comparison of both techniques led to the conclusion that they are interesting and complementary. MALDI-MSI is very useful when analysing larger tissue regions, while confocal Raman spectroscopy has higher spatial resolutions. The possibility of obtaining qualitative maps of the biodistribution of compounds and combining it with quantitative data is very helpful in developing drug delivery systems that accumulate in specific anatomical regions. Further work needs to be done on the validation of the quantification method using both techniques to obtain robust data with different molecules.

9.6. Bibliography

Ali Jaafar, Malik H. Mahmood, Roman Holomb, László Himics, Tamás Váczi, Anton Y. Sdobnov, Valery V. Tuchin and Miklós Veres. *Ex-vivo* confocal Raman microspectroscopy of porcine skin with 633/785-NM laser excitation and optical clearing with glycerol/water/DMSO solution, *Journal of Innovative Optical Health Sciences* Vol. 14, No. 05, 2142003, 2021, DOI: 10.1142/S1793545821420037.

Benito-González, I, Martínez-Sanz, M, López-Rubio, A, Gómez-Mascaraque, LG. Confocal Raman imaging as a useful tool to understand the internal microstructure of multicomponent aerogels. *J Raman Spectrosc.* 2020; 51: 2022– 2035. <https://doi.org/10.1002/jrs.5936>

Caspers, P.J., Lucassen, G.W., Wolthuis, R., Bruining, H.A. and Puppels, G.J. (1998), *In vitro* and *in vivo* Raman spectroscopy of human skin. *Biospectroscopy*, 4: S31-S39. DOI: 10.1002/(SICI)1520-6343(1998)4:5+<S31::AID-BSPY4>3.0.CO;2-M.

Fitzgerald M. C., Parr G. R., Smith L. M. (1993). Basic matrixes for the matrix-assisted laser desorption/ionization mass spectrometry of proteins and oligonucleotides. *Anal. Chem.* 65, 3204–3211. DOI: 10.1021/ac00070a007.

Guy, R. H., & Hadgraft, J. (2003). *Transdermal Drug Delivery* (2nd ed). CRC Press, ISBN 9780824708610.

Handler AM, Pommergaard Pedersen G, Troensegaard Nielsen K, Janfelt C, Just Pedersen A, Clench MR. Quantitative MALDI mass spectrometry imaging for exploring cutaneous drug delivery of tofacitinib in human skin. *Eur J Pharm Biopharm.* 2021 Feb;159:1-10. DOI: 10.1016/j.ejpb.2020.12.008. Epub 2020 Dec 25. PMID: 33352255.

Hong H, Wang Y. Derivatization with Girard reagent T combined with LC-MS/MS for the sensitive detection of 5-formyl-2'-deoxyuridine in cellular DNA. *Anal Chem.* 2007;79(1):322-326. DOI:10.1021/ac061465w.

Hua Zhang, Xudong Shi, Nhu Q. Vu, Gongyu Li, Zihui Li, Yatao Shi, Miyang Li, Bin Wang, Nathan V. Welham, Manish S. Patankar, Paul Weisman, and Lingjun Li. On-Tissue Derivatization with Girard's Reagent P Enhances N-Glycan Signals for Formalin-Fixed Paraffin-Embedded Tissue Sections in MALDI Mass Spectrometry Imaging, *Anal. Chem.* 2020, 92, 19, 13361–13368, 2020, DOI: 10.1021/acs.analchem.0c02704.

Kong, K., Kendall, C., Stone, N., and Notingher, I. (2015). Raman spectroscopy for medical diagnostics — From in-vitro biofluid assays to in-vivo cancer detection. *Adv. Drug Deliv. Rev.* 89, 121–134. DOI: 10.1016/j.addr.2015.03.009.

Chapter 9 - *Ex vivo* MALDI-TOF Mass Spectrometry Imaging and Confocal Raman spectroscopy quantitative skin biodistribution of dexamethasone loaded nanoparticles.

Li, B., Bhandari, D., Römpf, A. et al. High-resolution MALDI mass spectrometry imaging of gallotannins and monoterpene glucosides in the root of *Paeonia lactiflora*. *Sci Rep* 6, 36074 (2016). <https://doi.org/10.1038/srep36074>

Lutz Franzen, Dominik Selzer, Joachim W. Fluhr, Ulrich F. Schaefer, Maike Windbergs, Towards drug quantification in human skin with confocal Raman microscopy, *European Journal of Pharmaceutics and Biopharmaceutics*, Volume 84, Issue 2, 2013, Pages 437-444, ISSN 0939-6411, <https://doi.org/10.1016/j.ejpb.2012.11.017>.

P.J. Caspers, G.W. Lucassen, G.J. Puppels, Combined *In Vivo* Confocal Raman Spectroscopy and Confocal Microscopy of Human Skin, *Biophysical Journal*, Volume 85, Issue 1, 2003, Pages 572-580, ISSN 0006-3495, DOI: 10.1016/S0006-3495(03)74501-9.

Pena-Rodríguez, E.; Lajarin-Reinares, M.; Mata-Ventosa, A.; Pérez-Torras, S.; Fernández-Campos, F. Dexamethasone-Loaded Lipomers: Development, Characterization, and Skin Biodistribution Studies. *Pharmaceutics* 2021, 13, 533. DOI: 10.3390/pharmaceutics13040533.

Perry WJ, Patterson NH, Prentice BM, Neumann EK, Caprioli RM, Spraggins JM. Uncovering matrix effects on lipid analyses in MALDI imaging mass spectrometry experiments. *J Mass Spectrom*. 2020 Apr;55(4):e4491. DOI: 10.1002/jms.4491. Epub 2020 Feb 11. PMID: 31860760; PMCID: PMC7383219.

Peter J. Caspers, Hajo A. Bruining, Gerwin J. Puppels, Gerald W. Lucassen, Elizabeth A. Carter, *In Vivo* Confocal Raman Microspectroscopy of the Skin: Noninvasive Determination of Molecular Concentration Profiles, *Journal of Investigative Dermatology*, Volume 116, Issue 3, 2001, Pages 434-442, ISSN 0022-202X, DOI: 10.1046/j.1523-1747.2001.01258.x.

Raj S, Jose S, Sumod US, Sabitha M. Nanotechnology in cosmetics: Opportunities and challenges. *J Pharm Bioallied Sci*. 2012;4(3):186-193. DOI:10.4103/0975-7406.99016

Ryabchykov Oleg, Popp Juergen, Bocklitz Thomas, Fusion of MALDI Spectrometric Imaging and Raman Spectroscopic Data for the Analysis of Biological Samples, *Frontiers in Chemistry*, 6, 2018, DOI: 10.3389/fchem.2018.00257.

Chapter 10 - Overall discussion of the results obtained

There is a wide variety of nanoparticles, and the scaling process for each of them is different and involves several difficulties. In addition, very little is known about the cutaneous biodistribution of these nanoparticles. A comparative study of the physicochemical properties, stability, scalability and cutaneous biodistribution of the different nanoparticles is an exercise that can be of great use to the scientific community when choosing the appropriate nanosystem for each treatment. Moreover, the development of *in vitro* models to test the cytotoxicity and efficacy of encapsulated and non-encapsulated active ingredients could help to determine the higher non-cytotoxic doses.

10.1. Physico-chemical comparison of nanoparticles

Different drug encapsulation nanosystems were developed with the aim of increasing the delivery of active ingredients to epidermis and hair follicles. Four types of nanosystems were developed: Transfersomes, Nanotransfersomes, Nanostructured lipid carriers (NLCs) and polymer-lipid hybrid nanoparticles (lipomers).

Nanoparticles's size, surface charge and Pdl affect their bioavailability and biodistribution. Therefore, it is important to study them to optimise formulations.

In the case of NLCs, a DoE screening was performed to find out which parameters influence their size, Pdl and surface charge. The parameters included in the screening DoE were % Cationic surfactant, % Tween 80, % API and Sonication energy (Ws). It is described in the literature that the surfactants can influence different nanoparticle characteristics [Kullavadee Karn-Orachai et al 2014]. The % Tween 80 was found to have an impact on the size and Pdl of the NLCs. As the concentration of this surfactant increased (from 1 to 5% w/w) the average size decreased from 185 to and 155 nm, and the Pdl decreased from 0.200 to 0.175. In the case of lipomers, the influence of the concentration of Tween 80 and Span 60 on their size, Pdl, and surface charge was also studied. In this case, the surfactant concentration did not prove to be significant neither for the size nor for the Pdl. However, by increasing the % Tween 80 (from 1.5 to 2.5 % w/w) the Z-potential decreased from +28 mV to about +22 mV. Likewise, increasing the concentration of Span 60 from 0.16% to 0.32% showed a slight surface charge reduction from +26 mV to +24 mV. One explanation for this influence is that the hydroxyl groups of the surfactants shield the surface charge of the nanoparticles by coating them on the surface. Tween 80 levels were different in lipomers and NLCs. Perhaps, if the levels used in the case of lipomers were the same as in the case of NLCs (1 and 5% w/w), effects on size and Pdl could be also observed.

Furthermore, NLCs surface response was subsequently performed by adding central and axial values to the significant factors of the design of experiments: % Tween 80 and Sonication Energy (Ws). Thanks to the surface response studies, it was possible to obtain accurate predictive models for the nanoparticle's size and Pdl. Once the predictive models were obtained, an optimization was made to obtain the minimum values of Pdl and Z-average within the design space. The predictive model was restricted at 3% Tween 80 concentration because viscosity was too high to be sprayed at higher concentrations. The results were corroborated by producing a batch with 3% Tween 80 subjected to the value of sonication energy that allowed to obtain smaller nanoparticles (3729 Ws). The BIAS calculated between the predicted and empirical values was 22.87 and 8.94% for Z-average and Pdl respectively, which corroborates the good predictive ability of the model.

FD-DEX lipomers were found to be bigger than non-FD-particles. One hypothesis for the size increase is the crystallization of the lipid droplets within the nanoparticle structure during the lyophilization process. FD lipomers showed lower DEX release and permeation profiles on synthetic membrane and dermatomed pig skin, than non-FD-lipomers. The biopharmaceutical properties achieved with non-freeze-dried particles were of major interest (higher permeation, smaller size and Pdl) but the stability in suspension is a risk due to the drug release during storage. A more exhaustive study could also be carried out by determining different concentrations of cryopreservatives and establishing freeze-drying processes using DoE that minimize the physicochemical differences of the nanoformulation. There are other techniques, such as spray drying, which are promising to stabilise nanoparticles. Although the water residues by spray drying are higher and this fact can compromise the stability, it is possible that the initial properties of the nanoparticle are less modified by avoiding the freezing process the use of cryopreservatives [Beck RC et al 2012]. Adequate balance between stability, efficacy, patient texture preference, and biopharmaceutical properties must be established when developing drug delivery systems.

The different properties of each developed nanosystem are compared (Table 15).

Table 15 Transfersomes, Nanotransfersomes, Nanostructured lipid carriers (NLCs) and lipomers biopharmaceutical comparison.

Formulation	Average size	Average Pdl	Z-Potential	Active ingredient	EE%	Preferential Targeting
Transfersomes	≈ 300 nm	≈ 0.45	≈ -10 mV	Retinyl Palmitate	100%	Epidermal
Nanotransfersomes	≈ 90 nm	≈ 0.20	≈ - 48 mV	Latanoprost	100%	Transepidermal
NLCs	≈ 250nm	≈ 0.25	≈ + 40 mV	██████████	≈ 98%	Follicular
Non-FD-lipomers	≈ 115 nm	≈ 0.24	≈ + 30 mV	Dexamethasone	≈ 98%	Follicular

The smallest size and Pdl obtained was achieved with Nanotransfersomes, which was below 100 nm and Pdl=0.20. Transfersomes of 300 nm were also developed, focused on a cosmetic application, loaded with RP in the lipid bilayer. A possible cause of the increase in size and Pdl of transfersomes compared to Nanotransfersomes could be the high percentage of lipids, in transfersomes (1.78% vs 0.93% w/w of nanotransfersomes) the surfactants (the use of unsaturated phospholipid in nanotransfersomes), the stabilizers (cholesterol was used in nanotransfersomes and ceramide in transfersomes), and the active ingredient that make up the transfersomes (1.1% of RP in transfersomes vs 0.005% of LAT in nanotransfersomes) [Samuel Maritim et al 2021]. Thanks to the deformability of these systems, despite the increase in size, transfersomes were shown to still be able to mediate the penetration of retinyl palmitate into the epidermis.

The Z-potential of transfersomes and nanotransfersomes was negative while, due to the presence of BAK, both lipomers and NLCs showed a positive Z-potential.

All the developed nanosystems showed good stability under accelerated conditions (40°C/75%RH) for 6 months and long term (25°C/75%RH) for 12 months. Retinyl Palmitate, Latanoprost, ██████████ and Dexamethasone were encapsulated in the different nanoparticles achieving %EE >97% in all cases, thus avoiding further purification processes and simplifying the

scalability of these nanoformulations. All the encapsulated active ingredients were hydrophobic small molecules, which possibly allowed such high EE% to be obtained. It would be of interest to compare the EE% of hydrophilic drugs and biomolecules in each of the nanosystems.

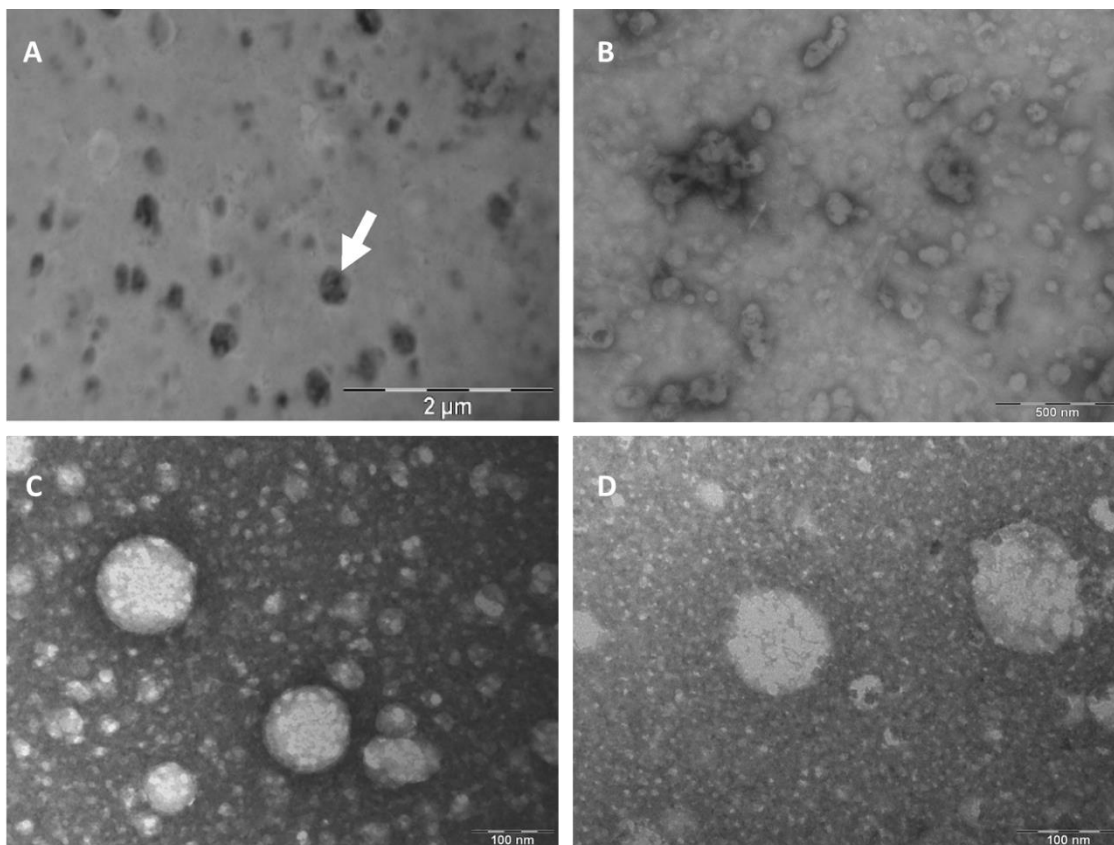


Figure 39 TEM images of A) transfersomes B) nanotransfersomes C) lipomers and D) NLCs.

TEM images (Figure 39) show the morphology of each nanosystem. Due to evaporation of the aqueous core during sample preparation, the structure of transfersomes (Figure 39 A) and nanotransfersomes (Figure 39 B) is slightly deformed. No particle aggregation was observed neither in TEM nor in DLS analysis. Thanks to the high resolution obtained by TEM, it is possible to observe the internal core structure of NLCs and lipomers.

The size of the transfersomes before and after passing through an extrusion membrane with a pore diameter of 100 nm (three times smaller than the diameter of the transfersomes) was analysed. It was found that transfersomes were able to recover the initial size, which demonstrates the flexibility of this type of vesicles [Teixeira et al 2010]. Release studies of retinyl palmitate encapsulated in transfersomes were performed. Due to its structure, retinyl palmitate is intercalated in the membrane of the transfersomes. No retinyl palmitate peaks were observed in the receptor medium during the first 6 hours of the experiment. At longer times, retinyl palmitate peaks were observed in the receptor medium, which could be due to diffusion of the drug from the liposomal film to the receptor medium, which is the classical theory of release. The drug release of DEX-lipomers, significantly modified the release mechanism and reduced the release rate as compared with the non-encapsulated drug, showing that the lipomers could act as slow-release drug delivery systems. Furthermore, as previously described, the freeze-

drying process significantly altered the release mechanism, compared with non-FD lipomers, with a significant reduction of the release rate.

One of the least studied aspects in the literature is to know the stability of nanoparticles when they are included in creams or classic formulations. Different phenomena like detergent binding, lamellar-micellar phase transition or vesicle disruption can occur when nanoparticles are incorporated into classic formulations [C. Nastruzzi et al 1993]. In this work it was found that the transfersome absorption-promoting effect was maintained after being formulated in a cream, compared to a cream without transfersomes. This fact infers that the transfersomes maintain its structure once included in the emulsion. FD-DEX-lipomers were incorporated in hydrogel formulations. The rheological, release and skin permeations profiles were studied, and it was found that FD formulations significantly modified particle size, drug release, and drug permeation profiles, compared with non-FD-Lipomers.

10.2. Scalability of nanoparticles

The most difficult nanosystems to scale were the lipomers. To produce them, it is necessary to solubilise ethyl cellulose in an organic solvent. Subsequently, the organic solvent must be extracted by rotary evaporation, which makes the process more difficult to scale up [Rishi Paliwal et al 2014]. Lipomers can suffer different instability processes, such as drug leakage in aqueous medium, aggregation, hydrolysis etc.

Scale-up of NLCs was performed through DoE with an UIP1000HdT industrial ultrasonic processor. Amplitude, sonication cycles, batch volume and temperature were included in the DoE. Amplitude and sonication cycles were found to have a significant influence on Z-average and Pdl of NLCs. A higher amplitude in the sonotrode oscillation caused a higher cavitation energy and, consequently, smaller particle sizes were obtained. Also, the more times the formulation passes through the flow cell of the sonicator, the more the particle size is reduced and the more monodisperse the particle population is. From the sonication energy data and the characterisation performed with the extracted aliquots during the scale-up studies, it was possible to perform non-linear regression and obtain a mathematical model (Figures 24 and 25) to determine the sonication energy (normalised per batch volume (L)) needed to obtain NLCs smaller than 260 nm and monodisperse (Pdl<0.3).

The fact that batch size was not a significant factor neither on the size nor the Pdl of the NLCs during the scale-up, means that the scalability of the NLCs is feasible since increasing the batch volume did not affect to the NLCs properties. Furthermore, due to their high lipid content (up to 18% w/w), NLCs can encapsulate larger amounts of hydrophobic compounds, compared to lipomers and nanotransfersomes and they do not need any rotary evaporation step since no organic solvents are added to the formulation.

DoE scale-up was also performed for nanotransfersomes, including the same factors (amplitude, sonication cycles, temperature, and batch volume) and characterizing the same responses (size and Pdl) as in the case of NLCs. In this case, batch volume was found to be significant on size and Pdl for nanotransfersomes, although with a very low coefficient. The factors with the highest significance on both responses were amplitude and sonication cycles.

Although different regression equations were obtained after the scaling of NLCs and nanotransfersomes, in both cases it was observed that most of the variability in size and Pdl can be explained by the cavitation energy. In both cases, exponential equations were obtained for size and Pdl as a function of cavitation energy normalized by batch volume. In this way it was

possible for both NLCs and nanotransfersomes to obtain predictive mathematical models, which allow obtaining nanoparticles with the desired sizes and PDI within the design space.

10.3. *In vitro* cell culture studies

In addition to the development of nanoencapsulation platforms, it is useful to have *in vitro* efficacy and toxicity testing platforms. By means of the screenings, it could be possible to determine the most suitable active ingredients, the highest non-toxic concentrations, and even allows to find synergies and additive effects. In parallel to the development of nanoparticles, an attempt was made to set up *in vitro* cytotoxicity, anti-inflammatory, and proliferation efficacy screening platforms for different free and nanoencapsulated active ingredients in skin-derived cells (keratinocytes, HEK001 and HaCaT and dermal papilla cells, DPCs).

Seeding concentration, medium supplementation, method (starvation process) and extracellular matrix concentration were established to test the proliferation of different treatments in keratinocytes and DPCs.

This kind of studies were used with DEX lipomers. A viability reduction was observed in keratinocytes exposed to high concentrations of DEX-loaded and placebo lipomers (see Figure 7 A, chapter 4), compared to untreated cells. To investigate the cause for this toxicity, different lipomer components analysed at the same concentration present in lipomers, showing that the cause for the viability reduction was the presence of benzalkonium chloride, probably caused by its cationic charge. Despite being cytotoxic, concentrations do not represent safety concerns for clinical use. As described in the FDA inactive ingredients data base, **[Available online: <http://www.accessdata.fda.gov/scripts/cder/iig/index.cfm> (accessed on 18 March 2021)]**, several commercial formulations are available with the same concentrations of preservative. Moreover, the use of these cell models enables to demonstrate the anti-inflammatory efficacy of DEX-lipomers, with TNF α as a tracker.

In addition, analyses of the cytotoxicity and anti-inflammatory TNF α efficacy of FD and non-FD DEX-lipomers were studied in keratinocytes. The FD process seemed to confer a little protection to cytotoxicity in HEK001 cells. The cytotoxicity of the tested non-FD lipomers was attributed to the benzalkonium chloride. The surface charge of the lipomers after FD process was a little lower (but not significant) compared with the non-FD particles. This could be caused by the interaction between the cryoprotectant and the cationic surfactant. This could reduce the toxicity of FD-lipomers. No cytotoxic effects were detected in HaCaT cells after any of the treatments. The differences in the cytotoxic profile of both cell lines could be caused by the immortalization procedure, which can modify the cell sensibility to xenobiotics. No differences in efficacy after the lyophilization process were observed (See chapter 5 Figure 9).

10.4. Biodistribution comparison of nanoparticles

There are several techniques to study skin absorption (IVPTs, skin layer separation, confocal fluorescence, immunohistofluorescence etc). IVPTs consist of permeating a formulation on dermatomized skin (animal or human) and quantifying the amount of active ingredient passing through the skin. By studying formulations with free and nanoencapsulated active ingredient it is possible to analyse the absorption promoting capacity of each nanosystem. NLCs showed a significant absorption-promoting effect versus a non-encapsulated XXXXXXXXXX control by IVPTs in dermatomed pig skin. In the case of transfersomes, by quantifying the amount of RP in the different layers of the skin, the absorption-promoting effect of the transfersomes suspension and cream formulations were corroborated.

An approach to qualitatively study the cutaneous biodistribution and promoter effect of nanosystems is fluorescence confocal microscopy [Ana-Maria Pena et al 2020]. The nanosystems labelled with red-emitting fluorophores (LRB for nanotransfersomes, NLCs and lipomers and Nile red in the case of transfersomes), and green-emitting fluorophores (C6 in the case of NLCs and lipomers, and NaFl in nanotransfersomes) were nanoencapsulated. Once the fluorescent nanosystems were obtained, they were permeated on full-thickness human and pig skin, to subsequently obtain cryosections and analyse the skin biodistribution of both fluorophores by confocal fluorescence. Immunohistofluorescence studies were performed after application of DEX-NLCs and DEX-lipomers to study the biodistribution of DEX.

Transfersomes, lipomers and NLCs showed an absorption-promoting effect versus non-vectorized controls by means of IVPTs. However, different pig skin and human scalp biodistributions were observed for each nanosystem (Figure 40).

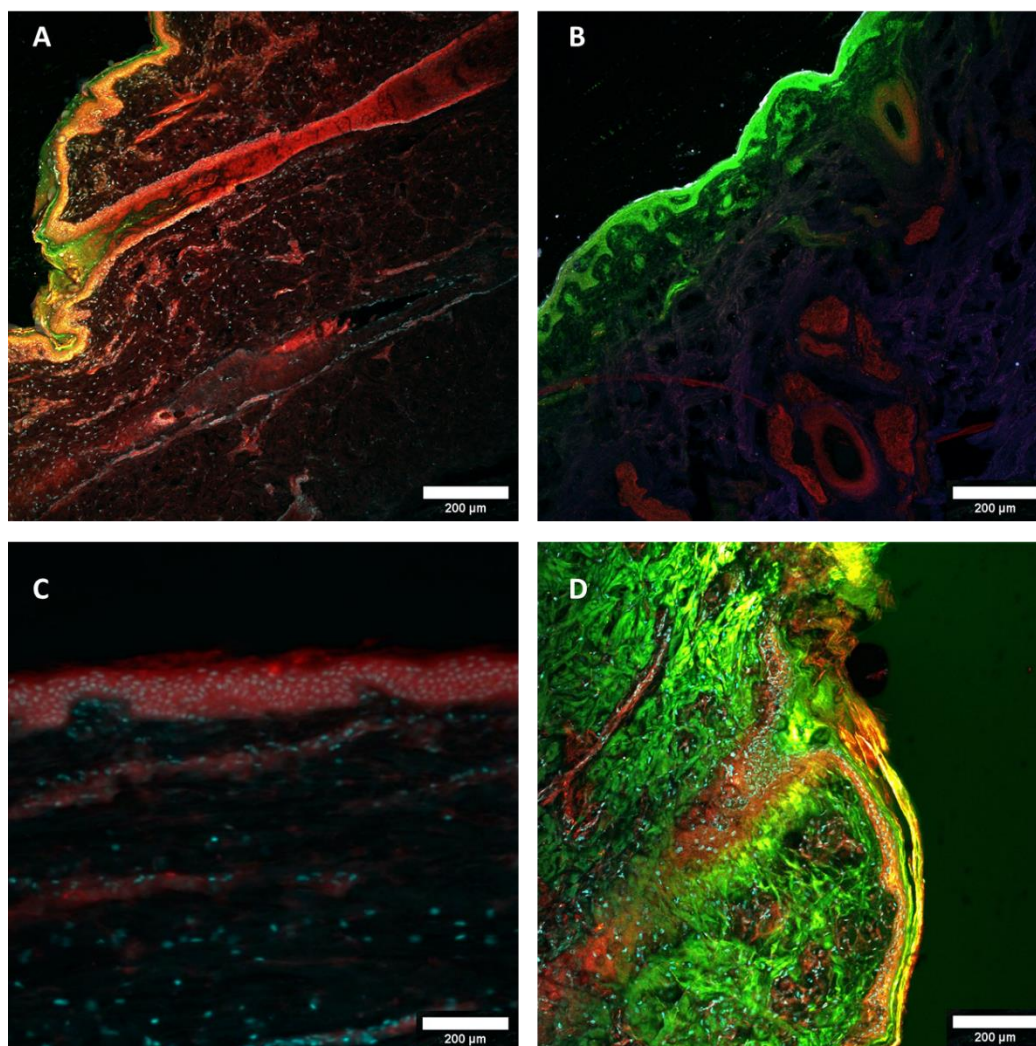


Figure 40 Skin cryosections fluorescence biodistribution of: A) Pig skin cryo-section after permeation of LRB-labelled C6-loaded lipomers. B) Human scalp cryo-section after permeation of LRB-labelled C6-loaded NLCs, C) Pig skin cryo-section after permeation of Nile-red labelled Transfersomes, and D) Pig skin cryo-section after permeation of LRB-labelled NaFl loaded Nanotransfersomes.

Following confocal fluorescence studies, a similar pattern was observed for lipomers (Figure 40 A) and NLCs (Figure 40 B). Both types of nanoparticles were labelled with LRB and encapsulated

C6 at the same concentrations. An accumulation of nanoparticles was observed in deep areas of hair follicles, sebaceous glands (Figure 40 B, only present in Human skin) and epidermis, while the encapsulated hydrophobic active (C6) was restricted to more superficial areas of the follicles and epidermis. One possible hypothesis is that upon contact with lipids in the more superficial areas of the skin, the encapsulated and nanoparticle's surface-adsorbed compound is released while the nanoparticles continue to penetrate deeper areas. Due to their geometry and higher rigidity compared to liposomes, it is believed that this type of nanoparticles accumulates in the different cutaneous appendages and hair follicles.

As for nanotransfersomes (Figure 40 D), it is difficult to compare the results because in this case the encapsulated active ingredient (NaFl) was hydrophilic, and consequently the penetration mechanisms were different. An accumulation of LRB was observed in the superficial areas of the skin, corresponding to the nanotransfersomes and a very important absorption-promoting effect was observed for the encapsulated NaFl, with accumulation being observed in deep areas of the dermis. The hypothesis in this case is that the nanotransfersomes fuse with the lipids of the stratum corneum and release the hydrophilic active ingredient encapsulated in the aqueous core, making it permeate into the dermis.

In the case of the transfersomes (Figure 40 C), no hydrophilic active ingredient was encapsulated, so it is not possible to compare this effect. However, transfersomes were labelled with Nile red and an accumulation in the epidermis was observed.

NLCs and nanotransfersomes were permeated both on pig skin and human scalp. Confocal fluorescence microscopy showed similar biodistributions in both species. Pig skin has a thicker stratum corneum and does not contain sebaceous glands. Accumulation of LRB labelled NLCs and nanotransfersomes in sebaceous glands were observed when permeated on human scalp, probably due to the lipid nature of the nanoparticles and the hydrophobicity of the sebocyte environment.

10.5. *Ex vivo* skin quantitative techniques setting up and comparison

Finally, during this work, two quantitative techniques were developed to analyse the *ex vivo* biodistribution of lipomers encapsulating DEX. Two of the more promising techniques in terms of skin imaging and quantifying are Confocal Raman [Ana-Maria Pena et al 2020] and MALDI-TOF-MSI [Anne Mette Handler et al 2020]. In this work, both techniques were set up and compared. BAK was the tracer of the lipomers and DEX was the encapsulated active ingredient.

Due to the slower sampling rate, smaller regions of the tissues were analysed in Raman than in MALDI-MSI. The higher spatial resolution of Confocal Raman (350 nm) with respect to MALDI-MSI (50 μm with the configuration used in these studies) allowed to observe the biodistribution of DEX with a higher degree of detail. It was not possible to trace BAK by Confocal Raman due to the low signal obtained. The signal of DEX in MALDI-MSI was also too low, but thanks to a derivatization process with GirT, it was possible to increase the signal significantly and obtain the quantitative biodistribution of both DEX-GirT and BAK by this technique. Derivatization with GirT, was performed on the ITO slide (inside and outside the tissue) by spraying GirT, which allowed to study the matrix effect, and on cryosections of permeated samples with DEX-lipomers and Free-DEX. In all cases the derivatization was successful showing an intense peak at $m/z=506.3$ Da.

Calibrators were deposited on skin cryosections, and exponential regressions were obtained with a good fit in both Confocal Raman and MALDI-MSI. By interpolating the intensities obtained

in the analysed regions, it was possible to compare the amount of DEX penetrated in tissue by both techniques. The results were normalized by the amount of tissue (in μg) corresponding to each of the analysed regions so that the results obtained by both techniques could be compared.

The amount of DEX quantified by MALDI-MSI was found to be lower than the amount obtained by Confocal Raman. One hypothesis as to why lower amounts of DEX were obtained in MALDI-MSI compared to Confocal Raman is that the MALDI laser may not extract all the DEX present in the tissue.

Although the differences were not significant, a clear trend was observed in confocal Raman showing more DEX penetrated when loaded in lipomers. In MALDI-MSI, the amounts of DEX penetrated into tissue were similar when comparing DEX-lipomers and Free-DEX. In immunohistofluorescence experiments, an adsorption-promoting effect was observed for DEX-lipomers. Perhaps, by MALDI-MSI, as less DEX is detected in the tissue compared to Immunohistofluorescence or Confocal Raman, it is not possible to observe differences between free-DEX and DEX-lipomers skin penetration.

One of the most interesting features of these techniques is the ability to simultaneously analyse quantitative data together with qualitative images of biodistribution. Using both techniques, the adsorption-promoting effect of these nanoparticles versus the Free-DEX control can be observed. Free-DEX permeated samples showed DEX in the more superficial layers of skin while DEX-lipomers samples showed DEX accumulation around hair follicle and deeper skin layers. In this way, the DEX biodistribution results obtained by immunohistofluorescence in previous studies were corroborated, and it was also possible to obtain in an approximative way the amount of active ingredient (DEX) and nanoparticle (BAK) corresponding to the qualitative images.

In addition, by MALDI-MSI it was possible to quantify the amount of BAK penetrated into tissue, which provides an idea of the amount of lipomers that crossed the stratum corneum into deeper layers. By observing the biodistribution maps of the two BAK homologues (BAK C₁₂ and BAK C₁₄), penetration into deeper layers of the epidermis was observed.

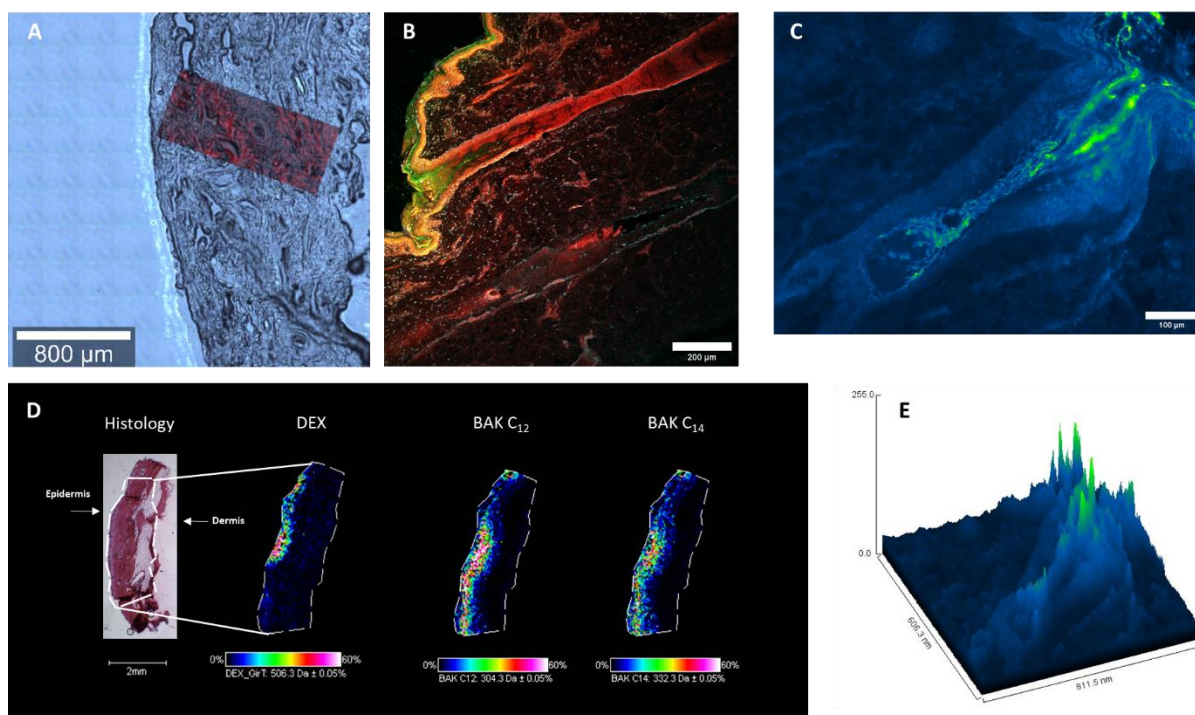


Figure 41 Biodistribution maps after *ex vivo* skin permeation of lipomers. A) Confocal Raman DEX biodistribution map after permeation of DEX-lipomers on human scalp,.B) Confocal fluorescence biodistribution map of C6-loaded LRB-labelled lipomers permeated on pig skin, C) Immunohistofluorescence biodistribution map after permeation of DEX-lipomers on pig skin, D) Histology of the MALDI-TOF-MSI human scalp cryosection and biodistribution maps of DEX, BAK C₁₂ and BAK C₁₄, E) Surface plot of the immunohistofluorescence biodistribution map after permeation of DEX-lipomers on pig skin.

As a summary, Figure 41 shows all the techniques used to study the cutaneous biodistribution of lipomers. The penetration capacity of these nanoparticles can be observed. Figure 41 A, in red, shows the Confocal Raman biodistribution of DEX in deep layers of the skin (up to approximately 1000 μm deep). In the case of Confocal Raman, DEX has been detected directly (without the need for derivatization or the use of antibodies) on the tissue, which has allowed a more selective analysis that is closer to what would happen in a real *in vivo* DEX application. Figure 41 B shows the follicular targeting ability of fluorescently LRB-labeled-lipomers encapsulating C6 by confocal fluorescence microscopy. The red color corresponds to the localization of lipomers in the deep zones of the follicle, the green color shows the accumulation of the C6-encapsulated fluorophore in more superficial zones of the follicle, and the yellow color shows the co-localization of C6 and LRB-labeled-lipomers in the epidermis. Figure 41 C and E show the biodistribution of DEX after cutaneous permeation of DEX-lipomers where the accumulation of the active ingredient in hair follicles can be observed. Finally, Figure 41 D shows the MALDI-TOF-MSI results. A histological image of a slice contiguous to the ones analysed by MALDI-MSI is shown, in addition to the biodistribution map of DEX-GirT, BAK C₁₂ and BAK C₁₄. DEX appears to be accumulated in stratum corneum and epidermis. BAK (corresponding to lipomers), show a deeper penetration, in a similar way of the LRB biodistribution found by the confocal fluorescence studies.

This exhaustive analysis allows to determine the most appropriate techniques for the development of cutaneous drug delivery systems, as well as to better understand the processes that nanoparticles and encapsulated molecules undergo once they penetrate the cutaneous tissue.

10.6. Bibliography

Ana-Maria Pena, Xueqin Chen, Isaac J. Pence, Thomas Bornschlögl, Sinyoung Jeong, Sébastien Grégoire, Gustavo S. Luengo, Philippe Hallegot, Peyman Obeidy, Amin Feizpour, Kin F. Chan, Conor L. Evans, Imaging and quantifying drug delivery in skin – Part 2: Fluorescence and vibrational spectroscopic imaging methods, *Advanced Drug Delivery Reviews*, Volume 153, 2020, Pages 147-168, DOI: 10.1016/j.addr.2020.03.003.

Beck RC, Ourique AF, Guterres SS, Pohlmann AR. Spray-dried polymeric nanoparticles for pharmaceuticals: a review of patents. *Recent Pat Drug Deliv Formul.* 2012 Dec;6(3):195-208. doi: 10.2174/187221112802652651. PMID: 22845040.

C. Nastruzzi, E. Espósito, E. Menegatti and PP.Walde, Use and stability of liposomes in dermatological preparations, *Journal of Applied Cosmetology*, Volume 11 (3), pages 77-91, 1993, <http://hdl.handle.net/20.500.11850/121086>.

FDA Inactive Ingredient Database. Available online: <http://www.accessdata.fda.gov/scripts/cder/iig/index.cfm> (accessed on 18 March 2021).

Handler AM, Pommergaard Pedersen G, Troensegaard Nielsen K, Janfelt C, Just Pedersen A, Clench MR. Quantitative MALDI mass spectrometry imaging for exploring cutaneous drug delivery of tofacitinib in human skin. *Eur J Pharm Biopharm.* 2021 Feb;159:1-10. doi: 10.1016/j.ejpb.2020.12.008. Epub 2020 Dec 25. PMID: 3335225

Karn-Orachai K, Smith SM, Phunpee S, Treethong A, Puttipatkhachorn S, Pratontep S, Ruktanonchai UR. The effect of surfactant composition on the chemical and structural properties of nanostructured lipid carriers. *Journal of Microencapsulation.* 2014, 31(6), 609-18, DOI: 10.3109/02652048.2014.911374.

Paliwal R, Babu RJ, Palakurthi S. Nanomedicine scale-up technologies: feasibilities and challenges. *AAPS PharmSciTech.* 2014;15(6):1527-1534. DOI:10.1208/s12249-014-0177-9.

Samuel Maritim, Pierre Boulas, Yiqing Lin, Comprehensive analysis of liposome formulation parameters and their influence on encapsulation, stability and drug release in glibenclamide liposomes, *International Journal of Pharmaceutics*, Volume 592, 2021, 120051, ISSN 0378-5173, DOI: 10.1016/j.ijpharm.2020.120051.

Teixeira, Z.; Zanchetta, B.; Melo, B.A.; Oliveira, L.L.; Santana, M.H.; Paredes-Gamero, E.J.; Justo, G.Z.; Nader, H.B.; Guterres, S.S.; Durán, N. Retinyl palmitate flexible polymeric nanocapsules: Characterization and permeation studies. *Colloids Surf. B Biointerfaces* 2010, 81, 374–380.

Chapter 11 - Conclusions

Different skin drug delivery platforms (transfersomes, lipomers, NLCs and nanotransfersomes) for epidermal and follicular targeting were successfully developed and characterised, probing to be stable and reproducible.

- Transfersomes demonstrated a significant increase in the administration of RP to the epidermis through RP quantification in the different layers of the skin. RP loaded transfersomes were incorporated in cream as final product and the absorption-promoting effect was still observed.
- NLCs and nanotransfersomes scale up was performed through DoE. Predictive mathematical models were obtained allowing to adjust the needed cavitation energy per L of batch to obtain the desired size and Pdl of the nanoparticles.
- The lyophilization process significantly modified DEX-lipomers internal structure and size and significantly modified the drug release characteristics and skin permeation profiles compared with non-freeze-dried lipomers.
- Cytotoxicity, proliferation, and anti-inflammatory efficacy of different free and nanoencapsulated active ingredients were determined using the *in vitro* established screening platforms.
- NLCs and lipomers accumulation in hair follicles and cutaneous appendages was observed through *ex vivo* confocal fluorescence and DEX immunohistofluorescence studies, thus proving their ability to achieve follicular targeting. Transfersomes showed an accumulation in epidermis through *ex vivo* fluorescence assays. Penetration up to deeper layers of the dermis with nanotransfersomes-loaded-NaFl was also probed by *ex vivo* confocal fluorescence.
- MALDI-TOF-MSI and Confocal Raman *ex vivo* techniques were set up for DEX-lipomers and Free-DEX human scalp biodistribution studies. Quantitative biodistribution of DEX was obtained through both techniques with higher DEX detected amounts by Confocal Raman. Whereas, by MALDI-TOF-MSI, it was also possible to obtain quantitative biodistribution of BAK (lipomer tracer).

Chapter 12 – RESUMEN GLOBAL

Se desarrollaron diferentes nanoplataformas de administración tópica de fármacos para conseguir direccionamiento epidérmico y/o folicular. Concretamente se desarrollaron nanostructured lipid carriers (NLCs), transfersomas, nanotransfersomas y lipomeros. Dichas nanoformulaciones fueron optimizadas y caracterizadas fisicoquímicamente con técnicas complementarias. Además, se han realizado estudios para caracterizar la biodistribución en piel de cerdo y humana de manera cualitativa y cuantitativa mediante diferentes técnicas.

Se desarrollaron con éxito transfersomas encapsulando el ingrediente activo retinil palmitato (RP). Se obtuvieron dos tipos de formulaciones con transfersomas: suspensión y crema. Mediante cuantificación del RP en las diferentes capas de la piel (estrato corneo, epidermis y dermis) se evaluó el efecto promotor de la absorción de los dos tipos de formulaciones frente a controles sin transfersomas. Mediante la técnica de separación de capas de la piel y posterior cuantificación por HPLC, se observó un aumento significativo de la acumulación en epidermis de cerdo del RP vehiculizado en transfersomas, tanto en suspensión como en crema.

Además, los transfersomas también se marcaron fluorescentemente (con Nile Red). Estos transfersomas fluorescentes se permearon en piel de cerdo junto con una formulación de Nile Red libre. Se observó un aumento de la permeación gracias a la encapsulación en transfersomas, concretamente se observó una acumulación en epidermis. Estos resultados sugieren que los transfersomas pueden ser un vehículo eficaz para la administración de retinoides a las capas internas de la piel, como la epidermis.

Se realizaron pruebas de inducción de proliferación *in vitro* en queratinocitos epidérmicos humanos (HEK001) y en células de papila dérmica de folículos pilosos humanos (DPCs) inmortalizados para examinar la eficacia de distintos principios activos. En este caso, es necesario aumentar el número de experimentos antes de sacar conclusiones a nivel de inducción de proliferación. En cuanto a los ensayos realizados en DPCs, no se observó ningún efecto inhibitorio sobre la proliferación cuando se incubaron con Testosterona, tal y como se describe en la literatura. Sería interesante realizar los experimentos en DPCs primarias sensibles a los andrógenos para poner a punto una plataforma *in vitro* que permita comparar la eficacia de diferentes inhibidores de la 5 alfa reductasa.

Se desarrollaron y optimizaron nanopartículas híbridas polímero-lipídicas (lipomers) de etilcelulosa. Una vez desarrollados se encapsuló dexametasona (DEX) en su interior (DEX-lipomers) y se evaluaron biofarmacéuticamente tras permeación en piel de cerdo versus un control de DEX libre (Free-DEX). Los lipomers también se marcaron fluorescentemente para posteriores estudios de biodistribución. Se escogieron dos fluoróforos, LRB para trazar las nanopartículas y C6 como modelo de fármaco encapsulado. La biodistribución de ambos fluoróforos fue diferente, sugiriendo una liberación del activo encapsulado en epidermis y partes superficiales (hasta unos 400 μm aproximadamente) de folículos pilosos, mientras que las nanopartículas mostraron ser capaces de penetrar hacia el bulbo de folículos pilosos más profundos. La inmunofluorescencia de los DEX-lipomers también mostró direccionamiento folicular. Se investigó la citotoxicidad *in vitro* de la nanoformulación y se demostró la eficacia antiinflamatoria de los DEX-lipomers *in vitro* en cultivos celulares de queratinocitos humanos.

Con la finalidad de mejorar la estabilidad de suspensiones de DEX-lipomers, en las que existe un riesgo de liberación del activo durante almacenamiento, se realizó una puesta a punto de un

proceso de liofilización. Una vez liofilizados, los DEX-lipomers se incorporaron en un hidrogel y se estudiaron sus perfiles reológicos, de liberación y de permeabilidad cutánea. El proceso de liofilización modificó el tamaño de las partículas, y también se alteraron las propiedades de liberación y permeabilidad del fármaco. Las formulaciones liofilizadas mostraron una liberación y permeación cutánea más lenta que las suspensiones sin liofilizar. Se realizaron los análisis en queratinocitos humanos de la citotoxicidad y la eficacia antiinflamatoria de las partículas antes y después de liofilizar y no mostraron diferencias.

Se desarrollaron y optimizaron con éxito nanostructured lipid carriers (NLCs). En primer lugar, se realizó un diseño de experimento de cribaje para determinar los parámetros con una influencia significativa en el tamaño y polidispersión de las NLCs. La concentración de Tween 80 y la energía de sonicación demostraron ser los parámetros con una mayor influencia sobre el tamaño y Pdl de las nanopartículas. Se realizó un diseño experimental de superficie de respuesta para estudiar los parámetros significativos y fue posible obtener modelos para predecir su tamaño y su índice de polidispersión (Pdl). A partir del modelo obtenido tras la optimización se fabricó un lote con los parámetros obtenidos con el modelo predictivo y determinó su tamaño y Pdl. Los resultados fueron satisfactorios mostrando la precisión del modelo predictivo. Se llevó a cabo un escalado de las partículas mediante DoE. El tamaño de lote mostró no tener influencia en las propiedades de las nanopartículas, lo que significa que dentro del espacio de diseño (de 1 a 8L de lote) el escalado fue satisfactorio. Las NLCs demostraron ser estables con una vida útil extrapolada de 36 meses en base a la ICH Q1E. Se realizaron ensayos de permeación *in vitro* (IVPT) y se observó un efecto promotor de la absorción del fármaco encapsulado en NLCs frente a un control de solución hidroalcohólica del fármaco.

Se desarrollaron NLCs marcadas fluorescentemente y se administraron en piel (en este caso tanto en piel humana como de cerdo) para observar su biodistribución cualitativa mediante microscopio confocal de fluorescencia. De manera análoga a los lipomeros, las nanopartículas fueron marcadas con LRB y encapsularon C6 como modelo de pequeña molécula hidrofóbica. También se observó una acumulación en folículos pilosos, con una liberación de C6 en epidermis y zonas superficiales (alrededor de 400 μm aproximadamente) de folículos pilosos y una acumulación de LRB-NLCs en zonas más profundas de folículos pilosos (hasta unos 1000 μm de profundidad). Al comparar los resultados en piel de cerdo y piel humana se observaron biodistribuciones similares, con una acumulación de NLCs en glándulas sebáceas en el caso de la piel humana. Estos resultados fueron confirmados mediante inmunohistofluorescencia tras la encapsulación de DEX. Los resultados mostraron que las NLCs, al acumularse en folículos pilosos y liberar poco a poco el activo encapsulado, podrían proporcionar un efecto de depósito dentro de la unidad pilosebácea, lo que sería útil de cara a reducir la frecuencia de administración de tratamientos actuales para enfermedades como la alopecia o el acné. Los perfiles de seguridad y eficacia de las DEX-NLCs deberán verificarse en ensayos clínicos para comparar los efectos secundarios.

También se desarrollaron con éxito nanotransfersomas, en estas nanovesículas flexibles se encapsuló latanoprost, un análogo de prostaglandina. Además, se obtuvieron nanotransfersomas marcados fluorescentemente con un fluorocromo hidrofóbico intercalado en su membrana (LRB), y un fluorocromo hidrofílico (fluoresceína sódica) encapsulado en su núcleo acuoso. Se estudió la biodistribución cutánea *ex vivo* en cuero cabelludo humano y en piel de cerdo. Mediante microscopía láser confocal se observó que ambos fluorocromos aumentaron su penetración, con patrones similares en ambas especies, en comparación con las soluciones de fluorocromos libres. Los nanotransfersomas demostraron ser estables durante 6

meses en condiciones aceleradas (40°C/75% RH) y durante 12 meses en condiciones a largo plazo (25°C/60% RH), sin mostrar diferencias en el tamaño de las vesículas ni en la polidispersión cuando se encapsuló latanoprost. Se realizó un estudio de escalado con el método de ultrasonidos para evaluar las variables significativas. Fue posible obtener modelos predictivos que permitieron determinar la cantidad de energía requerida por litro de lote para obtener el tamaño y Pdl deseados.

Se realizaron permeaciones en el cuero cabelludo humano con DEX-lipomers y Free-DEX. Se seleccionó el cloruro de benzalconio (BAK) como trazador de los lipomers ya que se encuentra formando parte de las nanopartículas. Se analizaron calibradores de DEX y BAK en crio-secciones transversales de piel para estudiar la biodistribución cuantitativa de ambas moléculas mediante Raman confocal y MALDI-TOF MSI. Se desarrolló con éxito un proceso para la derivatización de DEX con el reactivo Girard's T (DEX-GirT), para amplificar la intensidad del pico correspondiente en espectrometría de masas. Se obtuvo una biodistribución cutánea cuantitativa de DEX y BAK mediante MALDI-TOF-MSI. En Confocal Raman no fue posible detectar BAK, pero la cantidad detectada de DEX fue significativamente mayor que en MALDI-TOF-MSI. Se compararon ambas técnicas como herramientas para estudiar la biodistribución cutánea cuantitativa de diferentes compuestos. MALDI-MSI fue muy útil a la hora de analizar regiones de mayor tamaño dentro de un tejido, mientras que Confocal Raman permitió obtener biodistribuciones de regiones más pequeñas, pero con resoluciones espaciales más altas. La posibilidad de obtener mapas cualitativos de la biodistribución de los compuestos y combinarlos con datos cuantitativos es una herramienta de gran utilidad a la hora de desarrollar sistemas de administración de fármacos que se acumulen en regiones anatómicas específicas. Es necesario seguir trabajando en la validación del método de cuantificación utilizando ambas técnicas para obtener datos robustos con diferentes moléculas.

Annex 1 - Transungual delivery, anti-inflammatory activity, and *in vivo* assessment of a cyclodextrin polypseudorotaxanes nail lacquer

Annex 1 - Transungual delivery, anti-inflammatory activity, and *in vivo* assessment of a cyclodextrin polypseudorotaxanes nail lacquer

Summary

Se desarrolló una nueva laca de uñas de polipseudorotaxanos de ciclodextrina (Regenail®) que contiene biotina, metilsilfonilmetano (MSM) y salicilato de dimetilsilanodiol, y se evaluó *in vitro* e *in vivo*. El producto se desarrolló para mejorar el estado de las uñas y disminuir los signos de las alteraciones patológicas de las mismas. Se utilizó un producto de referencia (Betalfatrus®) con fines comparativos. Un experimento de permeación *in vitro* en uñas mostró una elevada absorción de MSM y biotina. También se comprobó que el contenido de azufre y silicio en las uñas era superior al del producto de referencia. El MSM se probó en queratinocitos humanos, mostrando un buen perfil de citotoxicidad y actividad antiinflamatoria por la reducción de IL-8 y TNF- α bajo estímulos de Lipopolisacardo (LPS). Se realizó un estudio clínico para comprobar la seguridad y la eficacia del producto contra la fragilidad de las uñas y las alteraciones como las líneas de Beau y la onicorrexis. Se observó una reducción de ambas alteraciones y de la rugosidad de la superficie sin alterar la estructura de la uña, con un buen nivel de aceptación y satisfacción por parte de los pacientes.



Article

Transungual Delivery, Anti-Inflammatory Activity, and In Vivo Assessment of a Cyclodextrin Polypseudorotaxanes Nail Lacquer

Francisco Fernández-Campos ^{1,*} , Francesc Navarro ¹, Adrian Corrales ¹, Jordi Picas ¹, Eloy Pena ¹, Jordi González ¹ and Francisco J. Otero-Espinar ^{2,3}

¹ R & D Department. Reig Jofre Laboratories, Avda dels Flors, s/n, 08970 Sant Joan Despi, Spain; fnavarro@reigjofre.com (F.N.); acorrales@reigjofre.com (A.C.); jpicas@reigjofre.com (J.P.); epena@reigjofre.com (E.P.); jgplagaro@gmail.com (J.G.)

² Department of Pharmacology, Pharmacy and Pharmaceutical Technology, Faculty of Pharmacy, University of Santiago de Compostela (USC), 15782 Santiago de Compostela, Spain; francisco.otero@usc.es

³ Paraquasil Group, Health Research Institute of Santiago de Compostela (FIDIS), 15782 Santiago de Compostela, Spain

* Correspondence: ffernandez@reigjofre.com; Tel.: +34-93-480-6710

Received: 27 June 2020; Accepted: 31 July 2020; Published: 4 August 2020



Abstract: A new cyclodextrin polypseudorotaxanes nail lacquer (Regenail[®]) containing biotin, methyl sulphonyl methane (MSM), and dimethylsilanediol salicylate was developed and evaluated in vitro and in vivo. The product was developed to improve nail status and diminish signs of pathological nail alterations. A reference product (Betalfatrus[®]) was used for comparative purposes. An in vitro permeation experiment in hooves showed high MSM and biotin absorption. The content of sulfur and silicon in hooves was also found to be higher compared with the reference product. MSM was tested in human keratinocytes, exhibiting a good cytotoxicity profile and anti-inflammatory activity by the reduction in IL-8 and TNF- α under LPS stimuli. A clinical study was performed to check product safety and efficacy against nail brittleness and alterations such as Beau's lines and onychorrhexis. A reduction in both alterations and in surface roughness without alteration of nail structure was observed, with a good level of patient acceptance and satisfaction.

Keywords: nail lacquers; cyclodextrins; methylsulfonylmethane; active penetration; biotin

1. Introduction

Nails are a complex structure composed of a nail bed (the deeper layer), nail matrix, nail folds, and the outer layer, nail plate. The nail bed is formed of a noncornified living epithelium tissue underlying the papilla dermis and contains blood vessels, nerves, and lymphatic fluid [1]. The nail plate contains between 80 and 90 layers of dense keratinized (mainly α -keratin) dead cells, with desmosome unions. This structure protects the nail bed from external damage. Nail folds are attached to the nail matrix and are a continuation of the skin, developing the cuticle, which seals the nail surface, preventing the entrance of chemicals and microorganisms. Finally, the nail plate is the outermost layer, formed by translucent dead keratinocytes and with a high keratin content, rich in cysteine, glycine, and tyrosine proteins. Lunula is the most characteristic distal semicircular white section of the nail plate [2–4]. Unlike the skin, nails have a low lipid content (around 1%), mainly composed of cholesterol, and the water content is higher than in the stratum corneum at around 10–30% (as a protein solvate) in a normal state [4]. These facts mean nails have different permeability properties from skin, which should be considered in formula development.

Different factors could affect nail status, such as environmental conditions, external factors, and several diseases. Environmental factors (e.g., low relative humidity, winter, etc.) could reduce the water content, leading to nail brittleness. Constant use of nail cosmetic products (nail polish) based on a high amount of organic solvents (e.g., butyl acetate, ethyl acetate) could extract nail water and lipids, leading to progressive dehydration. These products also contain chemical compounds (plasticizers, i.e., dibutyl phthalate and dioctyl phthalate; pearlizers, i.e., bismuth oxychloride; resins, i.e., toluene sulphonamide formaldehyde, shellac; etc.), that could induce contact dermatitis and nail plate coloration [5]. Nutritional deficiencies (biotin deficiencies [6]) and diseases (i.e., microbial infections, psoriasis, lichen planus, alopecia areata, Darier's disease, etc.) could affect the nail structure [7,8].

Fungal infections (onychomycosis) are one of the most common nail diseases and are highly recurrent [9,10]. The prevalence ranged between 8% and 14% in North America, increasing with age up to 50% in the elderly [11,12]. They could be caused by dermatophytes, with *Trichophyton rubrum* being the main microorganism involved in around 71% of fungal infections, and the second most common cause being *Trichophyton mentagrophyte* (20%). Nondermatophyte microorganisms are less common, with *Candida albicans* responsible for 5.6% of nail infections [12]. Several clinical presentations could be present—hyperkeratosis, onycholysis, dyschromia (melanonychia), longitudinal striates, and inflammation—leading to nail structure alteration and function impairment. Topical antifungals are usually employed, and an oral alternative is reserved to treat more invasive and/or extensive manifestations [11].

Onychomycosis is present in 18% of patients, with nail psoriasis being an aggravating factor of the disease [13]. Psoriasis is a chronic immune disease affecting the skin. Keratinocyte hyperproliferation and inflammation are observed in patients and the involvement of the nail apparatus happens in around 50% of cases [14]. Nail alterations in psoriasis usually involve the nail matrix (pitting, leukonychia or white spots, and crumbling) and the nail bed (onycholysis, hyperkeratosis, and discoloration). In addition, longitudinal (onychorrhexis) and transversal ridges (also known as Beau's lines) are usually present as a clinical manifestation.

Topical drug delivery systems to treat nail alterations are usually preferred to avoid the adverse effects of systemic medications. In addition, they have good patient acceptance and are cost-effective. The main drawback of topical therapy is low drug absorption due to the limited permeability of the nail structure, reducing the access of the drug to the nail bed. In addition, the nail bed turnover increases the reduction in drug concentrations [15]. To maintain an effective drug flux, several strategies (physical and chemical) are reported in the literature. Physical agents such as iontophoresis have been reported to increase antifungal and corticoid concentrations in the nail structure, improving therapeutic outcomes. Ultrasounds, photodynamic and laser therapy were also described as promising tools to increase drug effectiveness [12]. Physical abrasion with sandpaper aimed to reduce nail thickness and thereby increase drug diffusion across the unguis structure. This has been reported to increase terbinafine effectiveness in onychomycosis [16].

Transient chemical modification of the nail structure by permeation enhancers to increase drug diffusion is widely described in the literature. Considering that the main constituent of the nail is keratin, an alteration in protein packing is one mechanism of enhancement. Sulfhydryl compounds, such as cysteine, acetyl cysteine, and mercaptoethanol [17], and papaine, an endopeptidase with reactive sulfhydryl residues, reduce disulfide bounds and destabilize keratin. Softening compounds (urea and salicylic acid) have keratolytic properties and increase water uptake and swell keratin, making it less dense and compact and increasing the pore size [4]. Surfactants such as sodium lauryl sulfate could also alter the protein packing by electrostatic repulsion, induce micelle formation and absorption promotion, and reduce the contact angle between the formulation and nail surface to ensure better water access, increasing swelling [18]. Cyclodextrins are cyclic oligosaccharides and had the ability to form complexes with various active ingredients, involving the active ingredient in the lipophilic center. Their complex formation allows us to change the physical and chemical properties of

the active ingredients [19,20]. Cyclodextrins had been reported to increase drug absorption across nails due to the solubilization of hydrophobic molecules—increasing the hydration of the nail plate, making pores broaden, and interacting with aromatic amino acids, limiting the protein folding. It was also demonstrated that the water itself could act as an unguinal enhancer by the hydration and swelling of keratin fibers [21–23]. In addition, the hydroalcoholic-based formulation causes a higher concentration of the drug in the film than from the originally applied formulations after the evaporation of the solvent, leading to thermodynamic activity increase, which favors drug diffusion [24].

Nogueiras-Nieto et al. developed in situ gelling formulations of Poloxamer 407 and hydroxypropyl β -cyclodextrin (HP- β -CD), obtaining a polypseudorotaxane supramolecular structure that increases the delivery of antifungals (ciclopirox) and corticoid (triamcinolone) across human nails and hooves [25]. Later, the same group used methyl- β -cyclodextrin and Poloxamer 407 in a hydroalcoholic solution to deliver ciclopirox olamine and compared the results with other marketed ciclopirox olamine formulations. The proposed polypseudorotaxane lacquer increased the permeation and accumulation of the drug into the nail structure [22]. Chouhan et al. also demonstrated in vitro the enhancing effect of HP- β -CD for terbinafine unguinal delivery [21]. Cutrin-Gomez et al., in 2018, showed the capacity of the soluble cyclodextrin derivatives (methyl- β -cyclodextrin and HP- β -CD) to modify the microporous characteristics of the nail plate via interaction with nail components. These modifications produce a significant increase in the drug permeability and drug accumulation in the nail [23].

There are a limited number of products on the market to treat nail alterations topically, based on hydroalcoholic solutions. Most of them are antimycotic drugs, formulated in a variety of nail lacquers bases. There are few nonmycotic agents to treat other nail alterations or protect from external aggressions.

Methyl sulfonyl methane (MSM), an important volatile component in the sulfur cycle, has long been thought of as a sulfur donor for sulfur-containing compounds such as methionine, cysteine, homocysteine, taurine, and many others [26–28]. MSM is present in keratin, where it is responsible for making nails hard and is a crucial component of collagen production [26]. MSM is structurally related to DMSO but differs in the oxidation state; it is a small (MW 94.14 Da) and hydrophilic compound ($\log P = 1.41$). It is nonionizable in ambient conditions.

The presence of soft and brittle nails can also indicate a systemic deficiency of silicon [29,30]. Silicon also helps with the synthesis of glycosaminoglycans, along with collagen [30]. Barel et al. [31] evaluated the effect of the intake of supplements containing choline-stabilized orthosilicic acid (ch-OSA) on the skin, hair, and nails. After treatment, they observed a significant improvement in the fragility of nails and hair in the group using the ch-OSA. Dimethylsilanediol salicylate is an organic form of water-soluble silicon (MW 212.3 Da, $\log P$ 3.13, $\log D$ (pH 5.5) 2.59). A salicylic radical could enhance properties for nail penetration.

Biotin has an important role in protein synthesis, especially in keratins, and has been claimed to contribute to healthy nails and hair. Oral biotin led to improved hardness and thickness in nails [6,32,33]. In vitro studies of keratinocytes showed the stimulation of cell differentiation and the production of cytokeratins [34]. They were also shown to stimulate lipid synthesis, responsible for the binding of keratinocytes in the nail plate [33]. Biotin is a small molecule of 244.3 Da, slightly soluble in water in its nonsalt form ($\log P$ 0.39, pK_a 4.4) and leading to good permeability across nails.

We hypothesized that the topical administration of MSM, dimethylsilanediol salicylate, and biotin in polypseudorotaxane hydroalcoholic nail lacquer will effectively deliver these compounds across the nail barrier and thereby improve nail status and diminish signs of nail pathological alterations.

Hence, the aim of this study was to further investigate the transungual permeation/penetration profiles of MSM and biotin, as well as the amounts of sulfur and silicon in the nail, after the application of an experimental nail lacquer (Regenail[®]: REG) and a commercial nail lacquer (Betalfatrus[®]: BET). Secondary objectives included the evaluation of the clinical efficacy and safety of the experimental lacquer and of the user-friendliness, as gauged by the subject's self-assessment and a medical examination and the effect in terms of the improvement of alterations in nails achieved by Regenail[®].

2. Materials and Methods

2.1. Materials

MSM (10% *w/w*) and bamboo glycolic extract (Pracofar S.A., Barcelona, Spain), biotin (0.2% *w/w*) (Siemgluss Iberica S.A., Barcelona, Spain), HP- β -CD (8.7% *w/w*) (molar substitution degree of 0.65 and molecular weight of 1399 Da, HPB Kleptose, Roquette, Lestrem, France), dimethylsilanediol salicylate (0.246% *w/w*, Exsymol, Monaco), sodium lauryl sulfate (0.87% *w/w*, BASF, Barcelona, Spain), ethanol 96° (34.7%, Alcoholes Oliva, Barcelona, Spain), and purified water were used for the experimental nail lacquer (REG) production. Components were added one by one, from the least to the most concentrated, to the ethanol-water mixture.

The commercial nail lacquer (BET) chosen as a reference had the following composition: *Equisetum arvense*, methyl-sulfonyl-methane (~5.55% *w/w*), hydroxypropyl-chitosan, ethanol, water, and diethylglycol monoethylether.

2.2. Methods

2.2.1. Regenail Formulation Characterization

The produced formulation, Regenail, was characterized in terms of appearance (visual observation) and HPLC quantification of biotin and MSM. These determinations assessed the stability according to ICH long-term conditions 25 °C/60% HR, 30 °C/75% HR and in accelerated conditions 40 °C/75% HR. The HPLC quantification was as described in Section 2.2.2.

Finally, a release experiment was performed on Franz cells (VidraFoc, Barcelona, Spain; 100 mL volume and an effective diffusional area of 2 cm²) using a dialysis membrane (10–12 kDa). One milliliter of REG was placed in a donor compartment (*n* = 6) and 0.3 μ L samples were taken at 1, 2, 4, 20, 22, and 24 h and replenished with the same volume of fresh receptor medium (5% HP- β -CD in phosphate buffered saline (PBS, pH 7.4, to maintain sink conditions). The system was continuously stirred at 500 rpm and maintained at 37 °C throughout the experiment. Biotin and MSM release were quantified according to the methods described in Section 2.2.2.

2.2.2. In Vitro Penetration of the Nail Plate

We created in vitro permeation profiles of MSM and biotin (only in the case of REG), and recorded the amounts of sulfur and silicon in the nails after treatment with the experimental nail lacquer or the commercial nail lacquer.

Permeation Study

The bovine hooves were obtained from freshly slaughtered cattle, stripped of adhering cartilaginous and connective tissue. Hooves were cut into flat sections of approximately 300–700 μ m in thickness and frozen until use.

The prepared hoof membrane was used in a Franz diffusion cell (*n* = 6 per formulation) with an effective diffusion area of 0.196 cm². For this, hoof samples were cut into small discs using an 8-mm punch and placed between two PTFE adapters with an O-shaped ring of 5 mm in diameter. The ratio between the area of the O-shaped ring and the bovine hoof samples was 0.392 and, therefore, in accordance with Palliyil et al. [35], the lateral diffusion caused by the edge effect is not expected to have a significant influence on our results. The receptor compartment was filled with 5 mL of phosphate buffered saline (PBS, pH 7.4) and with 5% of HP- β -CD, and the cells were equilibrated at 37 °C in a water bath with magnetic stirring.

Two milliliters of the nail lacquers or PBS (blank) were placed in the donor compartment to avoid depletion during the 11 days of the experiment. Once a day, a 1 mL sample of receptor medium was sampled and replenished with the same volume of fresh medium. The receptor fluid was sampled for the determination of MSM by gas chromatography (GC) and biotin by HPLC. In order to determine

the amounts of biotin, silicon and sulfur that remained in the hoof after the permeation experiment, hooves were cleaned with distilled water and dried using cellulose paper for further quantification.

Biotin Quantification in Receptor Medium and Hooves

The biotin content of the samples (from receptor medium, $n = 6$; from hoof, $n = 6$) was directly analyzed by a validated HPLC (Water Corporation, Barcelona, Spain) method (mobile phase: Acetonitrile/buffer (1 g sodium perchlorate, 10 mL phosphoric acid up to 1 L of purified water) (10:90), flow 1.0 mL/min, column Symmetry 200 C18 3.5 μm , 150 mm \times 4.6 mm). Biotin was extracted from hoof samples by incubation with 5 mL of 5% methanol in a PBS solution for five days (at 25 °C). To quantify biotin content, a calibration line in the range 0.7–506 $\mu\text{g/mL}$ was prepared. The cumulative amounts permeated were normalized versus the permeation surface. The slope of cumulative amounts (normalized by surface) vs. time (h) was calculated.

MSM Quantification in Receptor Medium

The MSM content of the receptor medium samples ($n = 6$ per formulation) was analyzed by CG (Agilent Technologies, Barcelona, Spain; mobile phase helium, flow 8.0 mL/min, column DB-1 50 m, 0.53 mm internal diameter, 5 μm). A calibration curve in the range of 3 to 13,300 $\mu\text{g/mL}$ was prepared in a methanol solvent. The cumulative amounts released were normalized versus the permeation surface.

Sulfur and Silicon Quantification in Hooves after Permeation

In order to determine the amount of sulfur and silicon in the hooves, they were treated by digestion for 120 min with 2 mL of a solution of 2.5% TMAH (tetramethylammonium hydroxide, Sigma-Aldrich, Barcelona, Spain) in water at 90 °C. The intensity value obtained for the blank was subtracted from the values obtained with each one of the samples. The sulfur and silicon content in hooves was analyzed by ICP-OES (Inductively Coupled Plasma-Optical Emission Spectrometry). Sulfur was determined at 182.0 nm and silicon was determined at 288.2 nm.

2.2.3. In vitro Cytotoxicity Assay

The cytotoxic effect of MSM was evaluated in vitro ($n = 6$) by direct contact with the cell, following the ISO 10993-5:2009 recommendation guidelines [36].

The HaCaT cells were seeded in a 96-well plate at a density of 10,000 cells/well, in a fresh culture medium supplemented with 10% fetal bovine serum, penicillin (100 IU/mL), and streptomycin (100 $\mu\text{g/mL}$) (Fisher Scientific, Barcelona, Spain). The plates were incubated for 24 h in a humidified atmosphere of 5% CO_2 at 37 °C and treated with different concentrations of MSM from 10 μM to 0.003 μM , diluted in growth medium. For cell proliferation quantification, the general cell viability endpoint MTT (Sigma-Aldrich, Barcelona, Spain) reduction (3-(4,5-dimethyl-2-thiazolyl)-2,5-diphenyl-2H-tetrazolium bromide) was used [37]. Accordingly, the previous culture medium was removed and replaced with a fresh medium containing MTT (1:10). The cells were incubated at 37 °C for 3 h; after this time, the medium was removed and the intracellular formazan crystals were solubilized and extracted with dimethylsulfoxide (Panreac, Barcelona, Spain). After 15 min at room temperature, the absorbance was measured at 550 nm in a microplate reader (Perkin Elmer, Barcelona, Spain).

2.2.4. $\text{TNF}\alpha$ and IL8 RNA Isolation and RT-PCR

RNA was isolated from cell samples ($n = 6$) using the method described by Chomczynski [38], using the RNeasy kit (Qiagen) and treating with DNase-I to remove any contamination from genomic DNA.

The purity of the RNA was estimated by 1.5% agarose gel electrophoresis, and the RNA concentration was determined by nano-drop spectrophotometry (Thermo Fisher Scientific, Barcelona, Spain).

Reverse transcription of 1 µg RNA for complementary DNA (cDNA) synthesis was performed using a First-strand Synthesis kit (Takara-Clontech, Saint-Germain-en-Laye, France). This cDNA from treated or untreated cells (control) was used to determine the relative gene expression of TNFα and IL-8 through RT-qPCR.

Real-time (RT)-qPCR was performed in a QuantStudio 5, Applied BioSystem (Barcelona, Spain) apparatus. For the normalization of cDNA loading in the PCR reaction, the amplification of ACT for every sample was used. Relative changes in gene expression were calculated using the Pfaffl method, following standard procedures [39].

2.2.5. Clinical Study Design

The main objective of the study was to evaluate the clinical efficacy and subjective perception of the improvement in nail alterations achieved by the experimental nail lacquer (REG) or the commercial nail lacquer (BET). The safety of both products was also evaluated as a secondary endpoint.

Thirty volunteers (between 18 and 65 years old) from both sexes were recruited to participate in the study. The inclusion criteria were: Both genders, general good health (physical and psychological), alterations on the surface of the nails of both hands, adequate understanding of the clinical study, agreement to participate, and availability to attend the visits. No other topical nail product could be used during the study and any other treatment that could affect the evaluation of the study endpoints was forbidden. Each subject received oral and written information concerning the studied product. Written consent was obtained before any study-specific procedures, in accordance with the Helsinki Declaration.

Eligible subjects were randomly assigned to an experimental group. Patients were treated for a period of 28 days. Both products were applied once daily, preferably at night (to ensure a contact time of 6 h), with a brush, covering the complete (cleaned) nail. After application of the nail lacquer, patients were instructed not to clean their hands, because the obtained film in nails is hydrophilic. The following day, patients could do their routine daily cleaning (shower, hand washing, etc.). Nails' evolution was evaluated at day 28, compared with D 0 (the baseline). On day 14, volunteers came to the study site for a control visit.

On day 0 and day 28, the nails were examined by a dermatologist to evaluate the nail alterations' progression (Beau's lines and onychorrhexis). A categorical scale ranging from 0 (alteration absence) to 4 (severe alteration) was used by the dermatologist for evaluation. The nail roughness was evaluated with PRIMOS-CR[®] (Canfield Scientific, NY, USA). The transonychial water loss (TOWL) was also evaluated with the Tewameter[®] TM 300 (Courage + Khazaka electronic GmbH, Köln Germany). Participants had washed their hands prior to the topographical evaluation. Measurements of camera distance and ambient illumination were standardized.

A subjective questionnaire was included at the end of the study to evaluate product usability and efficacy. A Likert scale (from 0—totally disagree, to 5—totally agree) was employed for this evaluation.

The compatibility of the product with nails and any undesirable effects were assessed at every visit by a dermatologist.

2.2.6. Data Analysis

The slope of the linear portion of the cumulative amounts vs. the time of permeation profile was estimated as the pseudo steady-state flux (J_s) of penetrant permeation. The lag times (Tlag) for each active compound were derived from the x-intercept of the slope at pseudo steady-state. The permeability coefficients (K_p) of each active compound were calculated as compound flux/compound concentration in the donor chamber. The diffusion parameter P_1 and the partitioning parameter P_2 were calculated according to Equations (1) and (2), respectively. The results were expressed as mean ± standard deviation (SD) and were statistically analyzed with Minitab software (Coventry, United Kingdom).

$$K_p = P_1 \cdot P_2 \quad (1)$$

$$T_{lag} = 1/(6 P_2) \quad (2)$$

The significance of the effect of the treatment over time on the response variables was evaluated using an ANOVA test. A significance value of 0.05 was established for all statistical tests used in the data analysis.

3. Results

3.1. Formulation Characterization

Figure 1 shows the results of biotin and MSM under different climatic conditions for 12 months. The data show low variation (less than 5%) compared with the initial time point for both active compounds in all conditions. The results at 30 °C/75% HR almost overlap with those at 25 °C/60% HR for both MSM and biotin, with no differences shown between these stability conditions. According to ICH Q1E [40], if no significant variation (less than 5%) is seen in the accelerated stability conditions, then an extrapolation of long-term conditions up to two years could be stated, based on the obtained results. A long-term study will continue until the proposed extrapolated shelf-life (two years) to confirm the obtained results. The regression equations at 25 °C/60% HR (long-term conditions at climate zone II) were for biotin $y = 102.57 - 0.067 \cdot \text{Time}$ and for MSM $y = 103.9 + 0.25 \cdot \text{Time}$. The regression equations at 30 °C/75% HR (long-term conditions at climate zone IVb) were for biotin $y = 102.43 - 0.117 \cdot \text{Time}$ and for MSM $y = 104.02 + 0.275 \cdot \text{Time}$. To evaluate whether there are differences in the regression lines, ANCOVA analysis (covariance analysis) was performed. In both biotin and MSM, there were no differences in interaction factor Time x Climate condition ($p < 0.05$), which means that the regression line slopes are considered parallel and the factor climate conditions (which represents the y -intercept) is not significant ($p < 0.05$). The overall biotin and MSM regression lines could be considered coincident at both climate conditions (25 °C/60% HR and 30 °C/75%HR).

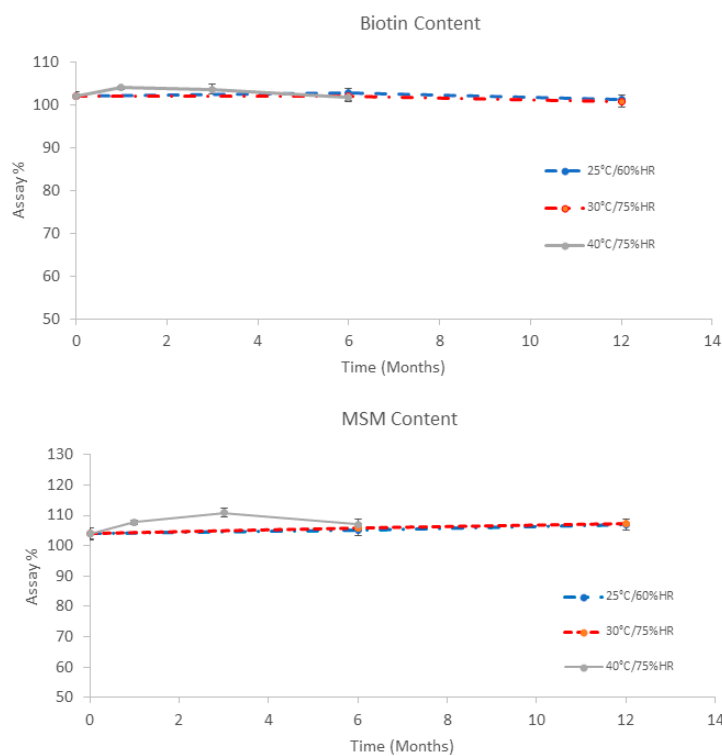


Figure 1. Biotin (upper panel) and methyl sulphonyl methane (MSM) (lower panel) content of Regenail® (REG) in stability studies under different climate conditions.

Release experiments (Figure 2) showed a slow release of both compounds, probably due to the dialysis membrane being the rate-limiting step (the active compounds are not expected to be

encapsulated, because the high solubility in the hydroalcoholic vehicle). This membrane was chosen to prevent the HP- β -CD polypseudorotaxane complex from passing through to the receptor medium. In addition, the small pore of these membranes could be more similar to hoof pores than the standard membranes of 0.22 or 0.45 μm usually employed in release experiments. A limitation of release experiments is that artificial membranes, such as cellulose dialysis membranes, are not sensitive to permeation enhancers. For this reason, *in vitro* permeation with hooves was performed.

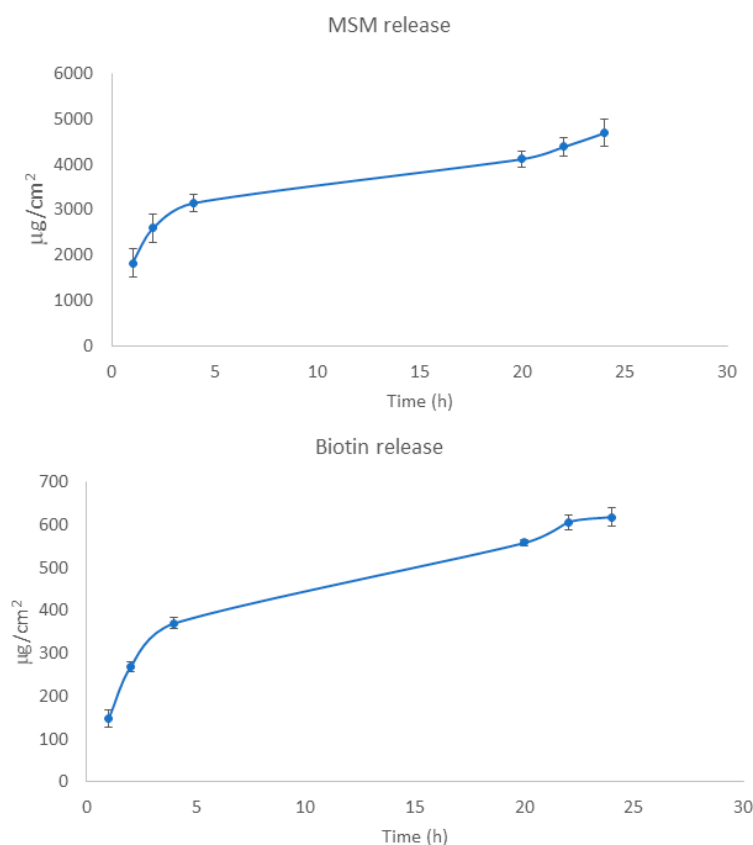


Figure 2. MSM (upper panel) and biotin (lower panel) release over time from REG nail lacquer.

3.2. *In Vitro* Permeation Study

Nail penetration of active compounds was investigated in Franz diffusion cells after topical application of experimental nail lacquer (REG) or commercial nail lacquer (BET) to hooves for 11 days. Infinite dose conditions were set up to assess formulation differences in terms of the permeation profiles. Both tested products permeated the bovine hoof plate, but differences in permeation parameters were noticed, related to the active compounds and the formulation. The permeation profiles of MSM across the hoof are shown in Figure 3. The transungual permeation parameters of active compounds containing the formulations are presented in Table 1.

The calculated permeation steady state flux of MSM through REG formulation, across the hoof plate, was observed to be 10,839.695 $\mu\text{g}/\text{h}/\text{cm}^2$, more than double that of the reference product. The lag times (T_{lag}) were statistically different: 105.12 h for REG vs. 98.77 h for BET ($p < 0.05$). The mean values for the P_1 (diffusion-related parameter) and permeability coefficients (K_p) of MSM were also more than double the corresponding values for the reference.

However, P_2 (the partitioning-related parameter) was similar for the two nail lacquers, thus indicating that the partitioning coefficient of the MSM between the formulation and the nail is similar, so both formulations are similar in terms of the relative polarity of the MSM.

These results clearly indicate that REG allows higher permeation levels of MSM than those obtained with the reference product BET.

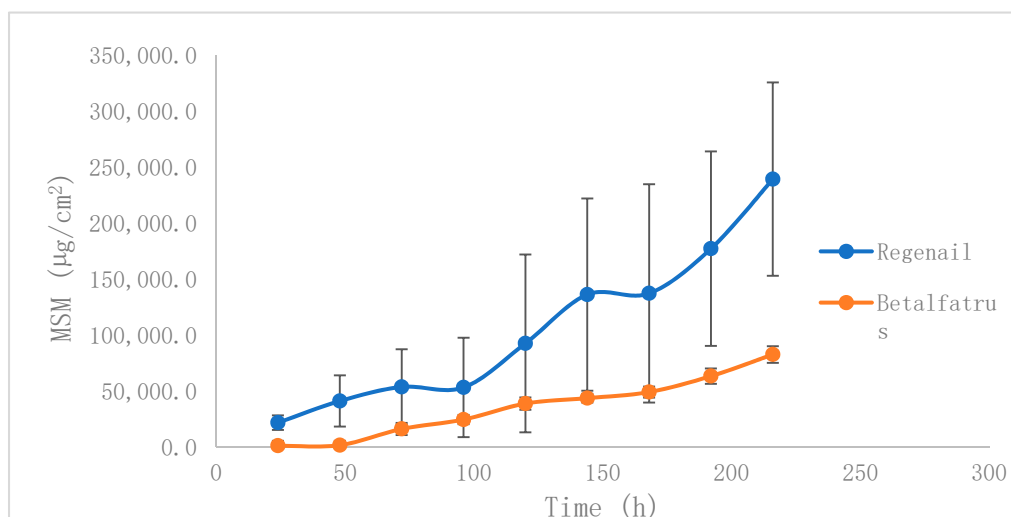


Figure 3. Permeation profiles of MSM through the bovine hoof plate as a model of human nail permeation.

Additionally, these data were normalized by the amount of MSM applied in each test (the MSM concentration between both products is different: 10% *w/w* for REG and around 5.5% *w/w* for BET).

When these normalized values are considered, the profiles of both formulations get closer. The mean values for the P_1 , P_2 , and K_p of MSM that permeated through hooves showed negligible differences between the two formulations. The permeation steady state flux values, however, were significantly different: 1083.97 $\mu\text{g}/\text{h}/\text{cm}^2$ for REG vs. 647.89 $\mu\text{g}/\text{h}/\text{cm}^2$ for BET. Although most of the differences between permeation parameters were caused by different MSM concentrations, the increased flux after dose normalization indicates the superiority of the test vehicle over the commercial formulation. According to the molecular structure of MSM, it is not expanded to encapsulate or interact with HP- β -CD, so the increase in transungual flux could be caused by the shelf promoting effect of the formulation. It was demonstrated previously [22,23,25] that cyclodextrin-soluble polypseudorotaxanes increase the size of nail channels and interact with keratin residues, reducing protein folding. Sodium lauryl sulfate could also increase the diffusivity of MSM by contribution to protein interaction. MSM is not expected to reduce disulfide bonds. In addition, the proposed formulation can increase the absorption of hydrophilic active compounds despite the well-known solubilization capacity of lipophilic molecules, which is the main promotion mechanism in these compounds.

When permeated concentrations of MSM at 24 h (around 21,700 $\mu\text{g}/\text{cm}^2$) are compared with release concentrations at the same time point (around 1800 $\mu\text{g}/\text{cm}^2$), we see the enhancing effect of REG caused by the interaction of the system with the hoof structure, compared with the pure diffusion seen in release experiments across dialysis membranes.

Table 1. Transungual permeation parameters of test and reference formulation. (*) = statistical differences between formulations with a *p*-value < 0.05.

Formulation	Active Compounds	J_s ($\mu\text{g}/\text{h}/\text{cm}^2$)	K_p (cm/h)	P_1 (cm)	P_2 (h^{-1})	T_{lag} (h)	Active Content ($\mu\text{g}/\text{mg}$)
Regenail	Biotin	74.98 \pm 35.34	0.0187 \pm 0.0102	6.7163 \pm 4.5610	0.00279 \pm 0.00118	59.72 \pm 5.34	0.161 \pm 0.098
	MSM	10,839.695 * \pm 5786.239	0.054 * \pm 0.014	34.185 * \pm 8.661	0.00159 \pm 0.00098	105.12 * \pm 3.56	–
Betalfatrus	MSM	3563.382 * \pm 963.993	0.0324 * \pm 0.011	19.198 * \pm 4.821	0.00170 \pm 0.00125	98.77 * \pm 3.01	–

The amount of sulfur obtained through the MSM at the end of experiments after application of REG formulation was 948.66 ppm, 2.3-fold higher than that obtained with the BET solution (412.78 ppm).

Biotin profiles from REG could not be compared with the reference product because it does not contain biotin. The permeation profiles of biotin across a hoof are shown in Figure 4. The transungual biotin parameters are shown in Table 1. As P_1 is higher than P_2 , diffusion is the main driving force that

allows for active penetration. There are no previous investigations that have described the topical absorption of biotin, so this is the first time that transungual delivery of biotin has been described. It is shown that this route of administration could lead to topical absorption across the nail plate, leading to pharmacological action at the nail bed.

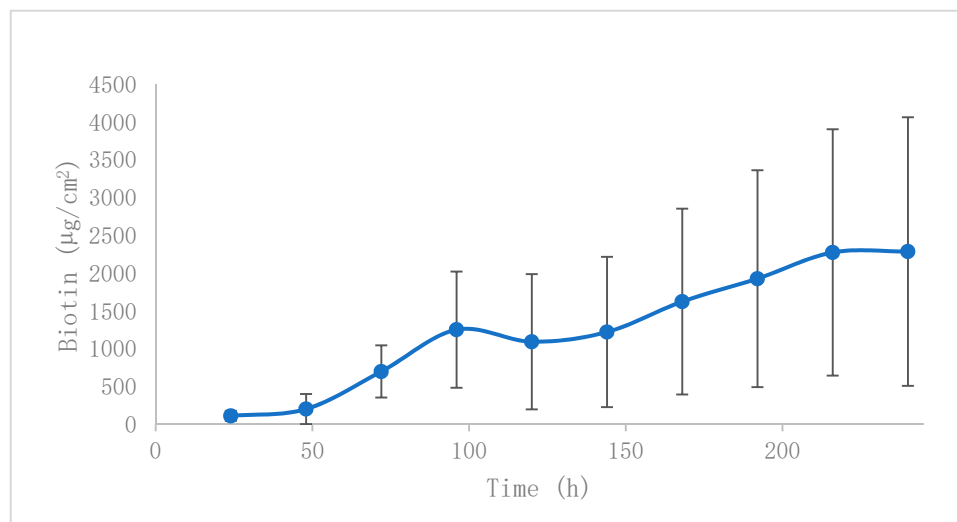


Figure 4. Permeation of biotin across the bovine hoof plate.

Biotin is also a hydrophilic molecule, and is not expected to be encapsulated, but it could form complexes with HP- β -CD [41], to ease biotin permeation, together with the previously described enhancement mechanism of CD-polypseudorotaxanes.

Although hooves are a good model to study transungual permeation, it should be considered that hooves have some differences compared to human nails. They are more porous and permeable than human nails due to the less dense keratin network. In addition, disulfide bonds are less abundant because of the lower content of cysteine, so hooves are less affected by enhancers that reduce these bonds [4]. Nail diseases, like psoriasis and onychomycosis, lead to higher porosity than in healthy nails; in this case, hoof results could be extrapolated more accurately [22]. Nevertheless, the study had comparative purposes, and was not used to obtain human absolute values. The experiment was performed according to the infinite dose paradigm, in order to maximize formulation differences and avoid analytical method quantification issues. In clinical applications, a lower dose of the nail lacquer is applied, which is another limitation of the permeation study.

When permeated concentrations of biotin at 24 h (around 90 $\mu\text{g}/\text{cm}^2$) are compared with release concentrations at the same time point (around 140 $\mu\text{g}/\text{cm}^2$), we observed a small reduction in hoof absorption compared with pure diffusion. This could be caused by a possible interaction between biotin and HP- β -CD [41], or even an interaction of the amino and/or carboxylic groups of the biotin molecule with hoof keratins.

Similar to MSM, the silicon content was determined in the reference product; the values obtained for silicon were around 150 ppm, while this content in the test product is around 300 ppm. The silicon values in the bovine hoof plate after diffusion studies were 3.54 ± 1.81 and 1.33 ± 0.77 ppm for the new nail lacquer and the reference, respectively. Although there are no statistical differences between treatments, the higher percentage of active compounds remaining in the membranes at the end of the permeation studies in REG is probably due to the higher silicon content of the new product and/or the nature of the silicon (dimethylsilanediol salicylate versus silicon in *Equisetum arvense*), as described in Section 2.2. In addition, salicylate could act as a permeation enhancer [4] and could form a complex with HP- β -CD by the aromatic ring [42], increasing the diffusion of the active ingredient.

The tissue levels of silicium decrease with ageing [43]. All silanols are known to prevent the formation of advanced glycation end products (AGEs), to have antioxidant properties, to stabilize

the structure of the extracellular matrix, and to induce the production of collagen. In addition, dimethylsilanediol salicylate also has anti-inflammatory and antioxidant properties and stimulates heat shock protein expression [44,45]. Brittle nails are often improved by silicon uptake [46]. The bioavailability of organic silicon (dimethylsilanediol salicylate) allows it to quickly integrate into the structure of the nails and could compensate for its natural age-related loss.

3.3. Cytotoxic Effect of MSM

First, the cytotoxic effects of a wide concentration range of MSM (0.003–1 μ M) on human keratinocytes (HaCaT line) without stimulation were assessed with a MTT test. Compared to the control (cells cultured in the absence of MSM), no differences in cell viability or proliferation were detected at doses of 0.1, 0.03, 0.01, or 0.003 μ M of MSM. However, significant reductions ($p < 0.05$) in cell viability occurred at 0.3 μ M of MSM (Figure 5). Concentrations of 1 μ M presented a significant reduction when considering a significance level $\alpha = 10\%$, but not at 5%. When different concentrations were compared, there was no statistically significant difference, showing that the slight reduction in cell viability is due to experimental variability. The significance obtained at 0.3 μ M compared with the control could be considered a statistical artifact.

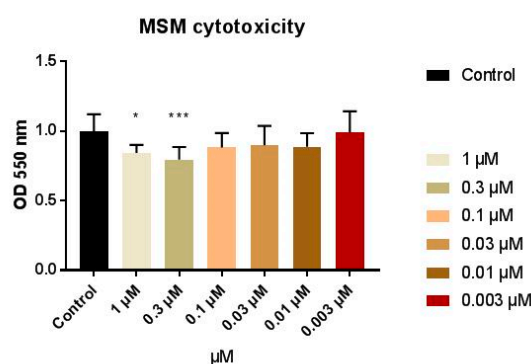


Figure 5. HaCaT cell viability by MTT after proliferation under different concentrations of MSM. (*) shows statistical differences at a significance level of $\alpha = 0.10$. (***) shows statistical differences at a significance level of $\alpha = 0.05$.

MSM is widely used orally for arthritis symptom relief due to its anti-inflammatory and antioxidant properties, with a broad dose range (up to 1.5 g/day) [47] with a good safety profile. In addition, it was considered to be a generally recognized as safe (GRAS) ingredient by the FDA (United States Food and Drug Administration) up to 4845.6 mg/day [27]. This fact is in concordance with the obtained results, despite the statistical artifact.

3.4. Anti-Inflammatory Effect of MSM

In order to assess the anti-inflammatory activities of MSM, human keratinocyte (HaCaT line) cells were exposed to LPS (100 ng/mL) in the presence or absence of MSM, and the gene expression of TNF- α and IL-8 were measured. Because of LPS exposure, the TNF- α and IL-8 gene expression significantly increased by $848.2 \pm 69.8\%$ and $710.4 \pm 83.2\%$, respectively. MSM treatment prevented significant increases in TNF- α and IL-8. The results indicate that MSM at 0.1 and 1 μ M significantly decreased TNF α expression by $76.4 \pm 8.6\%$ and $81.9 \pm 7.4\%$, and IL-8 expression by $66.1 \pm 11.9\%$ and $62.7 \pm 10.3\%$, respectively, compared to the Control + LPS.

It was found that MSM strongly inhibits IL-8 and TNF- α production in LPS-stimulated human keratinocytes (Figure 6). Our data are in accordance with previous publications. So, in bone marrow-derived macrophages, MSM inhibits ROS production and attenuates the transcriptional expression of IL-1a, IL-1b, IL-6, and NLRP3 [48]. Furthermore, Kim and colleagues demonstrated that MSM blocks NF- κ B activation, thereby inhibiting NF- κ B-mediated transcription of inflammatory genes [49]. Previous findings demonstrate an increased expression of tumor necrosis factor (TNF)- α ,

nuclear factor-kappa B, IL-6, and IL-8 in psoriasis-affected nails [50]. An important observation of our study is that treatment with MSM reduced the expression of (TNF)- α and IL-8; like a principal component of REG, the proposed nail lacquer could be used not only for the treatment of nail alterations, but also for the treatment of nail diseases related to inflammation, such as nail psoriasis. On the other hand, MSM enhanced the passage of other drugs such as ciprofloxacin across the porcine membrane, as compared to not using MSM [51]. This could be useful to increase the therapeutic effect of antimicrobial drugs in the nail plate.

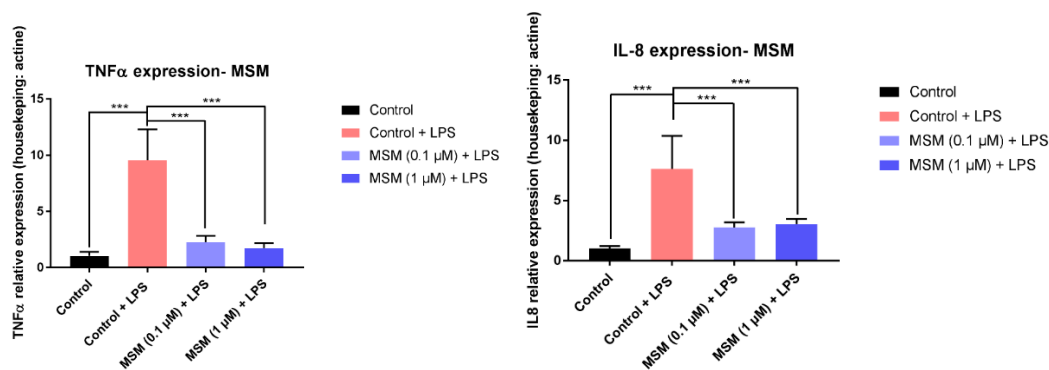


Figure 6. Effect of MSM on gene expression of TNF- α and IL-8 of LPS activated human keratinocytes (HaCaT line). (***) show statistical differences at a significance level of $\alpha = 0.05$.

3.5. Clinical Evaluation

The main nail brittleness alterations found in the volunteers were Beau's lines and onychorrhexis. Beau's lines are transversal depressions caused by temporary nail bed mitosis disruption and can be associated with everything from trauma to rheumatic disease, malaria, pemphigus, and Raynaud's disease, among other pathologies [52]. Beau's lines-related conditions could be improved with adequate nail hydration and compounds that increase fibroblast proliferation [53]. Onychorrhexis is commonly observed in advanced age, resulting in brittle nails, but also appeared in a more severe pattern in collagen vascular disease, rheumatoid arthritis, psoriasis, and nutritional deficiencies [54].

According to the dermatologist's clinical evaluation, the onychorrhexis decreased in the BET group, with an improvement observed in 68% of subjects after 28 days of application. As shown in Figure 7, the percentage of volunteers with improvement of onychorrhexis was 73% in the REG group after 28 days of treatment. The observed difference was comparable between the two treatment groups.

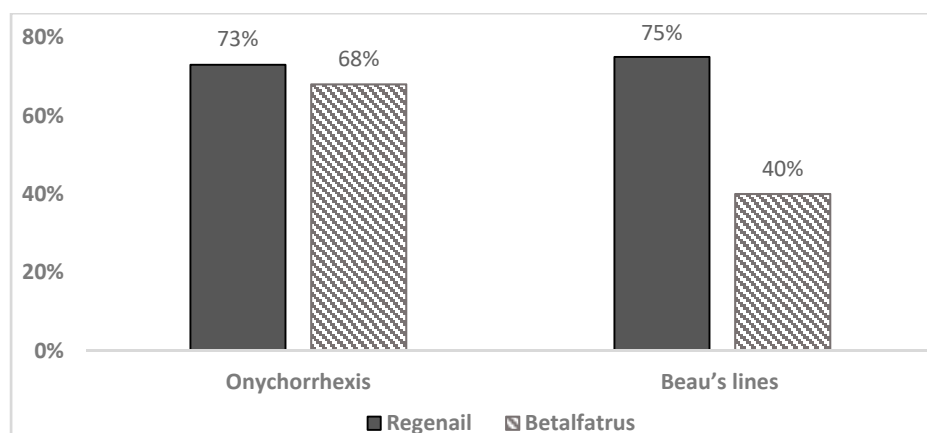


Figure 7. Percentage of volunteers whose nail onychorrhexis and Beau's lines improved after 28 days of treatment versus the baseline (%).

Improvements in Beau's lines were observed by a dermatologist in both treatment groups (Figure 5). In the REG group, the severity of the Beau's lines decreased in 75% of subjects after 28 days of treatment compared with the baseline. In 40% of the subjects who applied BET, the Beau's lines severity decreased after 28 days of treatment compared with the baseline.

As previously described, Beau's lines and onychorrhexis are indirect markers because they could appear in different nail alterations, such as onychomycosis and nail psoriasis. Regenail's properties could be useful in both pathologies. MSM has been demonstrated to have anti-inflammatory activity, reducing some of the cytokines overexpressed in psoriasis. It was previously shown that MSM has a high permeation rate and could be available in the nail matrix. It is difficult to correlate the levels of MSM found in the receptor compartment of Franz cells (Section 3.2) with the *in vitro* concentrations assayed in cell experiments (Sections 3.3 and 3.4) because of the different experimental protocols and scale (tissue vs. cell), but the clinical study showed that the proposed treatment has benefits over the reference product: It improved signs of nail alterations, and delivered safe and effective concentrations of active ingredients to human nails.

Cyclodextrins exhibit antimicrobial properties because they could interact with the protein and lipid components of a microorganism [42]—for example, ergosterol of the fungal membrane, increasing permeability and the loss of cell content. This could have additional benefits for onychomycosis treatment.

Biotin could act as a promoter of keratin production to restore nail function after disease, and the silicon derivate helps to reduce the nail fragility caused by the disease. Chessa et al. reported that nail brittleness could be improved by correct nail hydration, protection from external aggressions (i.e., detergents, irritants), biotin supplementation (to increase hardness), and intake of silicon as well as other trace elements [55].

PRIMOS-CR is a high-resolution small-field 3D system used to evaluate the surface characteristics of tissues *in vivo*. It allows us to quantify the topography of the skin or other body surface with the parameter Sa or arithmetic mean of surface roughness. In addition, software could produce color height maps (Figure 8). The evaluation showed a decrease in surface roughness (Sa)—that is, an anti-roughness effect—after REG administration. Sa decreased by 12% versus the baseline after 28 days of REG application (day 0: 0.69 ± 0.38 ; day 28: 0.61 ± 0.32). The evaluation of nail roughness in the group of volunteers after the application of BET showed a decrease of only 1% after 28 days of application (day 0: 0.66 ± 0.45 ; day 28: 0.65 ± 0.37). However, there was no significant difference in the surface roughness between treatments.

Alterations of nail topography (roughness) could be derived from ridges (Beau's lines and onychorrhexis) but also nail pitting (Rosenau's depressions), produced by Alopecia areata, lichen, pemphigus, and psoriasis [13]. Regenail has been demonstrated to reduce roughness and improve signs of possible nail diseases.

A decrease in TOWL was observed after the application of REG and BET, but without significant differences. So, after 28 days of application of REG, the TOWL decreased by 6%. In the case of BET, the same parameter was decreased by 4% after 28 days of application. There was no significant difference in nail permeability between the treatments. The lack of TOWL changes in both formulations reflects a lack of structural nail alterations and the maintenance of physiological performance and integrity.

Other studies have also shown improvements in nail condition with topical formulations. For example, in one study, 10% urea lacquer was applied once or twice daily for 28 days. The study demonstrated significant improvements in nail surface morphology and nail plate consistency with the urea lacquer [56]. Previous clinical studies showed that hydroxypropyl-chitosan nail lacquer, when applied to fingernails, reduced longitudinal grooves, lamellar splitting, and nail fragility in women with nail plate alterations [57].

Our results are in accordance with those of other studies in which the authors were able to demonstrate that HP- β -CD enhanced the permeation of other compounds across the nail plate by virtue of increasing the nail hydration ability as well as the aqueous solubility of the drug without damaging

the nail plate integrity. This establishes the suitability of HP- β -CD as a nail-friendly transungual permeation enhancer for poorly water-soluble drugs [21]. Additionally, the results are in accordance with those of Cutrin-Gomez et al., whose in vivo study optimized a ciclopirox olamine lacquer based on similar cyclodextrin polypseudorotaxanes that was applied to the nails of healthy volunteers for 45 days, leading to no negative effects on the nail surface [58].

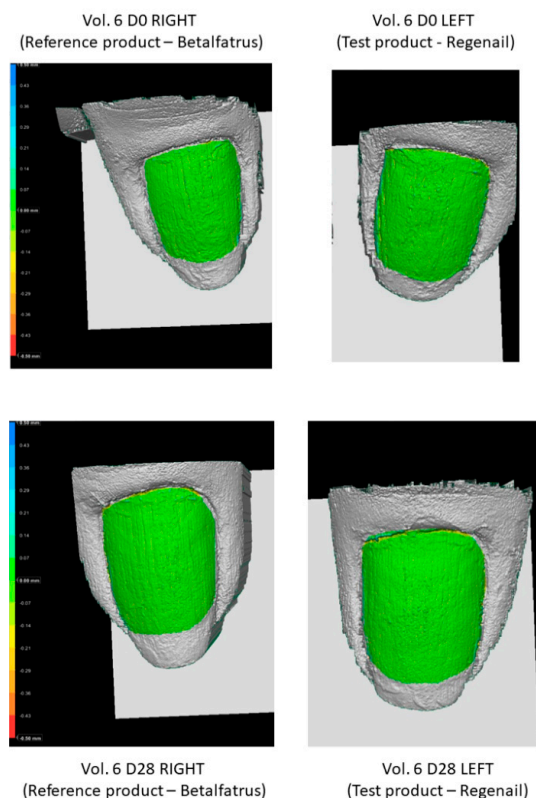


Figure 8. Nail images after the application of Betalfatrus and Regenail.

3.6. Self-Evaluation Questionnaire

Although the majority of subjects in this study considered fingernail resistance, smoothness, glossiness, growth, and general condition to be improved across all treatments, it can be seen that subjects rated REG higher than BET in terms of nail brittleness, nail smoothness, and moisturizing ability (Figure 9).

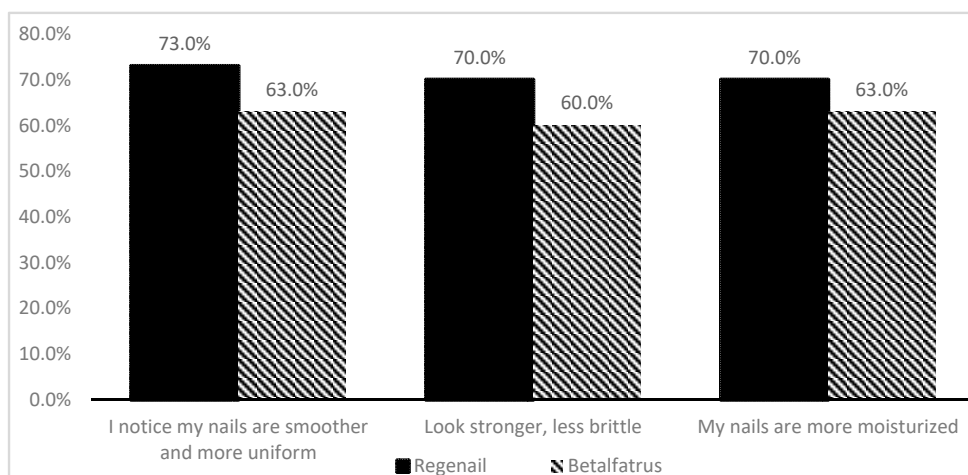


Figure 9. Subject assessment of the efficacy (by % of satisfied volunteers) of Regenail and Betalfatrus.

3.7. Safety Evaluation

None of the patients that started the study had any adverse effect (AE) during the study period, either pertaining to the treated area or system-wide. As no serious or treatment-related AEs leading to temporary or definitive discontinuation of the study were reported, it is possible to confirm that the treatments were well tolerated and demonstrated very good cutaneous compatibility. There are no particular safety concerns.

With the nail lacquer presented in this research, we demonstrated the good permeation profile of biotin with the proposed cyclodextrin polypseudorotaxanes vehicle. The water content of the product (around 35%) and the moisturizing effect of cyclodextrin led to adequate hydration of the nail. The higher water content of the liquid formulations is likely to hydrate the nail plate, generating more microporous channels for the permeant and therefore leading to an increased permeation of active ingredients. The active ingredients, MSM, biotin, and dimethylsilanediol salicylate, make the product a good candidate to treat nail alterations derived from ungual disease, such as psoriasis and onychomycoses. Further clinical studies should be performed to corroborate this hypothesis.

4. Conclusions

A new cyclodextrin polypseudorotaxanes nail lacquer, containing biotin, MSM, and dimethylsilanediol salicylate, was studied in vitro and in vivo. An improved transungual permeation profile was exhibited for both MSM and biotin, and increased amounts of sulfur and silicon were observed in the nail matrix after the studies. MSM demonstrated good anti-inflammatory activity in human keratinocytes, making it a promising product to treat nail inflammatory disorders. Clinical studies showed a good safety profile and efficacy on nail alterations, such as Beau's lines, with a smoothing effect on the ungual surface and improved moisturizing and hardness.

Author Contributions: Conceptualization, F.F.-C., F.J.O.-E., and J.P.; methodology, F.N., J.P., F.J.O.-E., and F.F.-C.; formal analysis, F.F.-C., F.N. and J.P.; investigation, F.N., J.P., F.J.O.-E., E.P., and F.F.-C.; resources, J.G.; writing—original draft preparation, F.F.-C. and A.C.; writing—review and editing, F.F.-C., F.J.O.-E., J.P., and A.C.; supervision, F.F.-C., F.J.O.-E., and J.P. All authors have read and agreed to the published version of the manuscript.

Funding: This research received no external funding.

Acknowledgments: We thank Zurko Bioresearch for clinical support.

Conflicts of Interest: This study was supported by Reig Jofre, Barcelona Spain. F.N., E.P., A.C., J.P., J.G., and F.F.-C. are employees of Reig Jofre. The funders had no role in the design of the study; in the collection, analyses, or interpretation of data; in the writing of the manuscript, or in the decision to publish the results. The authors are not involved in any commercial or marketing activities of the developed product.

References

1. Zaias, N.; Alvarez, J. The formation of the primate nail plate. An autoradiographic study in squirrel monkey. *J. Investig. Dermatol.* **1968**, *51*, 120–136. [[CrossRef](#)] [[PubMed](#)]
2. Dawber, R.P.R.; de Berker, D.A.R.; Baran, R. Science of the Nail Apparatus. In *Baran and Dawber's Diseases of the Nails and Their Management*; Baran, R., Dawber, R.P.R., de Berker, D.A.R., Haneke, E., Tosti, A., Eds.; Blackwell Science: Oxford, UK, 2001.
3. Garson, J.; Baltenneck, F.; Leroy, F.; Riekkel, C.; Müller, M. Histological structure of human nail as studied by synchrotron X-ray microdiffraction. *Cell. Mol. Biol.* **2000**, *46*, 1025–1034. [[PubMed](#)]
4. Murdan, S. Drug delivery to the nail following topical application. *Int. J. Pharm.* **2002**, *236*, 1–26. [[CrossRef](#)]
5. Chandra, S.; Das, A. The science of nail polish, nail polish remover and nail moisturizers. In *Nail Disorders, a Comprehensive Approach*; Sigla, A., Neema, S., Kumar, P., Eds.; Taylor & Francis: Boca Raton, FL, USA, 2019.
6. Colombo, V.E.; Gerber, F.; Bronhofer, M.; Floersheim, G.L. Treatment of brittle fingernails and onychoschizia with Biotin: Scanning electron microscopy. *J. Am. Acad. Dermatol.* **1990**, *23*, 1127–1132. [[CrossRef](#)]
7. Williamson, L.; Dalbeth, N.; Dockerty, J.L.; Gee, B.C.; Weatherall, R.; Wordsworth, B.P. Extended report: Nail disease in psoriatic Arthritis—Clinically important, potentially treatable and often overlooked. *Rheumatology* **2004**, *43*, 790–794. [[CrossRef](#)]

8. Zaias, N. *The Nail in Health and Disease*; Springer: Dordrecht, The Netherlands, 1980.
9. Ghannoum, M.A.; Hajjeh, R.A.; Scher, R.; Konnikov, N.; Gupta, A.K.; Summerbell, R.; Sullivan, S.; Daniel, R.; Krusinski, P.; Fleckman, P.; et al. A large-scale North American study of fungal isolates from nails: The frequency of onychomycosis, fungal distribution, and antifungal susceptibility patterns. *J. Am. Acad. Dermatol.* **2000**, *43*, 641–648. [[CrossRef](#)]
10. Haneke, E.; Roseeuw, D. The scope of onychomycosis: Epidemiology and clinical features. *Int. J. Dermatol.* **1999**, *38* (Suppl. 2), 7–12. [[CrossRef](#)]
11. Shemer, A. Non-dermatophytic onychomycosis. In *Nail Disorders, a Comprehensive Approach*; Sigla, A., Neema, S., Kumar, P., Eds.; Taylor & Francis: Boca Raton, Florida, 2019.
12. Baswan, S.; Kasting, C.B.; Li, S.K.; Wickett, R.; Adams, B.; Eurich, S.; Schamper, R. Understanding the formidable nail microstructure, composition, and diseases. *Mycoses* **2017**, *60*, 284–295. [[CrossRef](#)]
13. Bloom, R.; Tosti, A. The Clinical Features of Nail Psoriasis. In *Nail Psoriasis from A to Z*; Rigopoulos, D., Tosti, A., Eds.; Springer: Cham, Switzerland, 2014.
14. Yin, N.C.; Tosti, A. Differential diagnosis of nail psoriasis. In *Nail Psoriasis from A to Z*; Rigopoulos, D., Tosti, A., Eds.; Springer: Cham, Switzerland, 2014.
15. Del Rosso, J.Q. Current management of onychomycosis and dermatomycoses. *Curr. Infect. Dis. Rep.* **2000**, *2*, 438–445. [[CrossRef](#)]
16. Pinto, M.; Shenoy, M.M. Dermatophytic onychomycosis. In *Nail Disorders, a Comprehensive Approach*; Sigla, A., Neema, S., Kumar, P., Eds.; Taylor & Francis: Boca Raton, FL, USA, 2019.
17. Khengar, R.H.J.S.; Turner, R.B.; Forbes, B.; Brown, M.B. Nail swelling as a pre-formulation screen for the selection and optimisation of unguinal penetration enhancers. *Pharm Res.* **2007**, *24*, 2207–2212. [[CrossRef](#)]
18. Cutrín-Gómez, E.; Anguiano-Igea, S.; Delgado-Charro, M.B.; Gómez-Amoza, J.L.; Otero-Espinar, F.J. Effect of Penetration Enhancers on Drug Nail Permeability from Cyclodextrin/Poloxamer-Soluble Polypseudorotaxane-Based Nail Lacquers. *Pharmaceutics* **2018**, *10*, 273.
19. Sharma, N.; Baldi, A. Exploring versatile applications of cyclodextrins: An overview. *Drug Deliv.* **2016**, *23*, 739–757. [[CrossRef](#)] [[PubMed](#)]
20. Buschmann, H.J.; Schollmeyer, E. Applications of cyclodextrins in cosmetic products: A review. *J. Cosmet. Sci.* **2002**, *53*, 185–191. [[PubMed](#)]
21. Chouhan, P.; Saini, T.R. Hydroxypropyl- β -cyclodextrin: A Novel Transungual Permeation Enhancer for Development of Topical Drug Delivery System for Onychomycosis. *J. Drug Deliv.* **2014**, *2014*, 950358. [[CrossRef](#)]
22. Cutrín-Gómez, E.; Anguiano-Igea, S.; Delgado-Charro, M.B.; Gómez-Amoza, J.L.; Otero-Espinar, F.J. Otero-Espinar Effect on Nail Structure and Transungual Permeability of the Ethanol and Poloxamer Ratio from Cyclodextrin-Soluble Polypseudorotaxanes Based Nail Lacquer. *Pharmaceutics* **2018**, *10*, 156. [[CrossRef](#)]
23. Cutrín-Gómez, E.; Anguiano-Igea, S.; Gómez-Amoza, J.L.; Otero-Espinar, F.J. Evaluation of the promoting effect of soluble cyclodextrins in drug nail penetration. *Eur. J. Pharm. Sci.* **2018**, *117*, 270–278. [[CrossRef](#)]
24. Flagothier, C.; Piérard-Franchimont, C.; Piérard, G.E. New insights into the effect of amorolfine nail lacquer. *Mycoses* **2005**, *48*, 91–94. [[CrossRef](#)]
25. Nogueiras-Nieto, L.; Delgado-Charro, M.B.; Otero-Espinar, F.J. Thermogelling hydrogels of cyclodextrin/poloxamer polypseudorotaxanes as aqueous-based nail lacquers: Application to the delivery of triamcinolone acetonide and ciclopirox olamine. *Eur. J. Pharm. Biopharm.* **2013**, *83*, 370–377. [[CrossRef](#)]
26. Richmond, V.L. Incorporation of methylsulfonylmethane sulfur into guinea pig serum proteins. *Life Sci.* **1986**, *39*, 263–268. [[CrossRef](#)]
27. Williams, K.I.; Burstein, S.; Layne, D.S. Dimethyl sulfone: Isolation from human urine. *Arch. Biochem. Biophys.* **1966**, *113*, 251–252. [[CrossRef](#)]
28. Butawan, M.; Benjamin, R.L.; Bloomer, R.J. Methylsulfonylmethane: Applications and Safety of a Novel Dietary Supplement. *Nutrients* **2017**, *9*, 290. [[CrossRef](#)] [[PubMed](#)]
29. Reffitt, D.M.; Ogston, N.; Jugdaohsingh, R.; Cheung, H.F.; Evans, B.A.; Thompson, R.P.; Powell, J.J.; Hampson, G.N. Orthosilicic acid stimulates collagen type 1 synthesis and osteoblastic differentiation in human osteoblast-like cells in vitro. *Bone* **2003**, *32*, 127–135. [[CrossRef](#)]
30. Araújo, L.A.; Addor, F.; Campos, P.M. Use of silicon for skin and hair care: An approach of chemical forms available and efficacy. *An. Bras. Dermatol.* **2016**, *91*, 331–335. [[CrossRef](#)]

31. Barel, A.; Calomme, M.; Timchenko, A.; De Paepe, K.; Demeester, N.; Rogiers, V.; Clarys, P.; Berghe, D.V. Effect of oral intake of choline-stabilized orthosilicic acid on skin, nails and hair in women with photodamaged skin. *Arch. Dermatol. Res.* **2005**, *297*, 147–153. [CrossRef] [PubMed]
32. Floersheim, G.L. Treatment of brittle fingernails with Biotin. *Zeitschrift fur Hautkrankh.* **1989**, *64*, 41–48.
33. Hochman, L.G.; Scher, R.K.; Meyerson, M.S. Brittle nails: Response to daily Biotin supplementation. *Cutis* **1993**, *51*, 303–305.
34. Lipner, S.R.; Scher, R.K. Biotin for the treatment of nail disease: What is the evidence? *J. Dermatol. Treat.* **2018**, *29*, 411–414. [CrossRef]
35. Palliyil, B.B.; Li, C.; Owaisat, S.; Lebo, D.B. Lateral drug diffusion in human nails. *AAPS PharmSciTech.* **2014**, *15*, 1429–1438. [CrossRef]
36. International Organization for Standardization I. Biological Evaluation of Medical Devices—Part 5: Tests for In Vitro Cytotoxicity. 2009. Available online: http://www.iso.org/iso/home/store/catalogue_tc/catalogue_detail.htm?csnumber=36406 (accessed on 9 October 2019).
37. Morgan, D.M. Tetrazolium (MTT) assay for cellular viability and activity. *Methods Mol. Biol.* **1998**, *79*, 179–183.
38. Chomczynski, P. A reagent for the Single-Step simultaneous isolation of RNA, DNA and proteins from cell and tissue samples. *Biotechniques* **1993**, *15*, 532–534.
39. Pfaffl, M.W. A new mathematical model for relative quantification in real-time RT-PCR. *Nucleic Acids Res.* **2001**, *29*, e45. [CrossRef] [PubMed]
40. ICH. Available online: https://www.ema.europa.eu/en/documents/scientific-guideline/ich-q-1-e-evaluation-stability-data-step-5_en.pdf (accessed on 30 June 2020).
41. Schneider, H.J.; Hacket, F.; Rüdiger, V.; Ikeda, H. NMR studies of cyclodextrins and cyclodextrin complexes. *Chem. Rev.* **1998**, *98*, 1755–1786. [CrossRef] [PubMed]
42. Otero-Espinar, F.J.; Luzardo-Álvarez, A.; Mendez, J. Cyclodextrins: More than Pharmaceutical Excipients. *Mini Rev. Med. Chem.* **2010**, *10*, 715–725. [CrossRef] [PubMed]
43. Loeper, J.; Lemaire, A. Study of silicium in animal biology and during atheroma. *La Presse Medicale* **1966**, *74*, 865–868. [PubMed]
44. Paillet, C. Application of silicium for cosmetics. Interest of silanols in cosmetics: Silanols and cutaneous aging. *Fragr. J.* **2000**, *28*, 27–31.
45. Matsumoto, K. Application of silicium for cosmetics. Physiological activities of silicium. *Fragr. J.* **2000**, *28*, 32–48.
46. Lassus, A. Colloidal silicic acid for oral and topical treatment of aged skin, fragile hair and brittle nails in females. *J. Int. Med Res.* **1993**, *21*, 209–215. [CrossRef]
47. EFSA Panel on Dietetic Products, Nutrition and Allergies (NDA). Scientific Opinion on the substantiation of health claims related to methylsulphonyl methane (MSM) and contribution to normal collagen formation (ID 353, 388, 389, 394, **1695**, 1741, 1874), maintenance of normal hair (ID 353, 1741, 1874), maintenance of normal nails (ID **1695**, 1741, 1874), maintenance of normal acid-base balance (ID 387), “strengthens the immune system function” (ID 390), maintenance of normal bowel function (ID 391), contribution to the normal cysteine synthesis (ID 392) and “vitamin production needed for correct function of metabolism” (ID 393) pursuant to Article 13(1) of Regulation (EC) No 1924/2006. *EFSA J.* **2010**, *8*, 1746. [CrossRef]
48. Ahn, H.; Kim, J.; Lee, M.J.; Kim, Y.J.; Cho, Y.W.; Lee, G.S. Methylsulfonylmethane inhibits NLRP3 inflammasome activation. *Cytokine* **2015**, *71*, 223–231. [CrossRef]
49. Kim, Y.H.; Kim, D.H.; Lim, H.; Baek, D.Y.; Shin, H.K.; Kim, J.K. The anti-inflammatory effects of methylsulfonylmethane on lipopolysaccharide-induced inflammatory responses in murine macrophages. *Biol. Pharm. Bull.* **2009**, *32*, 651–656. [CrossRef]
50. Goldminz, A.M.; Au, S.C.; Kim, N.; Gottlieb, A.B.; Lizzul, P.F. NF-kappaB: An essential transcription factor in psoriasis. *J. Dermatol. Sci.* **2013**, *69*, 89–94. [CrossRef] [PubMed]
51. Zhang, M.; Wong, I.G.; Gin, J.B.; Ansari, N.H. Assessment of methylsulfonylmethane as a permeability enhancer for regional EDTA chelation therapy. *Drug Deliv.* **2009**, *16*, 243–248. [CrossRef] [PubMed]
52. Scher, R.K. Evaluation of nail lines: Color and shape hold clues. *Clevel. Clin. J. Med.* **2016**, *83*, 385. [CrossRef]
53. Braswell, M.A.; Daniel III, C.R.; Brode II, R.T. Beau lines, onychomadesis, and retronychia: A unifying hypothesis. *J. Am. Acad. Dermatol.* **2015**, *73*, 849–855. [CrossRef] [PubMed]
54. Tucker, J.R. Nail Deformities and Injuries. *Prim. Care Clin. Off. Pract.* **2015**, *42*, 677–691. [CrossRef]

55. Chessa, M.A.; Iorizzo, M.; Richert, B.; López-Esteban, J.L.; Rigopoulos, D.; Tosti, A.; Gupta, A.K.; Di Chiacchio, N.; Di Chiacchio, N.G.; Rubin, A.I.; et al. Pathogenesis, Clinical Signs and Treatment Recommendations in Brittle Nails: A Review. *Dermatol. Ther.* **2020**, *10*, 15–27. [[CrossRef](#)]
56. Krueger, N.; Reuther, T.; Williams, S.; Kersch, M. Effect of urea nail lacquer on nail quality. Clinical evaluation and biophysical measurements. *Der Hautarzt Zeitschrift für Dermatol. Venerol. Verwandte Geb.* **2007**, *57*, 1089–1094.
57. Sparavigna, A.; Setaro, M.; Genet, M.; Frisenda, L. Equisetum arvense in a new transungual technology improves nail structure and appearance. *J. Plast. Dermatol.* **2006**, *2*, 31–38.
58. Cutrín-Gómez, E.; Conde-Penedo, A.; Anguiano-Igea, S.; Gómez-Amoza, J.L.; Otero-Espinar, F.J. Optimization of Drug Permeation from 8% Ciclopirox Cyclodextrin/Poloxamer-Soluble Polypseudorotaxane-Based Nail Lacquers. *Pharmaceutics* **2020**, *12*, 231. [[CrossRef](#)]



© 2020 by the authors. Licensee MDPI, Basel, Switzerland. This article is an open access article distributed under the terms and conditions of the Creative Commons Attribution (CC BY) license (<http://creativecommons.org/licenses/by/4.0/>).

